

CYRIC
ANNUAL REPORT
2001

(January 2001 - December 2001)

CYCLOTRON AND RADIOISOTOPE CENTER
TOHOKU UNIVERSITY
<http://www.cyric.tohoku.ac.jp/>

1901

ANNUAL REPORT

1901

THE UNIVERSITY OF CHICAGO

UNIVERSITY OF CHICAGO
LIBRARY
540 EAST 57TH STREET
CHICAGO, ILL.

PREFACE

In this twenty-second issue of the CYRIC Annual Report, we summarize the activities for research and development and results of training for radioisotope safe-treatment at Cyclotron and Radioisotope Center (CYRIC) during the calendar year 2001.

Research programs in various fields such as nuclear physics, nuclear chemistry, solid state physics and element analyses by PIXE and activation were carried out, and radioisotopes were produced for use in biology and medicine. Several facility improvements have been carried out as well. A total of 2000 hours of the cyclotron beam-time was delivered for the scheduled operation for research works. It is plausible to point out that some scientific yields by the new K=110 MeV AVF cyclotron have been produced as reported in this issue.

Synthesis of radiopharmaceuticals for clinical research with PET (Positron Emission Tomography) and other applications have been continuously carried out. Positron emitting radio-nuclides were provided with 308 hours exposure by 12-MeV proton beams from the HM-12 cyclotron, while those by 6-MeV deuteron beams were done with 217 hrs exposure.

Among the various research programs, studies with PIXE technique have been continuously carried out by using electrostatic accelerator, installed at FNL (Fast Neutron Laboratory) in Graduate School of Technology, Tohoku University, under the scientific tie up between CYRIC and FNL. Indeed, more than nine groups are running under this project using a total of its 300 hours beam-time.

During 2001 school year, 576 of staff members and students of Tohoku University were trained in the beginner's course of safe handling of radiation and radioisotopes, while

215 staff members and students in the "x-ray course". In addition, 82 of staff members and students were trained in the course of safe handling of radiation from a SOR.

Vision of Cyclotron and Radioisotope Center (CYRIC), at the Beginning of the 21st Century, is as follows: CYRIC supports/participates in Education and Research at Tohoku University in the fields of multidisciplinary-use of the AVF-cyclotron and short-lived/high-level Radioisotopes. The other important aim of this Institute is to play a role as the Center of Tohoku University in the Safe-handling/control of Radiation/Radioactivity, together with training of beginners in the whole university scale. At the same time, CYRIC promotes and develops its own research programs, joining directly in the Educational and research programs of Faculties and Graduate Schools. Researches in this Institute cover broad academic fields, such as Material-science, the particle/nuclear physics in particular and Life-science, from basic to clinical medicine, and the Environmental science. As such, CYRIC takes a part in the cutting-edge scientific researches playing an active part in the Global and international standard through the collaborations with the scientists of Tohoku University and other organizations, including those from abroad. Since the AVF-cyclotron and related experimental equipment in CYRIC are one of the most powerful and unique facilities in the world, it is our mission to establish those as the Intelligent Infrastructures of Tohoku University to be a Distinctive University in the Competitive Environments, also taking consideration of the Public Opinions. Under the mission of the Tohoku University, which is going to reform itself as a New Independent and Autonomous Structure, CYRIC will share its roles in development from the Seedling stage to promote Interdisciplinary researches as well as in Nurturing talents of student for the Leaders of the next generation.

We are very grateful to Tohoku University and to the Ministry of Education, Sports, Culture, Science and Technology for their continuous support.

January, 2002

Hikonojo ORIHARA

Director

Cyclotron and Radioisotope Center, Tohoku University

EDITORS:

<i>Hikonojo</i>	ORIHARA
<i>Tatsuo</i>	IDO
<i>Masatoshi</i>	ITOH
<i>Mamoru</i>	BABA
<i>Tsutomu</i>	SHINOZUKA

WORD PROCESSED BY

Yu-ko YAMASHITA

Year	Value
1998	100
1999	100
2000	100
2001	100
2002	100
2003	100
2004	100
2005	100
2006	100
2007	100
2008	100
2009	100
2010	100
2011	100
2012	100
2013	100
2014	100
2015	100
2016	100
2017	100
2018	100
2019	100
2020	100
2021	100
2022	100
2023	100
2024	100
2025	100
2026	100
2027	100
2028	100
2029	100
2030	100

CONTENTS

I. PHYSICS AND TECHNOLOGY

- I. 1. ${}^6\text{Li}(p,n){}^6\text{Be}$ Reaction at $E_p = 70$ MeV..... 1
Kumagai K., Orihara H., Kikuchi Y., Fujisawa H., Uemori T., Sugimoto N., Suzuki H., Terakawa A., Ishii K., and Ohnuma H.
- I. 2. Excitation of the Lowest 0^+ State in ${}^{12}\text{N}$ through the $(\Delta J, \Delta L, \Delta S) = (0, 1, 1)$ Channel in the (p, n) Reaction on ${}^{12}\text{C}$ at $E_p = 35$ MeV..... 8
Orihara H., Kikuchi Y., Kumagai K., Fujisawa H., Uemori T., Sugimoto N., Suzuki H., Terakawa A., Ohnuma H., and Sagawa H.
- I. 3. ${}^{12}\text{C}(p,n){}^{12}\text{N}$ Reaction at $E_p = 70$ MeV: Reliability of the information obtained from DWBA analysis of 70-MeV (p, n) data..... 13
Kikuchi Y., Orihara H., Kumagai K., Fujisawa H., Uemori T., Sugimoto N., Suzuki H., Terakawa A., Ishii K., and Ohnuma H.
- I. 4. Isospin Excitations in Nuclei via the ${}^{42,44,48}\text{Ca}(p,n){}^{42,44,48}\text{Sc}$ Reactions..... 18
Suzuki H., Orihara H., Terakawa A., Itoh K., Kumagai K., Kikuchi Y., Fujisawa H., Uemori T., Sugimoto N., Maeda K., Katoh M., Ohnuma H., and Sagawa H. Terakawa A., Tanigaki M., Itoh K., Fujita M., Shinozuka T., and Orihara H.
- I. 5. Present Status of the 14.5 GHz ECR Ion Source at CYRIC..... 26
Yamazaki A., Tanaka E., Fujita M., and Shinozuka T.
- I. 6. Up Grated CYRIC Sinusoidal Beam Chopper for Fast-neutron TOF Experiment 29
Terakawa A., Tanigaki M., Itoh K., Fujita M., Shinozuka T., and Orihara H.
- I. 7. Development of Low-Pressure MWPC..... 35
Ozeki K., Otsu H., Okuda T., Watanabe K., Yakushiji T., Iwasa N., and Kobayashi T.
- I. 8. Development of the new tape transport system for ISOL..... 39
Fujita M., Ohshima T., Yamazaki A., Sonoda T., Goto A., Watanabe S., Tanaka E. and Shinozuka T.
- I. 9. Simultaneous Acquisition of Emission and Transmission Data in PET..... 45
Watanuki S., Ishii K., Itho M., and Orihara H.

I. 10.	Development of the Magnetic Aluminum Shield for MEG.....	49
	<i>Suzuki A., Ishii K., Yamazaki H., Matsuyama S., Aikawa K., Momose G., Watanuki S., Itoh M., and Orihara H.</i>	
I. 11.	Scatter Correction for 3D PET Based on Image Subtraction Method.....	54
	<i>Oishi Y., Sasaki K., Ishii K., Yamazaki H., Matsuyama S., Kikuchi Y., Rodriguez M., Aihara T., Yamaguchi T., Watanuki S., Itoh M., and Orihara H.</i>	
I. 12.	Research on the Development of a Method to Obtain the Attenuation Coefficients for Positron Emission Tomography Using the Single Event Rate.....	59
	<i>Rodriguez M., Ishii K., Yamazaki H., Matsuyama S., Kikuchi Y., Oishi Y., Aihara T., Yamaguchi T., Watanuki S., Itoh M., and Orihara H.</i>	
I. 13.	Measurement of the Row Energy Detection Efficiency of a Si(Li) Detector for PIXE Applications.....	64
	<i>Rodriguez M., Yonezawa T., Ishii K., Matsuyama S., Yamazaki H., Sato T., Amartaivan Ts., Sugihara S., Tanaka A., Kato K., and Komori Y.</i>	
I. 14.	Application of PIXE Analysis to Elemental Study of Drinking Water Supply.....	71
	<i>Yamazaki H., Ishii K., Amartaivan Ts., Matsuyama S., Takahashi Y., Satoh T., and Orihara H.</i>	
I. 15.	Development of a Mini Step Sumpier for Air-Pollution Monitoring.....	79
	<i>Matsuyama S., Sugihara S., Ishii K., Yamazaki H., Katoh K., Satoh T., Amartaivan Ts., Tanaka A., Komori H., Orihara H., Nakamura E., Satoh N., Futatsugawa S., and Sera K.</i>	
I. 16.	Coloration of Polyethylene Terephthalate (PET) Film by 3MeV Proton Beams.....	85
	<i>Matsuyama S., Ishii K., Yamazaki H., Endoh H., Yuki H., Satoh T., Sugihara S., Amartaivan Ts., Tanaka A., Komori H., and Orihara H.</i>	
I. 17.	PIXE Analysis of Trace Heavy-Metals in River Water Using an Ion-Exchange Cellulose Filter Paper.....	93
	<i>Amartaivan Ts., Yamazaki H., Ishii K., Matsuyama S., Takahashi Y., Satoh T., and Orihara H.</i>	

II. CHEMISTRY

II. 1.	Concentrations of Technetium-99 in Soils and Plants Collected in Forests within the 30-km Zone around Chernobyl Area.....	104
	<i>Tagami K., Uchida, S. and Sekine T.</i>	
II. 2.	A Simple On-column Preparation of [¹⁸ F]Fluorocholine from [¹⁸ F]Fluoromethyl Triflate.....	109
	<i>Iwata R., Furumoto S., Pascali C., Bogni A., Terasaki K., and Yanai K.</i>	

III. MEDICINE AND BIOLOGY (Basic)

- III. 1. Development of ¹⁸F-Labeled Matrix Metalloproteinase Inhibitors for Tumor Imaging by PET.....112
Furumoto S., Iwata R., Kubota K., Fukuda H., and Ido T.
- III. 2. Effect of Angiotensin -Converting Enzyme Inhibitor against MPTP Neurotoxicity in Mice : an Immunohistochemical Study.....116
Kuroski R., Muramatsu Y., Watanabe H., Michimata M., Matsubara M., Imai Y., Kimura S., and Araki T.
- III. 3. Neuroprotective Effect of Riluzole Against MPTP Neurotoxicity in Mice.....123
Muramatsu Y., Kuroski R., Watanabe H., Michimata M., Matsubara M., Imai Y., Kimura S., and Araki T.
- III. 4. Neuronal Nitric Oxide Synthase Inhibitor and Monoamine Oxidase B Inhibitor Attenuate MPTP Neurotoxicity.....129
Watanabe H., Muramatsu Y., Kuroski R., Michimata M., Matsubara M., Imai Y., Kimura S., and Araki T.

IV. MEDICINE AND BIOLOGY (Clinical)

- IV. 1. Raclopride and FDG PET Findings in Two Patients with Alzheimer's Disease with Behavioral and Psychological Symptoms of Dementia.....144
Tanaka Y., Meguro K., Yamaguchi S., Yamadori A., Yamaguchi K., and Itoh M.
- IV. 2. FDG-PET Study of Patient with a Novel Presenilin-1 Mutation in the Mild Cognitive Impairment Stage of Alzheimer's Disease.....150
Maruyama M., Matsushita S., Arai H., Okamura N., Ohmori T., Takasugi K., Matsui T., Iwatsubo T., Higuchi S., and Sasaki H.
- IV. 3. Imaging of Histamine H1 Receptors in Human Brain and Impaired Cognitive Performance Induced by Second Generation Antihistamines.....155
Tashiro M., Mochizuki H., Sakurada Y., Iwabuchi K., Kato M., Itoh M., and Yanai K.
- IV. 4. Neural mechanism of impaired visuomotor coordination by sedative antihistamine: A human PET study.....160
Mochizuki H., Tashiro M., Kano M., Itoh M., and Yanai K.

V. RADIATION PROTECTION AND TRAINING OF SAFE HANDLING

- V. 1. Application of an Imaging Plate to Radiation Dosimetry.....165
Ohuchi H. and Yamadera A.
- V. 2. Neutron Emission Spectrum and ^7Be Production in (d+Li, d-Be) Reaction with Thick Targets for 25 MeV Deuterons.....170
Aoki T., Hagiwara M., Baba M., Yonai S., Kawata N., Miura T., and Nakamura T.
- V. 3. Development of an Accelerator Beam Loss Monitor Using an Optical Fiber.....177
Kawata N., Baba M., Kato M., Miura T., and Yamadera A.
- V. 4. Training for Safe handling of Radiation and Radioisotopes and X-Ray Machines for Beginners in Tohoku University.....184
Baba M., Yamadera A., Miyata T., and Nakamura T.
- V. 5. Radiation Protection and Management.....187
Miyata T., Yamadera A., Baba M., Nakamura T., and Watanabe N.

VI. PUBLICATIONS

VII. MEMBERS OF COMMITTEE

VIII. PERSONNEL

I. PHYSICS AND TECHNOLOGY

THE UNIVERSITY OF CHICAGO

I. 1. ${}^6\text{Li}(p,n){}^6\text{Be}$ Reaction at $E_p = 70$ MeV

*Kumagai K., Orihara H., Kikuchi Y., Fujisawa H., Uemori T., Sugimoto N., Suzuki H.,
Terakawa A., Ishii K.*, and Ohnuma H.***

*Cyclotron and Radioisotope Center, Tohoku University
Department of Quantum Engineering, Tohoku University*
Department of Physics, Chiba Institute of Technology***

Because of their simple structure consisting of ${}^4\text{He}$ plus two nucleons, the mass 6 system provide a good place to explore the effective nucleon-nucleon interaction through, for example, charge-exchange scattering. ${}^6\text{Li}$ nucleus is only the odd-odd target which provides a strong $1^+ \rightarrow 0^+$ GT-like transition in a pure manner for scattering experiments. A number of experiments have been reported concerning nucleon and electron scattering, as well as charge-exchange reaction on ${}^6\text{Li}^{1-4}$. However, there should be interesting higher excited states, for which two nucleons are excited through a different type of spin-isospin excitation.

From the view points of effective nucleon-nucleon interaction between particles or particle-hole in such a simple system, it is significant to extend scattering experiments over high-lying states whereas no reliable data have not yet reported for the transitions including to the first excited state in ${}^6\text{Be}$. Petrovich and his collaborators have reported⁵⁾ consistent folding model descriptions of nucleon elastic, inelastic and charge-exchange scattering from ${}^6,7\text{Li}$ at 25-50 MeV.

In this report, we discuss spin-isospin excitation in nuclei through the ${}^6\text{Li}(p,n){}^6\text{Be}$ reaction by observing the transitions to the ground 0^+ state, 1.67-MeV 2^+ state and to the possible highly lying states. Observed neutron spectra are interpreted by particle-hole excitation and three- and four-body break up processes. Angular distributions of the differential cross section leading to the definite states are analyzed with distorted wave (DW) Born approximation, where one-body-transition-density (OBTD) has been obtained by full-space shell-model calculations.

The experiment was performed at the Cyclotron and Radioisotope Center, Tohoku

University, with a 70-MeV proton beam from the K=110MeV AVF-cyclotron and the new beam swinger system⁶. The details of the experimental setup have been described Ref. 6. Neutron energies were measured by the time-of-flight technique (TOF), where neutrons were detected by a detector array consisting of 16 pieces of the disk type detector located at 44.3 m from the target. The detectors were filled with 25.1-liter organic liquid scintillator BC501A in the total sensitive volume. The absolute efficiencies of the detectors were obtained from the ${}^7\text{Li}(p,n){}^7\text{Be}$ activation analyses with an error less than $\pm 6\%$. Errors in the absolute magnitude of (p,n) cross sections were estimated to be less than 12%. The target was a metallic foil of ${}^6\text{Li}$ isotopes with enrichments better than 95%.

Figure 1 illustrates the neutron excitation-energy spectrum measured at a laboratory angle of 30 degree for the ${}^6\text{Li}(p,n){}^6\text{Be}$ reaction at $E_p = 70$ MeV. Curves in the figure are results of the phase space calculation for three- and four-body break up, and those of peak fitting for the low-lying together with the high-lying proposed states. It is noticeable that extra states other than ground and 1.67-MeV states are seen at $E_x = 3, 15$ and 25 MeV as shown more clearly in the back-ground subtracted overlaid figure.

The angular distributions of neutrons for the (p,n) reactions leading to these five states are illustrated in Figs. 2 through 6 along with theoretical calculations. The data are compared with microscopic DW results calculated by the computer code DWBA-74⁷, which includes knock-on exchange effects in an exact manner. Note that fully antisymmetrized calculations were made in the present microscopic DW analysis, in which non-normal parity terms also contribute to the cross section. Optical potential parameters of Nadasen et al.⁸) were used for the entrance channel. Those for the exit channel were potential parameters derived by Varner et al.⁹) The effective nucleon-nucleon interactions used in the present DW analysis were those by Love and Franey¹⁰). Spectroscopic amplitudes (OBTD) for the microscopic DWBA analysis were obtained from full spsd shell model calculations using the code OXBASH¹¹) with the A-dependent interaction of Cohen, Kurath and Millener¹²). Single-particle radial wave functions used in DW calculations were generated in a harmonic-oscillator potential with $\alpha = 0.625 \text{ fm}^{-1}$.

Figure 2 shows experimental and theoretical angular distributions of the differential cross section for the (p,n) reaction to the 0^+ ground state of ${}^6\text{Be}$. Four kinds of DW calculations are shown. "pm3y(LF-100)" denotes that the (p,n) calculation is carried out by Love - Franey 100MeV effective interaction with OBTD obtained by the M3Y interaction in the p-shell space, while "spsd(LF-50)" corresponds to the calculation by Love

- Franey 50MeV effective interaction with OBTD by Cohen, Kurath and Millener interaction over the large spsd-shells space. The cross section magnitude at 0-degree is explained reasonably by these calculations. Over all fitting is obtained by the set of spsd(LF-100) like the case in the $^{12}\text{C}(p,n)^{12}\text{N}$ reaction as reported in Cyric Annual Report 2001 in this issue¹³. Here after analyses are carried out by the set of spsd(LF-100) including negative parity transitions.

In Fig. 3, we present the angular distribution of neutrons leading to the 2^+ first excited state in ^6Be along with theoretical curves. This state is assigned to be the first 2^+ state in the shell-model prediction. There are three components in the 1^+ to 2^+ transition contributing incoherently to the cross section. The $\Delta J = 1$ component, the main part in which is $\Delta J(\Delta L, \Delta S) = 1(0,1)$ GT-transition, dominates over small angle cross section, while the $\Delta J = 3$ component does those at larger angles. An extra peak is firstly observed at $E_x \sim 3\text{MeV}$ in the (p,n) spectrum. The angular distribution in Fig. 5 shows forward peaked one suggesting an $\Delta L = 0$ transition. We tentatively assign this state to be the second 2^+ state predicted by the shell-model. Other transitions to the 1^+ and 0^+ states give much smaller theoretical cross sections. As illustrated in Fig. 4, the $\Delta J = 1$ component dominates over small angle cross section, while the $\Delta J = 2$ component does those at larger angles. Note that observed cross sections are absolutely fitted.

As seen in Fig. 1, two broad peaks have been observed at $E_x \sim 15$ and 25MeV . These transitions are tentatively assigned to the fourth 1^- , and the fifth 2^- states predicted by the shell-model calculations. Of course, the main contribution to the continuum in the neutron spectrum in Fig. 1 is due to the $\Delta L=1$ dipole transition¹⁴. Among them, some transitions give strong intensities, thus exhibiting broad peaks, e.g. $E_x \sim 15$ and 25MeV , as mentioned above. Comparison with theoretical predictions are shown in Figs. 5 and 6.

In a summary, the experimental study for the $^6\text{Li}(p,n)^6\text{Be}$ reaction has carried out at $E_p=50 \sim 80$ MeV region. Differential cross sections of neutrons leading to the five states in the residual nucleus were measured. Results have been compared with the large-space shell-model prediction based on DW theory. The newly observed low-lying state at $E_x=3\text{MeV}$ has been tentatively assigned to be 2^+ , $T=1$ one. Two broad bump observed at $E_x=15$ and 25MeV were discussed as 1^- and 2^- components of the $\Delta L=1$ giant resonance. This work is supported by grant in aid for scientific research of Ministry of Education, Culture, Sports, and Science and Technology No.13640257.

References

- 1) Batty C. J. et al., Nucl. Phys. **A120** (1968) 297.
- 2) Rapaport J. et al., Phys. Rev. **C41** (1990) 1920.
- 3) Glover C. W. et al., Phys. Rev. **C41** (1990) 2487.
- 4) Glover C. W. et al., Phys. Rev. **C43** (1991) 1664.
- 5) Petrovich F. et al., Nucl. Phys. **A563** (1993) 387.
- 6) Terakawa A. et al., Nucl. Instrum. and Methods **A491** (2002) 419.
- 7) R. Schaeffer and J. Raynal, the computer program DWBA70 unpublished.
- 8) Nadasen A. et al., Phys. Rev. **C 23** (1981) 1023.
- 9) Varner et al., Phys. Rep. **201** (1991) 57.
- 10) Franey M. A. and Love W. G., Phys. Rev. **C 31** (1985) 488.
- 11) The shell model code OXBASH, Echevoya A. E., National Superconducting Cyclotron Laboratory Report No. 524 (1984).
- 12) Kohen S. and Kurath D., Nucl. Phys. **A101** (1967) 1.
Millener D. J. and Kurath D. Nucl. Phys. **A255** (1975) 315.
- 13) Kikuchi Y. et al., CYRIC Ann. Rep. 2001.
- 14) Yang X. et al., Phys. Rev. **C 52** (1995) 2535.

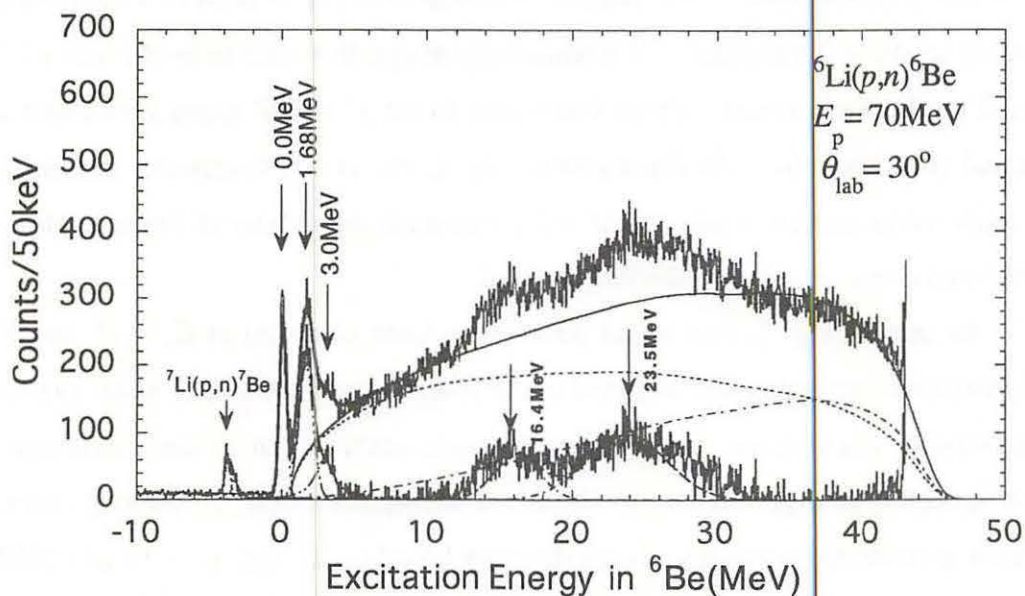


Fig. 1. A sample excitation energy spectrum from the ${}^6\text{Li}(p,n){}^6\text{Be}$ reaction taken at 30° with a flight path of 44.3 m. Energy per bin is 50 keV.

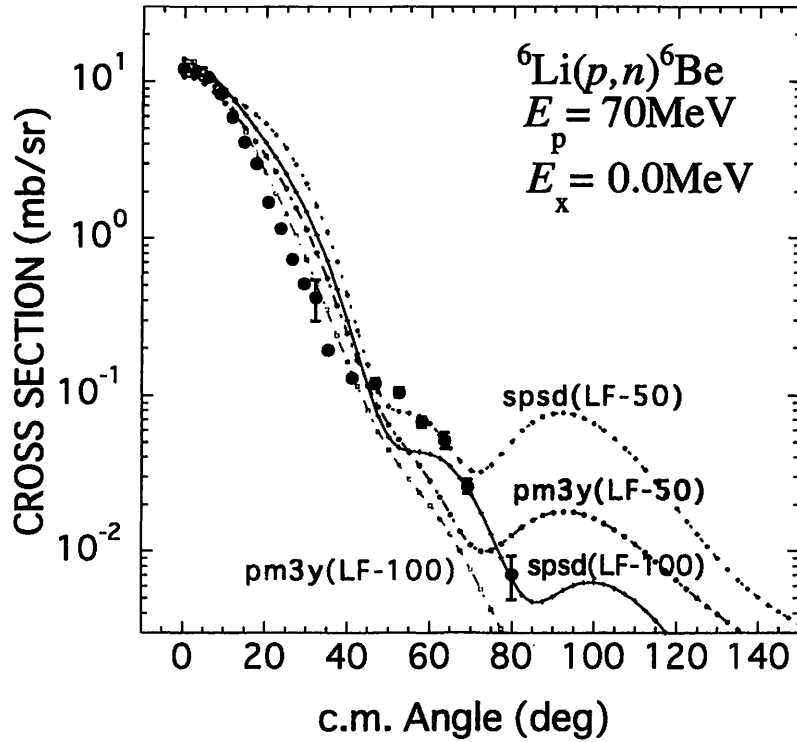


Fig. 2. Differential cross sections for neutrons leading to the ground state of ${}^6\text{Be}$.

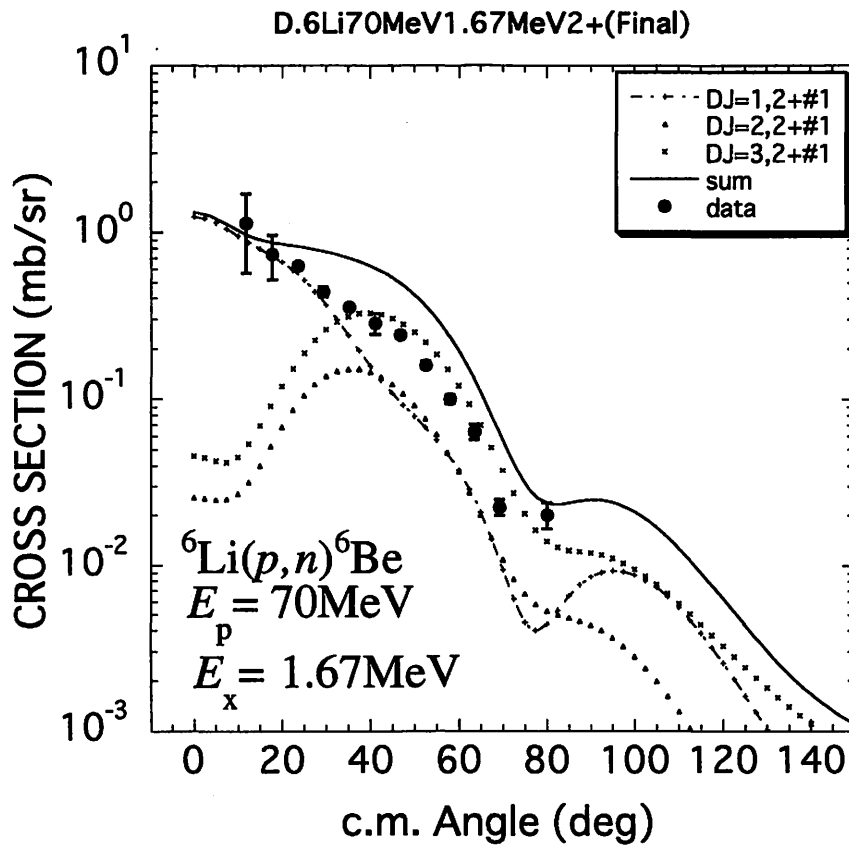


Fig. 3. Differential cross sections for neutrons leading to the 1st excited state in ${}^6\text{Be}$.

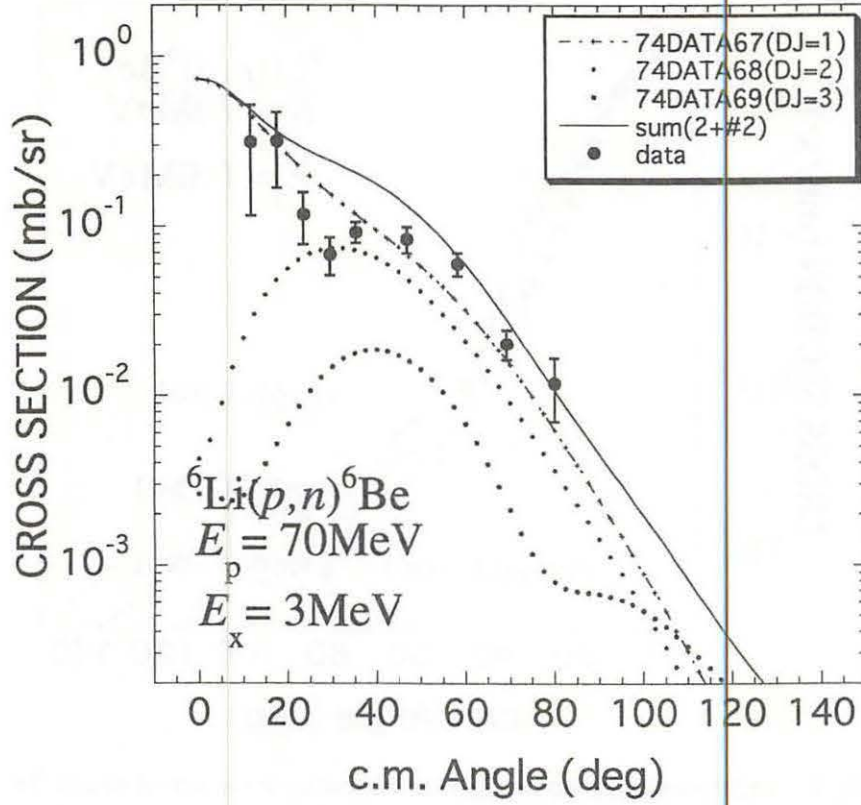


Fig. 4. Differential cross sections for neutrons leading to the excited state at $E_x = 3\text{MeV}$ in ${}^6\text{Be}$.

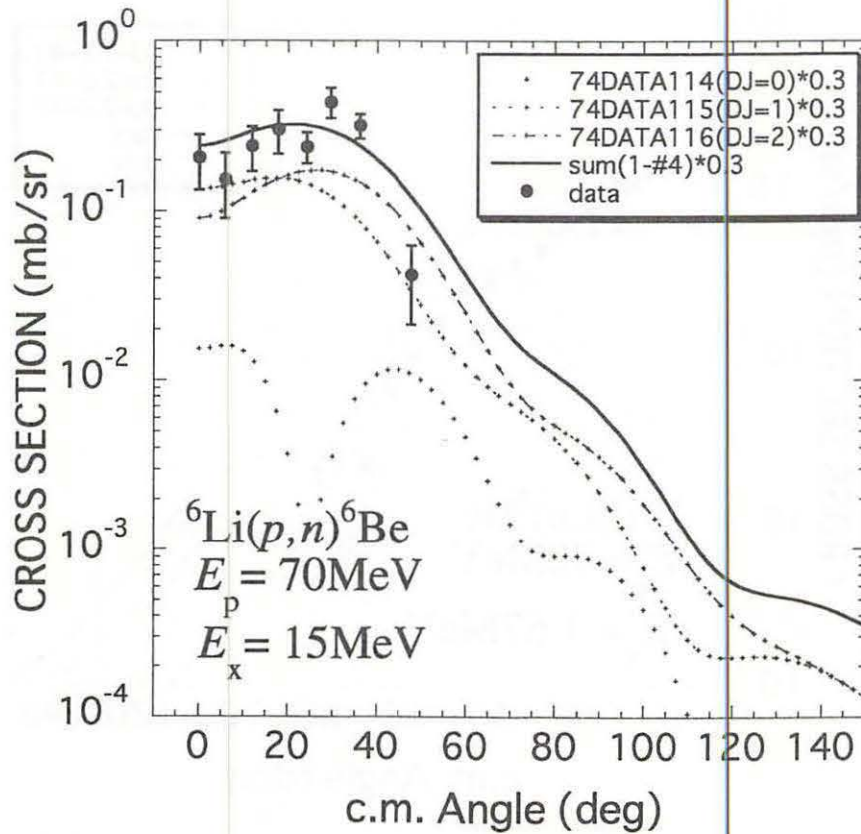


Fig. 5. Differential cross sections for neutrons leading to the excited state at $E_x = 15\text{MeV}$ in ${}^6\text{Be}$.

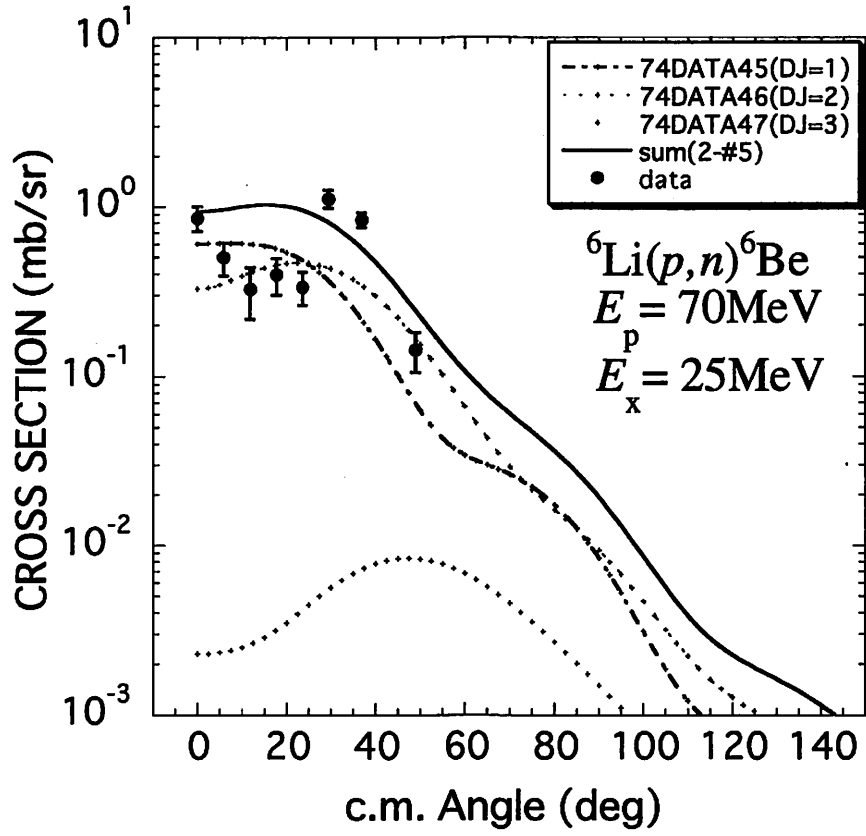


Fig. 6. Differential cross sections for neutrons leading the excited state at $E_x = 25\text{MeV}$ in ${}^6\text{Be}$.

I. 2. Excitation of the Lowest 0^+ State in ^{12}N through the $(\Delta J, \Delta L, \Delta S) = (0, 1, 1)$ Channel in the (p, n) Reaction on ^{12}C at $E_p = 35\text{MeV}$

Orihara H., Kikuchi Y., Kumagai K., Fujisawa H., Uemori T., Sugimoto N., Suzuki H., Terakawa A., Ohnuma H.* , and Sagawa H.**

*Cyclotron and Radioisotope Center, Tohoku University
Department of Physics, Chiba Institute of Technology*
Center of Mathematical Science, The University of Aizu***

The (p, n) reaction is a promising tool to study the isospin and spin-isospin excitation modes in nuclei, such as the isobaric analog state (IAS) and Gamow-Teller (GT) resonance. The low energy (p, n) reaction¹⁻³⁾ provides better energy resolution of the excited spectra than the intermediate (p, n) reaction. The proton neutron pairing in $N = Z$ nuclei is the subject under intensive studies. There are nine stable $N = Z$ nuclei in the mass table. However, the $0^+ T = 1$ state is found experimentally only in ^{12}C at 17.77 MeV. Thus it is interesting to study by the (p, n) reaction the correlations in $T = 1, J = 0$ state of ^{12}N at 2.43 MeV, which is the analog state of ^{12}C at 17.77 MeV.

Cecil et al.⁴⁾ have carried out the spin parity-assignments for the 2.43-MeV state, its existence being reported by $^{10}\text{B}(^3\text{He}, n)^{12}\text{N}^{5)}$ reaction, to be 0^+ by studying analog relation between $^{12}\text{C}(^3\text{He}, t)^{12}\text{N}$ and $^{12}\text{C}(^3\text{He}, ^3\text{He}')^{12}\text{C}^*$ reactions exciting 2.43 and 17.77 MeV states, respectively. However, more direct evidence have been awaited for. They measured as well the differential cross sections for the $^{14}\text{N}(p, t)^{12}\text{N}$ reaction leading to the 2.43-MeV state, and interpreted the angular distribution by those with the two-step process.

Reliability of the information obtained from DWBA analysis of low-energy (p, n) data has been discussed in detail by Ohnuma et al.⁵⁾ with $^{12}\text{C}(p, n)^{12}\text{N}$ and $^{16}\text{O}(p, n)^{16}\text{F}$ reaction at $E_p = 35$ and 40 MeV. If one assume the pure $(1p_{3/2})^8$ -configuration for the ground state of ^{12}C , the direct charge-exchange process cannot excite the $J = 0, T = 1$ state in ^{12}N , since $(1p_{1/2})_\pi(1p_{3/2})_v$ configuration does not couple to the $J = 0, T = 1$ state. Therefore, the strong ground state correlations might be crucial to observe the $J = 0, T = 1$ state in ^{12}N through the direct (p, n) reaction process on ^{12}C .

In this report we present observation of the 2.43-MeV state by the high-resolution

low-energy (p,n) reaction. The cross-section magnitudes and their angular distribution is explained reasonably by the microscopic distorted wave analysis with knock-on exchange effects, where one body transition densities (OBTD), derived from the precise shell-model wave function, are taken into accounts.

The experiment was performed at the Cyclotron and Radioisotope Center, Tohoku University, with a 35-MeV proton beam from an AVF-cyclotron and a beam swinger system. The details of the experimental setup were described elsewhere^{6,7}. Neutron energies were measured by the time-of-flight technique (TOF), where neutrons were detected by a detector array located at 44.3 m from the target. The ten detectors, 23.2 liters in the total sensitive volume, were filled with organic liquid scintillator NE213. The absolute efficiencies of the detectors were obtained from the ${}^7\text{Li}(p,n){}^7\text{Be}$ activation analyses with an error less than 6%. The errors in the absolute magnitude of (p,n) cross sections were estimated to be less than 12%. The targets were a carbon foil enriched to 99% in ${}^{12}\text{C}$ with the thickness of $2.0\text{mg}/\text{cm}^2$, prepared by the clacking method.

Figure 1 shows the neutron energy spectrum of the ${}^{12}\text{C}(p,n){}^{12}\text{N}$ reactions measured at $\theta_{\text{lab}} = 0^\circ$. In addition to the prominent isolated peaks of neutrons leading to the 1^+ ground- and 2^+ 1.19-MeV states, peaks due the 2.43-MeV state is clearly seen. Differential cross sections of the ${}^{12}\text{C}(p,n){}^{12}\text{N}$ reaction exciting the 0^+ 2.43-MeV state are shown in Figs. 2, and those for the 1^+ ground-state is shown in Fig. 3 as well for comparison purpose. Curves in the figures are results of the microscopic DWBA analyses.

The microscopic DWBA results are obtained by using shell model wave functions for the computer code DWBA-70⁸, which takes into accounts knock-on exchange effects properly. The optical potential parameters of Becchetti and Greenlees⁹ are used for the entrance channel. Those for the exit channel are the self-consistent potential parameters derived by Carlson et al¹⁰. The effective nucleon-nucleon interactions used in the present DW analysis are M3Y interactions by Bertsch et al¹¹. A sensitivity of the calculations to the optical-potential parameters is elaborated in Ref. 5. The one body transition densities (OBTD) for the microscopic DWBA calculation are obtained by the shell-model computer code OXBASH¹². The latter for the prominent $0^+ \rightarrow 0^+$ is listed in Table1, together with those for the prominent $0^+ \rightarrow 1^+$ transition to the ground state of ${}^{12}\text{N}$.

In an ordinary one-step zero-range direct reaction, the $0^+ \rightarrow 0^+$ transition proceeds through $[\Delta J, \Delta L, \Delta S] = [0, 0, 0]$ channel, thus the angular distribution of deferential cross section for such a $0^+ \rightarrow 0^+$ transition may exhibits the similar shape with that for the $0^+ \rightarrow 1^+$

transition, which proceeds through the $[1, 0, 1]$ channel showing typical $\Delta L = 0$ pattern as shown in Fig. 3. The striking difference between these two angular distribution patterns is remarkable. The latter for the $0^+ \rightarrow 1^+$ transition in Fig. 3 exhibits the normal bell-shape for an $L = 0$ transition, familiar to that for the prominent GT-type (p, n) reaction¹³. On the other hand, the $0^+ \rightarrow 0^+$ transition to the 2.43-MeV state shows the 0-degree peaked angular distribution with highly hindered cross-section magnitudes, suggesting the existence of other kinds of reaction dynamics encountered into this transition.

As listed in Table 1, the main contributions for the $0^+ \rightarrow 1^+$ transition are $1p_{1/2} \leftarrow 1p_{3/2}$ and $1p_{3/2} \leftarrow 1p_{1/2}$, while they are $1p_{1/2} \leftarrow 1p_{1/2}$ and $1p_{3/2} \leftarrow 1p_{3/2}$ for the $0^+ \rightarrow 0^+$ transition. These magnitudes themselves are quite large suggesting strong ground state correlations in ^{12}C . Hindrance of the cross-section in the $0^+ \rightarrow 0^+$ transition might be due to significant cancellation between two contributions. Thus, the origin of observed cross section is the non-local exchange contributions through the $[\Delta L, \Delta L, \Delta S] = [1, 1, 0]$ channel.

In summary, the weakly populated 0^+ state was firstly observed by the (p, n) reaction with high resolution measurement at $E_p = 35$ MeV. By the analysis with microscopic DW theory, it was found that the $[1, 1, 0]$ channel exchange process played the dominant role.

This work is supported by grant in aid for scientific research of Ministry of Education, Culture, Sports, and Science and Technology No.13640257.

References

- 1) Ohnuma H. et al., Nucl. Phys. **A467**, 61(1987).
- 2) Kabasawa M. et al., Phys. Rev. C **45** (1992) 1220.
- 3) Kang G. C. et al., Nucl. Phys. **A499** (1989) 339.
- 4) Cecil F. E. et al., Phys. Lett. **B64** (1976) 411.
- 5) ($^3\text{He}, n$).
- 6) Orihara H. and Murakami T., Nucl. Instrum. and Methods **181** (1981) 15.
- 7) Orihara H. et al., Nucl. Instrum. and Methods **A257** (1987) 189.
- 8) Schaeffer R. and Raynal J., the computer program DWBA70 (unpublished).
- 9) Becchetti F. D. and Greenlees G. W., Phys. Rev. **182** (1969) 1190.
- 10) Carlson J. D., Zafiratos C. D. and Lind D. A., Nucl. Phys. **A249** (1975) 29.
- 11) Bertsch G., Borysowics J., McManus H. and Love W. G., Nucl. Phys. **A284** (1977) 399.
- 12) The shell model code OXBASH, Echegoyen A. E. et al., National Superconducting Cyclotron Laboratory Report No. 524 (1984).
- 13) Orihara H. et al., Phys. Lett. **B 539** (2002) 40.

Table 1. One body transition densities for the $0^+ \rightarrow 0^+$ and $0^+ \rightarrow 1^+$ transitions in the $^{12}\text{C}(p,n)^{12}\text{N}$ reaction calculated by the shell-model code OXBASH with the full psd model-space by psdmwk-interactions defined in the code OXBASH.

Particle-hole configuration	$0^+ \rightarrow 0^+$	$0^+ \rightarrow 1^+$
$1p_{1/2} \leftarrow 1p_{1/2}$	-0.45989	-0.04406
$1p_{1/2} \leftarrow 1p_{3/2}$	-	-0.71360
$1p_{3/2} \leftarrow 1p_{1/2}$	-	-0.32507
$1p_{3/2} \leftarrow 1p_{3/2}$	0.33419	-0.06326
$1d_{3/2} \leftarrow 1d_{3/2}$	0.00048	0.00025
$1d_{3/2} \leftarrow 1d_{5/2}$	-	-0.00238
$1d_{5/2} \leftarrow 2s_{1/2}$	-	-0.00031
$1d_{5/2} \leftarrow 1d_{3/2}$	-	-0.00036
$1d_{5/2} \leftarrow 1d_{5/2}$	-0.00771	-0.0041
$2s_{1/2} \leftarrow 1d_{3/2}$	-	0.00021
$2s_{1/2} \leftarrow 2s_{1/2}$	-0.00005	-0.00031

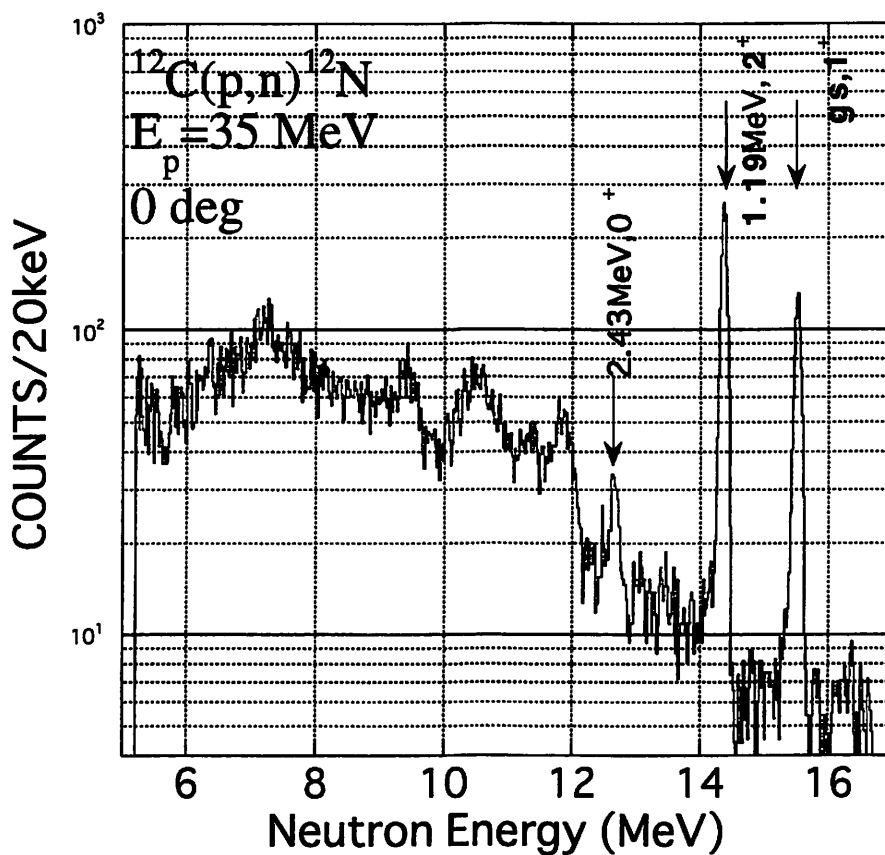


Fig. 1. Energy spectrum of the $^{12}\text{C}(p,n)^{12}\text{N}$ reaction at $\theta_{\text{lab}} = 0^\circ$ with a flight path of 44.3 m. Energy per channel is 25 keV.

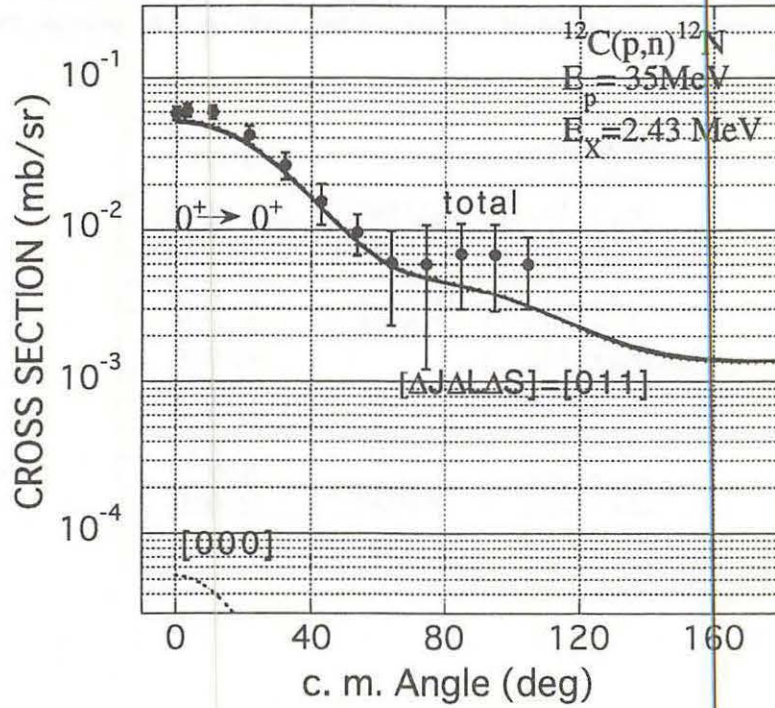


Fig. 2. Differential cross sections for neutrons leading to the 0^+ state at $E_x = 2.43 \text{ MeV}$ in ^{12}N . The curves are DWBA results described in the text.

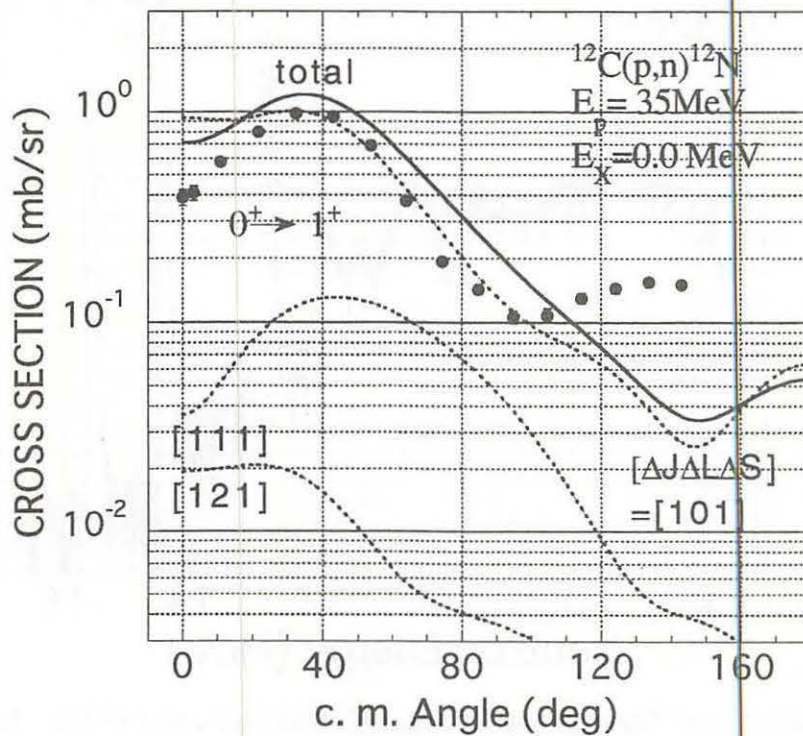


Fig. 3. Differential cross sections for neutrons leading to the 1^+ state at $E_x = 0.0 \text{ MeV}$ in ^{12}N . The curves are DWBA results described in the text.

I. 3. $^{12}\text{C}(p,n)^{12}\text{N}$ Reaction at $E_p = 70$ MeV: Reliability of the information obtained from DWBA analysis of 70-MeV (p,n) data

*Kikuchi Y., Orihara H., Kumagai K., Fujisawa H., Uemori T., Sugimoto N., Suzuki H., Terakawa A., Ishii K. *, and Ohnuma H. ***

*Cyclotron and Radioisotope Center, Tohoku University
Department of Quantum Engineering, Tohoku University*
Department of Physics, Chiba Institute of Technology***

Intermediate energy (p,n) reaction have been proved¹⁾ to be an excellent tool to study spin-isospin excitation modes of nuclei. High sensitivity of the spin-flip excitation mode due to relatively strong spin-dependent interaction has been utilized in such studies¹⁾. Furthermore interpretation of the data in terms of the distorted-wave impulse approximation (DWIA) is expected to be reliable at reasonably high incident energies. Low-energy (p,n) reactions at e.g. $E_p = 35\text{MeV}$ ²⁾ are considered to be less transparent in their interpretation, because of the strong spin-independent interaction, relative importance of the distortion effect and the exchange process, ambiguities in the effective interaction, possible contributions from higher-order processes, etc. In low-energy (p,n) experiments, on the other hand, much better energy resolution can be achieved, making them very attractive to nuclear structure studies. The (p,n) reaction experiments at $E_p = 50 \sim 100\text{MeV}$, where spin flip strength dominates over spin non-flip one and higher resolution is expected, may provide a new fields for exploration of the nuclear spectroscopy.

It is necessary therefore first to test the reliability of the information obtained from the (p,n) reaction at $E_p = 70$ MeV, and second to compare such information with that from intermediate- and low-energies works. The $^{12}\text{C}(p,n)^{12}\text{N}$ reaction suits these purposes very well. The structure of mass 12 nucleus has been studied in detail, and shell-model wave functions is available, which describe various properties of these nuclei reasonably well. This reaction, as well as the (p,p') , (n,p) and $(^3\text{He},t)$ reactions to the analog final states, has been studied extensively at various energies³⁻⁸⁾. In this report we discuss a high-resolution study of the $^{12}\text{C}(p,n)^{12}\text{N}$ reaction leading to the low-lying states in the final nuclei at the incident proton energies of 70MeV. A detailed comparison of the results with DWBA

calculations and with the results obtained at intermediate energies is given.

The experiment was performed using 70MeV proton beams from the K= 110MeV AVF cyclotron and the time-of-flight facilities⁹⁾ at the Cyclotron and Radioisotope Center, Tohoku University. We have utilized a beam swinger system, and measured angular distributions of emitted neutrons between 0° and 60°. The ^{12}C target was 20 mg/cm² thick self-supporting foil of natural abundance. Overall time resolution was less than 1 ns. The detector efficiencies were calibrated at various neutron energies by using the $^7\text{Li}(p,n)^7\text{Be}$ reaction. The measured neutron yields are compared with the residual radioactivity from ^7Be to determine the absolute efficiencies of the detectors. They are found to be in good agreement with Monte Carlo calculations. The errors in the absolute magnitude of the cross sections are estimated to be less than 15% .

Figure 1 illustrates the neutron excitation-energy spectrum measured at a laboratory angles of 0 and 35 degree for the $^{12}\text{C}(p,n)^{12}\text{N}$ reaction at $E_p = 70$ MeV. Curves in the figure are results of the phase space calculation for three-body break up, and those of peak fitting for the low-lying together with the high-lying proposed states. Measured angular distributions are displayed in Figs. 2-5 along with the DWBA calculations described below.

The data are compared with microscopic DW results calculated by the computer code DWBA-74¹⁰⁾, which includes knock-on exchange effects in an exact manner. Note that fully antisymmetrized calculations were made in the present microscopic DW analysis, in which non-normal parity terms also contribute to the cross section. Optical potential parameters of Nadasen et al.¹¹⁾ were used for the entrance channel. Those for the exit channel were potential parameters derived by Varner et al.¹²⁾ The effective nucleon-nucleon interactions used in the present DW analysis were those by Franey and Love¹³⁾. Spectroscopic amplitudes (OBTD) for the microscopic DWBA analysis were obtained from shell model calculations, where psd model-space has been taken into accounts up to $4\hbar\omega$ -jump configurations using the code OXBASH¹⁴⁾ with the interaction of Cohen, Kurath and Millener¹⁵⁾. As for the single-particle radial wave functions used in DW calculations were generated in a Wood-Saxon type bound-state potential with $r_0 = 1.25$ fm, $a = 0.65$ fm and $V_{\text{LS}} = 6$ MeV, and the depth adjusted to reproduce the binding energy of the last neutron or proton.

Figure 2 illustrates experimental and theoretical angular distribution of cross sections for the (p,n) reaction on ^{12}C leading to the ground 1^+ and first excited 2^+ states in

^{12}N . Remarkably reasonable fitting with DW calculations mentioned above has been obtained. An important point to be noted is that calculations with the FL-100 effective interaction give much better explanation for the experimental cross sections, while those with the FL-50 effective interaction over estimate similarly to the cases in the analysis for the $^6\text{Li}(p,n)^6\text{Be}$ reaction at $E_p = 70 \text{ MeV}^{16}$. The cross sections for the 0^+ to 2^- transition are absolutely fitted as well with the DW calculation as shown in Fig. 3.

Beyond the excitation energy of 3MeV in ^{12}N or ^{12}B , many authors have discussed on spin-parity assignments for the observed transitions by charge-exchange reactions on $^{12}\text{C}^{3-8}$. A peak is seen at $E_x = 3.5 \text{ MeV}$ in the neutron spectrum measured at 35° illustrated in Fig. 1. The most provable spin-parity assignment for this state may be 2^+ predicted by shell model as second 2^+ state. Comparison with the calculation for differential cross sections is shown in Fig. 3.

In addition, two prominent and one broad peaks are observed in the neutron spectrum. The angular distribution of cross sections corresponding to the broad peak at $\sim 4.2\text{MeV}$ is fitted with the sum of $\Delta J^\pi = 2^-$ and 4^- transitions as illustrated in Fig. 4, where both theoretical predictions are multiplied by a factor of 0.35, suggesting that the shell model predictions for the transition strength too much concentrated on the transitions to the second 2^- and first 4^- state. Figure 4 shows the results for the transition to the 5.3 MeV-peak. The spin-parity assignment of $\Delta J^\pi = 3^-$ for this state seems to be reasonable. The last debate for the analyses of the differential cross sections is for the broad peak spreading over $E_x = 6 - 8 \text{ MeV}$ in ^{12}N as seen clearly at the 0-degree neutron spectrum in Fig. 1. The angular distribution exhibits the typical $\Delta L = 1$ pattern as illustrated in Fig. 5. The experimental cross sections are fitted with sum of predictions over 6, $\Delta L = 1$ transitions. The DW cross sections are multiplied by a factor of 0.5. Other strength may be presumably scattered into higher excited states.

In a summary, an experimental study of the $^{12}\text{C}(p,n)^{12}\text{N}$ reaction have been carried out at $E_p = 70 \text{ MeV}$ with better resolution than those so far reported. Results were compared successfully with the predictions based on large-space shell-model and DW calculations where Franey and Love 100MeV effective interactions were applied. Spin-parity assignments for observed seven transition were consistent with previous report.

This work is supported by grant in aid for scientific research of Ministry of Education, Culture, Sports, and Science and Technology No.13640257.

References

- 1) Goodman C. D. et al., Phys. Rev. Lett. **44** (1980) 1755.
- 2) Orihara H. et al., Phys. Lett. **B539** (2002) 40.
- 3) Knudson et al., Phys. Rev. C **22** (1980) 1826.
- 4) Ohnuma H. et al., Nucl. Phys. **A469** (1987)61.
- 5) Rapaport et al., Phys. Rev. C **36** (1987) 500.
- 6) Sterrenburg W. A. et al., Nucl. Phys. **A405** (1983)109.
- 7) Bergqvist I. et al., Nucl. Phys. **A469** (1987)648.
- 8) Yang X. et al., Phys. Rev. C **48** (1993) 1158.
- 9) Terakawa A. et al., Nucl. Instrum. and Methods **A491** (2002)419.
- 10) R. Schaeffer and J. Raynal, the computer program DWBA70 unpublished.
- 11) Nadasen A. et al., Phys. Rev. C **23** (1981)1023.
- 12) Varner et al., Phys. Rep. **201** (1991)57.
- 13) Franey M. A. and Love W. G., Phys. Rev. C **31** (1985)488.
- 14) The shell model code OXBASH, Echevoyen A. E., National Superconducting Cyclotron Laboratory Report No. 524 (1984).
- 15) Kohen S. and Kurath D., Nucl. Phys. **A101** (1967)1.
Millener D. J. and Kurath D. Nucl. Ohys. **A255** (1975) 315.
- 16) Kumagai K. et al., CYRIC Ann. Rep. 2001.

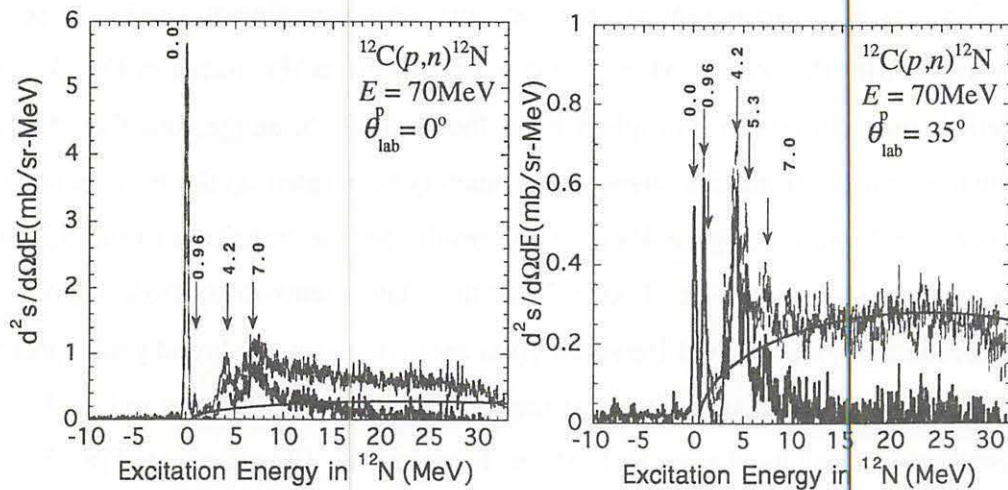


Fig. 1. Sample excitation energy spectra from the $^{12}\text{C}(p,n)^{12}\text{N}$ reaction taken at 0° and 30° with a flight path of 44.3 m. Energy per bin is 50 keV.

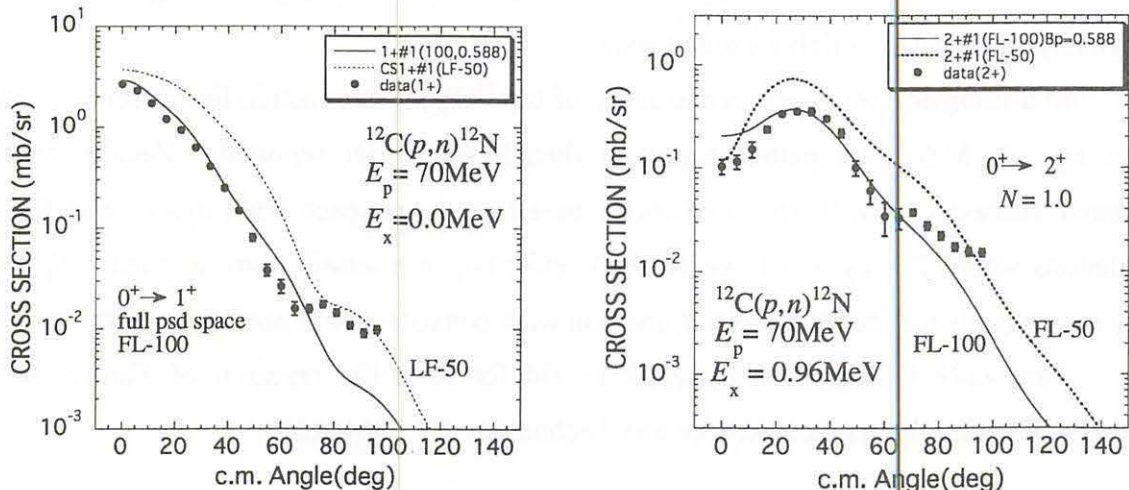


Fig. 2. Differential cross sections for neutrons leading to the ground and 0.96-MeV states in ^{12}N .

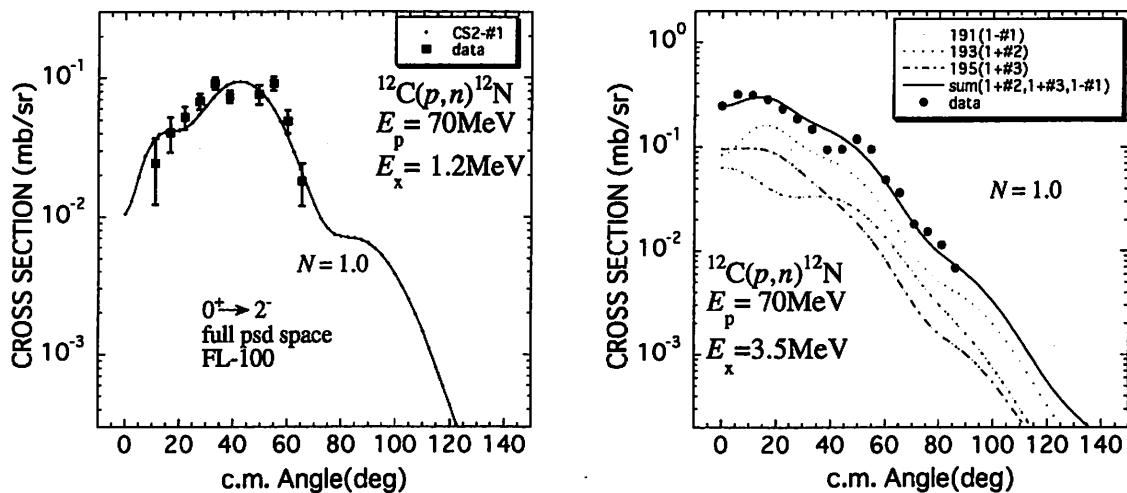


Fig. 3. Differential cross sections for neutrons leading to the 1.2 and 3.5-MeV states in ^{12}N .

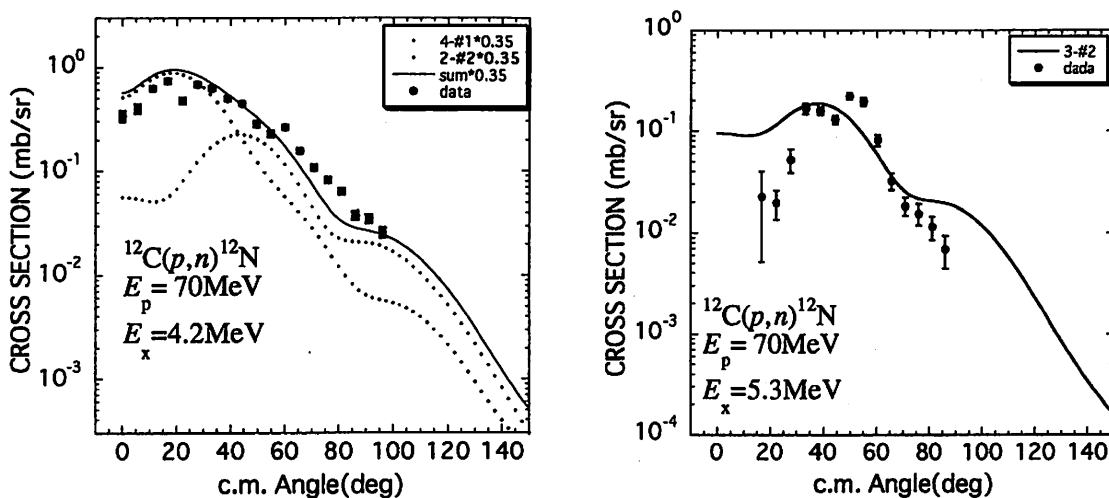


Fig. 4. Differential cross sections for neutrons leading to the 4.2 and 5.3-MeV states in ^{12}N .

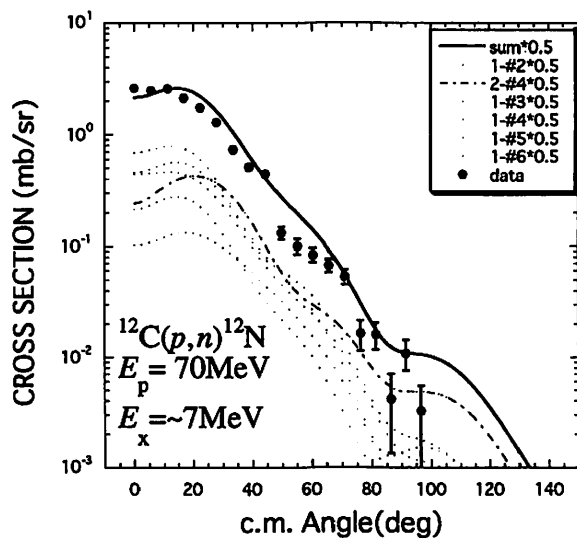


Fig. 5. Differential cross sections for neutrons leading to the ~ 7 -MeV state in ^{12}N .

I. 4. Isospin Excitations in Nuclei via the $^{42,44,48}\text{Ca}(p,n)^{42,44,48}\text{Sc}$ Reactions

Suzuki H., Orihara H., Terakawa A., Itoh K., Kumagai K., Kikuchi Y.,
Fujisawa H., Uemori T., Sugimoto N., Maeda K.*, Katoh M.*,
Ohnuma H.** ,and Sagawa H.***

Cyclotron and Radioisotope Center, Tohoku University
*Department of Physics, Tohoku University**
*Department of Physics, Chiba Institute of Technology***
*Center of Mathematical Science, The University of Aizu****

The charge exchange (p,n) reaction is a powerful tool to explore isospin and spin-isospin response in nuclei. Intermediate energy (p,n) reactions at $E_p \geq 135$ MeV selectively excite the spin-flip components through the strong energy dependence for the spin-isospin effective interaction $V_{\sigma\tau}$. On the other hand, low energy (p,n) reactions provide us equivalent information on both excitation modes owing to the relatively strong spin non-flip isovector effective interaction V_τ . Moreover, its sufficient energy resolution enables us to discuss (p,n) strength for individual nuclear levels. Various problems associated with distorted-wave (DW) analysis of low energy (p,n) data have been discussed in detail by Ohnuma et al¹⁾.

Recently, Orihara et al. have reported a method to obtain the Gamow-Teller (GT) matrix elements $B(\text{GT})$ for $N = Z+2$ nuclei²⁾. Experimental results for prominent GT-type $0^+ \rightarrow 1^+$ transitions observed via the (p,n) reactions at 35 MeV are compared with analog GT-transition strengths among $T = -1, 0, 1$ isobar triplet. This method provides us reasonable $B(\text{GT})$ values including the energetically inaccessible β -decay for the isobar triplets ranging from $A = 14$ (^{14}C - ^{14}N - ^{14}O) to 42 (^{42}Ca - ^{42}Sc - ^{42}Ti).

Furthermore, the ratios of isovector effective interaction strengths $|J_{\sigma\tau}/J_\tau| = V_{\sigma\tau}/V_\tau$ at $E_p \geq 100$ MeV by the $^{13,14}\text{C}(p,n)^{13,14}\text{N}$ reactions have been reported^{3,4)}. However, the information for the ratio of $|J_{\sigma\tau}/J_\tau|$ derived from the (p,n) reaction on medium-heavy nuclei at $E_p \leq 100$ MeV is quite insufficient.

In this report, we discuss the isospin excitations in nuclei via the

$^{42,44,48}\text{Ca}(p,n)^{42,44,48}\text{Sc}$ reactions at $E_p = 35, 50, 70$ and 80 MeV. Angular distributions of the cross sections are measured and analyzed with the distorted-wave Born approximation (DWBA) calculation. Based on the data at 35 MeV, $B(\text{GT})$ values corresponding to the $^{42,44,48}\text{Ca}(0^+) \rightarrow ^{42,44,48}\text{Sc}(1^+)$ transitions are deduced. In addition,, incident proton-energy dependence of $|J_{\sigma}/J_{\tau}|$ is discussed for the $^{42}\text{Ca}(p,n)^{42}\text{Sc}$ reaction at $E_p = 50, 70$ and 80 MeV.

The present experiments were carried out with a 35 -MeV proton beam from the $K = 50$ AVF cyclotron, and with $50, 70$ and 80 -MeV proton beams from the $K=110$ AVF cyclotron at Cyclotron and Radioisotope Center (CYRIC), Tohoku University. Neutron energies were measured by using the time-of-flight (TOF) facilities equipped with the beam swinger system⁵⁻⁷⁾. Emitted neutrons were detected with the neutron detector array located at 44 m from the target. The detectors were filled with organic liquid scintillator NE213 (or BC501A), where difference in the mechanism of scintillation light-yields makes it possible to separate the events by neutrons from those by γ -rays.

In 35 -MeV $^{42,44,48}\text{Ca}(p,n)^{42,44,48}\text{Sc}$ experiments, neutrons were detected by an array of 12 -detectors containing a total of 23.2 liter of the scintillator⁶⁾. The energy resolution, estimated by the FWHM in the Gaussian shape spectrum, was about 160 keV for the IAS peaks in the $^{42,44,48}\text{Sc}$ nuclei. The angular distributions of the differential cross sections were measured from 0° to 130° in the laboratory system. The targets were enriched metallic $^{42,44,48}\text{Ca}$ foils of $1.80, 1.62$ and 1.82 mg/cm² in their thickness, respectively.

In the $^{42}\text{Ca}(p,n)^{42}\text{Sc}$ reactions at $50, 70$ and 80 MeV, an array of 16 detectors, the total volume of which was 25.9 liter⁷⁾, was utilized. The energy resolutions obtained for the ground state in ^{42}Sc were $440, 300$ and 450 keV for $E_p = 50, 70,$ and 80 MeV, respectively. The measurements were carried out at 0° for emphasizing the observations of the $\Delta L = 0$ transition, which is characteristic of the IAS and GT transitions. The target was a self-supporting ^{42}Ca foil of 5.5 mg/cm² in the thickness. The target was prepared from enriched $^{42}\text{CaCO}_3$ powder by a vacuum de-oxidation deposition method as reported elsewhere⁸⁾.

The angular distributions of the cross sections at $E_p = 35$ MeV are analyzed by comparing the data with microscopic DWBA calculations by the code DWBA70⁹⁾, in which contributions from the knock-on exchange effect are included in an exact manner. The DW calculations use the effective interaction M3Y¹⁰⁾ and optical potential parameters for a proton by Becchetti and Greenlees¹¹⁾ and those for a neutron by Carlson et al¹²⁾. The one-body-transition-densities (OBTD) which are used for microscopic DWBA, are calculated

with the shell model computer code OXBASH¹³⁾. Furthermore, macroscopic DWBA calculations are carried out for the IAS transition using the code DWUCK4¹⁴⁾. The isovector potential parameters for the IAS excitation are those obtained by Jon et al¹⁵⁾.

As an example of the present results, Fig. 1 shows four experimental and calculated angular distributions of the differential cross sections for neutrons leading to (a) g.s., 0^+ in ^{42}Sc , (b) 0.968-MeV, 3^+ and 0.986-MeV, 7^+ states in ^{44}Sc , (c) 2.516-MeV, 1^+ state in ^{48}Sc , and (d) 3.675-MeV, 3^- state in ^{48}Sc . The normalization factor N in figures was introduced to fit the theoretical cross sections to the data. Table 1 lists the spin-parities, the isospins and the normalization factors for the presently assigned levels.

For positive parity transitions, the calculations in the full $0f1p$ -shell space are carried out with the effective interaction by Richter et al¹⁶⁾. As shown in Table 1, the calculations absolutely reproduce the observed angular distributions of the cross sections except for the cases of the GT-type $0^+ \rightarrow 1^+$ transition, where normalization factors of 0.3 ~ 1.0 are needed. It is noticeable that the $0^+ \rightarrow 7^+$ transitions, corresponding to $0\hbar\omega$ stretched state excitations in $0f1p$ shell nuclei, are successfully explained by DW calculation without normalization factors. Similar results have been reported in the case of the $0\hbar\omega$ stretched transitions in $1s0d$ shell nuclei¹⁷⁾, while OBTD's have been calculated with the interactions by Brown and Wildenthal¹⁸⁾. This result may indicate that the shell model wave functions obtained from the $0f1p$ interaction by Richter are reasonable for Ca isotopes. As shown in Fig. 1(a), the macroscopic DWBA calculation reproduces the cross section absolutely for IAS transition in ^{42}Sc . Similar results have been obtained for the IAS transitions in the (p,n) reactions on $^{44,48}\text{Ca}$ isotopes.

As reported by Orihara et al. in Ref. 2, the $B(\text{GT})$ value for a nucleus with $T = (N-Z)/2 = 1$ may be extracted from the relationship between IAS and GT differential cross sections, the angular distribution of which exhibit a peak around $\theta \approx 30^\circ$, by the following relation;

$$B(\text{GT}) = \langle N \rangle \left(\frac{d\sigma}{d\Omega} \right)_{\text{GTpeak}} / \left(\frac{d\sigma}{d\Omega} \right)_{\text{IASpeak}}, \quad (1)$$

where $\langle N \rangle = 1.96 \pm 0.11$.

Meanwhile, in the factorized distorted-wave impulse approximation⁴⁾, $B(\text{GT})$ is approximately written as;

$$B(\text{GT}) = \langle N \rangle \left(\frac{d\sigma}{d\Omega} \right)_{\text{GT}} / \left(\frac{d\sigma}{d\Omega} \right)_{\text{IAS}} \frac{N-Z}{R^2} \frac{k_f^{\text{IAS}}}{k_f^{\text{GT}}}, \quad (2)$$

where k_f is the kinematic factor. R^2 represents the ratio of unit cross sections;

$$R^2 = \frac{\hat{\sigma}_{\text{GT}}}{\hat{\sigma}_{\text{IAS}}} \approx \frac{N_{\sigma\tau} |J_{\sigma\tau}|^2}{N_{\tau} |J_{\tau}|^2} \approx \left[\frac{E_p}{54.9 \pm 0.9} \right]^2. \quad (3)$$

In the present work, R^2 and $k_r^{\text{IAS}}/k_r^{\text{GT}}$ are taken to be constant even for $E_p = 35$ MeV. Thus, the proportionality relationship is written as;

$$B(\text{GT}) \propto (N - Z) \left(\frac{d\sigma}{d\Omega} \right)_{\text{GTpeak}} / \left(\frac{d\sigma}{d\Omega} \right)_{\text{IASpeak}} \quad (4)$$

By Using eq.(1), the $B(\text{GT})$ value for the 0.611 MeV state in ^{42}Sc has been deduced in Ref.2. Then, those for the cases of ^{44}Sc and ^{48}Sc are obtained by multiplying the factor $(N - Z)$ following eq.(4). Thus, three $B(\text{GT})$ values-for the 0.698, 3.163 and the 3.672-MeV states in ^{44}Sc and that for the 2.516-MeV state in ^{48}Sc are obtained as listed in the fifth column of Table 2. It should be noted that these values for ^{44}Sc are deduced for the first time by the present study, and that for ^{48}Sc is consistent with the result from the 135-MeV experiment by Anderson et al²¹⁾.

For negative parity transitions, on the other hand, the OBTD for $1\hbar\omega$ jump into $0f1p$ -shell are taken into accounts with the $1s0d-0f1p$ model space, using the interaction by Warburton et al¹⁹⁾. From agreement of angular distribution between the measurements and calculations, the 2.272 MeV state in ^{42}Sc is assigned $J^\pi = 2^-$, and also 3.027 and 3.675 MeV states in ^{48}Sc are $J^\pi = 2^-$ and 3^- , respectively, although normalization factors are required.

Figure 2 illustrates the 0 degree neutron spectra for the $^{42}\text{Ca}(p,n)^{42}\text{Sc}$ reaction at $E_p = 50, 70$ and 80 MeV taken for the purpose to find the proton energy dependence of the ratio of isovector effective interaction strengths $|J_{\sigma\tau}/J_{\tau}|$. It is remarkable in Fig. 2 that peaks leading to the 0^+ , ground and 1^+ , 0.611-MeV states are observed separately. The experimental intensity ratio is plotted in Fig. 3 as the function of the proton energy. The curve in Fig. 3 is the theoretical prediction deduced from the phase-shift analysis^{20,22,23)}. The result seems to be similar to that from the $^{13,14}\text{C}$ experiments reported by Taddeucci et al³⁾.

In a summary, neutrons from the $^{42,44,48}\text{Ca}(p,n)^{42,44,48}\text{Sc}$ reactions at $E_p = 35$ MeV and $^{42}\text{Ca}(p,n)^{42}\text{Sc}$ reaction at $E_p = 50, 70$ and 80 MeV were observed by the high resolution TOF technique. The shell model calculation and analyses with DWBA theory have provided a set of spin-parity assignment over 7, 8 and 10 levels for $^{42,44}\text{Sc}$, and ^{48}Sc nuclei, respectively. The GT matrix elements $B(\text{GT})$ were obtained from the IAS and the GT cross sections. The energy dependence of the ratio of isovector effective interaction strengths $|J_{\sigma\tau}/J_{\tau}|$ was obtained for the (p,n) reaction on a medium mass nucleus in a energy

range between 50 and 80 MeV.

References

- 1) Ohnuma H. *et al.*, Nucl. Phys. **A467**, 61 (1987).
- 2) Orihara H. *et al.*, Phys. Lett. **B 539**, 40 (2002).
- 3) Taddeucci T. N. *et al.*, Phys. Rev. C **29**, 764 (1984).
- 4) Taddeucci T. N. *et al.*, Nucl. Phys. **A469**, 125 (1987).
- 5) Orihara H. and Murakami T., Nucl. Instrum. Method, **181**, 15 (1981).
- 6) Orihara H. *et al.*, Nucl. Instrum. Method A, **257**, 189 (1987).
- 7) Terakawa A. *et al.*, Nucl. Instrum. Method A, in press.
- 8) Suzuki H. *et al.*, CYRIC Annual Report 2000, p.50 (<http://www.cyric.hokoku.ac.jp>)
- 9) Schaeffer R. and Raynal J., Computer code DWBA70, unpublished
- 10) Bertsch G. F. *et al.*, Nucl. Phys. **A284**, 399 (1977).
- 11) Becchetti F. D. and Greenlees G. W., Phys. Rev. **182**, 1190 (1969).
- 12) Carlson J. D. *et al.*, Nucl. Phys. **A249**, 29 (1975).
- 13) Etchegoyen A. E. *et al.*, The shell model code OXBASH, National Superconducting, Cyclotron Laboratory Report 524 (1984).
- 14) Kunz P. D., Computer code DWUCK4, unpublished
- 15) Jon G. C. *et al.*, Phys. Rev. C **62**, 0044609 (2000).
- 16) Richter W. A. *et al.*, Nucl. Phys. **A523**, 325 (1991).
- 17) Orihara H. *et al.*, Phys. Rev. C **41**, 2414 (1990).
- 18) Brown B. A. and Wildenthal B. H., Phys. Rev. C **27**, 269 (1983).
- 19) Warburton E. K. *et al.*, Phys. Rev. C **41**, 1147 (1990).
- 20) Taddeucci T. N. *et al.*, Phys. Rev. C **25**, 1094 (1981).
- 21) Anderson B. D. *et al.*, Phys. Rev. C **31**, 1161 (1985).

Table 1. The spin-parities, isospins and normalization factors for the assigned levels in the (p,n) reactions at 35 MeV.

	E_x (MeV)	J^π	T	N	comment
^{42}Sc	0.0	0^+	1	1.0	IAS transition
	0.611	1^+	0	0.4	GT transition
	0.611	7^+	0	1.0	$0\hbar\omega$ stretched transition
	1.586	2^+	1	1.0	Excited analog state (EAS)
	1.586	5^+	0	1.0	natural parity transition
	2.272	2^-	0	0.5	negative parity transition
	4.820	2^+	0	1.0	natural parity transition
^{44}Sc	0.0	2^+	1	0.9	natural parity transition
	0.698	1^+	1	0.75	GT transition
	0.968	3^+	1	1.0	unnatural parity transition
	0.968	7^+	1	1.0	$0\hbar\omega$ stretched transition
	2.786	0^+	2	1.0	IAS transition
	3.163	1^+	1	0.3	GT transition
	3.672	1^+	1	0.7	GT transition
	4.1	2^+	2	1.0	EAS transition
^{48}Sc	0.0	6^+	3	1.5	natural parity transition
	0.130	5^+	3	0.5	unnatural parity transition
	0.252	4^+	3	1.0	natural parity transition
	0.623	3^+	3	0.5	unnatural parity transition
	1.096	2^+	3	1	natural parity transition
	1.096	7^+	3	1.0	$0\hbar\omega$ stretched transition
	2.516	1^+	3	1.0	GT transition
	3.027	2^-	3	0.15	negative parity transition
	3.675	3^-	3	0.78	negative parity transition
	6.677	0^+	4	1.0	IAS transition

Table 2. The matrix elements $B(GT)$ for $^{42,44,48}\text{Ca}(0^+) \rightarrow ^{42,44,48}\text{Sc}(1^+)$ deduced from the (p,n) reactions at 35 MeV.

	$E_x(\text{MeV})$	$(d\sigma/d\Omega)_{\text{IAS}}(\text{mb/sr})$	$(d\sigma/d\Omega)_{\text{GT}}(\text{mb/sr})$	$B(GT;pn)^a$
$^{42}\text{Ca}(p,n)^{42}\text{Sc}$	0.000	1.1310 ± 0.0423		
	0.611		1.5215 ± 0.0279	2.640 ± 0.150
$^{44}\text{Ca}(p,n)^{44}\text{Sc}$	2.786	2.4850 ± 0.0690		
	0.698		0.7960 ± 0.0400	1.256 ± 0.101
	3.163		0.3820 ± 0.0410	0.603 ± 0.075
	3.672		0.3420 ± 0.0280	0.541 ± 0.055
$^{48}\text{Ca}(p,n)^{48}\text{Sc}$	6.677	3.4430 ± 0.0864		
	2.516		0.8910 ± 0.0487	2.026 ± 0.166

$$^a) B(GT;pn) = (N-Z) \cdot N \cdot [(d\sigma/d\Omega)_{\text{GT}} / (d\sigma/d\Omega)_{\text{IAS}}], \text{ see eq.4 in text}$$

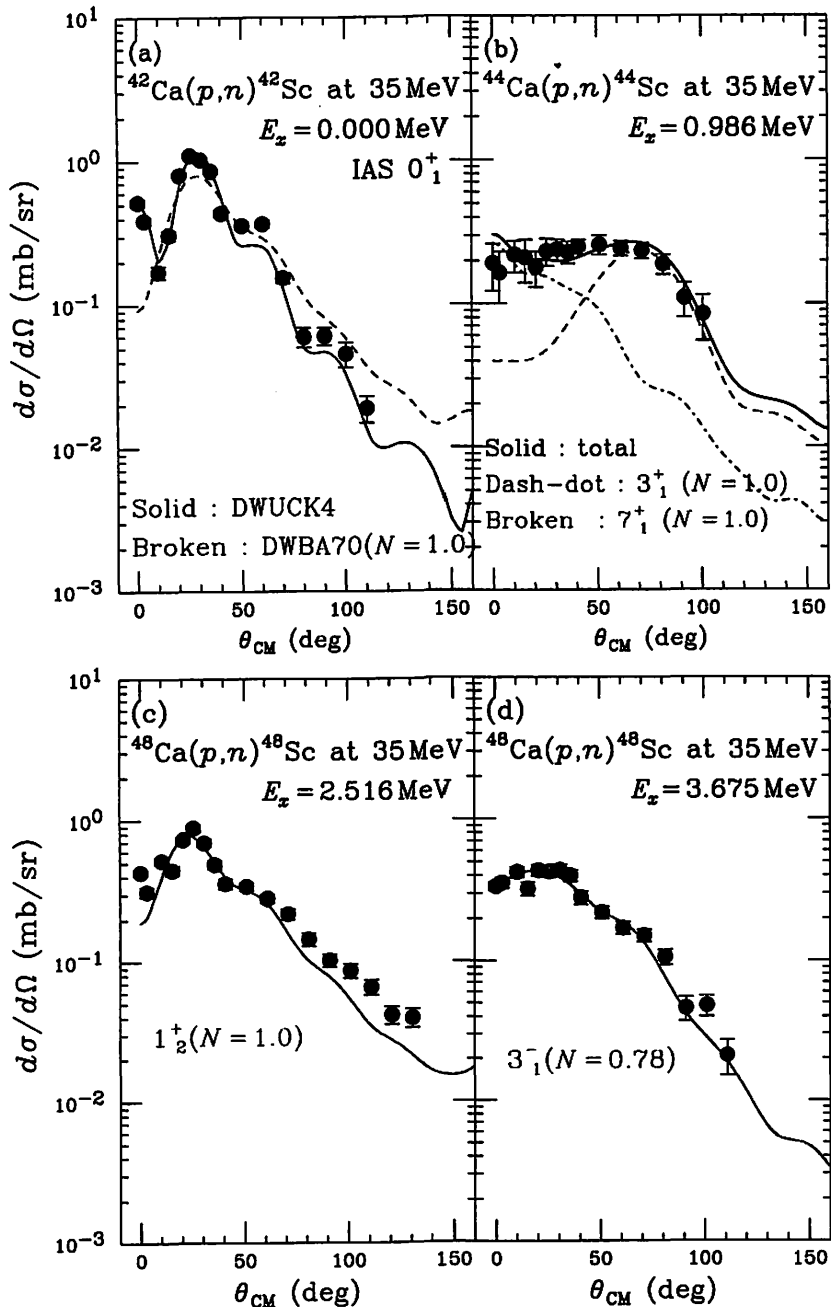


Fig. 1. The examples of differential cross sections leading to the 0^+ IAS state at 0.0 MeV in ^{42}Sc , to the $(3^+ + 7^+)$ mixed state at 0.986 MeV in ^{44}Sc , to the 1^+ GT state at 2.516 MeV, and to the 3^- state at 3.675 MeV in ^{48}Sc . The curves are DWBA calculations described in text.

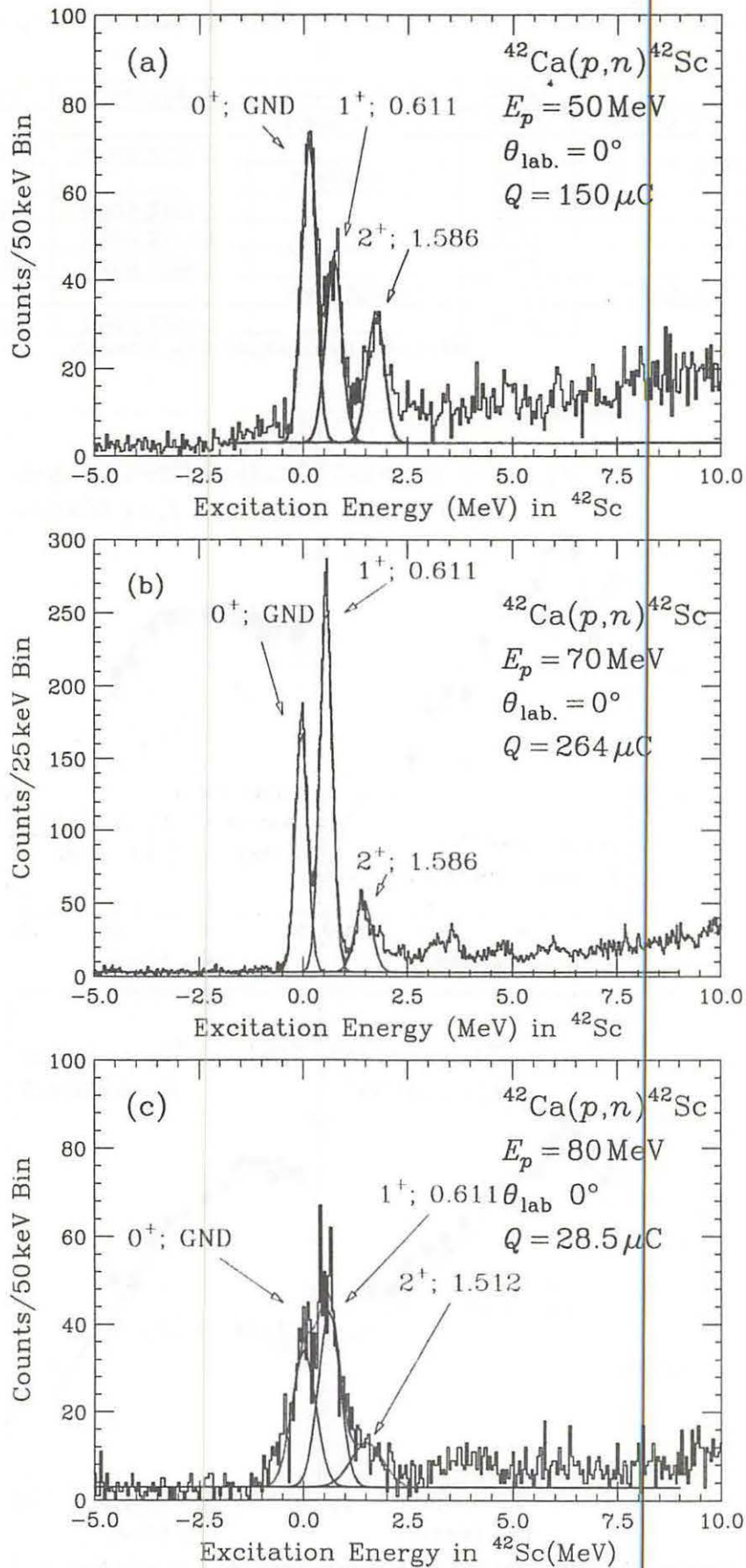


Fig. 2. Excitation energy spectra for the $^{42}\text{Ca}(p; n)^{42}\text{Sc}$ at 0° : (a) $E_p = 50 \text{ MeV}$, (b) $E_p = 70 \text{ MeV}$, and (c) $E_p = 80 \text{ MeV}$

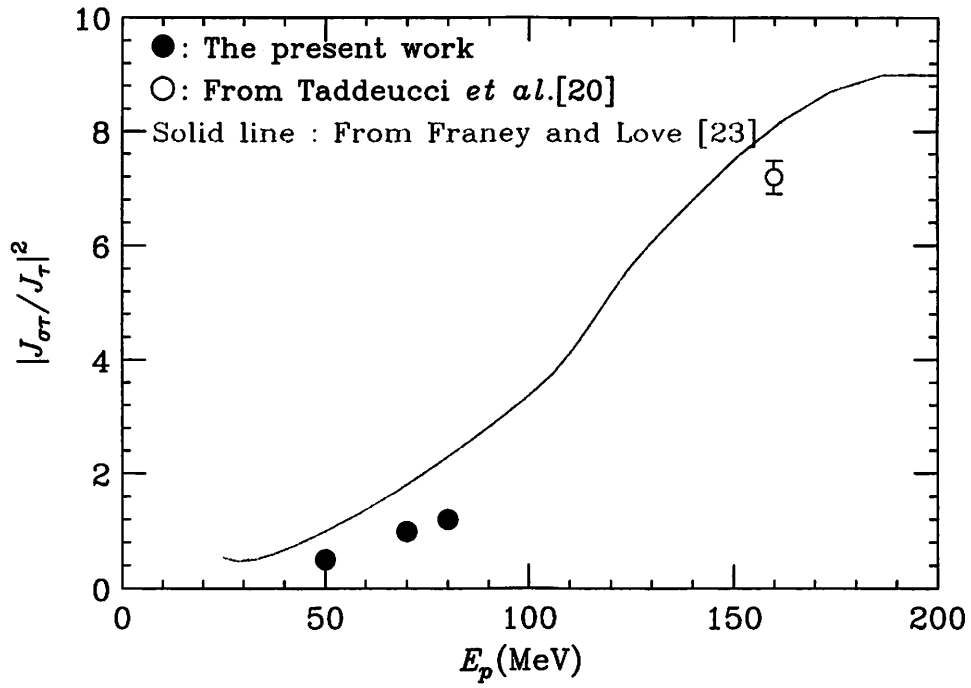


Fig. 3. Proton energy dependence on of ratios of squares of the spin flip to spin non-flip isovector effective interaction. The closed circles represent the data obtained in the present work. The open circle is from Ref 20. The solid line is the results deduced from phase-shift analysis.

I. 5. Present Status of the 14.5 GHz ECR Ion Source at CYRIC

Yamazaki A., Tanaka E., Fujita M., and Shinozuka T.

Cyclotron and Radioisotope Center, Tohoku University

A new 14.5 GHz electron cyclotron resonance (ECR) ion source has been designed and constructed, and it has been installed in February, 2001. This ion source is a full-permanent-magnet system. This type of source with all-permanent magnet design has advantages of its simple structure and easy handling, but it has several disadvantages like the difficulty obtaining strong magnetic field and field adjusting system. In order to overcome these disadvantages, this source has characteristic features of the permanent magnets as follows:

- (1) V-style magnetization,
- (2) flat-bottomed magnetic-field distribution,
- (3) fractionally field adjusting system.

This ECR ion source aims to obtain a flat-bottomed field distribution which can form the ECR-"volume" suggested by Alton and Smithe¹⁾. It can form the conventional ECR zone (ECR-"surface") using the field adjusting system. The cross sectional view of the ECR ion source is shown in Figure 1. Detail structure and characteristics of the ion source have been reported in a previous paper²⁾

The first plasma was ignited by the hydrogen gas in March, 2001. And then test operations are processing using various gas such as He, CO₂, O₂, and Ar. Since the CYRIC new cyclotron(K = 110 MeV) has an acceleration mode with harmonic 1 to 3, the ion source is needed to produce the mass to charge ratio 4 at least for the heavy ions. It is, for example, needed 9⁺ charge state for Ar case.

There have been several improvements in the peripheral instruments. The gas injection line has been modified to the metal pipes to reduce impurity gases. All the instruments are remote-controlled by personal computers. It is useful for easy and safety operating of the ion source and for better tuning of the injection line. Figure 1 is the

present status of the charge state spectrum of the extracted beam from the Argon plasma. The operating condition was optimized for Ar⁸⁺ ion and gas-mixing method was not used. The resolution of the mass to charge state spectrum is about 1/65, it is sufficiently good for practical ion identification and separation. However the base pressure in the vacuum pumping stage is 3×10^{-7} Torr, which is about five times higher than the designed value. Further good condition for the vacuum pressure is necessary.

Extracted ion current is summarized in Table 1. The beam current of light ions H⁺, He²⁺ is sufficient, but that of the highly-charged heavy ion, for example (C⁴⁺, Ar⁸⁺), is still low. Several better operating conditions such as vacuum pressure, impurity, and extraction configuration are necessary for better source performance. Heavy ion produced by the source was first provided for the cyclotron in June, 2001. The light heavy ions, Carbon, Oxygen and Neon, have been accelerated by the new cyclotron for nuclear physics experiments and material science research. The stability of operating condition is one of the important parameters for the experiments. Practically it is required to be operated stable at least for one week. The stability of the beam current is sufficiently good.

In summary, a new all-permanent-magnet type ECR ion source was started to providing the heavy ion beams for the new cyclotron. The operation condition is being improved and stability is good. However the extracted multi-charged heavy ion current is still low. The operating test with varying microwave frequency (10 - 18 GHz) of traveling wave tube amplifier is planned for the improvement on the source performance. Also the modification of the extraction electrode have to be needed to optimize the extraction configuration.

References

- 1) Alton G. D. and Smithe D. N., Rev. Sci. Instrum. **65** (1994) 775.
- 2) Yamazaki A., Fujita M., Tanaka E., Shinozuka T., Yokoi T., Ozawa T., and Tanaka H., Rev. Sci. Instrum. **73** (2002) 589.

Table. 1. Extracted ion current for each charge state $e\mu A$. CO₂ gas was used for the carbon ion current measurement. Operating conditions for any ions are as follows; microwave power is 250 W of continuous wave mode, extraction voltage is 15 kV, no gas mixing method is used. The flow rate of the ionized gas was optimized for the high-charge state of every ions.

Ion	1 ⁺	2 ⁺	3 ⁺	4 ⁺	5 ⁺	6 ⁺	7 ⁺	8 ⁺	9 ⁺
H	2480								
He	400	440							
¹² C	420	580		14					
¹⁴ N	333	1110	370	40	4				
¹⁶ O	460	820	420		5	0.6			
²⁰ Ne	170	420	420		5	0.6			
⁴⁰ Ar		310	273	113		17	4.9	1.4	0.2

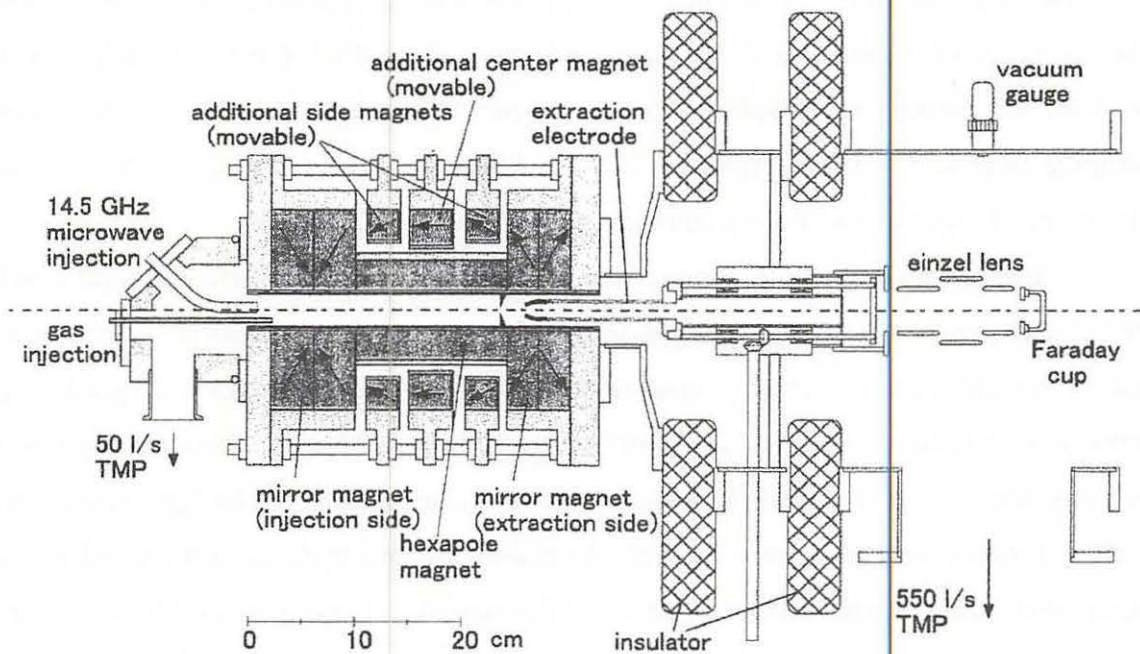


Fig. 1. Cross-sectional view of the new ECR ion source. Arrows represent magnetization directions of permanent magnets.

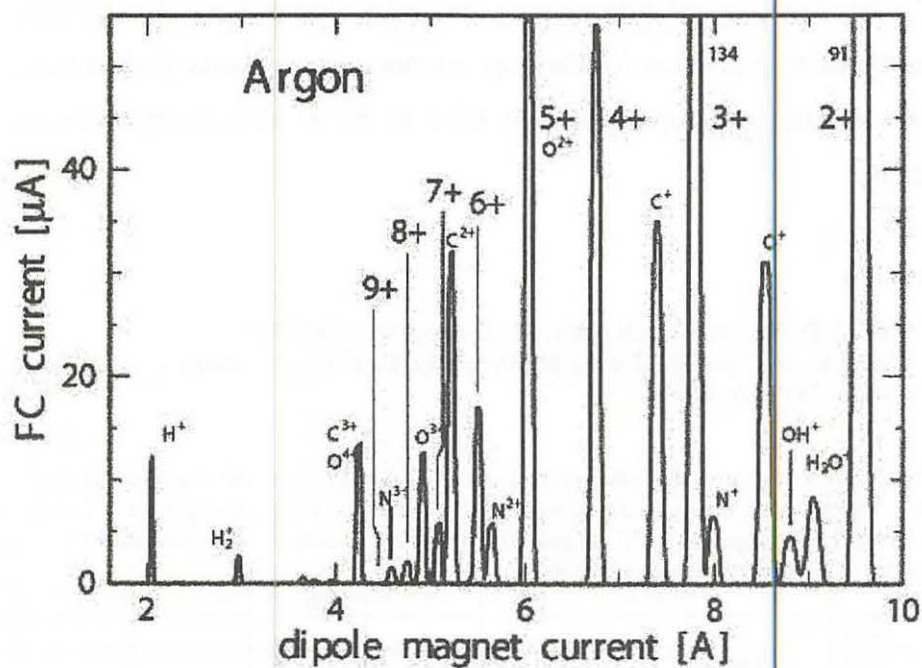


Fig. 2. Charge state spectrum of the extracted beam from argon plasma. Operation conditions are optimized for Ar^{8+} ions. Gas-mixing method is not used.

I. 6. Up Grated CYRIC Sinusoidal Beam Chopper for Fast-neutron TOF Experiment

*Terakawa A., Tanigaki M. *, Itoh K., Fujita M., Shinozuka T., Orihara H.*

*Cyclotron and Radioisotope Center, Tohoku University
Research Reactor Institute, Kyoto University, Noda, Kumatori, Osaka, 590-0494 Japan**

Introduction

The neutron time-of-flight (TOF) facility of CYRIC (Cyclotron and Radioisotope Center), Tohoku University^{1,2)} has made it possible for us to perform high energy-resolution measurement for fast neutrons in large dynamic range by means of both a long flight path up to 44m and a beam chopper system which increases time between each cyclotron beam burst. By using a good time-resolution beam from the K=50 MeV AVF cyclotron in combination with the TOF facility, 35 MeV (p,n) experiments have been performed for an extensive study on nuclear spin-isospin excitation³⁻⁵⁾, while (d,n) reaction at 25 MeV has been studied to obtain ground state properties of target nuclei as well as proton single-particle nature in residual nuclei^{6,7)}.

The beam chopper deflects the cyclotron beam bursts off the beam line axis by electric field of a pair of electrodes located in the beam line, and permits the beam bursts at 0 voltage between the electrodes to be transported to the target. The beam bursts deflected by the chopper are dumped with a subsequent slit.

The beam chopper installed in the TOF beam line at CYRIC is a sinusoidal type where a phase of 0 or 180 degree for the RF signal leads to 0 voltage between the electrostatic plates. Thus, the beam chopper driven at $1/2N$ (N : integral) of the cyclotron acceleration frequency gives the chopping rate of $1/N$ for the cyclotron beam bursts.

Recently, the K=50 MeV cyclotron at CYRIC was replaced by a new K=110 MeV AVF cyclotron. The maximum energy for a proton beam provided from the new cyclotron increases up to 90 MeV. The other light ions can be accelerated up to the respective maximum energies corresponding to the cyclotron K-number. The beam transport system at CYRIC was simultaneously improved for more energetic beams from the new cyclotron.

In addition, The neutron time of flight facilities, including the new beam swinger and the detector matrix. etc. have been up graded⁸⁾. The control system for the cyclotron and beam transport system was replaced by new one based on programmable logic controller (PLC) system (Yokogawa FA-M3 controller)⁹⁾.

The sinusoidal beam chopper at CYRIC has been improved by developing a new RF system as well as a PLC based control system. In the present paper the new RF system and control system are described together with results of a performance test for the new beam chopper system using a proton beam from the new cyclotron.

New control system

The PLC system generally used at automated factories is available to control experimental machines and instruments as well. It consists of the CPU and some modules such as DI/O(digital input / output), AD/DA, motor-control, and LAN modules. The CPU controls other modules on the basis of programs downloaded from a personal computer connected to the PLC system via the ethernet LAN. The DI (DO) and AD (DA) modules are used to monitor (control) machines via the status (control) signals from (to) the machines. Stepping motors can be controlled with motor-control modules connected to their motor-drivers. The PLC modules located in separated rooms can be controlled by the identical CPU using a light fiber cable connected between them. If the CPU is located in an experimental room it should sufficiently be shielded from neutron radiation because the CPU fault due to the radiation damage may be caused.

The new control system for the present beam chopper is illustrated in Figure 1. The CPU of the PLC system for the beam chopper is located in a control room. The PLC modules located in the separated rooms are connected with the optical fiber cables. Furthermore, the CPU for the beam chopper is connected to those for the cyclotron and beam transport system with link cables for interlock of the whole control system. Personal computers are used to control and monitor the system using the LabView visual interface¹⁰⁾ as well as to develop PLC programs downloaded to the CPU through the TCP/IP network.

New RF system

The RF system for the beam chopper determines chopping rate, magnitude and phase of RF voltage for the electrodes, and their stability. A new low level RF system for the present beam chopper has been installed because the previous system is not available

due to change of the control system for the beam transport lines. A diagram of the new RF system is shown in Figure 1. The basic specification of the improved beam chopper system is listed in Table 1.

Low level system

An input RF signal for the low level system from that for the cyclotron has the cyclotron acceleration frequency f . When the beam chopper operates at the chopping rate of $1/N$ where $N-1$ of N cyclotron beam bursts are deflected, the input signal is converted so that the output frequency of the beam chopper is $f/2N$. The frequency ranges of the input and output signals are 10.5 - 22 MHz and 0.5 - 1.6 MHz, respectively. The N values of 6 - 10 are available. As a result, a time interval between beam bursts ranges from 312.5 nsec to 1 usec. Phase shift for the output signal can be varied more than 360 degree in order to optimize the TOF spectrum. A TTL signal of $f/2N$ frequency is used for an RF stop for the TOF measurement.

In order to stabilize both electrode voltage and phase, an electrode signal is fed back to the low level system. The phase deviation of the output signal is compensated with an automatic phase controller (APC) on the basis of the phase difference between the input and feedback signals detected by a phase comparator while the amplitude is also kept constant with an automatic gain control unit (AGC) in a similar way. Finally, the RF low level system gives the output signal amplified by a 300 W preamplifier to an RF power amplifier.

The low level system is also controlled with PLC modules. The phase and amplitude of the electrode signal are set with 12 bit data from the DO module to the APC and AGC, respectively. The chopping rate data is also given by the DO module. Progressive and reflected waves of the output are monitored by measuring voltages of their monitor signals from the preamplifier with the AD module. The monitor signals are calibrated so that a rang of 0 - 10 V corresponds to 0 - 400 W for the progressive wave, and 0 - 200 W for the reflected wave.

RF power amplifier and electrode

The RF power amplifier used for the beam chopper system is a push-pull type consisting of a drive stage with two 4-125A tetrodes and a subsequent final stage with two 4CW10000 tetrodes. The present beam chopper system does not need the drive stage

because the new low level system can drive the final stage using the 300 W preamplifier which provides the output with a sufficient amplitude for the final stage. Thus, the output signal from the preamplifier enters directly into the final stage.

The power of the RF signal is supplied to the tank circuit from the final stage via a coupling coil. The maximum peak-to-peak amplitude of 50 kV between the electrodes is designed. The feedback loop signal to stabilize both phase and voltage of the electrode signal is provided from dividing condensers by which 1/1000 of the electrode voltage can be detected. Because the electrodes has a large capacity, the tank circuit needs to be tuned over the full frequency range by means of change in not only capacities of the variable condensers but also inductance of a tuning coil in the tank circuit by replacing it with the other one having different inductance. When the tuning coil is changed, a coupling strength of the coupling coil between the final stage and the tank circuit needs to be tuned to optimize the plate resistance of the 4CW10000.

The control system for the RF power amplifier was modified for the new PLC based system. Power supplies for the 4CW10000 were equipped with a newly developed interface for PLC based control. The control lines for the power amplifier were connected to the PLC modules through a distributor including some DC power supplies for electric circuits, AC power supplies for reversible AC motors, stepping motor drivers and some relay units. The capacities of the variable condensers, the distance between a pair of the electrodes and a gap of the slit can be changed with stepping motors controlled by the stepping motor module or reversible AC motors controlled by the DO module while the AD modules read the DC voltage from potentiometers indicating each position. Status signals from sensors for the upper / lower limits in each position and cooling water are read with the DI modules. The distributor and PLC modules were located in the same room as the beam chopper. The PLC modules were sufficiently shielded from the radiation damage.

Performance test of the new beam chopper system

Since the previous beam chopper system was used for a proton beam up to 40 MeV from the old cyclotron, a 50 MeV proton beam from the new cyclotron was used for a performance test of the improved beam chopper system. Figure 2 shows a measured TOF spectrum for gamma flash from the target with or without the beam chopper driven at 1/8 chopping rate. It is found that beam bursts from the cyclotron have clearly been deflected by the beam chopper. The maximum peak-to-peak voltage between the electrodes has been

achieved up to 50 kV with good stability in both voltage and phase of the RF signal. In the course of regular experiments at CYRIC, the performance test was successfully carried out with increasing proton beam energy up to 90 MeV.

Conclusion

The sinusoidal beam chopper for neutron TOF experiments at CYRIC has been improved by developing both the new RF system and the PLC based control system. The output frequency ranging from 0.5 to 1.6 MHz provides a dynamic range of 312.5 - 1000 nsec for TOF measurement. The maximum peak-to-peak amplitude of 50 kV between the electrodes has been obtained with good voltage and phase stability. The beam chopper driven by the new RF system has successfully been used for a more energetic beam from the new cyclotron. The PLC system is useful to develop and improve the control system for experimental instruments.

References

- 1) Orihara H. and Murakami T., Nucl. Instr. and Meth. **188** (1981) 15.
- 2) Orihara H. et al., Nucl. and Instru. and Meth. **A257** (1987) 189.
- 3) Orihara H. et al., Phys. Rev. Lett. **47** (1981) 301.
- 4) Orihara H. et al., Phys. Rev. Lett. **49** (1982) 1318.
- 5) Orihara H. et al., Phys. Rev Lett. **81** (1998) 3607.
- 6) Miura K. et al., Nucl. Phys. **A467** (1987) 79.
- 7) Terakawa A. et al. Phys. Rev. **C48** (1993) 2775.
- 8) Terakawa A. et al., Nucl. and Instru. and Meth. in press.
- 9) Yokogawa Electric Corporation, Musashino, Tokyo 180-8750, Japan (<http://www.yokogawa.co.jp>).
- 10) National Instruments Corporation, USA (<http://www.ni.com>).

Table 1. Specification of the sinusoidal beam chopper system.

Input frequency	10.5 ~ 22 MHz
Output frequency	0.5 ~ 1.6 MHz
Chopping rate	1/6, 1/7, 1/8, 1/9, 1/10
Maximum voltage	50 kV (peak to peak)
Voltage stability	< 1/100
Phase shift	-200 ~ 200 deg.
Phase stability	< 0.2 deg.

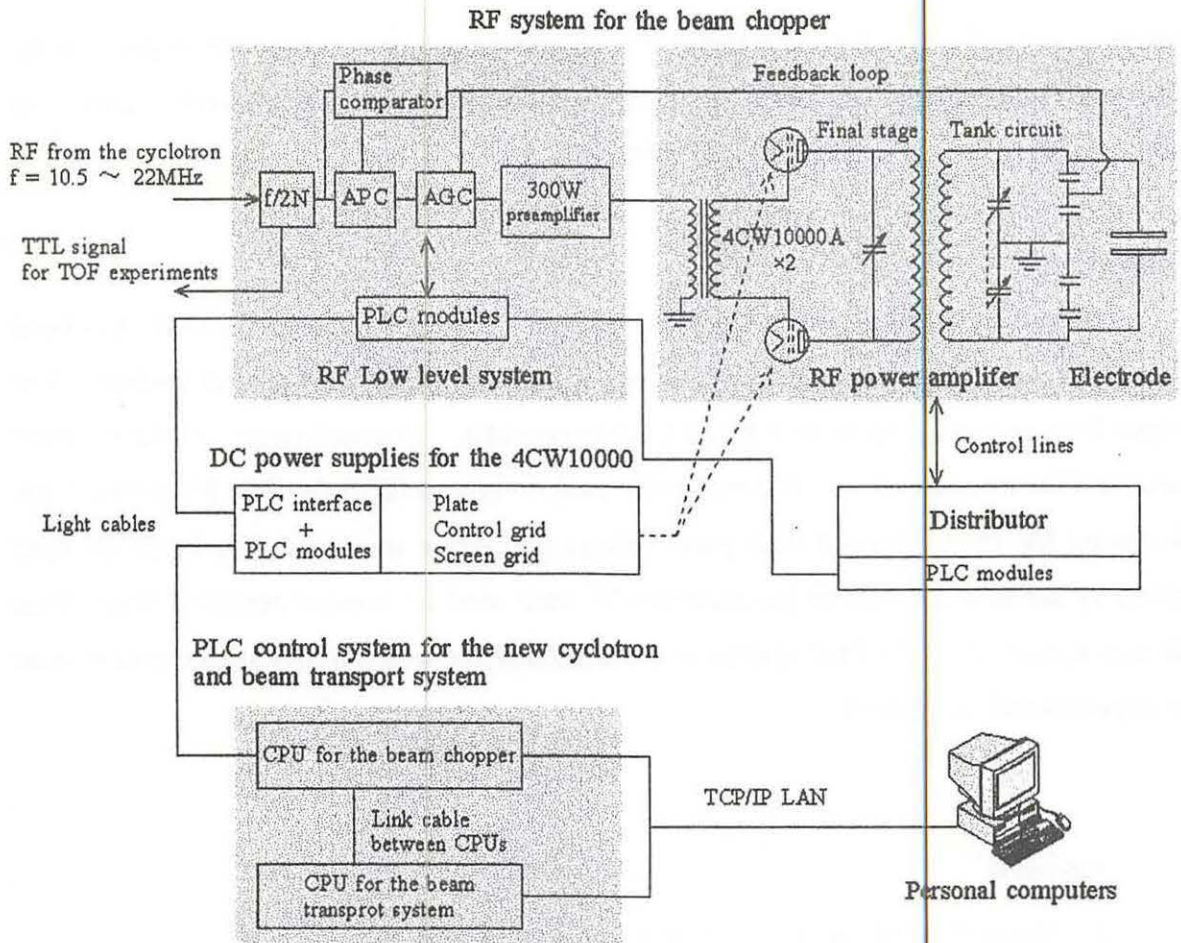


Fig. 1. Diagram of the RF and control systems for the CYRIC sinusoidal beam chopper.

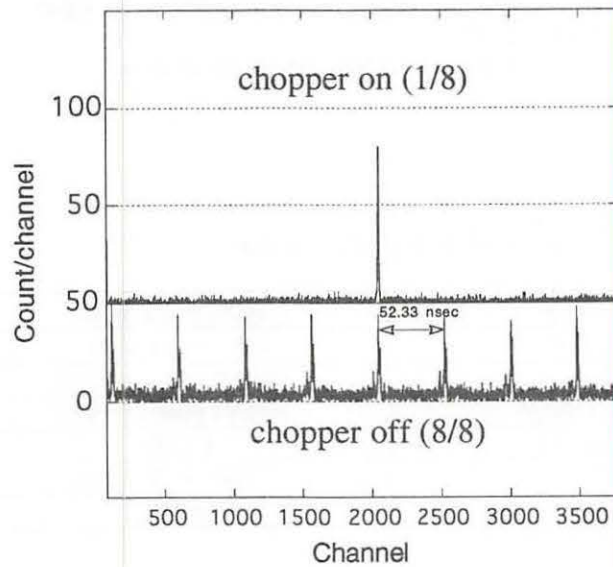


Fig. 2. TOF spectra for gamma flash measured using a 50 MeV proton beam with or without the beam chopper operated in 1/8 chopping rate mode.

I. 7. Development of Low-Pressure MWPC

Ozeki K., Otsu H., Okuda T., Watanabe K., Yakushiji T., Iwasa N., and Kobayashi T.

Department of Physics, Tohoku University

We have been engaged in developing Low-Pressure MWPC which can be used with less influence of multiple scattering by chamber gases. A practical application of the device is to measure the position of secondary beams at a momentum dispersive focal plane. It is necessary to decide the momentum for each particle in experiments using secondary beam with momentum deviation. A typical momentum dispersion is about $\pm 3\%$. One of the way to decide the momentum is to measure the time of flight between timing counters. This method has a disadvantage for large γ particles, which make the momentum resolution worse. In contrast, measurement of the position with high accuracy at momentum dispersive focal plane enables us to decide the momentum of each particle with wide energy range. Low-Pressure MWPC is designed as the focal plane detector. In addition to gas itself, low pressure property allows us to reduce the amount of substance of window foils separating MWPC and vacuum of about 10^{-6} Torr of secondary beam line. In developing, the following requirements are taken into account:

$$Z \geq 1,$$

Kinetic energy: $T \approx 250 \text{ MeV}/A$ (about two times larger than energy loss of the minimum ionizing particles),

Counting rate: 1-10M Hz/plane.

MWPC operates less stably when used at low pressure because of discharge. Until now, it was confirmed that efficiency of nearly 100 % could be achieved for minimum ionizing particles (β ray from ^{90}Sr) under 100 Torr by using pure *i*-C₄H₁₀. It is expected that the usage for particles which have larger energy deposit than minimum ionizing particles makes operating HV and pressure low. In order to confirm this expectation and to examine whether it could maintain high enough efficiency at high counting rate, we investigated operating characteristics using 70 MeV protons (about 5.7 times larger than

energy loss of the minimum ionizing particles). Hit patterns and time spectra of MWPC were measured by multi-hit TDC LeCroy LRS3377, via pre-amplifier REPIC RPV-041 and amplifier/discriminator card LeCroy 2735PC. The threshold of 2735PC was set to 5 V.

Operating characteristics were measured at various pressures as follows: 760, 380, 190, 100, 80, 60, 40, 30, 20, 10, and 5 Torr. Efficiency curves are shown in Fig. 1. It can be seen that efficiency curve shifts to lower voltage when the pressure becomes low. Fig. 2 shows optimum voltages at each pressure (for comparison, those for β rays are also shown). Optimum voltage decreases sharply under 40 Torr in contrast to gentle dependence at higher pressure. In order to interpret the relation between pressure and optimum voltage, we made a model from several assumptions as follows:

- (1) Translate the condition that efficiency reaches 100 % into the condition that the number of electrons which arrive at an anode wire per event always reaches a constant value (N),
- (2) The number of seeds is in proportional to pressure (eP , e is a constant),
- (3) Divide the electric field into two parts: the cylindrical field near anode wires and the constant field distant from anode wire, namely

$$E = d \frac{V}{r} \quad \text{if } r \leq \frac{s}{\pi},$$

$$E = d \frac{\pi V}{s} \quad \text{if } r \geq \frac{s}{\pi},$$

where s is the anode wire spacing and d is a constant which is decided from the geometry of MWPC¹⁾. The intermediate field is not considered here. An expression formulated by Aoyama²⁾ is used here as the first Townsend coefficient:

$$\frac{\alpha}{P} = KS^m \exp(-LS^{m-1}),$$

where $S=E/P$, K , L , m are constants ($0 \leq m < 1$). If a is the anode wire radius and b is the (averaged) starting point of the avalanche, relation between pressure P and optimum voltage V is expressed as

$$\frac{KdV}{L(1-m)} \exp\left\{-L\left(\frac{dV}{aP}\right)^{m-1}\right\} - \left\{\frac{KdV}{L(1-m)} - PK\left(\frac{d\pi V}{sP}\right)^m \left(b - \frac{s}{\pi}\right)\right\} \exp\left\{-L\left(\frac{d\pi V}{sP}\right)^{m-1}\right\} - \ln \frac{N}{eP} = 0.$$

The best fitting result for measured values is shown as solid lines in Fig. 2. The model fitting result succeeds in reproducing the measured points except the knee shape around 60

Torr. This difference around the knee point is expected to be improved by introducing intermediate field into the model. The model which includes only cylindrical field cannot reproduce sharp decrease at lower pressure. This result suggests that avalanche occurs not only in the region near the anode wires, but also in the outer region because of the increase of reduced field S .

The responses for high counting rate were measured. The rate dependence of the efficiency was measured at 190 Torr. The counting rates per about seven wires limited by a collimator installed were changed as follows: 1k, 10k, 100k, 1M, and 2M Hz. TDC spectra at 1k and 2M Hz are shown in Figs. 3 and 4, respectively. At 1k Hz, the component of wire multiplicity 1 occupies the greater part of all components, of which efficiency reaches practically almost 90 %. At 2M Hz, to the contrary, accidental events having same period with RF frequency increase. These accidental events make multiplicity 1 events not so. "Effective" efficiency was obtained by applying timing gate on TDC spectra to remove the accidental events. The location of gate is much the same as that of spectrum of wire multiplicity 1. Efficiencies with/without timing gate as a function of counting rate are shown in Fig. 5. Total efficiency keeps nearly 100 %, while efficiencies of wire/cluster multiplicity 1 decrease remarkably in the case without timing gate. On the other hand, efficiencies with timing gate hardly decrease even at high rate up to 2M Hz/7 wires. From this result, it was found that operation for high counting rate showed useful enough operating characteristics.

From these measurements, the feasibility of Low-Pressure MWPC on secondary beam line was confirmed. This device will be used practically at facilities such as HIMAC at NIRS, RIBF at RIKEN.

References

- 1) F. Sauli, PRINCIPLES OF OPERATION OF MULTIWIRE PROPORTIONAL AND DRIFT CHAMBERS.
- 2) Aoyama T., Nucl. Instr. and Meth. A **234** (1985) 125.

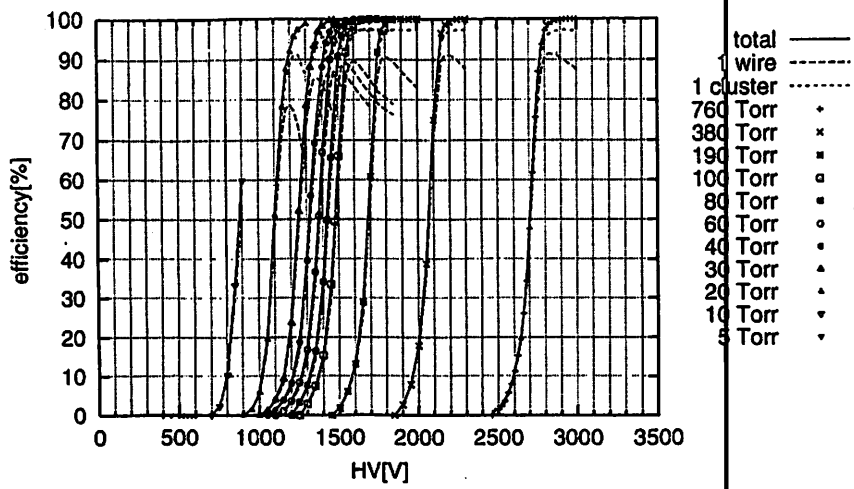


Fig. 1. Efficiency curves for protons at various pressures.

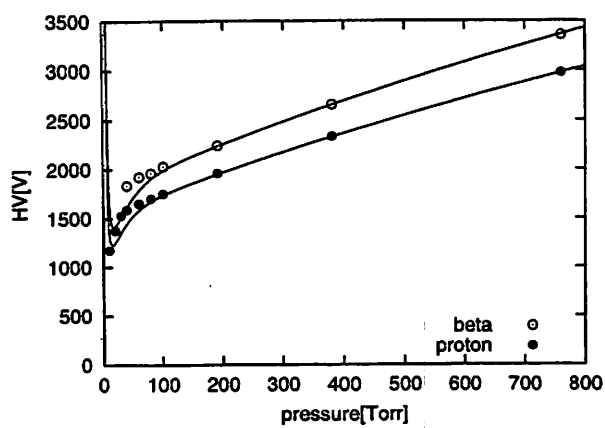


Fig. 2. Optimum voltage for protons and β rays at each pressure and model fitting result.

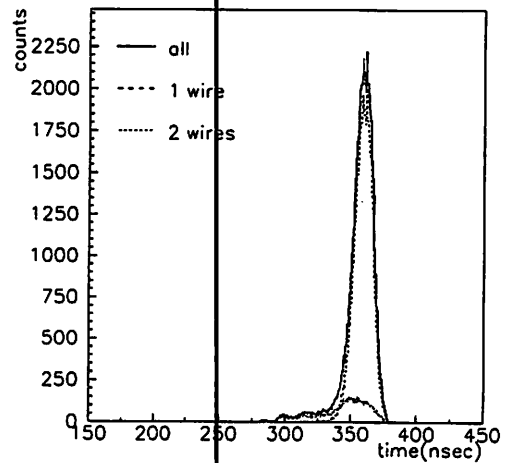


Fig. 3. TDC spectrum at 1k Hz.

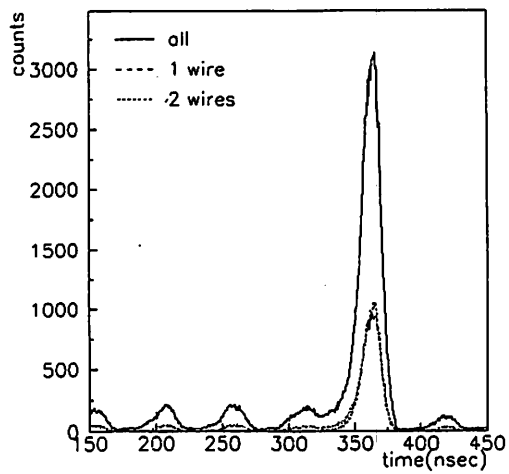


Fig. 4. TDC spectrum at 2M Hz.

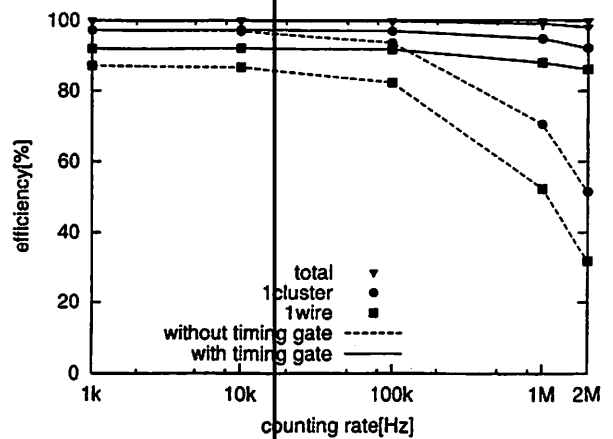


Fig. 5. Efficiencies with/without timing gate as a function of counting rate.

I. 8. Development of the New Tape Transport System for ISOL

Fujita M., Ohshima T., Yamazaki A., Sonoda T., Goto A., Watanabe S., Tanaka E. and Shinozuka T.

Cyclotron and Radioisotope center, Tohoku University

The ISOL (Isotope Separator On Line) facility at CYRIC has been used in a variety of research fields such as study of short-lived isotopes¹⁾ and implantations of RI combined with Mössbauer spectroscopy and perturbed angular distribution for solid-state physics²⁾. In recent years, search for the new isotopes far from the β -stability line³⁾ and precise β - γ and γ - γ spectroscopy measurements⁴⁾ have been achieved in combination with the ion-guide technique⁵⁾.

In ISOL experiments, mass separated RIs are collected for a given time duration and after that they are transferred to the detector position in order to measure under low background condition. For this purpose the tape transport systems have been used at many ISOL facilities. The tape transport system with three detector chambers had been installed to the ISOL beam line at CYRIC in 1978⁶⁾ and modified to enable higher speed operation in 1989⁷⁾. This tape transport system had been used for many experiments for more than twenty years, but recently frequent troubles became to occur because of its superannuation.

In this report, characteristic of the new tape transport system have been described in detail in addition to the result of a measurement of the spontaneous fission from ^{257}Cf source using the present system. In designing of the present tape-transport apparatus, we paid attention not only to the transport time and the accuracy of transport distance but also the stability in long operation and the flexibility of the system in various modification. For this purpose we adopted vertically-running of a tape as following. We also adopted a PLC (programmable logic controller) to control the entire system and to perform associated function, among others, the control of data acquisition.

The most drastic change between old and new tape transport system is the direction of running of the tape. In the old system, a tape had been traveled horizontally along with the guide rollers. In that case, a tape must be always stretched. When the tension of the tape become insufficient, it falls from the guide rollers. Once a tape falls, it takes several hours to recover including making a vacuum. Therefore we adopt the vertically traveling methods for the new tape transport system because a tape never falls even if it becomes loose. Though it was a simple change, it could decrease troubles markedly.

Another important feature of this system is that the whole system can be controlled by the PLC (Programmable Logic Controller), which is adopted to control the cyclotron and following beam transport system⁸⁾. The PLC works in accordance with the ladder programs described by relay-coil diagrams. These programs written in the ladder language are very intuitive and intelligible. In addition, so-called objective-oriented programming methods are applicable to them. This increases flexibility of reuse and custom design of programs, allowing development of the programs to be shared by two or more programmers.

Figure 1 shows the general view of the tape transport system. This system consists of three servomotors which is called as "taking", "feeding" and "capstan". The capstan controls exactly the transport length and speed of the tape. Each of the reel is driven directly by the taking and the feeding motor respectively, and the torque of which is regulated by the position of the tension arm; this position is converted to a voltage by a potentiometer and this voltage signal is inputted to the A/D module of PLC in order to apply to the feedback of the servomotor. The tape from the feeding reel is transported through the collector station behind the ISOL beam line and the detector station at 30 cm from the former and is accepted by the taking reel in the chamber. The maximum diameter of the both reels is 81 mm and an aluminized polyester tape of 16 μm thick, 12 mm wide is rolled. The moment of inertia of the fully-loaded reel is estimated as $3.9 \times 10^{-3} [\text{kg} \cdot \text{cm}^2]$, however this value is too large to use the servomotor of the adequate size. Therefore we decrease to a hundredth the effective moment of inertia by use of the reduction gear of which reduction ratio has 1:10. When it is accelerated to 3000 r/min within 0.01 s, the required torque of the servomotors is about 0.31 [N·m]. We have chosen the servomotors with sufficient torque of 0.64 [N·m] as listed in Table 1. As mentioned above, the distance between

the irradiation spot of the ISOL beam and the detector position is 30 cm. We aim to transfer the collected RIs to the detector position within 300 ms, because in many cases we are interested in short-lived isotopes of which half-lives are less than 1 second. In practice, we have achieved the transportation within 220 ms.

Figure 2 shows the flow chart of the tape transport operation. After the input of the required parameters and the trigger command, the radius measurement of each reel is executed. The radius of each reel is calculated from the position of the tension arm after a small fixed-length transport of the tape. It is very important to know accurately the current radius of each reel, because the rotation angle of each reel depends on its radius. During the routine of the fixed-length transport, the radius of each reel is always recalculated and is applied to the feedback of the rotation angle of the servomotor through the PLC. The accuracy of the stop position is also important because it influences the solid angle of the detectors at detector station. In the present apparatus, the accuracy of the stop position in 30 cm transport is within ± 1.0 mm and no dependence on the tape speed is confirmed.

Using the present tape transport system, we measured the gamma-ray spectra of the fission fragments from ^{252}Cf source (232 kBq). The source is located 1 mm away from the tape surface at the collection chamber. The fission products implanted into the tape in some period are transferred to the detector position 38 cm away from the source in 320 ms and then the gamma-ray spectra are measured by two clover-type HPGe detectors⁹⁾ placed face to face at the detector station. The measurement is carried out in three times and the interval of the tape transfer in each measurement is 3.7 sec, 30 sec and 30 min respectively. Figure 3 shows the comparison of three gamma-ray spectra and the identified isotopes in each spectrum are listed in table 2. As a result, we can obtain the effect of the present apparatus because only isotopes of which half-lives are close to the interval of the tape transfer are measured.

References

- 1) See for example, Yoshii M., Hama H., Ishimatu T., Shinozuka T., Fujioka M. and J.Ärje, Nucl.Inst.Meth., **B26** (1987) 410.
- 2) See for example, Hanada R., CYRIC Annual Report (1989).
- 3) See for example, Watanabe A., Shinozuka T., Fujita M., Kanai Y., Kohda T. and Fujioka M., CYRIC Annual Report (1995).
- 4) See for example, Fujita M., Shinozuka T., Watanabe A., Kimura Y., Kanai Y., Fujioka M and Sugai I., CYRIC Annual Report (1994).
- 5) J.Ärje, J.Äsdtö, Nucl.Inst.Meth., **186** (1981) 149.

- 6) Arai Y., Tanaka E., Ishimatsu T. and Fujioka M., Nucl.Inst.Meth., **186** (1981) 231.
- 7) Ikegami H., Master thesis, (1986) Tohoku University.
- 8) Fujita M., Chiba S., Ohmiya Y., Takahashi N., Tanigaki M., Terakawa A. and Shinozuka T., CYRIC Annual Report (2001).
- 9) Suzuki T., Master thesis, (2000) Tohoku University.

Table 1. Identified Isotopes in the gamma-ray spectra.

3.7 sec		30 sec		30 min	
Identified Isotopes	Halflife	Identified Isotopes	Halflife	Identified Isotopes	Halflife
^{102}Nb	1.3 sec	^{108}Tc	5.2 sec	^{130}Sb	6.3 min
^{99}Y	1.5 sec	^{146}La	6.3 sec	^{105}Tc	7.6 min
^{99}Zr	2.1 sec	^{144}Ba	11.5 sec	^{146}Ba	10.6 min
^{112}Rh	2.1 sec	^{110}Rh	28.5 sec	^{141}Ba	18.3 min
^{102}Zr	2.9 sec	^{139}Xe	39.7 sec	^{104}Tc	18.3 min
^{108}Tc	5.2 sec	^{144}La	40.8 sec	^{138}Cs	33.4 min
^{146}La	6.3 sec	^{148}Ce	56.0 sec	^{142}La	91.1 min
^{144}Ba	11.5 sec				

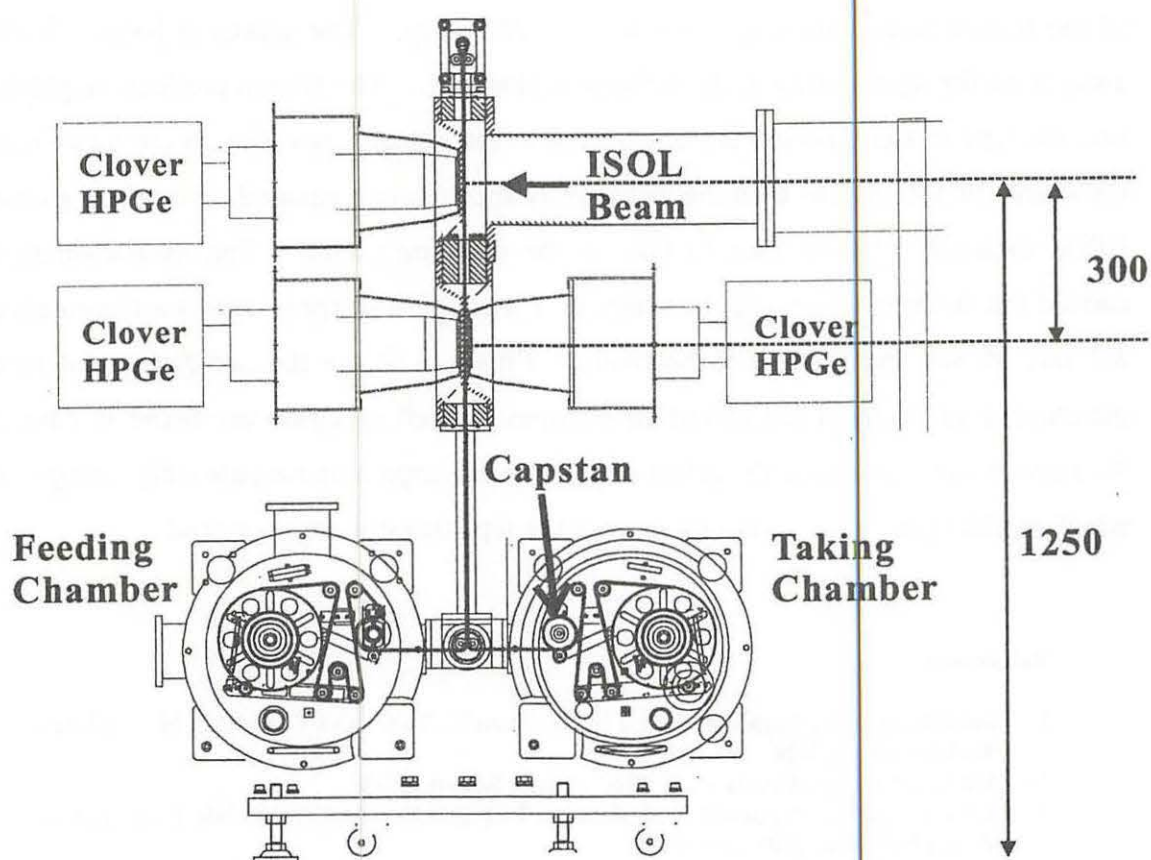


Fig. 1. A general view of the present tape transport system.

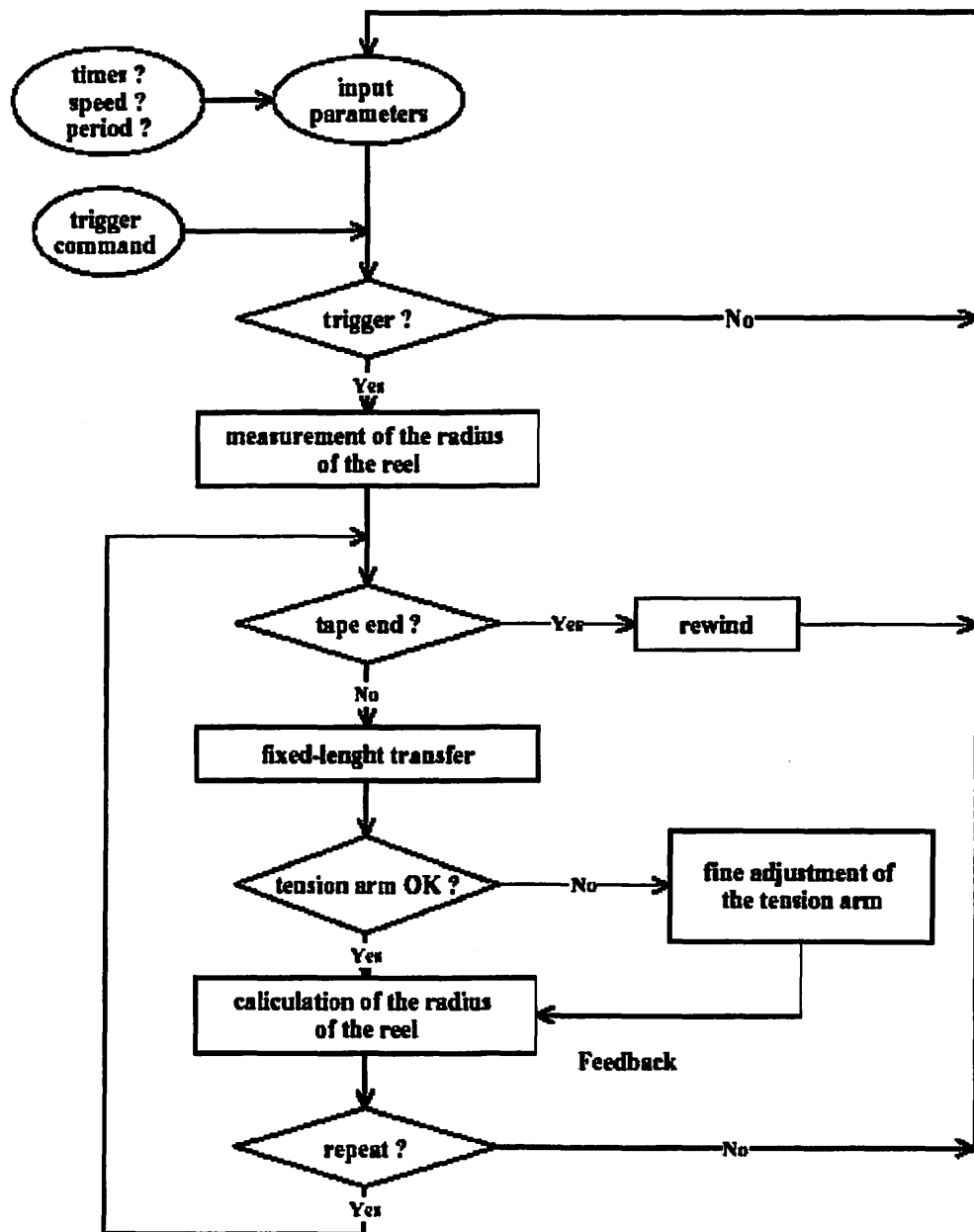


Fig. 2. A flow chart of "fixed-length transfer" operation of the present tape transport system.

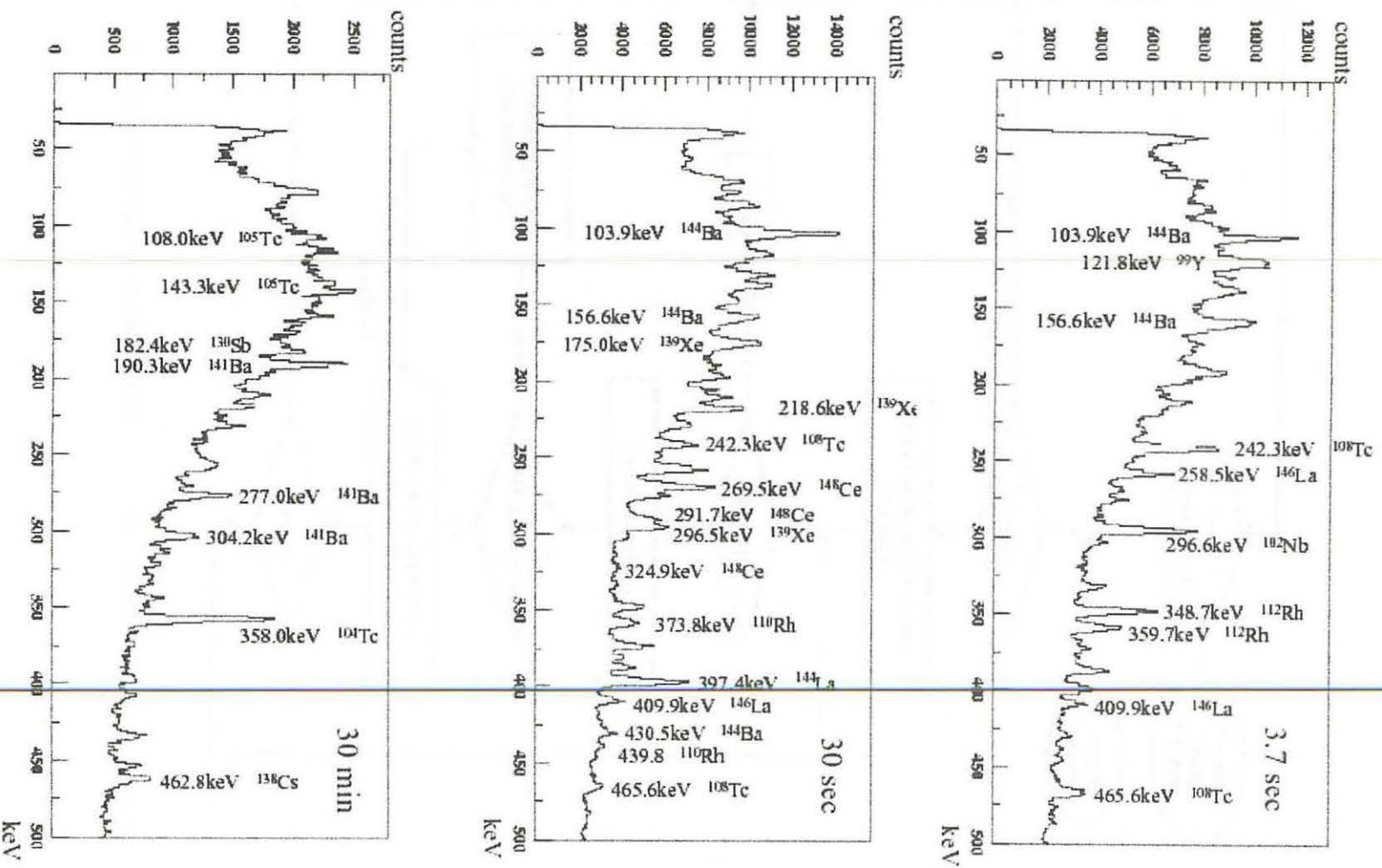


Fig. 3. Gamma-ray Spectra for the fission fragments from ^{252}Cf source. The repetition periods of the tape transfer are 3.7 sec, 30 sec and 30 min respectively.

I. 9. Simultaneous Acquisition of Emission and Transmission Data in PET

*Watanuki S., Ishii K. *, Itho M., and Orihara H.*

*Cyclotron and Radioisotope Center, Tohoku University
Department of Quantum Science and Energy Engineering, Tohoku University**

Introduction

The imaging error due to the mismatch between an emission data and an attenuation correction data obtained by transmission scan is one of the serious problems in the quantitative PET study. Simultaneous acquisition of emission and transmission (SET) data is employed to solve this problem¹⁻²⁾, and it enables to reduce a study time. But this method has a problem that degrades signal to noise ratio (SNR) in emission images. This problem is caused by contamination of emission data by random and cross-talk events from a transmission source²⁾. In this study, we examined the SNR of emission images in conventional scanning and also SET scanning and evaluated a suitable condition for SET scanning.

Material and Methods

All data were obtained by a SET-2400W PET system (Shimadzu Cop., Kyoto, Japan). SET was carried out by the scan mode of post-injection transmission (PIT) with a sinogram window technique where transmission window is defined with lines of response (LORs) containing a transmission source, and an emission window is defined with LORs except for transmission window. A border window should be provided between the transmission window and the emission window to omit their cross-talk. The fraction ratio of emission window in a whole sinogram is 83.8% at an average.

Experiment 1

We compared the SNR of emission image obtained by SET mode with that of normal emission (NE) image obtained by a usual mode. A 20 cm diameter cylindrical phantom was used in all scans. Dynamic NE scan and SET scan were carried out for 20 min comprising 20 frames, respectively. One frame was 1min duration scan. The emission activity varied from 9.6 to 1.1 KBq/ml at each dynamic scan. Two different

transmission activities (117 and 85 MBq) were used for SET acquisitions. Adding 1 min scan data each other in dynamic scan data sets, we made up emission data for the scan time of 1, 2, 3, 5, 7, 10, 15 and 20 min. Attenuation correction data was made from the dynamic SET transmission data by the same manner in emission data processing. Emission data were corrected with transmission data and was reconstructed by the filtered back projection method. Coefficients of variation (COV) in PET images which is useful for an indicator of the image SNR were estimated from ROIs of diameter 16 cm on the central regions of 59 image planes.

Experiment 2

We evaluated the influence on SNR of the crosstalk and random events from transmission source at the SET scan mode. We carried out SET scans without transmission source and with emission activity (: SET(T-)) and with transmission source and without emission activity (:SET(E-)) as same as in the experiment 1. By combining the emission data of SET(T-) with the emission data of SET(E-), scan data for 5, 10 and 20 min were obtained with the same process as in the experiment 1. Attenuation correction of these data set were done with the transmission data obtained at the experiment 1, and COV values were obtained by the same manner as in experiment 1.

Results and Discussion

Figure 1 shows COV as a function of the scan duration and COV for SET and NE emission images at the phantom activity of 3.7 KBq/ml. COV is proportional to the inverse of the square root in scan duration. COV of SET is higher than COV of NE at the same scan duration. The ratios of COV of SET to that of NE were 1.46 at the 117MBq transmission activity and 1.13 at the 85MBq. Consequently, SET scan duration should be 2.1 times longer than NE in the case of 117 MBq and also it is 1.7 times for 85 MBq. This reduction on SNR is due to a decrease in effective emission scan duration, crosstalk and random events from transmission source. The crosstalk and random events depend on the strength of transmission source. Therefore transmission source strength is required to be kept in proper range. When 10 minutes is adopted as maximum scan duration per position, normal transmission scan duration becomes about 7 min at 117 MBq source³⁾, and so emission duration become 3 min. ET is useful in this case, since 10 min SET scan is longer than twice of 3 min and the transmission data is more reliable than 7 min scan. But SET SNR would become worse than separate scan when transmission activity stronger than 180MBq, since emission duration become over 5.min. Conversely, when transmission activity weaker than 83 MBq, transmission scan needs over 10 min by itself then scan is absurd.

COV values of SET(T-) and SET(T-)+SET(E-) obtained in experiment 2 are

shown in table-1. Contribution fraction of the SNR reduction by the crosstalk and random events were derived from table-1 and are shown in table 2. Fraction of window, crosstalk and random were 11, 25 and 64% respectively at 10 min SET scan. This result means that major source of the reduction of SNR is random events obviously. Since random events are proportional to the square in count rate, it is supposed that the reduction by random becomes a main contribution at a stronger transmission source.

Conclusion

In this study, we showed clearly that random event from transmission source is major source of the reduction of SNR in the SET emission image.

We concluded that the following manners make SET scan be useful.

- 1) Transmission source activity should be from 83 to 180 MBq at SET-2400W.*
- 2) When transmission source activity is over 180 MBq, carry out a short transmission scan with SET and add its emission data to normal emission scan data*.
- 3) Use a short rod source method proposed by M. Dahibom et al.⁴⁾.
(* When scan duration will be 10 min per position.)

References

- 1) Meikle S.R., Bailey DL et al., J Nucl. Med. **36** (1995) 1680-1688.
- 2) Inoue T., Oriuchi N., et al., Nucl. Med. Com. **20** (1999) 849-857.
- 3) Wtanuki. S, Ishii K et al., CYRIC Ann. Rep. (1998) 173-178.
- 4) Dahlbom M., IEEE Trans. Nucl. Sci., **47** (2000) 1088-1092.

Table 1. COV values of emission image were obtained for different scan conditions and different scan duration with 117 MBq transmission source. Values of SET(T-) reflect the influence of emission window on a NE image. Value of SET(T-) + SET(E-) was added the influence of crosstalk of transmission events to SET(T-), and Value of SET was added the influence of random events to SET(T-) + SET(E-).

mode	Scan Duration		
	5 min	10 min	20 min
CE	83	59	43
SET(T-)	87	62	45
SET(T-) + SET(E-)	96	69	50
SET	121	87	62

Table 2. Contribution fraction was derived from the COV values in Table 1. The value is a fraction of each noise sources in total noise caused by SET on emission image.

Scan Duration mode	Relative Reduction Ratio (%)		
	5 min	10 min	20 min
Emission Wind	10	11	11
Crosstalk Event	24	25	26
Random Event	66	64	63

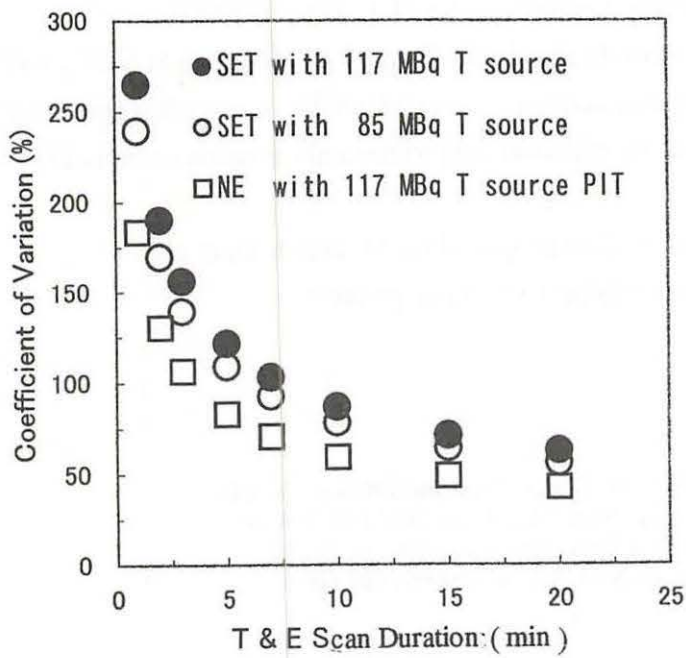


Fig. 1. COV values of emission image (3.7 KBq/ml) as a function of scan duration for the normal emission scan (NE) with PIT and for simultaneous emission/transmission scans (SET) with different transmission source activities of 117 and 85 KBq.

I. 10. Development of the Magnetic Aluminum Shield for MEG

*Suzuki A., Ishii K., Yamazaki H., Matsuyama S., Aikawa K.,
Momose G., Watanuki S.*, Itoh M.*, and Orihara H.**

*Department of Quantum Science and Energy Engineering, Tohoku University
Cyclotron and Radioisotope Center, Tohoku University**

Introduction

MEG (Magnetoencephalogram) generated by electrical neuron activities in the brain has an excellent feature of local signal without distortion. To measure MEG ($<10^{-12}\text{T}$), not only SQUID that is detectable to 10^{-15}T but also removal of environmental noise are necessary. In urban area, a very expensive magnetic shielded room made by a high permeability material is indispensable¹⁾. In order to construct simple measuring system without the expensive magnetic shielded room in our laboratory of low noise environment, the MEG measurement has been carried out with a second order gradiometer that is more insensitive to environmental noise than a magnetometer and a first order gradiometer²⁾. A first order gradiometer was used in our laboratory of low noise environment, but a 50Hz noise generated from a power supply was so big that tailing components of the 50Hz noise prevented the MEG measurement. By reducing the 50Hz noise, however, a first order gradiometer is expected to detect deep dipole sources producing MEG with a good SN ratio (MEG signal to magnetic noise). In this study, the magnetic aluminum shield that is relatively low cost and ease of construction was developed in order to improve the measurement environment in our laboratory.

Material and Method

In our laboratory, there is a simple shielding room which surrounded by aluminum plate of the about 0.04mm thickness and copper wire gauze(0.45mm ϕ) with about 1.7mm texture width. This shielded room removes the electromagnetic field with exceeding the modulation frequency (500Hz) of dc-SQUID feedback loop used in this experiment: this high-frequency electro-magnetic field causes a magnetic flux trap in the SQUID element.

As the magnetic field detector we used the commercial first order gradiometer SQUID system (Quantum Design Inc.) with a 30 mm diameter spaced 60 mm apart (baseline), and the second order gradiometer SQUID system (Quantum Design Inc.) with a 24 mm diameter spaced 30 mm apart. We tried to decrease electro-magnetic noise from the measurement system. For example, because the SQUID sensor detected the horizontal synchronizing signal from CRT display, we used a book-sized personal computer with a liquid crystal display. One channel output from the SQUID controller is taken into the book-size personal computer through the ADC card (National Instruments Co., DAQCard-1200). The software controlling measurement, LabVIEW, (National Instruments Co.), was installed in the computer, and the one-channel data was displayed on TFT display. In measuring mode, the data was stored into RAM in order to keep the processing speed of personal computer.

Results and Discussion

The spectral density in relatively low noise environment is shown in Fig. 1. From Fig. 1, the second order gradiometer is capable of measuring MEG without the shielded room in low noise environment, because the noise spectral density from 0 to 100Hz is about $10\text{fT}/\text{rtHz}^3$. On the other hand, in the measurement with the first order gradiometer, besides of a peak of the 50Hz noise, tailing components that extended from this peak to low frequency and high frequency were measured. These tailing components covered the frequency band of MEG. Fortunately it is possible to shield the alternative magnetic field such as 50Hz by the eddy current using a high conductivity material⁴⁾. The schematic diagram of a magnetic aluminum shield is shown in Fig. 2. This shield is very compact and surrounds only the head of an examinee and SQUID. In addition, it is possible to carry from place to place, because the shield is constructed by bolting and it can be decomposed easily. The thickness of aluminum plate was decided to 2cm by the simulation result of the finite element method⁵⁾. This is the thickness that can reduce the 50Hz magnetic field to 1/450.

In order to evaluate the applicability of the magnetic aluminum shield, the environmental noise inside the shield was measured with the first order gradiometer. The measurement was carried out under two different conditions; (1) the shield was perfectly closed and (2) front plate was pulled out from bottom to 31cm. The spectral density of the magnetic flux inside the shield is shown in Fig. 3. When the shield was perfectly closed,

the 50Hz noise was reduced to about 1/13. And it was reduced to about 1/10 without front plate. By reducing 50Hz noise, moreover tailing components (30~70Hz) were disappeared. According to the simulation of the finite element method, the 50Hz magnetic field should be reduced to 1/450, but it was actually about 1/13 due to the contact resistance in the juncture of aluminum plate.

We tried to measure magnetoencephalo waves from human brain using the aluminum shield with a front opening. Unfortunately, a vibrational noise due to the slight movement of an examinee such as the respiration was measured at 12Hz (Fig. 4). The vibrational noise was steadily generated during the measurement, and the strength was equivalent to that of $t \alpha$ rhythm ($< 10^{-12}T$). So, it is necessary to reduce the vibrational noise by improving a frame supporting SQUID, a bed of the examinee and using a rubber isolator.

In order to evaluate the possibility of MEG measurement inside the aluminum shield under the condition of no vibrational noise with the first order gradiometer, first noise signals measured with both the first order gradiometer inside the shield and the second order gradiometer outside the shield were averaged 100 times (Fig. 5). These amplitudes are, about 45fT for the first order gradiometer and 38fT for the second order gradiometer, respectively. Afterward we simulated a magnetic field generated from the current dipole as the source of MEG. Assuming that the head of the examinee is a sphere of 10cm radius, we calculated the magnetic flux at the surface of the sphere in the cases of the first order gradiometer and the second order gradiometer. Figure.6 shows the simulation result of the relationship between the depth of the current dipole and $B1/B2$. $B1$ and $B2$ mean the magnetic flux calculated in the cases of the first order gradiometer and the second order gradiometer respectively. It is revealed from Fig. 5 that the noise level is 1.2 times larger for the first order gradiometer compared to the second order gradiometer. From Fig. 6, the $B1/B2$ ratio exceeds the value of 1.2 when the depth of the current dipole is over 3cm, that is, better SN ratio of the first order gradiometer. Consequently, by using our shield in low noise environment, we can precisely detect MEG generated in the deep brain region with the first order gradiometer.

References

- 1) Magnetic shield room/ Magnetic shield product catalog of TOKIN.
- 2) Nagasawa M 1999 Phase correlation analysis between EEG and MEG simultaneously measured by a simple system composed of one channel SQUID fluxmeter and two channel EEG device CYRIC Annual Report 91.

- 3) Hara.H, Kuriki.S 1997 Noujirikagaku Ohmsha.
- 4) Zimmerman J 1977 SQUID instruments and shielding for low-level magnetic measurements J.Appl.Phys. 48 702.
- 5) FEMM.<http://hometown.aol.com/gmagnetics/download.htm>.

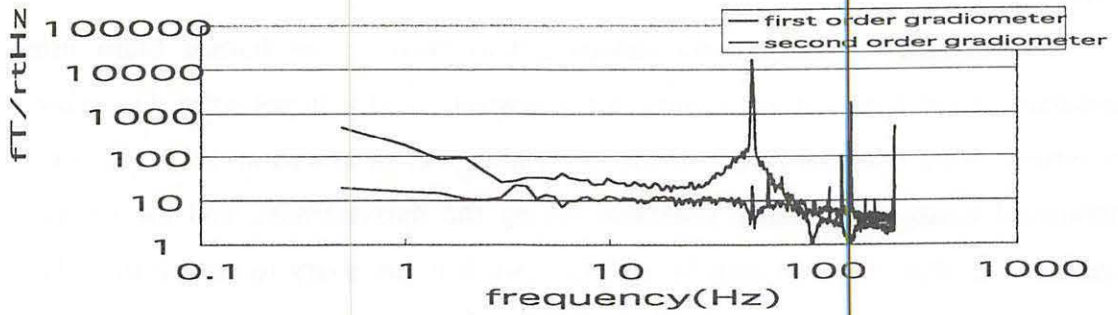


Fig. 1. The spectral density of magnetic flux measured with the first order gradiometer and the second order gradiometer in relatively low noise environment.

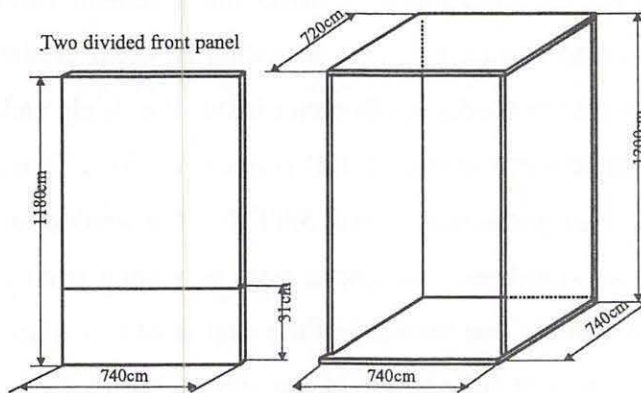


Fig. 2. Schematic design of the magnetic aluminum shield (2cm thickness aluminum plate).

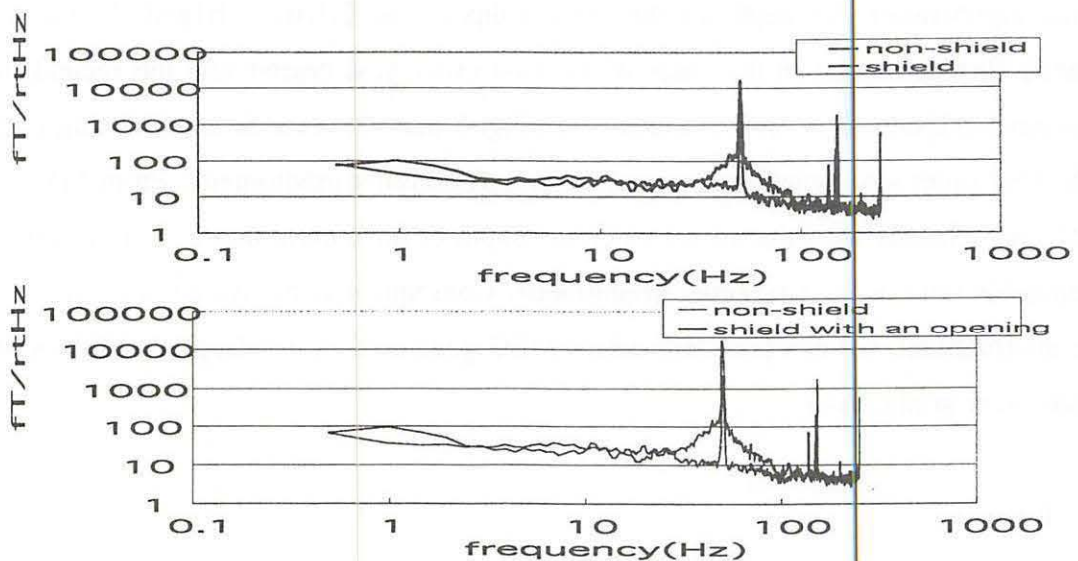


Fig. 3. The spectral density of magnetic flux measured with the first order gradiometer in the condition that the shield was perfectly closed (top) and that front plate was pulled out from bottom to 31cm (bottom).

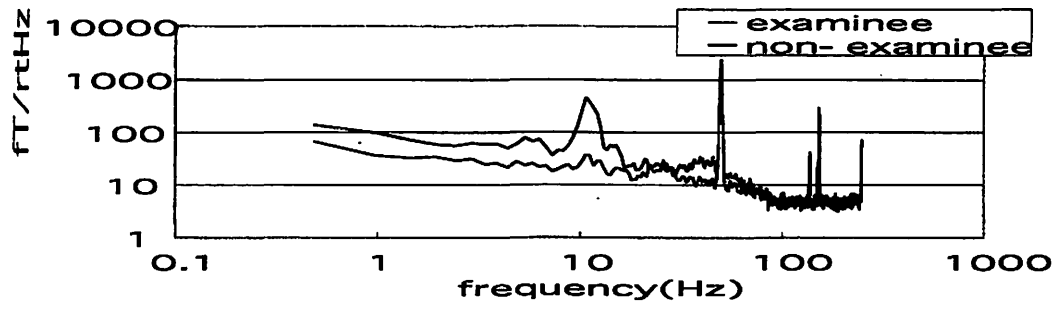


Fig. 4. The vibrational noise originated in the examinee.

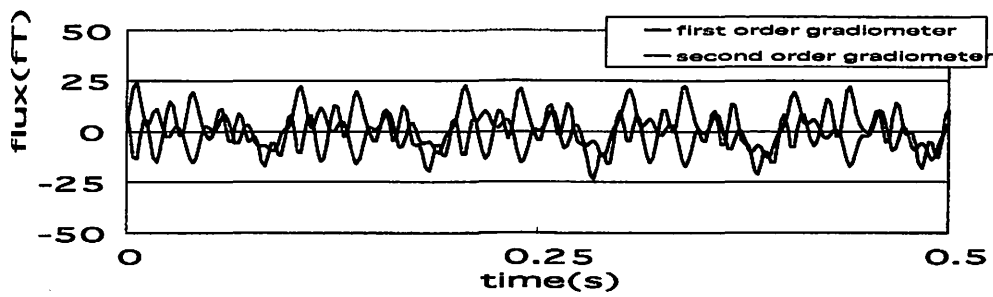


Fig. 5. The noise measured with the first order gradiometer inside the shield and the second order gradiometer outside the shield were averaged 100 times.

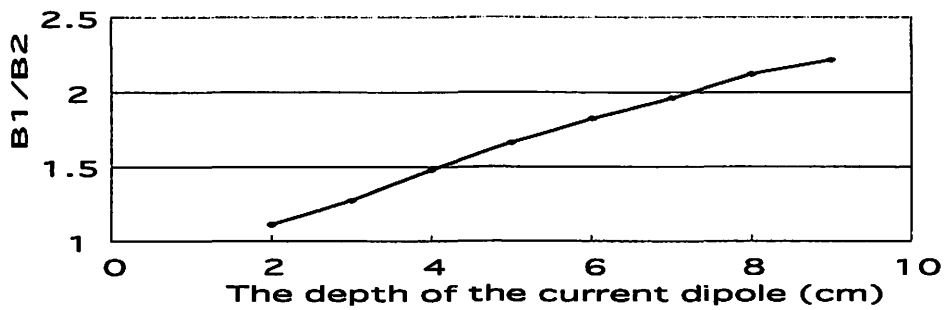


Fig. 6. The relationship between the depth of the current dipole and B1/B2.

I. 11. Scatter Correction for 3D PET Based on Image Subtraction Method

Oishi Y., Sasaki K., Ishii K., Yamazaki H., Matsuyama S., Kikuchi Y., Rodriguez M., Aihara T., Yamaguchi T., Watanuki S., Itoh M.*, and Orihara H*.*

*Department of Quantum Science and Energy Engineering, Tohoku University
Cyclotron and Radioisotope Center, Tohoku University**

Introduction

Development of PET scanner is basically addressed toward improvement of spatial resolution and increase of sensitivity. 3D PET was originated from the request of the latter. Sensitivity of 3D PET is higher than that of 2D PET because septa, which restrict detection coincidence lines in 2D PET, are removed. In the case of the Shimadzu SET-2400W scanner in CYRIC, sensitivity in 3D mode is about 15 times than the one in 2D mode. Therefore, 3D PET is suitable for children and normal volunteer because 3D scan has lower radiation limits compared to 2D scan.

However, the increased sensitivity brings the problem that a larger amount of scattered photons in objects are detected compared to 2D mode. This phenomenon increases the background if the scattered photon is detected in coincidence line, in other words, LORs defined by coincidence events coming from scattered photons are not true coincidence lines. The scatter fraction in 2D PET is only about 10% of total events, so that it can be neglected. However, in 3D PET, total events include a scatter fraction of about 40%. Therefore, it should be corrected in order to get accurate quantitative images.

In this paper, we propose an image subtraction method by using scatter distribution model. Scatter distribution is modeled as a Gaussian distribution. Using this model, true events distribution is determined from the total measured distribution (true + scatter distribution) by an iterative method.

Method

When a point source is set at the coordinates (x', y', z') , the scatter distribution is

modeled as follows:

$$g(x, y, z, x', y', z') = n(r) \cdot f(x - \epsilon x', y - \epsilon y', z - z')$$

$$f(x - \epsilon x', y - \epsilon y', z - z') = n_0 \exp \left\{ - \frac{(x - \epsilon x')^2 + (y - \epsilon y')^2}{a^2} - \frac{(z - z')^2}{b^2} \right\}$$

$$r = \sqrt{x^2 + y^2 + z^2}$$

where $g(x, y, z, x', y', z')$ is the scatter distribution, $n(r)$ is a function that corrects the intensity of the distribution and $\epsilon (<1)$ represents the scatter distribution center's shifts toward the origin direction. In this case, measured distribution ($m(x, y, z)$) shows as follows by using true distribution ($t(x, y, z)$) and scatter distribution ($s(x, y, z)$):

$$m(x, y, z) = t(x, y, z) + s(x, y, z)$$

$$= t(x, y, z) + \iiint n(r') t(x', y', z') f(x - \epsilon x', y - \epsilon y', z - z') dx' dy' dz'$$

This equation can not be directly calculated in the reconstructed image because it includes scatter fraction. Therefore, iterative method is carried out by substituting measured distribution for true distribution.

$$\begin{cases} s_i = t_{i-1} \otimes g \\ t_i = m - s_i = m - t_{i-1} \otimes g \\ t_0 = m \end{cases}$$

Parameters are determined by experimental data which was measured with pool phantom (diameter 20cm, length 20cm) and a sodium point source ($27\mu\text{Ci}$) set at the center of axial direction and 0, 2, 4, 6, 8 cm, respectively, of radial direction in the phantom filled with water. Scatter fraction is estimated on the projection and fitted with Gaussian function.

Experiment

All experiments were carried out with the Shimadzu SET-2400W scanner, which has the axial view of 20cm and 32 slices, in CYRIC. When scatter correction is applied, the numbers of iteration are 5 times in both experiments.

<Uniform phantom>

The radioisotope injected in the pool-phantom (20cm of the diameter, 28.5cm of height) was F-18 ($640\mu\text{Ci}$) and scan time was 10 minutes.

<Non-uniform phantom>

Used phantom are showed in Fig. 1. The hot area is filled with F-18 solution (250 μ Ci). Diameter of the three cold spots is 5cm and they are assumed to be water, air and Teflon. The center of cold spot is 6cm distance from the center of phantom Scan time was 5 hours both 2D and 3D mode.

Result and Discussion

<Uniform phantom>

Uncorrected (left) and corrected (right) images are shown in Fig. 2 and average of ROI's at 0 (center), 2, 4, 6 and 8cm in Fig. 3. In the uncorrected image, central part is found concave because of scatter fraction, but that part is suppressed and flat by scatter correction.

<Non-uniform phantom>

Uncorrected (left) and corrected (right) images are shown in Fig. 4 and profiles across water, air and Teflon cold area in Fig. 5. This scatter correction method is very successful in water cold area but underestimated in Teflon area and overestimated in air area (Fig. 5). It is because the parameters were experimentally determined only for a phantom filled with water. If scatter medium is not water, rate of Compton scatter changes compare to the case of water. Therefore, we must review this point.

Conclusion

This method is effective when scatter medium is water, for example in brain studies. However, if scatter medium is not uniform, for example in whole body studies, this correction method can not be applied because this correction method leads to under or over estimation according to the attenuation coefficient. Therefore, scatter distribution in air, Teflon and so on must be evaluated. For this point, most researches are carried out with Monte Carlo simulation^{1,2)}. We are making the simulator of SET-2400W and estimating the scatter distribution in air, Teflon and so on. We will continue this research for this point and develop a scatter correction method for all cases.

References

- 1) Zaidi H., Herrmann A. Morel S. and C., Computer Methods and Programs in Biomedicine, **58**, 133-145 (1999).
- 2) Adam L-E., Karp J. S. and Brix G., Phys. Med. Biol. **44**, 2879-2895 (1999).

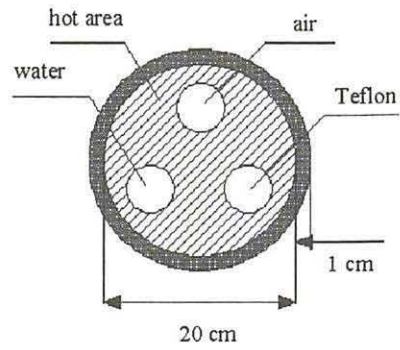


Fig. 1. Non-uniform phantom.

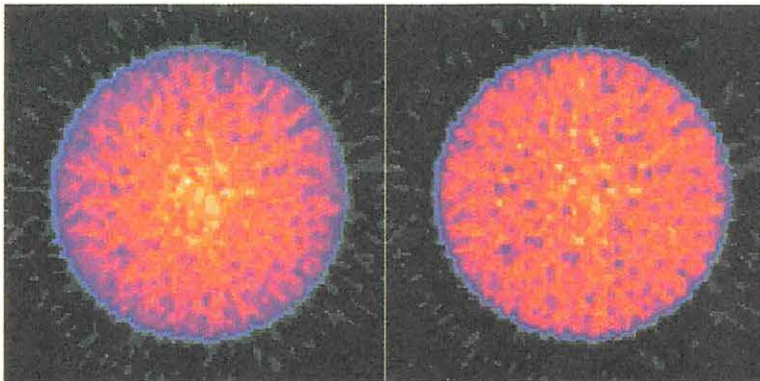


Fig. 2. Uncorrected (left) and corrected (right) images.

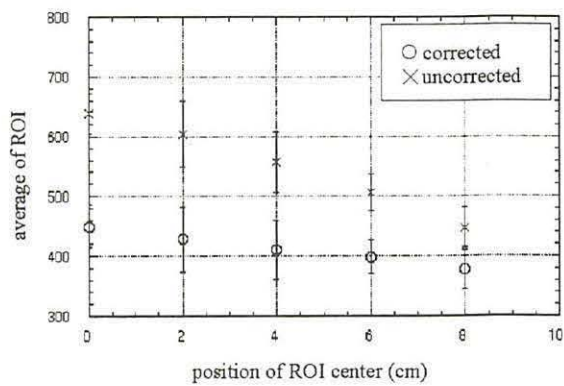
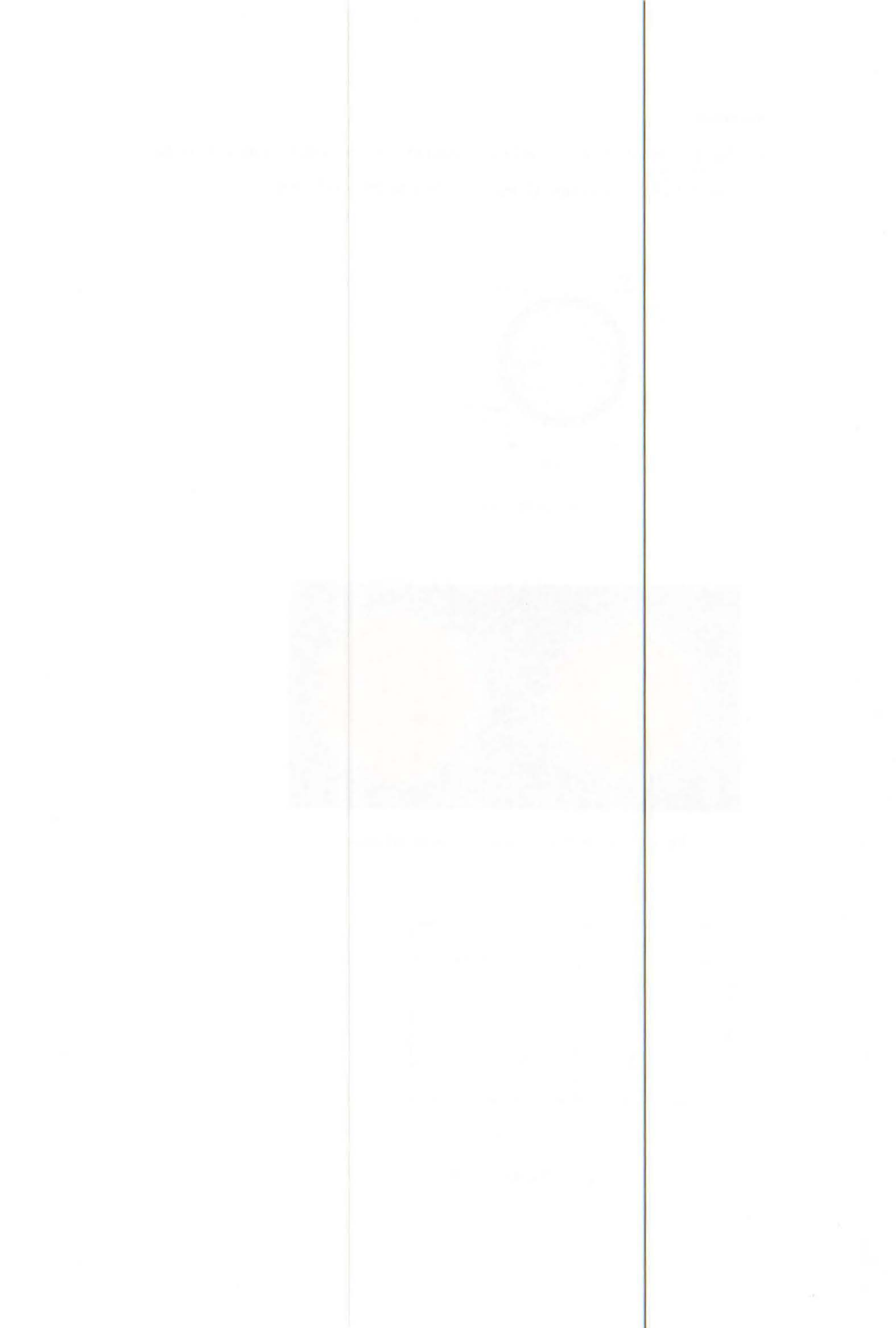


Fig. 3. Average of ROI.



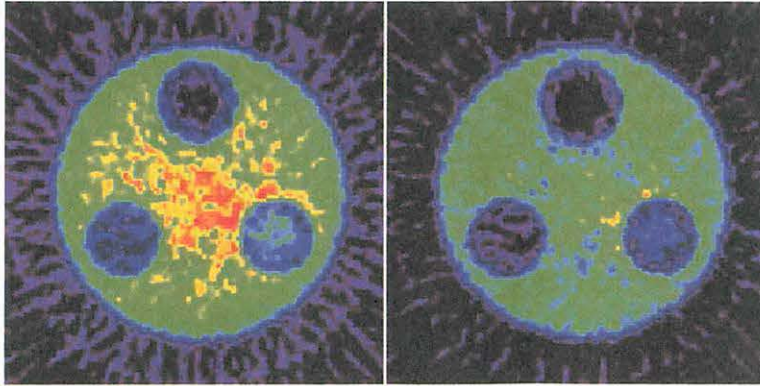


Fig. 4. Uncorrected (left) and corrected (right) images.

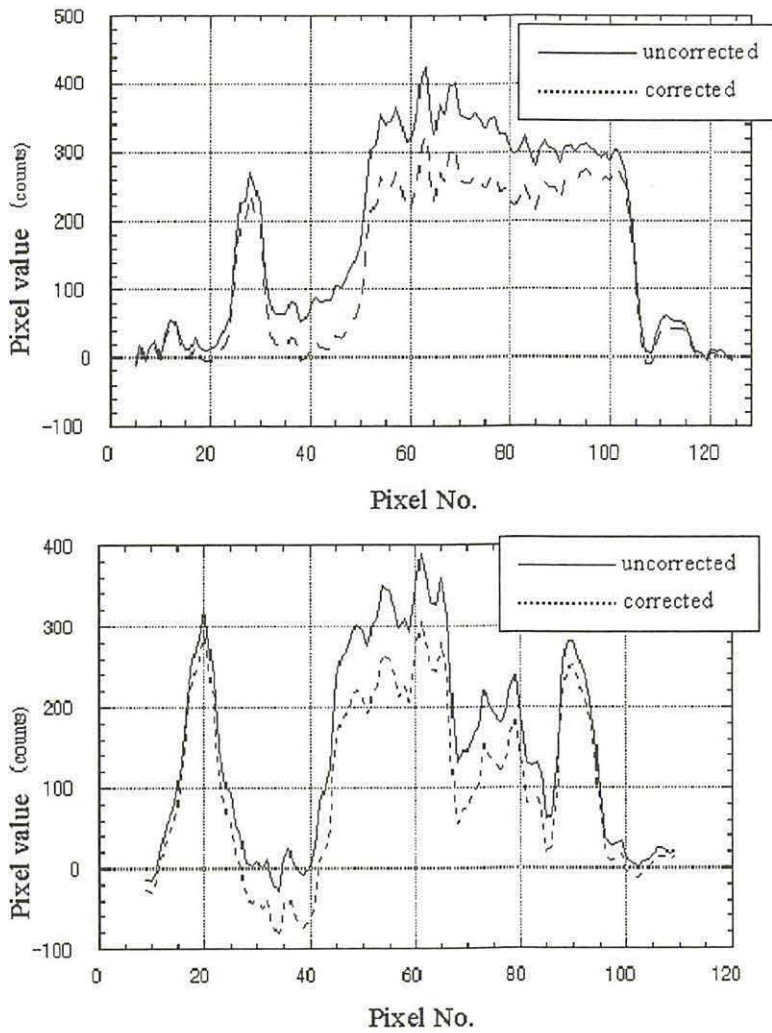


Fig. 5. Profiles including cold area (top:30-50 water, bottom:30-40 air and 70-85 Teflon).



I. 12. Research on the Development of a Method to Obtain the Attenuation Coefficients for Positron Emission Tomography Using the Single Event Rate

Rodriguez M., Ishii K., Yamazaki H., Matsuyama S., Kikuchi Y., Oishi Y., Aihara T., Yamaguchi T., Watanuki S. , Itoh M.* Orihara H.**

*Quantum Science and Energy Engineering, Tohoku University
Cyclotron and Radioisotope Center**

Introduction

Positron Emission Tomography (PET) requires accurate attenuation correction (AC) to obtain good quantitative results¹⁾. The imaged object attenuates photons traveling within an LOR. This attenuation has several detrimental effects: overall loss of counts, leading to higher image noise, image non uniformity due to the higher attenuation of photons from some body regions than other and distortions due to the differential attenuation of photons from a particular source location as a function of angle. Overall losses of counts in the body due to attenuation can be as high as 85% for a moderately large body, but the loss varies substantially with body size, resulting in varying noise levels²⁾. Two general approaches are currently used to correct for attenuation: calculated attenuation and measured attenuation³⁾. The former case, assumes that the outer body or organ (segmentation) contour is known and the attenuation properties within this contour are constant. The outer contour can be determined from a reconstructed image without attenuation correction⁴⁾. The measured attenuation is performed using one additional scan on the patient with an external radiation source. This transmission scan is used to determine the attenuation along each LOR. Those methods have their advantages and disadvantages. The calculated attenuation is easy to apply and do not require a second scan but the homogeneous attenuator assumption leads to serious errors in some types of scans. Usually for brain images, it gives good results. The measured attenuation can measure the attenuation discontinuities, which is desirable for heterogeneous attenuator as the case in whole body or thorax images. Measured attenuation introduces statistical errors since another set of measurements is required. High counting

can reduce this noise but it will imply either larger scanning time or higher radiation dose. This research aims to develop a method for determining the attenuation coefficient within the imaged object using the single event counts measured by each radiation detector in the PET system. Here we will present the conceptual development of the method.

Theory and description of the method

A PET system measures the coincidence events originated from the annihilation positron-electron within the subject. However, there are many events that do not have the conditions to be considered as coincidence events and the data acquisition system rejects them. Several PET systems can measure the single event counts since they are useful to correct for accidental coincidences. However, the single counts on each detector also carry useful information about the attenuation within the subject. Laymon and Turkington⁵⁾⁾ developed a method for PET and SPECT to calculate attenuation correction factors using single events. However, this method is not feasible for a ring PET since it requires septa for every single detector in the PET system. Our goal is to extract the information about attenuation that the detected single counts brings. Let us consider a ring detector array for PET measurements as shown in the figure 1. The system is formed by $d=[1,\dots,D]$ detector pairs counting n_d coincidence events each one. Each detector pair d has two detectors: d_1 and d_2 . The two dimensional image can be discretized into $b=[1,\dots,B]$ pixels. Each pixel has activity λ_b which might be different from pixel to pixel. Each detector counts N single events. The coincidence events counted by each pair d can be written as:

$$n_d = \sum_{b=1}^B \lambda_b C_{db} \exp\left(-\sum_{b'=1}^B \mu_{b'} J_{db'}\right) \quad (1)$$

where $\mu_{b'}$ is the attenuation coefficient for each pixel b' within the strip defined by the pair d . $J_{db'}$ is the distance within the pixel b' that a photon should travel in the way to one of the pair d 's detector. C_{db} is the geometrical probability that the pair of photons emitted in the pixel b will be detected by the pair d . The fact that a coincidence event is actually two photons traveling at opposite directions results in the same attenuation factor for any coincidence event regardless the pixel where the photon pair is emitted. Therefore, equation (1) can be written as:

$$n_d \exp\left(\sum_{b'=1}^B \mu_{b'} J_{db'}\right) = \sum_{b=1}^B \lambda_b C_{db} \quad (2)$$

Each detector will have a single count defined as:

$$N_{d_1} = \sum_{b=1}^B \lambda_b S_{d_1 b} \exp\left(-\sum_{b'=1}^B \mu_{b'} r_{d_1 b'}\right) \text{ and } N_{d_2} = \sum_{b=1}^B \lambda_b S_{d_2 b} \exp\left(-\sum_{b'=1}^B \mu_{b'} r_{d_2 b'}\right) \quad (3)$$

where $S_{d_1 b}$ and $S_{d_2 b}$ are the geometrical probability that photon emitted in the pixel b will be detected by the detectors d_1 and d_2 respectively. The parameters $r_{d_1 b'}$ and $r_{d_2 b'}$ are the distance that a photon should travel within the pixel b' on its way to the respective detector either d_1 or d_2 . Our method proposes to mix the coincidence event information with the respective detectors single counts to obtain the attenuation coefficient for each pixel.

The equation (2) can be written as:

$$\begin{bmatrix} \lambda_1 \\ \lambda_2 \\ \lambda_3 \\ \vdots \\ \lambda_B \end{bmatrix} = \begin{bmatrix} C_{11} & C_{12} & C_{13} & \cdots & C_{1B} \\ C_{21} & C_{22} & C_{23} & \cdots & C_{2B} \\ C_{31} & C_{32} & C_{33} & \cdots & C_{3B} \\ \cdots & \cdots & \cdots & \cdots & \cdots \\ C_{D1} & C_{D2} & C_{D3} & \cdots & C_{DB} \end{bmatrix}^{-1} \begin{bmatrix} n_1 \exp\left(\sum_{b'=1}^B \mu_{b'} J_{1b'}\right) \\ n_2 \exp\left(\sum_{b'=1}^B \mu_{b'} J_{2b'}\right) \\ n_3 \exp\left(\sum_{b'=1}^B \mu_{b'} J_{3b'}\right) \\ \cdots \\ n_D \exp\left(\sum_{b'=1}^B \mu_{b'} J_{Db'}\right) \end{bmatrix} \quad (4)$$

This system will have a solution only if $D \geq B$. In other words, the amount of LORs should be at least equal to the amount of image elements. The equation (4) is known as discrete back projection.

The equation (3) is as follow:

$$\begin{bmatrix} N_{11} \\ N_{12} \\ N_{21} \\ \cdots \\ N_{D2} \end{bmatrix} = \begin{bmatrix} S_{111} \exp\left(-\sum_{b'=1}^B \mu_{b'} r_{11b'}\right) & S_{112} \exp\left(-\sum_{b'=1}^B \mu_{b'} r_{11b'}\right) & S_{113} \exp\left(-\sum_{b'=1}^B \mu_{b'} r_{11b'}\right) & \cdots & S_{11B} \exp\left(-\sum_{b'=1}^B \mu_{b'} r_{11b'}\right) \\ S_{121} \exp\left(-\sum_{b'=1}^B \mu_{b'} r_{12b'}\right) & S_{122} \exp\left(-\sum_{b'=1}^B \mu_{b'} r_{12b'}\right) & S_{123} \exp\left(-\sum_{b'=1}^B \mu_{b'} r_{12b'}\right) & \cdots & S_{12B} \exp\left(-\sum_{b'=1}^B \mu_{b'} r_{12b'}\right) \\ S_{211} \exp\left(-\sum_{b'=1}^B \mu_{b'} r_{21b'}\right) & S_{212} \exp\left(-\sum_{b'=1}^B \mu_{b'} r_{21b'}\right) & S_{213} \exp\left(-\sum_{b'=1}^B \mu_{b'} r_{21b'}\right) & \cdots & S_{21B} \exp\left(-\sum_{b'=1}^B \mu_{b'} r_{21b'}\right) \\ \cdots & \cdots & \cdots & \cdots & \cdots \\ S_{D21} \exp\left(-\sum_{b'=1}^B \mu_{b'} r_{D2b'}\right) & S_{D22} \exp\left(-\sum_{b'=1}^B \mu_{b'} r_{D2b'}\right) & S_{D23} \exp\left(-\sum_{b'=1}^B \mu_{b'} r_{D2b'}\right) & \cdots & S_{D2B} \exp\left(-\sum_{b'=1}^B \mu_{b'} r_{D2b'}\right) \end{bmatrix} \begin{bmatrix} \lambda_1 \\ \lambda_2 \\ \lambda_3 \\ \vdots \\ \lambda_B \end{bmatrix} \quad (5)$$

The vector $[\lambda_b]$ in the equation (5) can be substituted with its value defined by equation (4).

It will result in the equation:

$$\begin{bmatrix} N_{11} \\ N_{12} \\ N_{21} \\ \cdots \\ N_{D2} \end{bmatrix} = \begin{bmatrix} S_{111} \exp\left(-\sum_{b'=1}^B \mu_{b'} r_{11b'}\right) & S_{112} \exp\left(-\sum_{b'=1}^B \mu_{b'} r_{11b'}\right) & S_{113} \exp\left(-\sum_{b'=1}^B \mu_{b'} r_{11b'}\right) & \cdots & S_{11B} \exp\left(-\sum_{b'=1}^B \mu_{b'} r_{11b'}\right) \\ S_{121} \exp\left(-\sum_{b'=1}^B \mu_{b'} r_{12b'}\right) & S_{122} \exp\left(-\sum_{b'=1}^B \mu_{b'} r_{12b'}\right) & S_{123} \exp\left(-\sum_{b'=1}^B \mu_{b'} r_{12b'}\right) & \cdots & S_{12B} \exp\left(-\sum_{b'=1}^B \mu_{b'} r_{12b'}\right) \\ S_{211} \exp\left(-\sum_{b'=1}^B \mu_{b'} r_{21b'}\right) & S_{212} \exp\left(-\sum_{b'=1}^B \mu_{b'} r_{21b'}\right) & S_{213} \exp\left(-\sum_{b'=1}^B \mu_{b'} r_{21b'}\right) & \cdots & S_{21B} \exp\left(-\sum_{b'=1}^B \mu_{b'} r_{21b'}\right) \\ \cdots & \cdots & \cdots & \cdots & \cdots \\ S_{D21} \exp\left(-\sum_{b'=1}^B \mu_{b'} r_{D2b'}\right) & S_{D22} \exp\left(-\sum_{b'=1}^B \mu_{b'} r_{D2b'}\right) & S_{D23} \exp\left(-\sum_{b'=1}^B \mu_{b'} r_{D2b'}\right) & \cdots & S_{D2B} \exp\left(-\sum_{b'=1}^B \mu_{b'} r_{D2b'}\right) \end{bmatrix} \begin{bmatrix} C_{11} & C_{12} & C_{13} & \cdots & C_{1B} \\ C_{21} & C_{22} & C_{23} & \cdots & C_{2B} \\ C_{31} & C_{32} & C_{33} & \cdots & C_{3B} \\ \cdots & \cdots & \cdots & \cdots & \cdots \\ C_{D1} & C_{D2} & C_{D3} & \cdots & C_{DB} \end{bmatrix}^{-1} \begin{bmatrix} n_1 \exp\left(\sum_{b'=1}^B \mu_{b'} J_{1b'}\right) \\ n_2 \exp\left(\sum_{b'=1}^B \mu_{b'} J_{2b'}\right) \\ n_3 \exp\left(\sum_{b'=1}^B \mu_{b'} J_{3b'}\right) \\ \cdots \\ n_D \exp\left(\sum_{b'=1}^B \mu_{b'} J_{Db'}\right) \end{bmatrix} \quad (6)$$

Finally, the product between the single counts for each pair d is obtained by the following operation:

$$\begin{bmatrix} N_{1_1} \\ N_{1_2} \\ N_{2_1} \\ \dots \\ N_{D_2} \end{bmatrix} \begin{bmatrix} N_{1_1} \\ N_{1_2} \\ N_{2_1} \\ \dots \\ N_{D_2} \end{bmatrix}^T \quad (7)$$

The result of this operation will be a set of equations where the unknown variables are the attenuation coefficients μ_b for each image element.

The PT-711 (Time of Flight type PET system) located at CYRIC permits single counting. This method will be tested with the data acquired in that system. In order to test this method, several measurements with different attenuators are required. We plan to use data without attenuator (air), uniform attenuator and a heterogeneous attenuator obtained from a phantom. The attenuation coefficients obtained with this method will be compared with the real values to test the validity of this method. The method does not include dead time corrections. Therefore, we expect the method will have limitations when high activity is injected to the patient.

Conclusion

The theoretical fundamentals for a method to calculate the attenuation coefficient of the imaged subject are presented in this report. A well performance of this method will reduce the patient radiation exposure since the transmission scan will not be necessary. In addition to the lower radiation dose, the noise introduced by the transmission measurements is eliminated. The single count detected by each individual detector is statistically good hence, the attenuation coefficients are expected to show good accuracy.

References

- 1) Huang S. et al, J. Nucl Med **22** (1981) 627-637.
- 2) Harkness B., Comparison of currently available PET scanners, Society of Nuclear Medicine, 47th annual meeting, June 2000.
- 3) Turkington T., J Nucl Med Technol **29** (2001) 1-8.
- 4) Mizuta T. et al, Attenuation Correction in 3D-PET, CYRIC annual report, 165-167, 1998.
- 5) Laymon C. and Turkington T., IEEE Trans Med Imag, **18** (1999) 1194-1200.

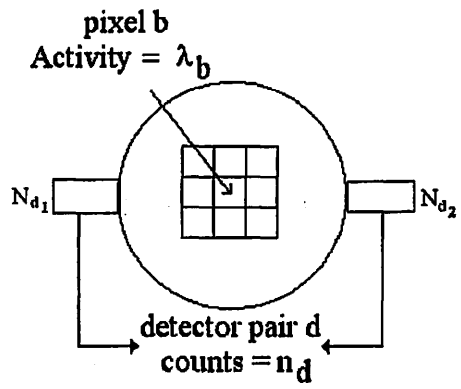


Fig. 1. Discretized 2D image viewed by a pair of radiation detectors.

I. 13. Measurement of the Low Energy Detection Efficiency of a Si(Li) Detector for PIXE Applications

Rodriguez M., Yonezawa T., Ishii K., Matsuyama S., Yamazaki H., Sato T., Amartaivan Ts., Sugihara S., Tanaka A., Kato K., and Komori Y.

Quantum Science and Energy Engineering, Tohoku University

Introduction

In PIXE applications, there is an increasing interest for an accurate method to determine the low X ray energy detection efficiency since many important elements are characterized by low X ray energy emissions. For example, the elements from Na to Ti have characteristic X rays ranging from 1 to 5 keV. The detector dead layer, which is usually unknown, effectively absorbs these energies. Therefore, the knowledge of the Si(Li) detector efficiency dependence on the photon energy becomes very important. The detector efficiency can be calculated from the photon transmission and absorption probabilities in the detection system. However, manufacturer specifications are not always reliable and it led to erroneous efficiency estimations. Measurements through radioactive standard sources are not a practical choice for low energies since there are no appropriate radioactive sources with energies lower than 4 keV. In this work, a method to measure the efficiency for low X ray energy of a Si(Li) detector is developed. The reference source is the continuous bremsstrahlung produced by bombarding a carbon target with an electron beam. A continuous radiation spectrum allows precise measurements of discontinuities of the efficiency curve¹⁾. The theoretical shape of the electron bremsstrahlung can be obtained using the doubly differential bremsstrahlung cross section²⁾. It is compared to the spectrum measured with the Si(Li) detector for three incident electron energies. Mathematically, this comparison results in the relative detector efficiency for low X ray energies. The relative efficiency results were compared to an efficiency calculation based on the probability of transmission and absorption of the bremsstrahlung radiation within the detector components.

Materials and Method

The measurement system is sketched in Fig. 1. The biased tungsten filament provides the electron beam, which is accelerated through a variable high voltage. It allows choosing beam energies up to 15 keV. One solenoid lens is used to focus the beam on the target geometrical center and two magnetic steerers. An X ray detector is orientated 90 degrees respect to the electron beam. The detector signal is amplified and analyzed by the spectroscopy amplifier (APTEC 6300) that sends the information to the ADC. The APTEC software receives the detector counts from the ADC. This system can be used to measure the detection efficiency for any X ray detector. In this experiment it is used to measure the detection efficiency of the EURISYS ESLX 80-150 Si(Li) detector.

The experiment is performed at 0.001 Pa and the filament current was adjusted until the dead time losses is lower than 1%, for all measurements, to avoid pile up effects. The purity of the carbon sample is 99.98% and its thickness is 1 mm. It is a full stop target for the electron beam because the range of a 15 keV electron in carbon is about 2.5 μm . The thickness of the target avoids dealing with problems related with material losses during the experiment. A thin target is preferable because problems as bremsstrahlung self-absorption are avoided. However, a thin C target for 15 keV electrons would be extremely fragile and difficult to handle. Therefore, it is decided to perform the measurements with a thick C target.

Theoretical shape of the bremsstrahlung spectra

The theoretical shape of the bremsstrahlung spectrum for a given incident electron energy E_0 on the thick C target can be calculated using tabulated cross section values²⁾. The shape for the thick target bremsstrahlung can be achieved by modeling the thick target as a group of several thin targets. It should be assured that the energy loss in each thin target is small compared to the incident electron energy. The Fig. 2 illustrates the model.

The electron beam strikes the C target with incident energy E_0 and it lose energy while traveling through the group of thin targets. The criterion to define a thin layer is to fix the electron energy loss (ΔE), within each thin layer, to a small value compared to the incident electron energy. It means that the thicknesses of the thin layers are different from each other. From each thin layer, a bremsstrahlung spectrum is emitted and attenuated within the target along its way to the radiation detector. The shape of the bremsstrahlung spectrum emitted from the thin layer n is $f(k, E_n)$, where E_n is the electron energy when it

reaches the thin layer n and k is the bremsstrahlung X-ray energy. It is defined by the equation

$$f(k, E_n) = B \frac{d^2 \sigma(E_n)}{dk d\Omega} dx_n, \quad (1)$$

where B is a constant value and the second factor is the bremsstrahlung cross-section differential in both photon energy and photon angle. The attenuation factor will be given by:

$$A(k, E_n) = \exp \left(- \mu(k) \int_{E_0}^{E_n} \frac{1}{\frac{dE}{dx}} dE \right). \quad (2)$$

The factor $\frac{dE}{dx}$ is the stopping power and is determined from the Bethe equation. The differential cross section data are tabulated for some specific values of electron energies. Therefore, analytical functions relating the differential cross section in terms of the electron energy were derived in order to interpolate for the required and non-tabulated cross section values. From (1) and (2), the shape of the bremsstrahlung spectrum for the thick target is written by:

$$g(k, E_0) = \int_k^{E_0} f(k, E_n) A(k, E_n) dE_n \quad (3)$$

$$g(k, E_n) = \int_k^{E_0} B \frac{d^2 \sigma(E_n)}{dk d\Omega} \frac{dE}{\frac{dE(E_n)}{dx}} \exp \left[- \mu(k) \int_{E_0}^{E_n} \frac{dE}{\frac{dE(E_n)}{dx}} \right]. \quad (4)$$

B is set to be 1 and it will not affect the bremsstrahlung shape. Since the equation (2) cannot be solved by analytical means, the numerical solution is written as:

$$g(k, E_n) = \sum_{E_0=0}^{E_0} \frac{d^2 \sigma(E_n)}{dk d\Omega} \frac{\Delta E}{\frac{dE(E_n)}{dx}} \exp \left[- \mu(k) \sum_{i=0}^n \frac{\Delta E}{\frac{dE(E_i)}{dx}} \right]. \quad (5)$$

The attenuation coefficient as a function of the photon energy k is given by Ref. 4

$$\frac{\mu(k)}{\rho} = CA\lambda^b \frac{cm^2}{g}, \quad (6)$$

where $C=3.8531$, $A=0.2838$, $b=3.094$ and $\lambda = \frac{12.3981}{k}$.

The theoretical shape of the bremsstrahlung produced by three incident electron energies E_0 : 10, 12 and 15 keV were calculated by choosing $\Delta E = 0.1$ keV. The results are showed in the Fig. 3.

Results and discussion

The bremsstrahlung yield is also measured for E_0 of 10, 12, and 15 keV using the detector EURISYS ESLX 80-150 Si(Li) which manufacturer specifications are $x_{Be}=12\mu\text{m}$, $x_{Au}=0.02\mu\text{m}$, $x_{Si\text{ dead layer}}=0.5\mu\text{m}$ and $x_{Si}=4\text{mm}$. The measured spectra, $m(k,E_0)$, are showed in fig. 4. We can clearly see the Si absorption edge (1.84 keV). These spectra are used to determine the efficiency of the Si(Li) detector for a range of photon energy. The experimental relative efficiency (ϵ_{exp}) is determined by the equation:

$$\epsilon_{\text{exp}} = c \frac{m(k, E_0)}{g(k, E_0)}, \quad (7)$$

where c is a constant value which is chosen to produce $\epsilon_{\text{exp}} = 1$ for $k = 8$ keV. Therefore, the results represent the efficiency respect to the one for 8 keV. The results for the relative efficiency are shown in the Fig. 5. It shows the results for the chosen incident electron energies. In addition, the experimental results are compared to a calculated efficiency, since the detector efficiency can be obtained from the detector design, by using the manufacturer specifications. The mathematical expression is:

$$\epsilon_{\text{cal}} = \sum_i \exp(-\mu_i \rho_i x_i) [1 - \exp(-\mu_{Si} \rho_{Si} x_{Si})], \quad (8)$$

where μ_i , ρ_i and x_i represent the photon energy dependent mass absorption coefficients, densities and thicknesses of the absorbing layers in front of the active region of the detector and μ_{Si} , ρ_{Si} and x_{Si} are the same parameters for the active region of the Si(Li) detector. The first exponential term of this expression is the probability that a photon will be transmitted through the layers in front of the active detector area and the second one is the probability that the detector active area will absorb the photon. It is assumed that the area illuminated in front of the detector surface is the same that the actual illuminated detector active area, there is no contribution due to photoelectric effect in the layers in front of the detector active area and no losses because scattering of photons within the detector active area.

The results for $E_0=15$ keV have a large deviation for photon energies larger that 12.5 keV because the low counts. It determines the range of photon energy within which the results are valid which is $0.8 \text{ keV} < k < 12.5 \text{ keV}$. The measured relative efficiencies

are consistent within 8 %. It means that the calculation of $g(k, E_0)$ gives good results for efficiency measurements. In other words, it is reliable to use the equation (5) when experiments to measure efficiency are carried out. In the photon energy region $2 \text{ keV} < k < 6 \text{ keV}$, the calculated efficiency is significantly lower, if manufacturer specifications are used. It suggests that the Si dead layer is actually thinner than the manufacturer specifications because variations in the Si dead layer mainly affect the photon energy region $2 \text{ keV} < k < 6 \text{ keV}$. Furthermore, other works have also reported disagrees between actual and manufacturer specified Si dead layer^{3,5}). It was also assumed the Si(Li) detector did not have ice layer which seems to be true since ϵ_{cal} would decrease in case of having the ice layer and it disagrees with the experimental data. A lower value in the thickness of the Be and window would affect mainly the photon energy region below the Si K edge. Other factors are not included in the calculated efficiency as the contribution from photoabsorption in the layers in front of the active area and scatter into the active region of the detector. It would affect the values used for the comparison.

The accuracy of the theoretical shape of the bremsstrahlung spectra is expected to be about 10-15%²). The accuracy of the measured bremsstrahlung spectrum depends mainly on the statistical counting error. Therefore, the accuracy of the measured efficiency depends on the photon energy. Based on the best accuracy of the theoretical shape of the bremsstrahlung spectrum, the measured relative efficiency shows its best accuracy in the energy region $1 \text{ keV} < k < 7 \text{ keV}$ and it is about 11-12%.

Finally, the efficiency calibration for any detector used for PIXE analysis can be achieved since the experimental system is available and the theoretical bremsstrahlung shape showed to give good results.

Acknowledgement

The authors sincerely thank to T. Takahashi, K. Komatsu, T. Nagaya and C. Akama from the Machinery Shop of the Quantum Science and Energy Engineering Department at Tohoku University for manufacturing the experimental system used in this work.

References

- 1) Wolters, U., et. al., **Low-energy intensity calibration of a Si(Li) detector using thick target bremsstrahlung**, J. Phys. D: Appl. Phys, Vol. 31,(1998) 2112-2116.
- 2) Lynn K. et. al., **Shape functions for atomic-field bremsstrahlung from electrons of kinetic energy 1-500 keV on selected neutral atoms $1 \leq Z \leq 92$** , Atomic Data and Nuclear Data Tables, Vol. 28 (3), (1983) 381-460.
- 3) Baker C.A. et. al., **Efficiency of Si(Li) X-ray detectors at low energies**, Nucl. Instr. and Meth. In Phys. Res., A259 (1987) 501-505.
- 4) Johansson S.A.E. and Campbell J.L., **PIXE. A novel technique for elemental analysis**, Wiley, Great Britain, 1988.
- 5) Sera K. et al., **Determination of physical quantities for PIXE by means of PIXE. Efficiency curve**, IJPIXE, Vol. 4 Nos 2&3 (1994) 181-191.

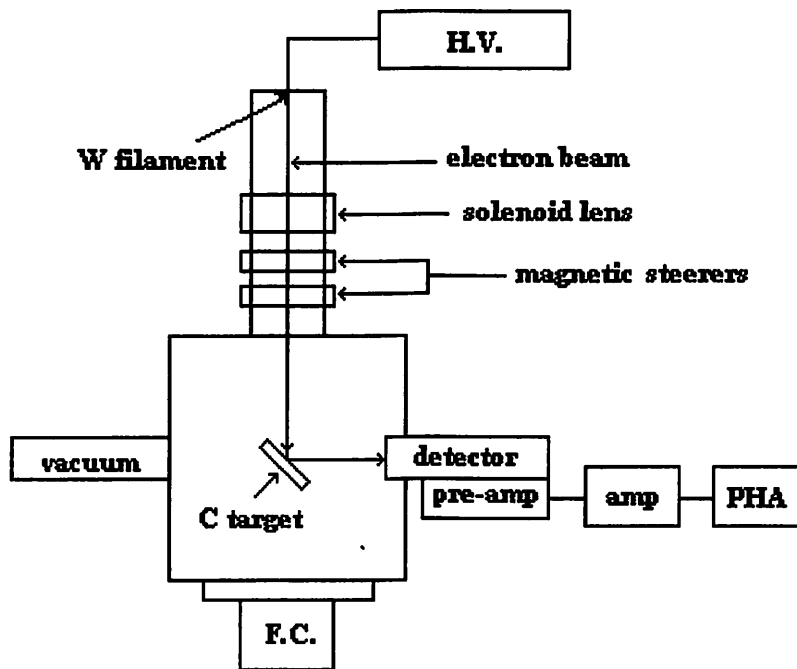


Fig. 1. Experimental system diagram.

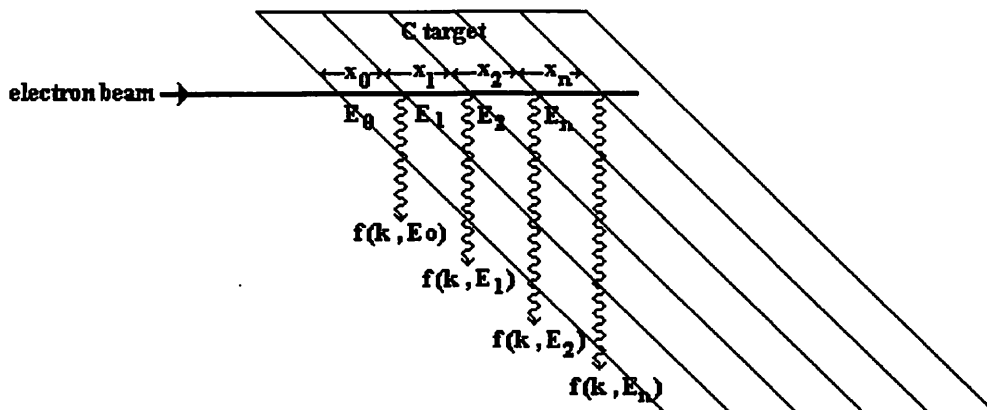


Fig. 2. Thick target model illustration.

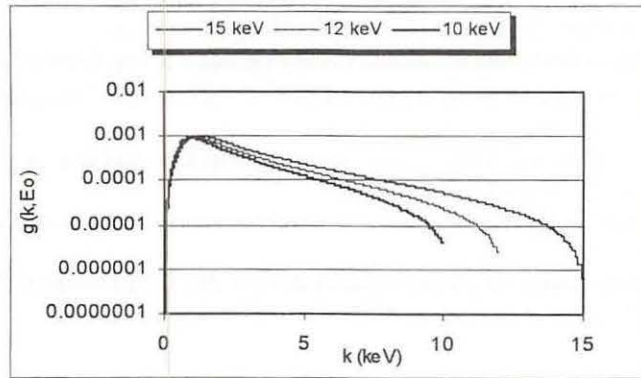


Fig. 3. Theoretical shape of the bremsstrahlung spectrum for three incident electron energies E_0 .

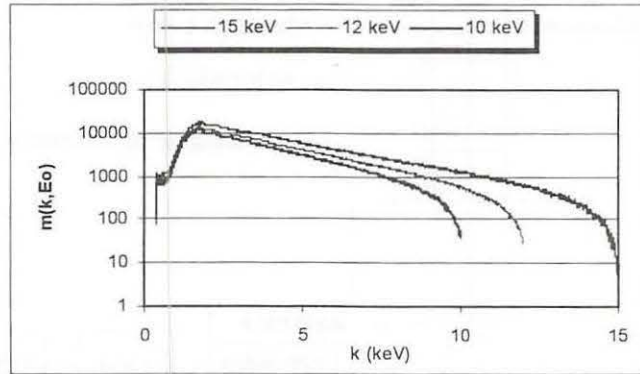


Fig. 4. Measured bremsstrahlung spectra for three incident electron energies E_0 .

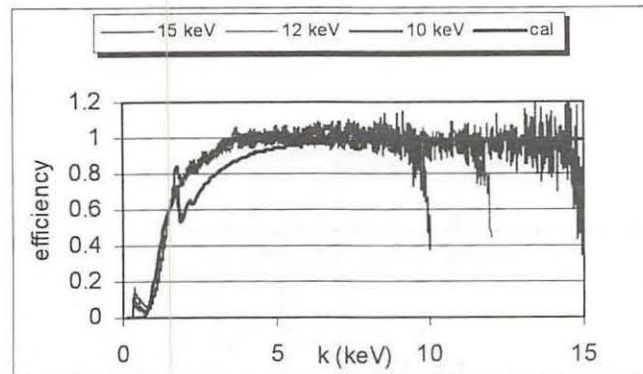


Fig. 5. Measured relative efficiency for three incident electron energies E_0 .

I, 14. Application of PIXE Analysis to Elemental Study of Drinking Water Supply

*Yamazaki H., Ishii K., Amartaivan Ts., Matsuyama S., Takahashi Y., Satoh T. and Orihara, H.**

*Department of Quantum Science and Energy Engineering, Graduate School of Engineering,
Tohoku University
Cyclotron and Radioisotope Center, Tohoku University**

INTRODUCTION

The toxic effects of various species of heavy metals in the biosphere have been pointed out in many studies^{1,2)}. Since drinking water is one of the most essential pathways to uptake harmful heavy metals by people, the quality control is particularly important in water supply. A wide variety of analytical techniques are currently available for monitoring water quality and many new techniques are still emerging³⁻⁶⁾. PIXE offers the advantages of a truly multi-elemental nature, high sensitivity and high speed analysis with a small amount of samples. In addition, PIXE measurement allows direct determination of both soluble and insoluble species of elements in water samples due to versatility in the form of specimens to be analyzed.

In this study, we examined the capability of PIXE in monitoring quality of drinking water supply in our city, especially the incidence of metal contamination. In our city of around the 1 million populations, five water treatment plants are located, and each plant supplies drinking water after physicochemical treatment of raw water from different sources. We carried out PIXE analysis for both raw water and clear water at the five plants as well as tap water at several houses located in each supply region. This test should recognize in a simple and fast way trace level concentrations of heavy metals in water samples. In this context, we used a simple and rapid procedure for preparing thin uniform targets of inorganic components in both soluble and insoluble fractions of aqueous samples in combination with pre-concentration of trace heavy metals⁷⁻⁹⁾.

EXPERIMENTAL

PIXE target preparation

We collected 1dm³-volume of both raw and purified waters at the five treatment plants on January 21 and 23, 2002. These water treatment plants take in raw water from three different rivers flowing through Sendai city or from three multi-purpose dams upstream each river, as shown in Table 1. On January 22 and 24, we also collected domestic tap water samples at 7 houses located in each water-supply region.

Water samples were stored in Nalgene-linear polyethylene containers and processed into PIXE-targets within 24 hours. Three kinds of PIXE targets were prepared from raw water samples collected at each water treatment plant using the three-step method developed previously; that is, the Nuclepore filter target for insoluble constituents (FILT), the pre-concentration target for heavy metal ions (PRECON), and the deposit target for soluble major constituents (DEP)⁷⁻⁹.

The residue on Nuclepore filter of 0.4- μ m pores in filtration was classified into an insoluble fraction and the filtrate was regarded as a soluble one. This classification is a rather rough way, and it is more proper to consider that the FILT target contains only a coarse fraction of insoluble components and the DEP target also includes a fine fraction of insoluble ones. In the case of clear water and tap water, residue on the filter was not detected in an appreciable amount, and hence these samples were processed into two kinds of PIXE targets such as DEP and PRECON.

PIXE analysis

The targets of water samples were irradiated for 3 to 10 minutes in a vacuum chamber by 3 MeV protons (beam currents, 10-70 nA; beam diameter, 4 mm). X-rays from targets were measured with two Si(Li) detectors; No.1 detector having 500- μ m Mylar absorber and high geometric efficiency allows the detection of X-rays > 4 keV, and No.2 detector with a low geometric efficiency is well suited for the detection of elements of the atomic number $Z \leq 20$ ¹⁰. For PIXE-spectrum analysis, we used a least-squares fitting computer program, which has been developed in our laboratory based on the pattern analysis method¹¹. The lower detection limit was obtained based on the statistics 3σ error of the background counts integrated over the width of detector resolution (FWHM) at the position of the X-ray energy characteristic to the element of interest in PIXE spectrum for a sample.

RESULTS AND DISCUSSION

The *K* and *L* X-ray lines were observed for 19 elements in PIXE spectra obtained from three kinds of water samples collected from different sources. The ionic fraction of heavy metals in trace concentration (< 10 ppb) were clearly detected in spectrum for target-PRECON. On the other hand, the spectrum on target-DEP allowed us to determine concentrations of major elements excluded in the preconcentration step, *e.g.*, alkali metals, alkaline earth metals and anionic species of P, S and Cl along with the fine particulate fraction of hydrolysable elements like Al, Si and some heavy metals in water with neutral pH, which pass through Nuclepore filter of 0.4- μ m pores. An important result is that the PIXE analysis for the three kinds of target reveals elemental distribution in the widespread concentration range between the soluble and insoluble fractions of water samples.

Figure 1 shows elemental concentrations in raw water and clear water samples collected two times at five water treatment plants. The detection limits of the PIXE analysis were on the order of several tenths of ppb for elements producing X-rays > 5 keV, while the large continuum background of backings in PIXE spectra incurred an inferior limit, that is, several tens of ppb for elements of atomic number $Z < 20$. In the plant F which takes raw water mainly from river, concentrations of Al and Si, element derived from soil, largely increased immediately after a heavy rainfall on Jan. 21. Since the plant N gets raw water at a river water intake just downstream a dam, such a carrying-in of soil components to the river seems difficult to appear immediately after rainfall. In the other plants with raw water intake from a dam, similar time lag in the concentration change was observed. In either case, the increase in concentration of Mn, Fe, Cu, Zn and Pb corresponds to that of soil components like Al and Si. On the other hand, the concentration fluctuation by the heavy rainfall was not remarkable for major components such as K, Ca and the anionic species of P, Cl and S in raw water.

In the case of clear water at the five plants, concentrations of elements except trace level Cu and Zn did not vary largely among the samples with physicochemical treatment of raw waters for which the concentrations of soil components and heavy metals largely differed. Samples of clear water did not include coarse particles of the major and minor constituents to be removed by Nuclepore filter of 0.4- μ m pores. By the elimination of the coarse particulate fraction, concentrations of hydrolysable components such as Al and Si in clear water decreased to 50-85% in raw water, and then concentrations of heavy metals adsorbed in hydroxide colloids of Al and Si were also reduced to several tens of ppb or less

irrespective of the composition of raw water. In addition, the result in Fig.1 shows little difference in water quality among five water supply systems in our city.

PIXE results for alkali metals, alkaline earth metals and heavy metals in both raw and clear waters were compared with the concentration range of these elements determined using colorimetry, AAS and ICP-AES techniques at each water treatment plant during last year. PIXE showed the concentrations close to the results of other analytical techniques for both major and minor components except Al; the concentration of Al was two or three times higher by PIXE than by AAS analysis. Apart from nonconformity of analysis of Al, we confirmed the applicability of PIXE method in monitoring the incidence of heavy metal contamination of water supply in our city.

For the F and M plants with different time lag for the concentration change by rainfall, the fraction of dissolved states for each element is tabulated in Table 2. Silicon is a major constituent as colloids in river water with neutral pH¹²). The PIXE analysis of raw water samples at the water treatment plants showed the result of agreeing with this preview, and it is confirmed that above mentioned heavy metals were mainly adsorbed to the coarse and fine particles of a soil component which rain brought in river. Therefore, the rainfall greatly influences the grade of raw water at each water treatment plant. As shown in Table 2, the quite small portion of a major element such as Ca was included in particulates of soil component like Si. In addition, it was revealed that concentrations of these major elements were almost constant in raw waters from different sources, as shown in Fig. 1. The ionic fraction of the heavy metals dissolved in clear water greatly increased compared with the results of raw water. In clear water, therefore, the coarse particulates of major components and the heavy metals adsorbed on them seem to be efficiently removed by the flocculation and the filtration with polyaluminum chloride at water treatment plants.

Figure 2 shows the comparison of elemental concentrations in drinking water in each service area of five water treatment plants. As shown in Table 1, samples were collected at 2 places in the water supply district of the K and M treatment plants. We compared the mean value of concentrations including both particle and ionic fractions in two samples taken on January 22 and 24, 2002, because the elemental concentrations did not largely fluctuate. The concentrations of major components like Al, S, Si, K and Ca were similar in all supply systems and close to the concentrations in clear water samples at the five plants. In the domestic sampling points of T, K2 and F which belong to the different supply system, however, concentrations of heavy metals like Fe, Cu or Zn were much

higher than those in other tap water, and this concentration largely increased compared with the concentrations in clear water supplied from either plants. Most of these heavy metals were present as a soluble component in the range of concentration from 0.016 to 0.12 ppm. Lead, which was not detected in clear water from the plants, existed as ionic species of the resolved state in all domestic tap water samples in the concentration range of 0.4 to 1.7 ppb, and a rather high concentration of Pb, 1.0-1.7 ppb, was detected in tap water samples in which concentrations of other heavy metals were relatively high. Drinking water distribution systems are primarily composed of iron and steel pipes that are subject to corrosion. The apparent rise in concentrations of some heavy metals compared to the clear water samples indicates the possibility of corrosion of the piping at these domestic sampling points. Besides this, the elemental concentrations in the drinking water samples are much lower than the quality standards of drinking water in Japan; [Na] and [Cl] \leq 200 ppm, [Mg] and [Ca] \leq 300 ppm, [Cu] and [Zn] \leq 1 ppm, [Fe] \leq 300 ppb, [Pb] and [Mn] \leq 50 ppb, [Ni] and [As] \leq 10 ppb.

CONCLUSION

In this study, the techniques developed for PIXE target preparation can be successfully applied to examine quality of water supply in our city. The target preparation and the PIXE measurement are not time-consuming; the pre-concentration step requires less than 10 minutes, and the samples are analyzed by PIXE in which targets are irradiated with 3-MeV proton beams for 3 to 10 minutes. Many kinds of elements can be detected simultaneously in the widespread concentrations from several tenths of ppb to a few tens of ppm due to the multielemental nature and wide dynamic range of detection of the PIXE analysis. PIXE analysis for three kinds of targets, which are prepared from a small volume of water such as 30 ml, reveals the increase of insoluble component of some heavy metals in raw water taken from rivers on a day with heavy rainfall and elution of Cu, Zn and Pb in drinking water by corrosion of the piping on some of water distribution systems. Hence, the methodology developed in this study promotes the PIXE analysis to a truly effective means for monitoring the incidence of heavy metal contamination in a distribution system of drinking water.

References

- 1) Gruiz K., *et al.*, *Wat. Sci. Tech.*, **37**, 273-281 (1998).
- 2) Wilken R. D., *Fresenius J. Anal. Chem.*, **342**, 795-801.
- 3) Goulden P. D. and Anthony D. H. J., *Anal. Chem.*, **54**, 1678-1683 (1982).

- 4) Barreiros M. A., *et al.*, X-ray Spectrometry, **26**, 165-171 (1997).
- 5) Romberg B. and H. Müller, *Anal. Chem. Acta*, **353**, 165-172 (1997).
- 6) Bobeldijk I., *et al.*, *J. Chromatogr. A*, **929**, 63-74 (2001).
- 7) Yamazaki H., *et al.*, *Int. J. PIXE*, **7**, 31-40 (1997).
- 8) Yamazaki H., *et al.*, *Int. J. PIXE*, **7**, 101-107 (1997).
- 9) Yamazaki H., *et al.*, *Int. J. PIXE*, **9**, 83-102 (1999).
- 10) Sera K., *et al.*, *Int. J. PIXE*, **2**, 325-330 (1992).
- 11) Murozono K., *et al.*, *Nucl. Instrum. Meth. B150*, 76-82 (1999).
- 12) Base C. F. and Mesmer R. E., John Wiley & Sons, New York (1976), 112-123; 215-219; 336-342; 365-370.

Table 1. Raw water intake at five water treatment plants and sampling of domestic tap water.

Plant	Raw Water Intake Ratio		Water Supply in Sendai city	Sampling Point of domestic Tap Water
	River Water	Dam Water		
F	0.85 the Nanakita River ¹⁾	0.15 Nanakita Dam ²⁾	Northern region	<i>F</i>
K	-	1.0 Ohkura Dam ³⁾	Northeast region	<i>K1, K2</i>
N	1.0 the Ohkura River ⁴⁾	-	Western region	<i>N</i>
M	-	1.0 Kamafusa Dam ⁵⁾	Eastern region	<i>M1, M2</i>
T	0.2 the Natori River ⁶⁾	0.8 Kamafusa Dam ⁵⁾	Southern region	<i>T</i>

1): the first class river which flows through the northern region in Sendai city, 2): the multiple purpose dam upstream the Nanakita River in northern hill zone of the city, 3): the multiple purpose dam upstream the Hirose river which flows through the central part of the city, 4): the tributary of the Hirose river, flowing in the mid west hill zone of the city, 5): the multiple purpose dam upstream the Natori River in southwest hill zone of the city, 6): the first class river which flows through the southern region in the city.

Table 2. The fraction of dissolved states for typical elements in three kinds of water samples.

Element		Plant F / Domestic F						Plant M / Domestic M1							
		Raw		Clear		Tap Water		Raw		Clear		Tap Water			
		Coarse	Fine	Ion	Fine	Ion	Fine	Ion	Coarse	Fine	Ion	Fine	Ion	Fine	Ion
Si	A	0.33	0.67	-	1.0	-	1.0	-	0.08	0.92	-	1.0	-	1.0	-
	B	0.10	0.90	-	1.0	-	1.0	-	0.35	0.65	-	1.0	-	1.0	-
Ca	A	0.03	0.97	-	-	1.0	-	1.0	0.01	0.99	-	-	1.0	-	1.0
	B	0.01	0.99	-	-	1.0	-	1.0	0.03	0.97	-	-	1.0	-	1.0
Mn	A	0.84	0.09	0.07	0.91	0.09	0.85	0.15	0.59	0.28	0.13	0.87	0.13	0.88	0.12
	B	0.69	0.27	0.03	0.73	0.27	0.78	0.22	0.71	0.10	0.19	0.92	0.08	0.79	0.21
Fe	A	0.97	0.01	0.02	0.67	0.33	0.01	0.99	0.87	0.01	0.12	0.63	0.37	0.25	0.75
	B	0.92	0.01	0.07	0.41	0.59	0.03	0.97	0.95	0.02	0.03	0.52	0.48	0.19	0.81
Zn	A	0.54	0.14	0.32	0.32	0.68	0.22	0.78	0.16	0.05	0.79	0.20	0.80	0.03	0.97
	B	0.18	0.41	0.41	0.18	0.82	0.16	0.84	0.40	0.14	0.46	0.33	0.67	0.11	0.89

Alphabetical symbols of plants are the same as those in Table 1. A: the samples collected on Jan. 21st, 2002 with intense rainfall, B: the samples collected 2 days later on Jan. 23rd, 2002, besides domestic tap water was collected one day after sampling at the plants.

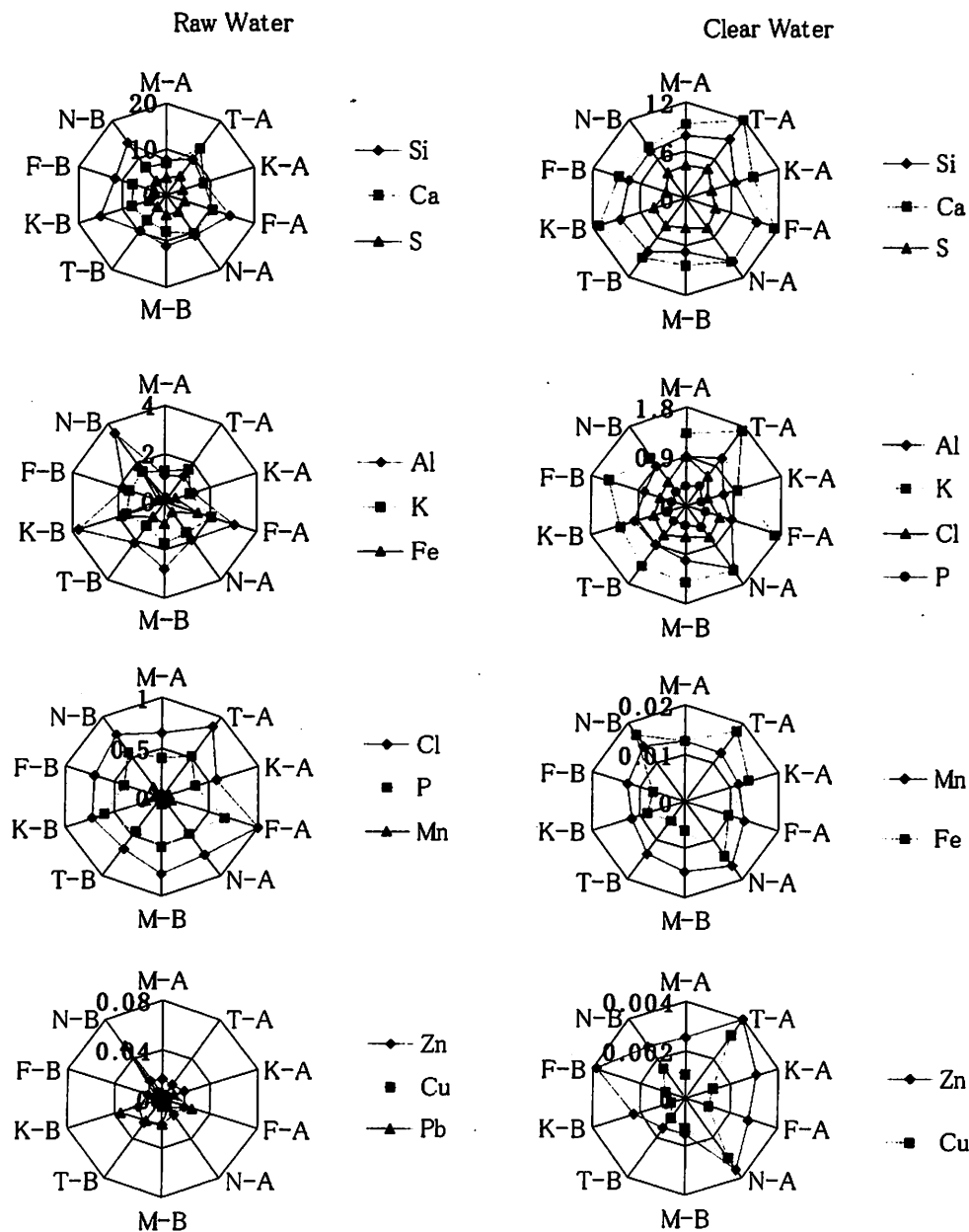


Fig. 1. Concentrations in ppm for components in raw water and clear water at five water treatment plants. Alphabetical symbols are the same as those in Table 1. A: the analysis value of samples collected on Jan. 21st, 2002 (heavy rainy day), B: the analysis value of samples collected on Jan. 23rd, 2002 (cleared up day).

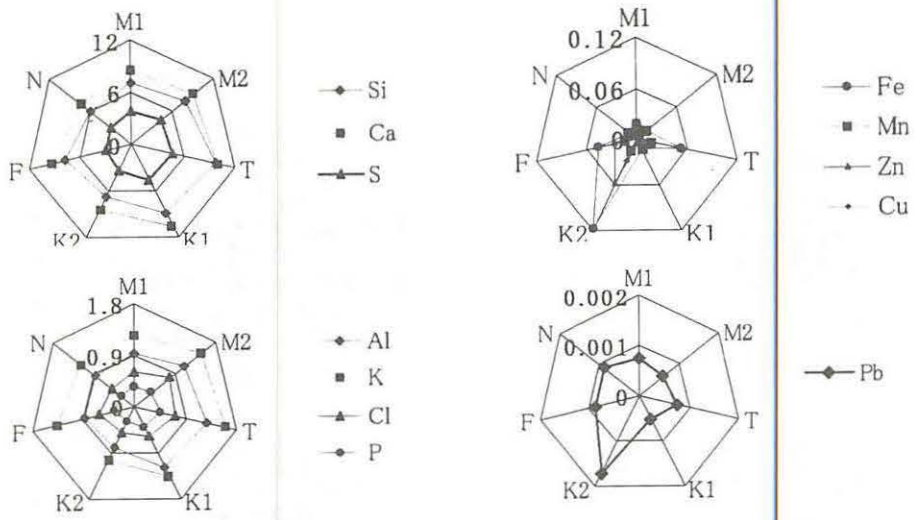


Fig. 2. Concentrations in ppm for typical elements in drinking water (average value of 2 samples).

I. 15. Development of a Mini Step Sumpler for Air-Pollution Monitoring

*Matsuyama S. Sugihara S., Ishii K., Yamazaki H., Katoh K., Satoh T., Amartaivan Ts., Tanaka A., Komori H., Orihara H. *, Nakamura E. **, Satoh N. **, Futatsugawa S. ***, and Sera K. *****

*Department of Quantum Science and Energy Engineering, Tohoku University,
*Cyclotron and Radioisotope Center, Tohoku University
**Miyagi Prefectural Institute of Public Health and Environment, Sendai 983-0836, Japan
***Nishina Memorial Cyclotron Center, Japan Radioisotope Association,
Takizawa, Iwate 020-0173, Japan
Department of Cyclotron Research Center, Iwate Medical University,
Takizawa, Iwate 020-0173, Japan*

Introduction

Atmospheric aerosol is small particulate matter caused by sandy dusts, smoke from factories, exhaust gas of cars and their deformed particles by photo chemical reactions in the atmosphere¹⁻³⁾. Elemental concentrations in atmospheric aerosol reflect air pollution and its generating process. Therefore, elemental analysis of atmospheric aerosols is useful for aerosol source determination. Combination of aerosol collection on thin filter and PIXE analysis is one of the effective methods for elemental analysis of atmospheric aerosols¹⁾. In previous study, we performed successive collection of aerosol samples with meteorological data and analyzed them by PIXE. The concentrations of Mn, Fe, Zn and Pb elements depended strongly on the direction of wind and their distributions for wind directions reflected to the position of aerosol sources. This result suggests that the aerosol source location can be determined by measuring the elemental concentrations of aerosols and wind directions at several positions with short sampling period⁴⁾. For this purpose, it is important to develop a compact sampler with low manufacturing and running costs for simultaneous sampling at several positions. The compact sampler is also useful for indoor sampling such as subway and houses. In this study, we developed mini step samplers and applied them to room aerosol monitoring.

Development of Mini Step Samplers

Sampler with smaller suction nozzle diameter is desirable for continuous sampling over extended periods and for the running cost. However, it causes problems as non-uniformity, choke of filter and high detection limit. Atmosphere is sucked through Nuclepore filter⁵⁾ of 1.0 μm pore size in diameter, and aerosols are collected on the surface of this filter. Since the sizes of collected aerosol depend on face velocity as well as pore size⁶⁾, these parameters must be determined when the sampler is designed. The suction nozzle of the step sampler (Green blue Co. LTD), which we used in previous studies, is 4 mm in diameter⁷⁾. In order to get a more compact sampler, we tested the samplers of 2 mm-suction nozzle and 4 mm-suction nozzle. Test sampler is composed of filter holder, mass flow meter, fine control valve, vacuum pump and shelter. The suction nozzle of the filter holder can be easily changed. Aerosols were collected with the same face velocity of 80 m/min. The 50 % cutoff diameter of the sampler was less than 0.2 μm ⁸⁾ which is sufficient for anthropogenic aerosol collection. Sampling was performed at the same time using the two samplers for 3 hours at the campus of Tohoku University.

The samples were analyzed by the submilli-PIXE camera at Tohoku University⁹⁾ Proton beams of $0.5 \times 0.5 \text{ mm}^2$ were uniformly scanned vertically and horizontally over the area of $5 \text{ mm} \times 7 \text{ mm}$. These samples contained Fe and Ca which are originating mainly in the soil. Elemental concentration ratios at the same time sampling using the same suction nozzle diameters of 4 mm are shown in Fig. 1. Figure 2 shows the results for the sampling using 4 mm- and 2 mm-suction nozzles. Elemental concentration ratios for both cases were consistent within $\pm 20 \%$ except for few cases. Typical elemental distributions of Fe for suction nozzle diameters of 4 mm and 2 mm are shown in Fig. 3. While sample uniformity does not show meaningful changes among each other, it shows large deviation around 40%. In this case, a beam with uniform intensity across its cross sectional areas is required in the quantitative analysis. It is easier to get uniform beam over the small area. Therefore, sampling with small suction nozzle does not affect aerosol collections and is preferable for quantitative analysis.

Then we developed mini step samplers of 2 mm-suction nozzle diameter. The mini step sampler, shown in Fig. 4, is composed of a sampling unit, mass flow meter, fine control valve, vacuum pump, programmable control unit and shelter. A small reversible motor moves the suction nozzle. The programmable controller controls the movement of the suction nozzle one dimensionally and vacuum pump. The sampler collects more than 70

samples. The weight of the sampler is about 6 kg. The compact sampler allows easy setting.

Application for in-door Monitoring

We applied the mini step samplers to room aerosol monitoring. Aerosol samples were collected at two rooms inside our laboratory and a hall outside, during the period 11(Fri.)-15(Tue.) January 2002. Sampling points are in the second floor and are shown in Fig. 5. In our laboratory, no shoes are allowed. We change shoes in at the entrance. Sampling point 2 (Lab2) is near the entrance. The laboratory has only one entrance. The sampling point 1 (Lab1) is far from the entrance and student area. Sampling point 3 (Hall) is the corner of a hall and is near the copy machine. The hall can be accessed by anyone who wants to use.

The collected samples were analyzed by the Vertical in-air PIXE (ViaPIXE) system at Tohoku University^{10,11)}. Beam spot size was around 1.5 mm in diameter. It covered 60 % of the sample area, which is sufficient for quantitative analysis. Seven elements (Ca, Fe, Zn, Pb, Ti, Ni and Cu) were observed in these samples. The main elements were Ca, Fe and Zn. Their average, maximum and minimum values are written in Fig. 5. Time distribution of elemental concentration of Ca, Fe and Zn are shown in Figs. 6-8. Elemental concentrations increased periodically in the daytime and decreased at night. The correlation between the elemental concentrations of Ca and Fe was very strong in the hall. The concentrations in weekday were several times higher than in holiday, especially at the hall and the Lab2. Since elements of Ca and Fe are components of soil dust, time distribution of elemental concentration is caused by up flung soil with human movement. Elemental concentrations of the hall were always higher than the Lab1 and Lab2. Concentrations at the Lab1 were almost the same as those of Lab 2 in holiday. In our laboratory, we change shoes at the entrance of the room. This is the reason why the elemental concentrations were lower than that of the hall.

The mini step sampler is very useful for in-door sampling and will be a powerful tool for air-pollution monitoring.

Acknowledgements

The authors are pleased to acknowledge the assistance of Messrs. R.Sakamoto and M.Fujisawa for their maintenance works for the Dynamitron accelerator. We also

appreciate our thanks to T.Takahashi, K.Komatsu and T.Nagaya for their help on manufacturing the sampler.

References

- 1) Johansson S.A.E. and Campbell J.L., PIXE:A Novel Technique for Elemental Analysis, (JohnWiley and Sons, 1988).
- 2) Kasahara M., Park J.H. and Yamamoto K., Nucl. Instr. and Meth., **B109/110**, 471 (1996).
- 3) Cahill T.A., Nucl. Instr. and Meth., **B49**, 345 (1990).
- 4) Matsuyama S. et.al., International Journal of PIXE, **9**, Nos 1&2, 51(1999)
- 5) Spurny K.R., Lodge J.P., Frank E.R. and Sheesley D.C., Environmental Science and Technology, **3**, 5,453 (1969).
- 6) Kemp K. and Kownacka L., Nucl. Instr. and Meth., **B22**, 340 (1987).
- 7) Hashimoto Y. et. al., Proc. 7th World Clean Air Congress (II), (1986) p.11.
- 8) H.Liu B.Y. and Lee K.W., Environ.Sci. Technol., **10**, 345 (1976).
- 9) Matsuyama S. et. al., International Journal of PIXE, **8**, 2&3, 209 (1998)
- 10) Iwasaki S., Ishii K., Matsuyama S. et. al, International Journal of PIXE, **5**, 2&3, 163 (1995).
- 11) Iwasaki S., Ishii K., Matsuyama S. et. al, International Journal of PIXE, **6**, 1&2, 117 (1996).

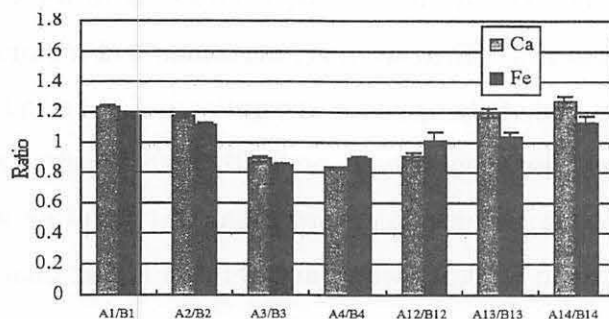


Fig. 1. Elemental concentration ratios for simultaneous sampling using the samplers of suction nozzle diameters of 4 mm.

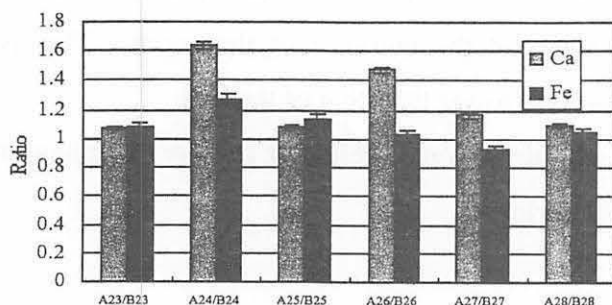


Fig. 2. Elemental concentration ratios for simultaneous sampling using the samplers of suction nozzle diameters of 4 mm and 2 mm.

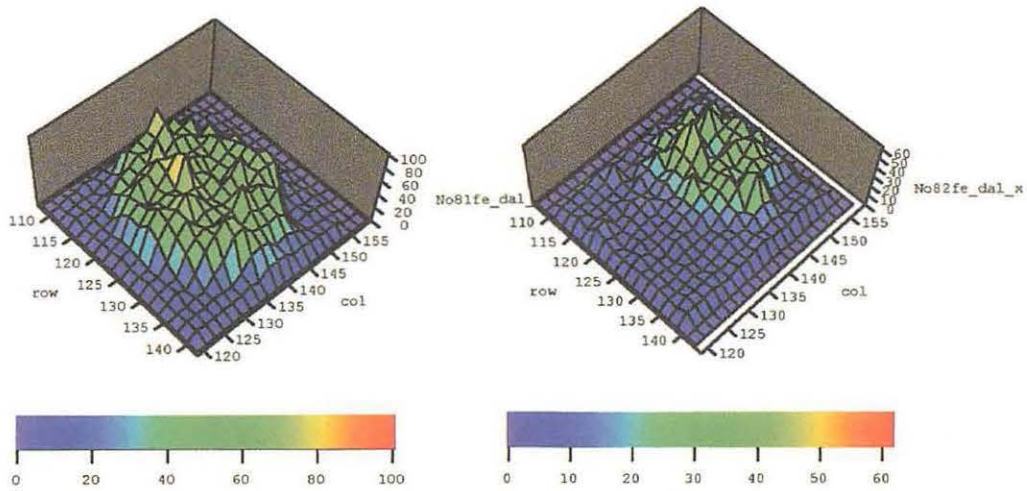


Fig. 3. Elemental distributions of Fe using the sampler of 4 mm-suction nozzle (left) and that of 2 mm-suction nozzle (right).

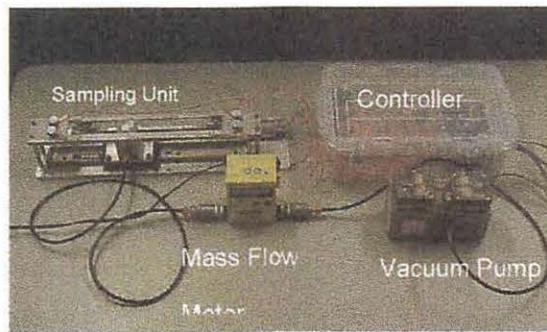


Fig. 4. Multi-step sampler.

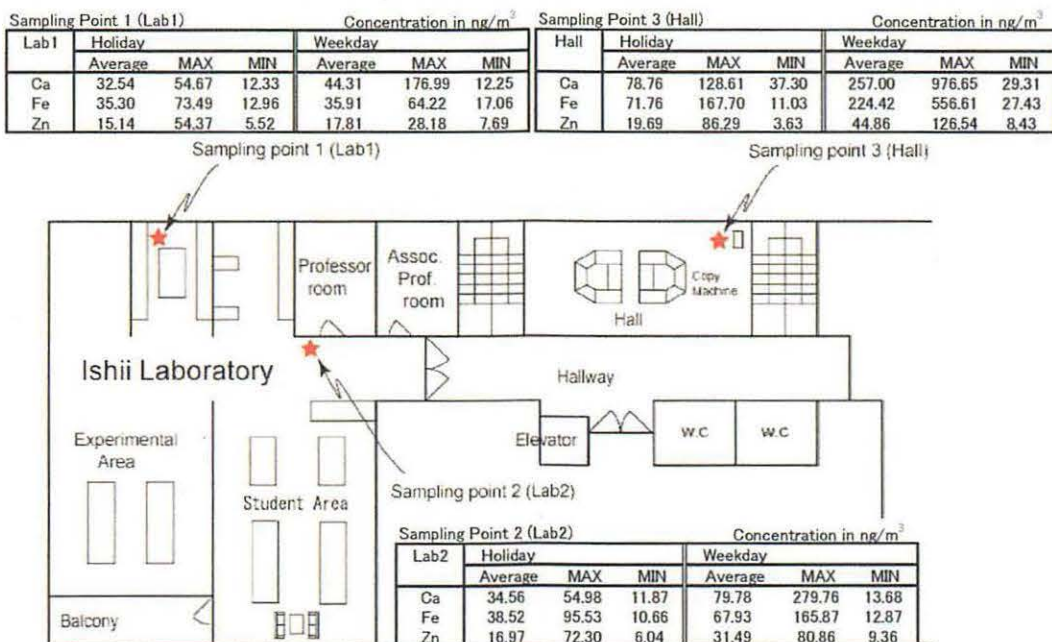
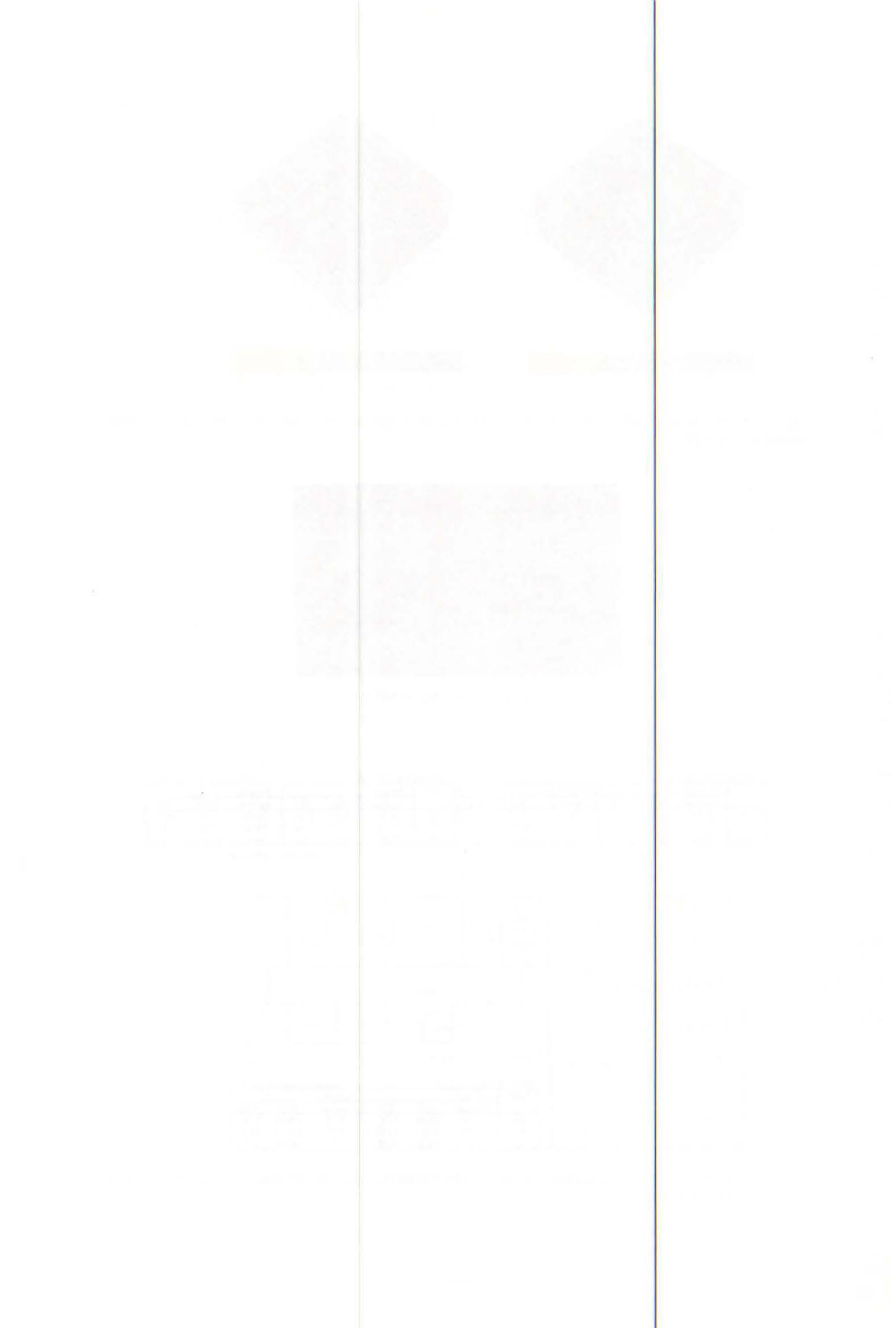


Fig. 5. Sampling Points and the average, maximum and minimum values for the main elements (Ca, Fe and Zn) at the sampling points.



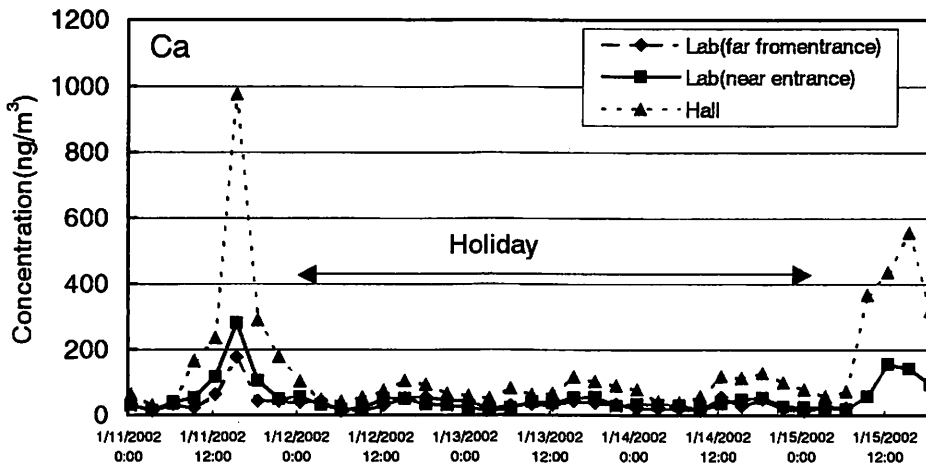


Fig. 6. Time distribution of Elemental Concentrations (Ca).

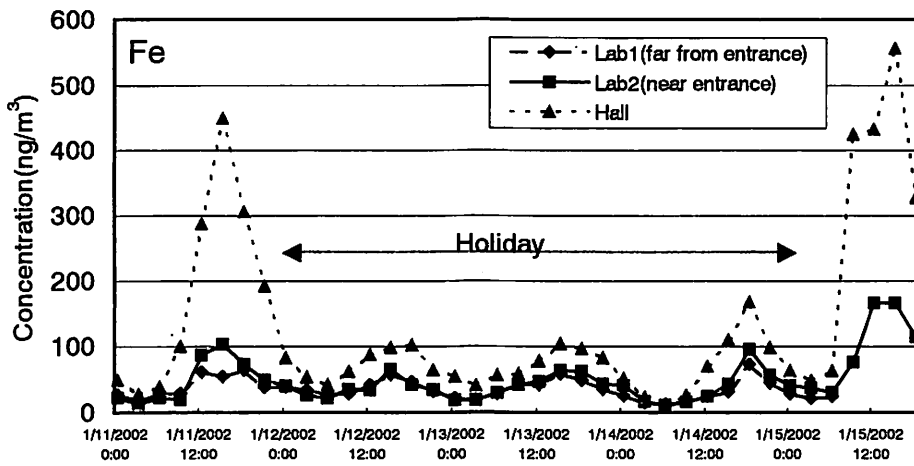


Fig. 7. Time distribution of Elemental Concentrations (Fe).

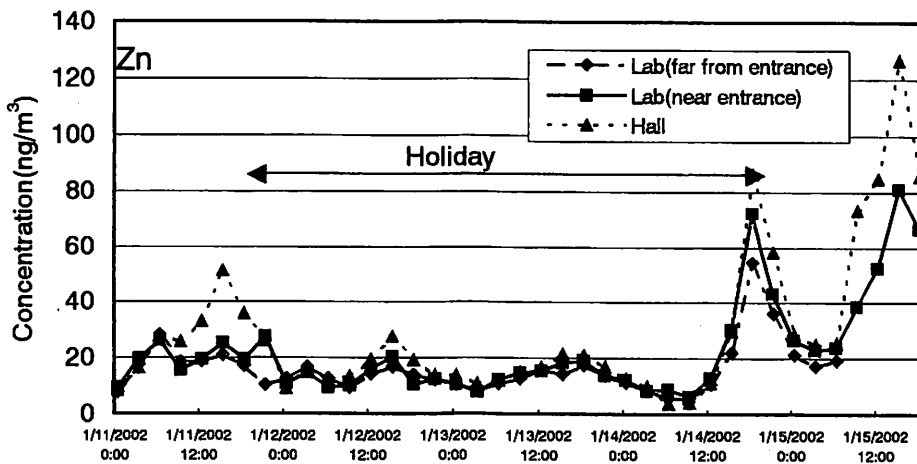


Fig. 8. Time distribution of Elemental Concentrations (Zn).

I. 16. Coloration of Polyethylene Terephthalate (PET) Film by 3MeV Proton Beams

*Matsuyama S., Ishii K., Yamazaki H., Endoh H., Yuki H., Satoh T., Sugihara S., Amartaivan Ts., Tanaka A., Komori H., and Orihara H.**

*Department of Quantum Science and Energy Engineering, Tohoku University,
Cyclotron and Radioisotope Center, Tohoku University**

Introduction

Though the PIXE analysis is well known as a nondestructive method, discoloration of samples occurs by beam irradiation, which is a serious problem for very important archaeological samples. The discoloration of glass, glazed ceramics, china and paper samples in PIXE analysis has been reported. We previously investigated discoloration of samples such as paper, Japanese vessels and japan bowls. The degree of discoloration was different for each sample. In the case of glazed ceramics, discoloration increased with the dose and gradually disappeared after irradiation. In recent years, discoloration of plastic items has become a problem in commercial applications.

Coloration of glassy materials using γ -rays has been extensively studied and the colored materials are commercially produced. Coloration of polymeric materials by ion beams has not been studied until quite recently and has been treated as an unwanted phenomenon. In this study, we consider proton beam irradiation as a coloring technique. Because ion beams can be controlled two-dimensionally using magnetic or electrostatic fields and beam energy is concentrated in the Bragg peak at the end of range, the coloration by proton beam irradiation can be carried out in 3 dimensions by varying beam energy.

Experiments

Experiments were performed by the use of a Dynamitron accelerator at Tohoku University. Thin films were uniformly scanned horizontally and vertically by means of a submilli-PIXE camera with 3 MeV proton beams. The scanning area was 10 x 10 mm². Beam irradiation was carried out in air with average beam currents of ~1.6nA. Proton

beams were extracted from the beam duct through a Kapton window. Irradiation effects were investigated by means of absorption spectroscopy, electron spin resonance (ESR) spectroscopy and Fourier transform infrared absorption (FT-IR) spectroscopy. The time dependence of the absorbance and the ESR signal was measured.

Results and Discussion

PET films of 100 μm thickness were irradiated in-air with doses of 0.5–30 $\mu\text{C}/\text{cm}^2$. The PET films used in this study were obtained from a commercial source (Toray, Lumirror, T60). The films discolored to light brown. Since the coloration faded as a function of time, the absorption spectra were measured within 10 min. after irradiation. The absorption spectra are shown in Fig. 1 for irradiation doses of 0–30 $\mu\text{C}/\text{cm}^2$. The absorbance strongly increased with the dose in particular in the ultraviolet region (UV) and had a broad peak in the green region (500 nm). The absorbance at 400 nm and 500 nm as a function of dose is shown in Fig. 2, where the absorbance measured one year after irradiation is also plotted.

Figure 3 shows the changes in absorbance with time after the irradiation with a dose of 30 $\mu\text{C}/\text{cm}^2$. The absorbance decreased gradually after irradiation. The absorbance at long wavelength > 500 nm recovered after 3 months. However, the absorbance at short wavelength < 500 nm still shows higher values than those of unirradiated film.

Figure 4 shows the absorption spectra in the ultraviolet (UV) region. A red shift was observed in the irradiated films. Similar phenomena are reported for samples irradiated by γ -rays and explained by changes in the molecular structure. The absorbance at 400 nm as a function of time after irradiation is shown in Fig. 5. The absorbance decreases exponentially except during the first 100 minutes. The decay constant of the absorbance curve decreases with the dose.

These results show that at least three types of color centers, permanent, long-lived and short-lived, are formed by irradiation. The absorbance by permanent color centers as a function of dose is shown in Fig. 2. The degree of absorbance by permanent color centers is very feeble at wavelength of 500 nm. Since annealable color centers decay during the irradiation, absorbance at 500 nm is nearly saturated as exponential build up of defects compete with their exponential decay.

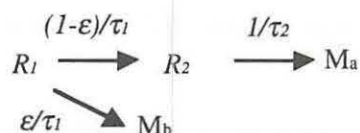
The ion beam irradiation causes chain scission, creation of free radicals and cross linking and forms color centers⁸⁾. The annealable color centers are formed by reactive

species such as free radical. Radical ions are very reactive and unstable at room temperature. Radicals produced by beam irradiation were measured by using electron spin resonance (ESR) spectrometer. The intensity of ESR signals decreased with time and finally vanished. The time variation of ESR intensity for the dose of $10 \mu\text{C}/\text{cm}^2$ is shown in Fig. 6. While the decay time is three times shorter than that of absorbance, the decay curve shows a similar tendency. This result suggests that the annealable color centers arise from the formation of radicals.

Chemical changes of the irradiated films were studied by Fourier-transform infrared spectroscopy (FT-IR). Figure 7 shows the FT-IR spectra before and after irradiation for the dose of $2.5 \mu\text{C}/\text{cm}^2$ and $25 \mu\text{C}/\text{cm}^2$. We could not measure the spectra for wave-number below 1600 cm^{-1} which is typical of the vibration modes of aromatic rings, because the absorbance in $100 \mu\text{m}$ film was too large. The C-H and O-H stretching vibration appears in the region of $3600 \text{ cm}^{-1} \sim 2500 \text{ cm}^{-1}$. In the case of high dose, the degradation by beam irradiation is evident and a new band appeared at 2349 cm^{-1} , which disappeared after few days. This bond can be assigned to the vibration of CO_2 molecules. Since CO_2 molecules slowly diffuse out through the surface, the peak disappears after a few days.

We also measured the time variation of absorbance of the samples preserved under atmosphere of nitrogen, oxygen, air and in vacuum. Irradiation dose was around $10 \mu\text{C}/\text{cm}^2$. Figure 8 shows the time dependence of absorbance for oxygen gas, nitrogen gas and vacuum. Annealing proceeded rapidly in oxygen, but not in vacuum. It is thus apparent that the color centers react with oxygen gas which permeates into the sample. Figure 9 shows the time dependence of absorbance for temperatures of -10°C , $+20^\circ \text{C}$ and $+60^\circ \text{C}$ in air. The annealing time shows a strong temperature dependence and becomes short at high temperature. Since the permeability of oxygen and nitrogen increases with temperature, radicals are consumed through reactions with these gases.

Though a first order process and a second order (bimolecular) process have been proposed for the annealing process of irradiated polymers, the present results do not support this explanation. We propose the following sequential process:



Primary radicals (R_1) are formed by beam irradiation and transform into secondary radicals

(R_2) and inert molecules M_b with decay constants $(1-\varepsilon)/\tau_1$ and ε/τ_2 , respectively. The radicals (R_2) are forming the absorption centers. The molecules M_b do not absorb light. Subsequently, the radicals (R_2) decay into inert molecules M_a with decay time $1/\tau_2$ and M_a do not absorb light. The time variation of radical concentrations N_1 , N_2 for R_1 , R_2 can be written as follows.

$$\frac{dN_1}{dt} = -\frac{1}{\tau_1} N_1,$$

$$\frac{dN_2}{dt} = (1-\varepsilon)\frac{1}{\tau_1} N_1 - \frac{1}{\tau_2} N_2.$$

The absorbance A_λ at wavelength λ can be written as

$$A_\lambda = k_1 N_1 + k_2 N_2,$$

where k_1 , k_2 are extinction coefficients for wavelength λ .

Using the above formalism, the calculations are shown by solid lines in Fig. 8. The values of ε , τ_1 , τ_2 are varied corresponding to ambient conditions. The values of k_1 , k_2 are determined from the experimental results under vacuum condition. The values of ε , τ_1 , τ_2 for in-air preservation are derived from those of N_2 and O_2 preservation considering their partial pressures. The calculations reproduce the experimental data. This suggests that the coloration occurs by the proposed sequential reaction process. While the value of $1/\tau_1$ is almost constant, the values of $1/\tau_2$ and ε increase with the O_2 partial pressure. Figure 9 shows the calculated results at different preservation temperatures. The calculations reproduce the experimental data well.

The coloration of PET films under proton beam irradiation was examined, but faded within a few days. However, this fading phenomenon could be controlled by the beam dose and by the preservation technique, therefore, it can be used commercially. Figure 10 shows a demonstration of proton beam writing. The Chinese character of [和] was written on the PET film.

Acknowledgements

The authors acknowledge the help of Mr. R.Sakamoto and Mr. M.Fujisawa during operation of the Dynamitron accelerator. The authors express their gratitude to Dr M.Watanabe and Dr Y.Hakuta for help and advice with measurements of the ESR spectra.

References

- 1) Swann C.P. and Fleming S.J, Nucl. Instr. and Meth., **181**, 205 (1981).
- 2) Zeng X., et al., Nucl. Instr. and Meth., **B47**, 143 (1990).
- 3) Matsuyama S., et al., International Journal of PIXE, **9** (1&2), 57-61 (1999).
- 4) Matsuyama S., et al., International Journal of PIXE, **9** (1&2), 47-50 (1999).
- 5) R.L. Clough, et al., Polymer degradation and Stability, **49**, 305-313 (1995).
- 6) Clough R.L., et al., Radiat. Phys. Chem, **48** (5), 583-594 (1996).
- 7) Matsuyama S., et al., International Journal of PIXE, **8** (2&3), 209-216 (1998).
- 8) Steckenreiter T., et al., Nucl. Instrum. and Meth., **B131**, 159-166 (1997).
- 9) Harrah H.A., Organic solid State Chemistry, 197 (Gordon and Breach Science Publishers, New York).
- 10) Michaels A.S., Vieth W.R. and Barrie J.A., J. App. Phy., Vol. **34**, No1 13 (1963).
- 11) Wulkop B., et al., Nucl. Phys. **B44**, 542 (1995).

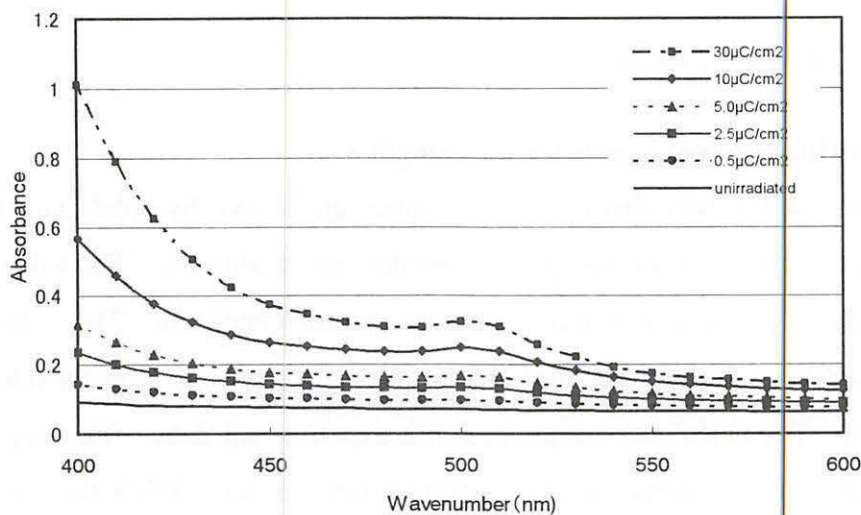


Fig. 1. Absorbance from 400 to 600 nm for irradiation dose of 0–30 $\mu\text{C}/\text{cm}^2$.

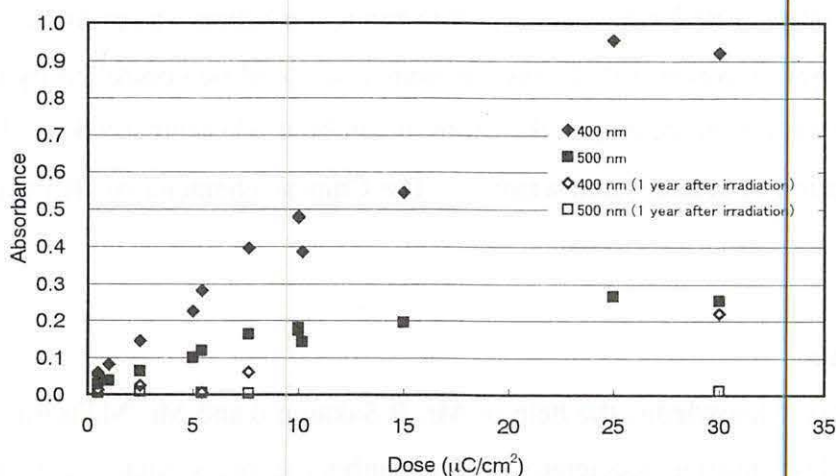


Fig. 2. Absorbance at 400 nm and 500 nm as a function of the irradiation dose.

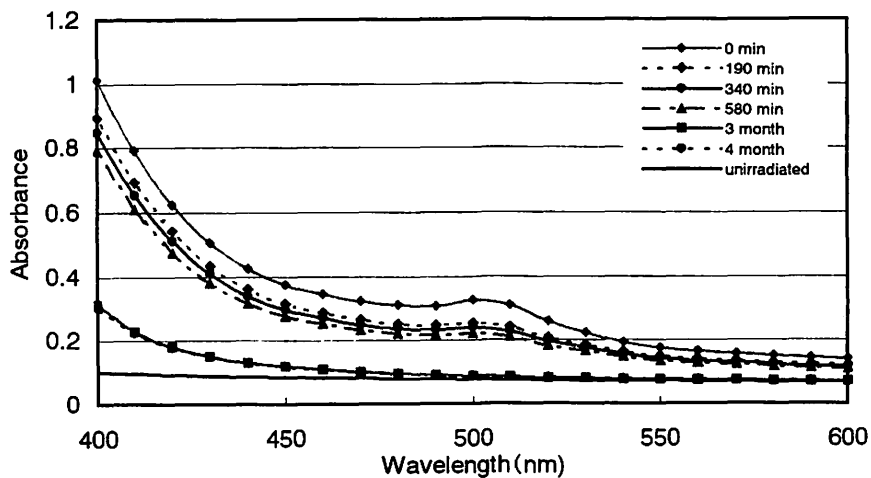


Fig. 3. Absorption spectra after irradiation.

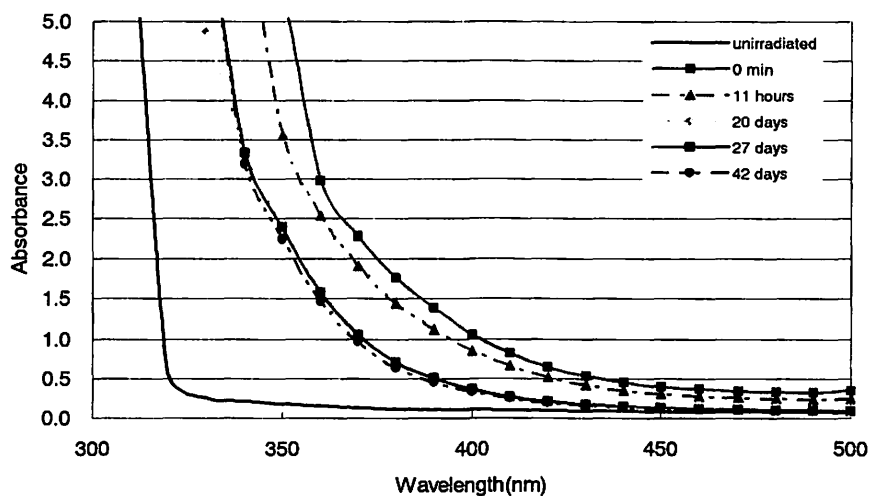


Fig. 4. Absorption spectra in the ultra-violet region.

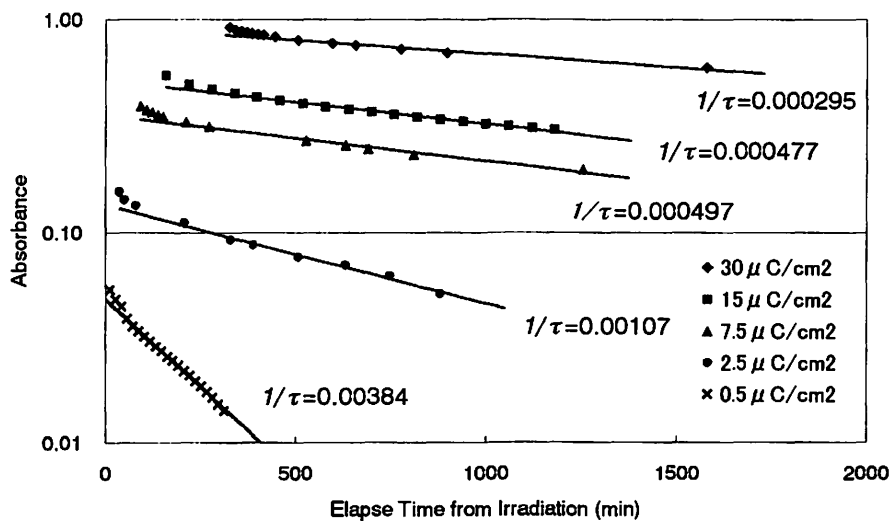


Fig. 5. Absorbance at 400 nm as a function of elapsed time from irradiation.

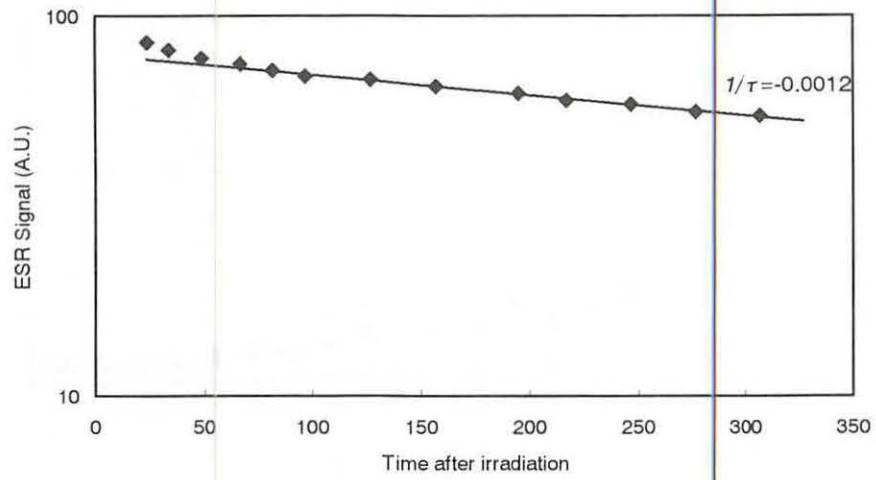


Fig. 6. ESR signal intensity as a function of time after irradiation.

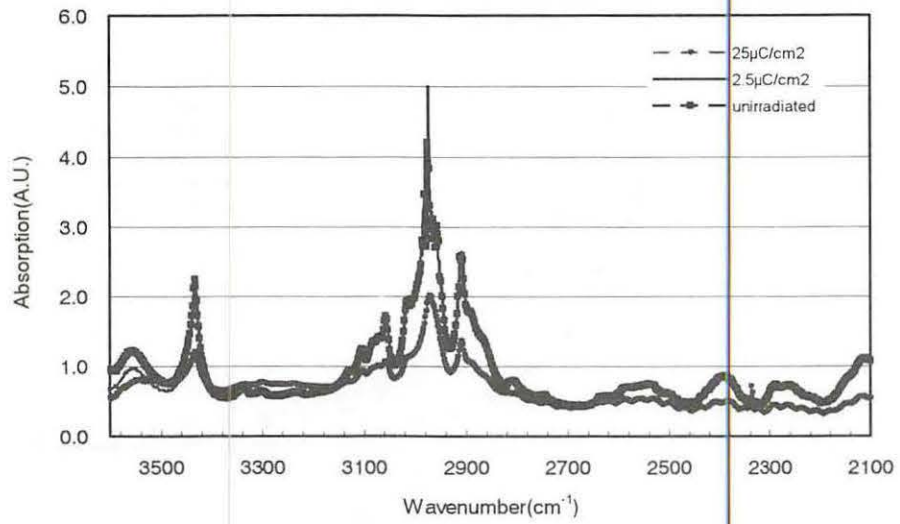


Fig. 7. FT-IR Spectra for irradiation dose of 2.5 and 25 μC.

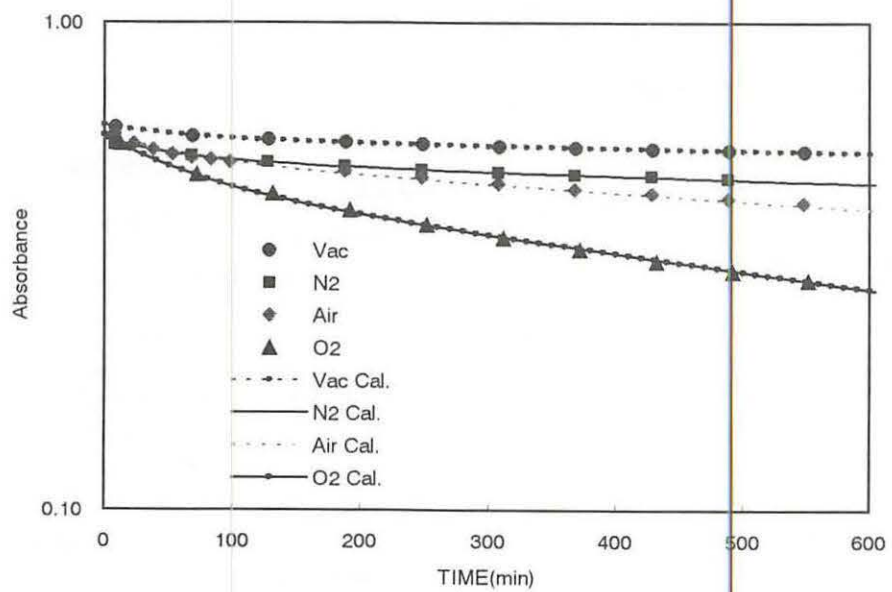


Fig. 8. Absorbance variation for preservation under atmospheric pressure of nitrogen, oxygen, air and in vacuum.

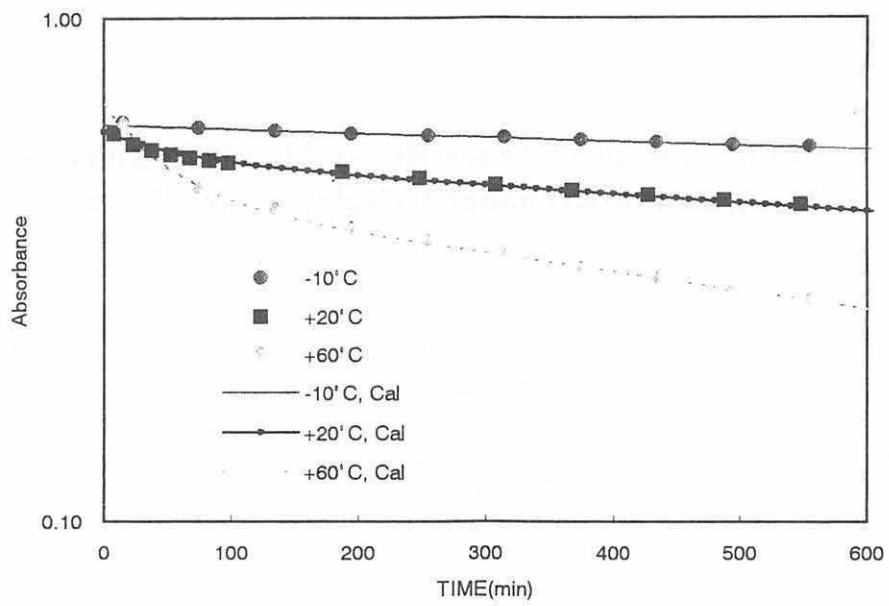


Fig. 9. Absorbance changes for preservation temperature.

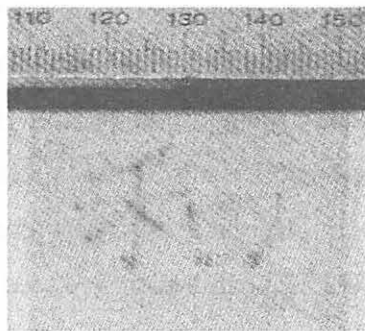


Fig. 10. Proton beam writing.

I. 17. PIXE Analysis of Trace Heavy-Metals in River Water Using an Ion-Exchange Cellulose Filter Paper

*Amartaivan Ts., Yamazaki H., Ishii K., Matsuyama S., Takahashi Y., Satoh T., and Orihara H.**

*Department of Quantum Science and Energy Engineering, Graduate School of Engineering,
Tohoku University,
Cyclotron and Radioisotope Center, Tohoku University**

INTRODUCTION

The toxic effects of various species of heavy metals in the biosphere have been pointed out in many studies^{1,2)}. Since the main source of heavy metal for humans is water and foods, monitoring of environmental water for trace heavy-metals plays an important role. For quantitative analysis of heavy metals in aquatic environment a number of sensitive instrumental methods, for example atomic absorption spectroscopy, are available, but they may suffer from systematic interference by major constituents in water samples. Particle-induced X-ray emission (PIXE) can be applied to direct determination of trace heavy metals in water due to the high sensitivity and the multi-elemental capability³⁻⁵⁾. Till now, however, PIXE is not extensively used for monitoring of a pollution problem in natural water because of some problems in preparing samples. We developed a three-step method for preparing PIXE targets from aqueous samples by combining pre-concentration of soluble constituents with filtration of insoluble ones^{6,7)}. This technique was successfully applied to a variety of water samples with a wide range of elemental concentrations⁸⁾.

In order to ascertain the quality of river water, very low concentrations of harmful heavy metals should be traced for a long term, and a relatively large number of samples must be taken from various locations during monitoring. When the method of sampling is chosen bearing PIXE analysis in mind, it is convenient that heavy metals in river water can be fixed directly on a PIXE target and no additional chemical treatment is required. The three-step method previously developed in our laboratory is not suitable for this purpose, because the method uses a chemical process with an unstable reagent such as

methanol solution of *N,N*-dibenzylthiocarbamic acid and filtration under suction. An ion-exchange cellulose phosphate in fiber type has already been applied to pre-concentration of heavy metal ions in aqueous samples, but chromatographic column operation and acid elution of adsorbed analytes are indispensable⁹⁻¹¹). This ion exchanger has a good selectivity for heavy metals and an excellent ion-exchange kinetics, which allows rapid pre-concentration of heavy metals from a large volume of water samples. Recently, phosphate cellulose filter paper with large ion-exchange capacity is commercially available. In this study, we developed a very simple but precise method for the PIXE analysis of trace heavy metals in aqueous samples using a cellulose phosphate ion-exchange filter paper. The newly developed method is compared with the method of preparing a target for each dissolved species of elements contained in river water.

EXPERIMENTAL

Materials

The cation-exchange cellulose filter paper with phosphate functional groups was purchased from Whatman Japan Ltd. under the brand name "Whatman-P81 Ion Exchange Cellulose Filter". The filter paper is a thin material of low density (0.23 mm thickness, 8.6 ± 0.2 mg / cm²) and has a large nominal exchange capacity (18.0 μ Eq / cm² (chemical equivalent)) and high water permeability (125 mm / 30 min). All the other reagents used in this experiment were the same as those described previously^{6,7}).

Preliminary Study on the Ion-exchange Reaction of Whatman-P81 Filter

In order to elucidate the ion-exchange reaction of the filter paper, two kinds of flow experiments were conducted by passing the test solution through a sheet of the filter placed in polypropylene disc filter holder (Advantec PP-25). A peristaltic pump (Masterflex type- 7550) was used to set a constant flow rate. First, we checked the breakthrough curves of cobalt ions as a function of the concentrations of cobalt ions, pH values and flow rates. In this experiment, radioisotope ⁶⁰Co was added to a test solution (5000 cpm/ml) as an indicator of cobalt ions in effluents. Second, various amounts of Ca, Mn, Co, Cu, Hg and Pb were loaded on the filter by passing test solutions containing various amounts of the metals at the flow rate of 1 ml/min. The metals loaded on a sheet of the filter were analyzed by PIXE in order to verify the quantitative collection of metals from a solution and the uniformity of ion-exchange sites on the filter. Test solutions were made from standard solutions of metals in the certified concentrations (1.00 mg/ml) for atomic

absorption spectrophotometry.

Sampling of River Waters

We collected 10 samples on July 3rd, 2001 from the basin of the Hirose river (a class A river). As shown in Table 1, the sampling points are located along the basin in the river in 3 to 10 km interval. River-water samples were stored in polyethylene bottles and processed into PIXE targets within 2 days. The chemical oxygen demand (COD / mg O₂ ml⁻¹) was determined by K₂Cr₂O₇ oxidimetry for an indicator of organic substance contents in the collected river waters.

Target Preparation

Four kinds of PIXE targets were prepared from each sample of the Hirose river by using the Whatman-P81 filter paper and the three-step method previously developed⁸⁾ that are, the ion-exchange filter target (WP81), the Nuclepore filter target for insoluble constituents (FILT), the pre-concentration target for heavy metal ions (PRECON), and the deposit target for soluble major constituents (DEP). In the case of three-step target preparation, the residues on Nuclepore filter of 0.4- μ m pores in filtration were classified into an insoluble component and the filtrate was regarded as a soluble component. This classification is a rough-and-ready way, and it is more proper to consider that the FILT target contains only a coarse fraction of insoluble components and the DEP target also includes a fine fraction of insoluble ones. We compared the results of PIXE analyses for these different targets in order to confirm the merit of using ion exchange filter (WP81) for preparing PIXE targets by the process of concentrating heavy metals in river waters.

PIXE Analysis

The four kinds of targets were irradiated for 10 minutes in a vacuum chamber by 3 MeV protons (5 nA beam current) from the single-ended type 4.5 MV Dynamitron accelerator at Tohoku University. Proton beams were scanned on 3.5x3.5 mm² of the sample surface in order to deal with nonuniform distribution of trace components on the filter paper. X-rays from targets were measured with two Si(Li) detectors; No.1 detector (0.012 mm thick Be window and 80mm² active area) with a low geometric efficiency is well suited for the detection of elements of the atomic number $Z \leq 20$, and No.2 detector (0.025 mm thick Be window and 28 mm² active area) with a 500- μ m Mylar absorber and the high

geometric efficiency allows the detection of X-rays > 4 keV.

For PIXE-spectrum analysis, we used a least-squares fitting program developed in our laboratory based on the pattern analysis method¹²⁾ In this program, first a background function for elements with atomic number $Z=6-30$ is obtained as a function of Z and X-ray energy from bremsstrahlung emission cross-sections derived from a theoretical formula based on PWBA and BEA¹³⁾.

Next, the spectra of continuous and characteristic X-rays of elements are folded with the background function to obtain the least-squares fit of a measured PIXE spectrum. From this, the relative surface density of each element detected is determined, so the concentration in a solution is calculated by referring to the one of the internal standard used in PIXE targets. The lower detection limit was taken to be the statistics 3σ error of the background counts, integrated over the width of the detector resolution (FWHM) at the X-ray energy characteristic to an element of interest in the PIXE spectrum of a sample. In this calculation, we used the X-ray yield and the analysis concentration of the element of interest in samples where the element was clearly detected above background.

RESULTS AND DISCUSSION

PIXE analysis of Whatman-P81 cellulose filter

A thin filter paper of low density with the characteristics shown in Table1 is advantageous for the PIXE analysis because of low emission of continuum X-ray background. Figure 1 shows the PIXE spectra of a sheet of clean filter paper; the spectrum on the left side was obtained by No.1 detector directed to low energy X-rays and that on the right side by No.2 detector directed to high energy X-rays. A continuum X-ray background from cellulose components, with which the large peak of phosphoric characteristic X-ray overlapped, was observed up to around 10 keV, and traces of Ca and Zn were detected. The amount of impurities and phosphorus in 6 sheets of the filter paper were determined quantitatively by PIXE analysis using 20- μg Y adsorbed on the papers as an internal standard. In quantitative analysis, phosphorus and calcium were assumed uniformly distributed in half the thickness of the filter paper, and the assay analysis was carried out by correcting the absorption of X-rays emitted and energy loss of incident protons at half-thickness of the filter paper. The average elemental content per sheet of filter paper was 1170 ± 230 μg of phosphorous, 6 ± 2 μg of calcium and 88 ± 43 ng of zinc, respectively. These amounts of calcium and zinc were used as BG values in the analysis of real

samples. The phosphoric ion-exchange group was assumed to be dibasic acid type (R-OPO(OH)₂) based on the nominal value of ion-exchange capacity (74.8 μEq) and the amount of phosphoric content per sheet of filter paper.

Ion-exchange reaction of Whatman-P81 cellulose filter

Among transition metals, cobalt ions are adsorbed with comparatively low selectivity by the phosphoric functional groups^{9,10}. To elucidate the ion-exchange performance of the filter, the quantitative adsorption of cobalt ions on a sheet of filter was examined in a flow experiment at breakthrough. In acidic solutions below pH 5, the filter cannot quantitatively collect cobalt ions even at a low concentration. This result seems to reflect an insufficient ion-exchange rate, since the dissociation of the phosphate groups is suppressed in acidic solutions. For the solutions above pH 5, the breakthrough of cobalt ions was observed only at high concentration like 25ppm even though solutions were passed at a speed over water permeability of the filter paper. The amount of exchange sites used for the quantitative collection of cobalt ions was estimated to be 16.9 μEq (chemical equivalent) for one filter paper on the basis of an effluent volume of 25ppm solution in which collection over 93% was possible. This result indicates that the ion-exchange rate is rapid due to the dissociation of a sufficient number of phosphoric groups and cobalt ions can be quantitatively retained up to about 20% of the nominal ion-exchange capacity of one filter paper of 0.23 mm thickness.

Figure 2 shows the calibration curve of the PIXE analysis for Mn, Co, Cu, Hg and Pb retained on a sheet of the filter paper at pH of 5.9-6.1. 2ml of Y standard solution (10 ppm) was dropped after 50 ml of solution containing the metals with concentrations of 50-200ppb was passed through the filter paper. In the PIXE analysis, the amount of each metal ($C_{Ex} / \mu\text{g cm}^{-2}$) was determined based on 20 μg of Y adsorbed on the filter paper. The results are plotted with the analyzed amounts as abscissa against the surface densities ($C_{Th} / \mu\text{g cm}^{-2}$) calculated from the effluent volume and concentrations as ordinate. The straight line corresponds to the relation of $C_{Ex} = C_{Th}$. For Mn, Co, Cu and Pb ions in the solution, the analysis value (C_{Ex}) agrees with the nominal one (C_{Th}) within ± 6% deviation. The fixed relation was obtained for elements emitting X-rays of different energies without correction for absorption of X-rays and energy loss of projectiles in the thickness of the filter paper. Hence, it is assumed that these ions are collected at the surface of the filter paper. In the case of Hg, such a quantitative relation was not obtained. As mercury ion

hydrolyzes in a solution of $\text{pH} > 3$, the large deviation from the quantitative relationship seems to reflect the imperfect filtration of mercury hydroxide colloids ($\text{Hg}(\text{OH})_2$). The constant quantitative relation was obtained, even if Y dosage of the internal standard varied in the range of 10-50 μg /filter paper. This range of Y amounts added after passing the sample solutions through a sheet of filter paper does not disturb the distribution of collected metal in a thin layer of the filter.

The application of Whatman-P81 filter paper to PIXE analysis for river water.

In order to elucidate the applicability of the filter paper to monitoring concentrations of heavy metals in river water, we compared the PIXE analyses for four kinds of targets of river water samples taken at ten sampling points; the ion-exchange filter target (WP81), the Nuclepore filtration target for coarse particulate fraction (FILT), the deposit target for fine particulate fraction and soluble major constituents (DEP), and the pre-concentration target for soluble fraction of heavy metals (PRECON). Figure 3 shows PIXE spectra for the four types of targets prepared from river water at No.7 sampling point in Table 1. The large peaks of Ga, Y and Zr were from the internal standards used. The *K* and *L* X-ray lines were observed for 17 elements in the spectra on targets prepared by the three-step method, but on the other hand some major components like Na^+ and $\text{VO}_2(\text{OH})_2^-$ were not collected by the filter paper. Hence, PIXE method using the ion-exchange filter offers the advantages of a truly multielemental nature and high speed analysis, although this method cannot be used for determining concentrations of harmful anionic species of chromium of hexavalent state and arsenic in river water¹⁴⁾.

In Fig.4, analysis concentrations on the four kinds of targets are compared for some typical elements in river water over all sampling points in order to clarify the collection efficiency of the ion-exchange filter paper. Aluminum and silicon are major constituents occurring as inorganic colloids in river water¹⁴⁾. The proportion of fine particulate which passed the Nuclepore filter of 0.4- μm pores is dominant for both elements, since the analysis concentrations are ten times higher for the DEP targets than for the FILT targets (Fig.4-1). The concentration in the fraction of coarse particulates increased almost 10 times downstreams of the river but is still much lower compared to the concentration of fine particulates. Since the analysis concentrations of aluminum and silicon on the WP81 target were almost the same as those on the FILT target, it is concluded that the filter paper cannot collect the fine-particulate fraction of these elements.

Titanium (IV) and iron (III) hydrolyze to neutral species in river water¹⁴). As the fine-particulate fraction of titanium hydroxide colloids in river water passed through the ion-exchange filter, its concentration is underestimated as in the case of the Nuclepore filtration target (Fig.4-1). On the other hand, the ion-exchange filter targets showed nearly the total concentration of iron when the coarse particulate fraction of iron(III) hydroxides became dominant. This may be due to the screening effect of the filter paper. Only in three sites in the downstream, trace mercury, which slightly exceeded the level of the lower detection limit, was detected on both the ion-exchange filter and the Nuclepore filtration targets; the detection limits were 0.9 ppb for the FILT target and 0.8 ppb for the WP81 target, respectively (Fig.4-1). Since mercury was not detected in the pre-concentration target with lower detection limit for the ionic species, the dissolved species of mercury in river water seems to be a particulate or flocculate. It is clear from Table 2 that the condensation effect by organic colloids became less effective for mercury colloids due to the comparatively low value of COD over the whole basin in the Hirose river. As concentrations of coarse particulates of aluminum and silicon increased by ten times downstreams of the river, mercury colloids attached to these coarse particulates may be collected on the two types of targets by filtration. On the other hand, three kinds of dissolved species of manganese intermingled, and the portion of cationic species became dominant downstream, since analysis concentrations for the PRECON target became nearly equal to those for the other kinds of targets (Fig.4-2). The portion of ionic species was high for lead and zinc, since the PRECON target showed comparatively high concentrations. For these ionic species except lead, the ion-exchange filter targets revealed almost the total concentrations. In the case of lead, the analysis concentration on the WP81 target was 1/2 to 1/5 of the value on the PRECON target. This may be ascribed to low affinity of phosphoric ion-exchange sites toward hydrolyzed species of lead, $PbOH^+$, in river water of pH of 7.3-8.1¹⁴). Though the filter paper also collected chromium, nickel and copper in trace concentrations (0.8-1.2 ppb), the dissolved species could not be clearly classified due to the detection limit in the FILT and DEP targets.

In addition, the ion-exchange filter paper showed low selectivity for major cationic components in river water such as sodium, magnesium, potassium, calcium and strontium. Hence, the competing reactions between these ions and trace heavy metals for occupying exchange sites in the filter paper do not pose a problem. For WP81 targets, the reproducibility of PIXE analysis was verified for soluble and insoluble components in

river water collected at No. 6 sampling point by using three targets prepared independently under the same conditions. A close agreement in concentrations between the three targets (within $\pm 9\%$ deviation) was obtained for detected elements like Ca, Ti, Mn, Fe, Ni, Cu, Zn and Pb.

CONCLUSION

We examined the cation-exchange reaction on cellulose phosphate ion-exchange filter paper commercially available under the brand name "Whatman-P81 Ion Exchange Cellulose Filter". Heavy metal ions in trace concentrations were quantitatively collected on a sheet of the filter paper due to its excellent performance in selectivity and kinetics of ion-exchange reactions. Using these excellent ion-exchange properties, we developed a simple method for PIXE analysis of trace heavy metals in aqueous samples, in which the PIXE targets are prepared by pre-concentrating metals on a sheet of the cellulose phosphate filter paper. For colloids in river water, this filter paper showed the screening effect equivalent to Nuclepore filters of 0.4- μm pores. The filter paper also showed quantitative collection of cationic species in river water samples until about 20% of the nominal ion-exchange capacity was consumed. It is concluded that this is a simple and effective method for on site preparation of PIXE targets and enables to perform an on-line PIXE analysis of aqueous samples.

References

- 1) Gruiz K., *et al.*, *Wat. Sci. Tech.*, **37**, 273-281 (1998).
- 2) Wilken R. D., *Fresenius J. Anal. Chem.*, **342**, 795-801 (1992).
- 3) Tanaka S., *et al.*, *Environ. Sci. Technol.*, **15**, 354-357 (1981).
- 4) Johansson E. M. and Johansson S. A. E., *Nucl. Instrum. Meth.* **B3**, 154-157 (1984).
- 5) John Kennedy V., *et al.*, *Nucl. Instrum. Meth.* **B150**, 277-281 (1999).
- 6) Yamazaki H., *et al.*, *Int. J. PIXE*, **7**, 31-40 (1997).
- 7) Yamazaki H., *et al.*, *Int. J. PIXE*, **7**, 101-107 (1997).
- 8) Yamazaki H., *et al.*, *Int. J. PIXE*, **9**, 83-102 (1999).
- 9) Schmitt P. H., Fritz J. S., *Talanta*, **15**, 515-524 (1968).
- 10) Brajter K., Slonawsha K., *Anal. Chim. Acta*, **185**, 271-277 (1986).
- 11) Magalhães P. de, *et al.*, *Talanta*, **45**, 317-323 (1997).
- 12) Murozono K., *et al.*, *Nucl. Instrum. Meth.* **B150**, 76-82 (1999).
- 13) Ishii K. and Morita S., *Nucl. Instrum. Meth.* **B3**, 57-61 (1984).
- 14) Base C. F. and Mesmer R. E., John Wiley & Sons, New York (1976), pp112-123; 215-219; 336-342; 365-370.

Table 1. Water samples at 10 sampling points along the whole basin of the Hirose river

No.	Sampling Distance ¹⁾ k m	Temp. °C	pH	COD mgO ₂ /ml
1	0	13.8	7.09	1.34
2	6.5	15.8	7.30	0.98
3	16.7	19.5	7.42	1.69
4	27.7	20.1	8.25	2.14
5	30.7	20.9	7.80	2.05
6	31.8	21.0	8.09	1.88
7	34.4	21.0	8.12	2.31
8	39.8	22.0	7.92	2.22
9	42.2	22.0	7.58	1.82
10	46.6	22.9	7.29	2.00

1): the distance to each sampling point from the first upstream point

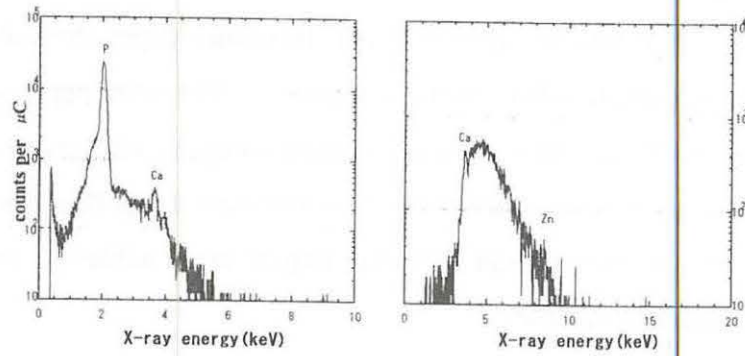


Fig. 1. PIXE spectra of clean Whatman-P81 cellulose filter

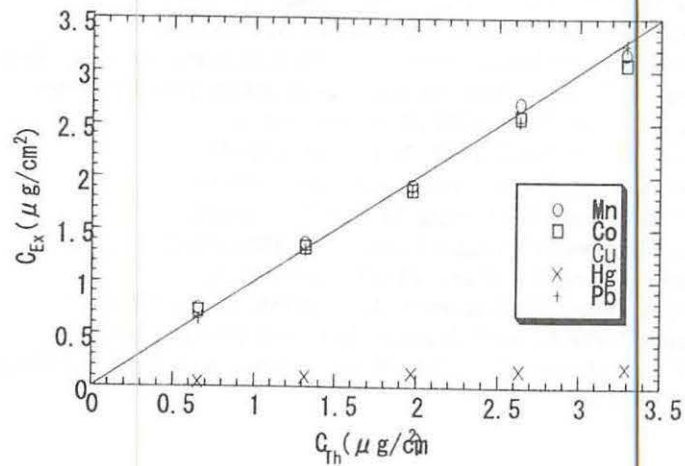


Fig. 2. Calibration curve for PIXE analysis of metal ions sorbed on Whatman-P81 filter paper. (3MeV protons, 3μC irradiation, 5.22 μg/cm² of Y internal standard)

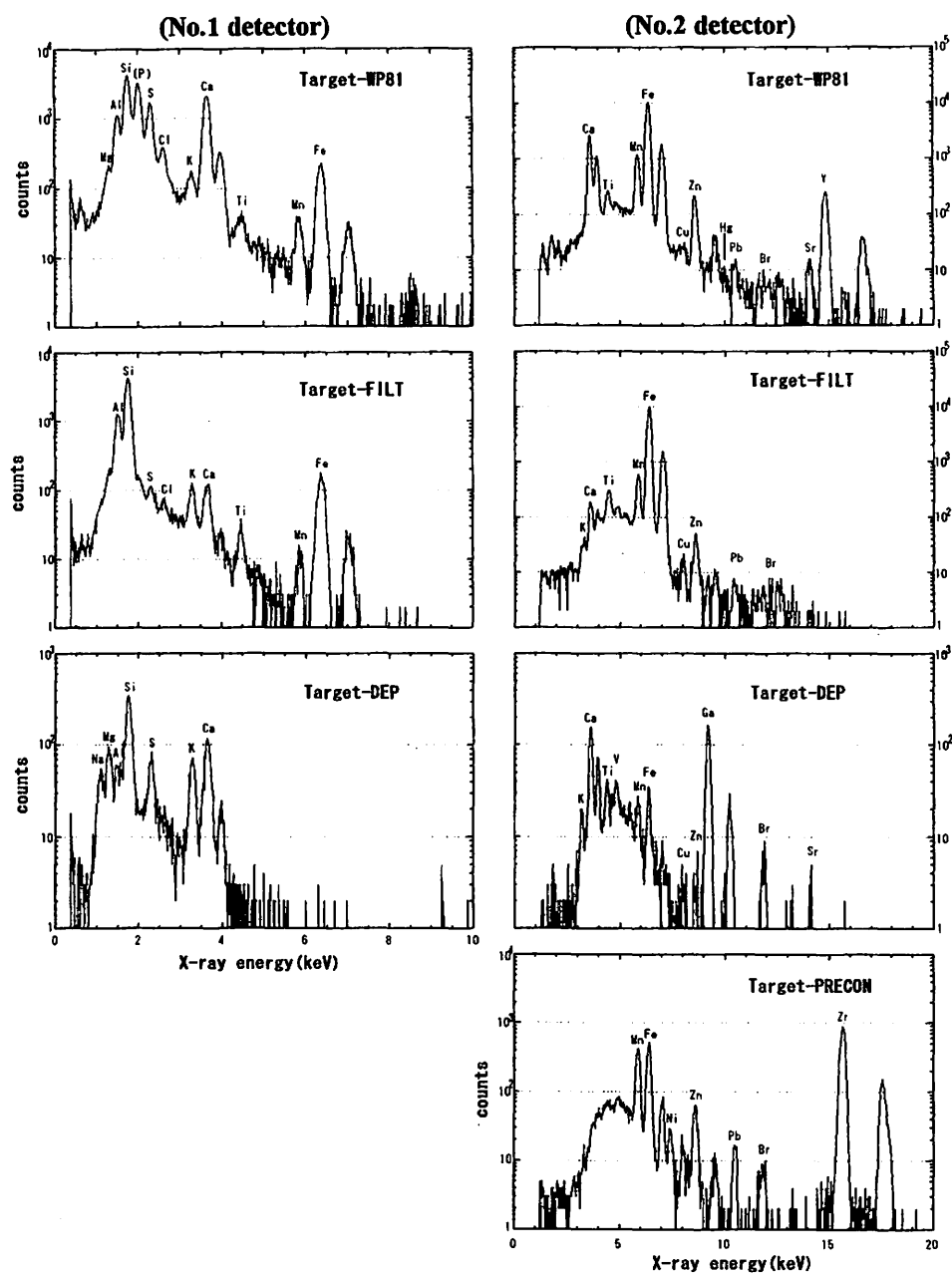


Fig. 3. PIXE spectra for river water sample collected at No.10 sampling point in the Hirose river. Irradiation: $3\mu\text{C}$ of 3MeV protons. The spectra on the left side was obtained by No.1 detector directed to low energy X-rays and those on the right side by No.2 detector directed to high energy X-rays.

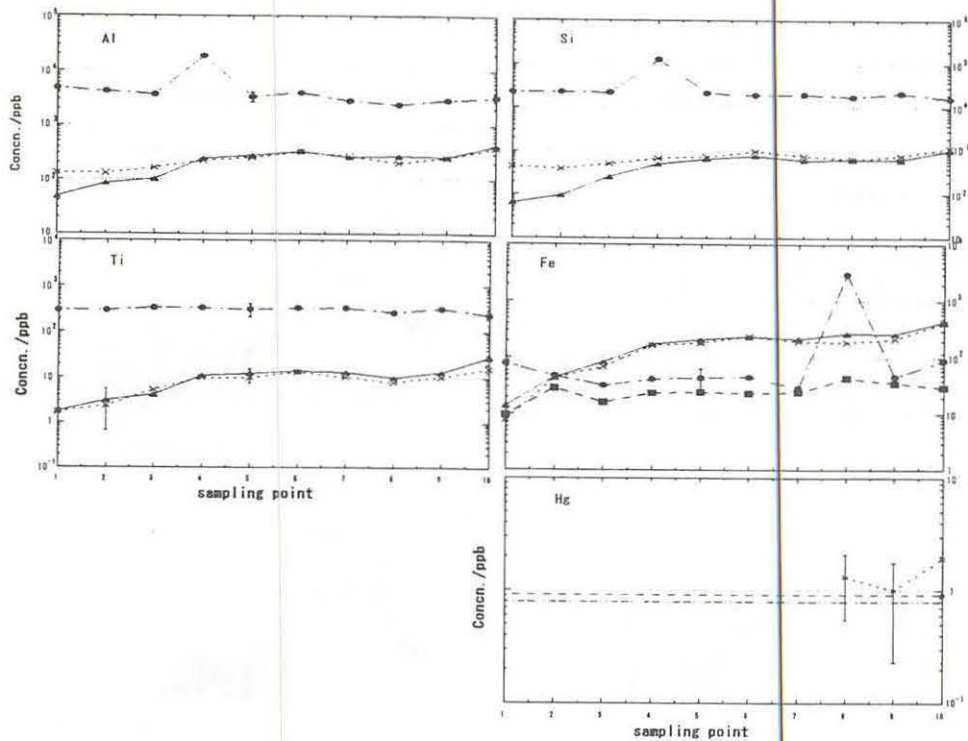


Fig. 4-1. Comparison of analysis concentrations for hydrolyzed species on four kinds of targets over whole basin of the Hirose river. Targets, \blacktriangle :FILT (the fraction of coarse particulates); \bullet :DEP (the fraction of fine particulates and soluble species); \blacksquare :PRECON (the soluble fraction of heavy metals); \times :WP81 (elements collected on Whatman-P81 filter paper). Detection limit, ----- : FILT; - - - - : DEP, - . - . - . : WP81. The numbers of sampling point are the same as those in Table 1.

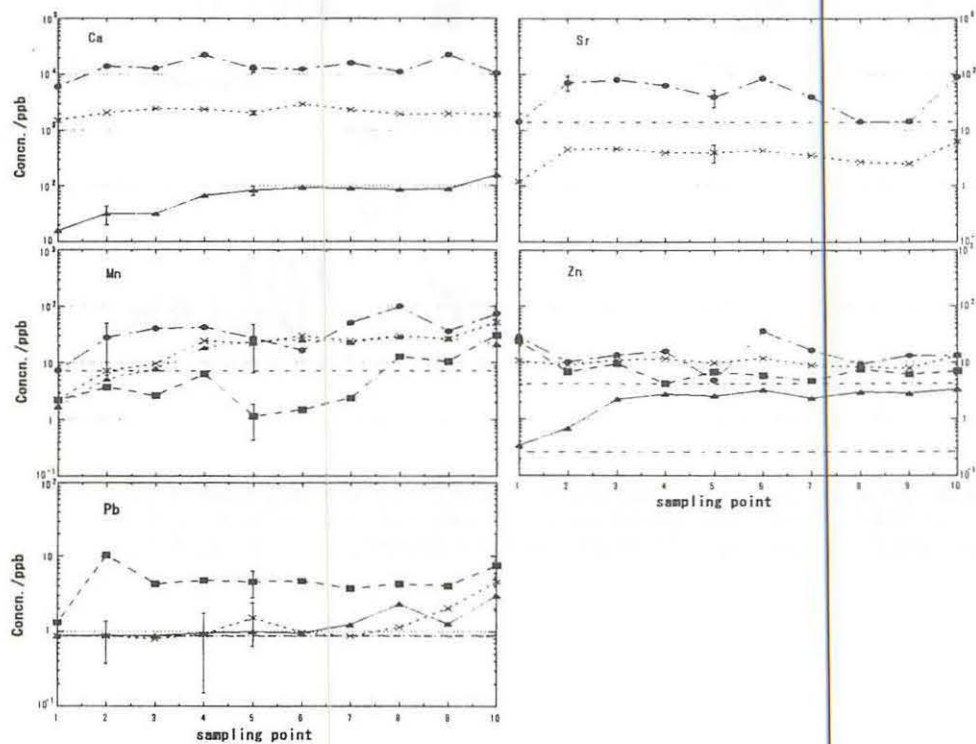
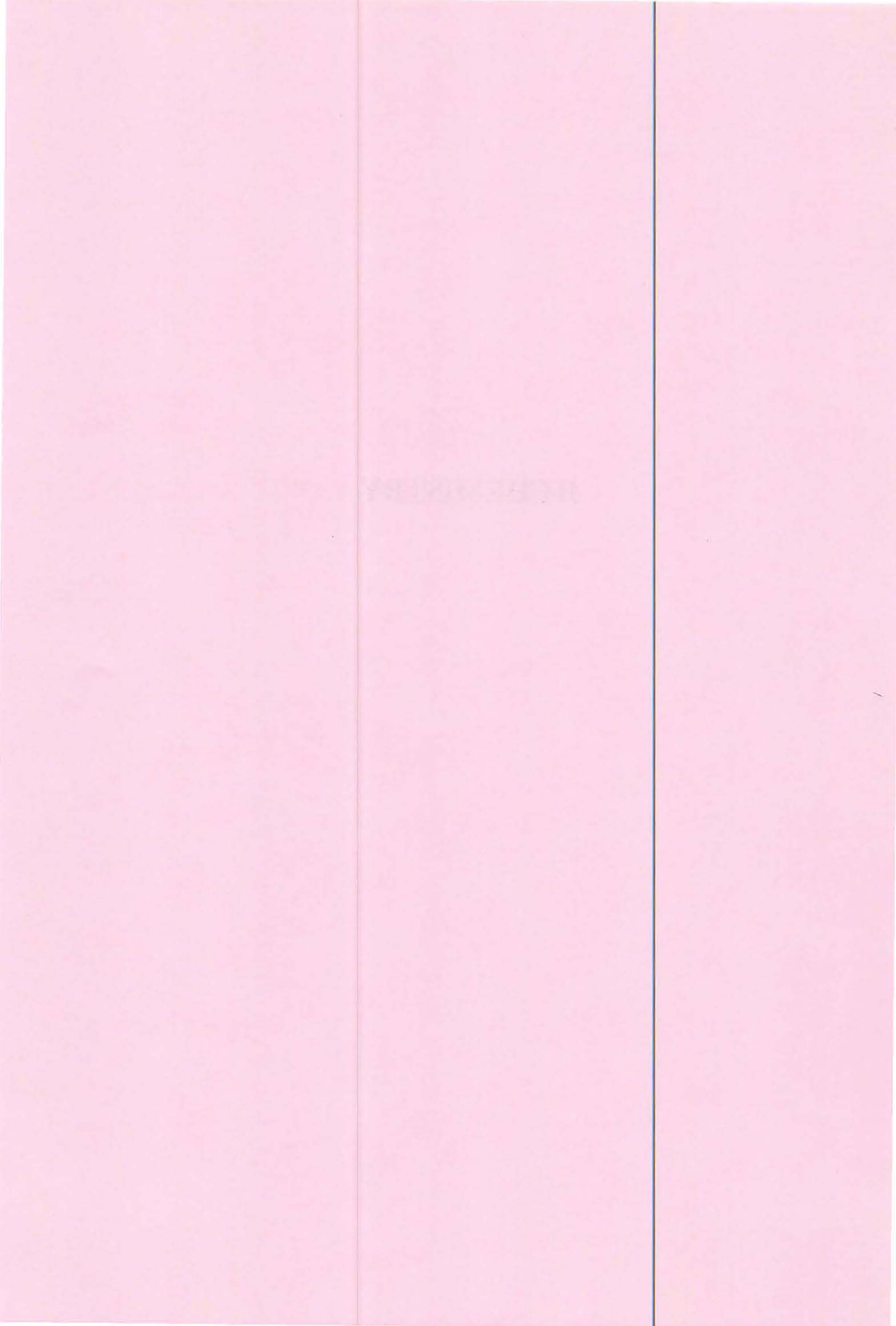


Fig. 4-2. Same as Fig.4-1 but for dissolved cationic species.

II CHEMISTRY



II. 1. Concentrations of Technetium-99 in Soils and Plants Collected in Forests within the 30-km Zone around Chernobyl Area

*Tagami, K., Uchida, S. and Sekine, T.**

*Environmental and Toxicological Sciences Research Group, National Institute of Radiological Sciences
Department of Chemistry, Graduate School of Science, Tohoku University**

INTRODUCTION

There have been many reports concerning radionuclides' concentrations in environmental samples due to the accident in Unit 4 of the Chernobyl Nuclear Power Station (CNPS). Some reports have shown ^{99}Mo concentrations in environmental samples¹⁻⁶. This radioisotope decays to ^{99}Tc [^{99}Mo ($t_{1/2}$: 65.9 h) \rightarrow $^{99\text{m}}\text{Tc}$ ($t_{1/2}$: 6.0 h) \rightarrow ^{99}Tc], but the amount may be negligible compared to the deposited ^{99}Tc released directly into the atmosphere with other radionuclides at the time of the accident. Because ^{99}Tc has a high fission yield of about 6% and a long half-life of 2.1×10^5 y and it has a high mobility in biogeochemical cycles; indeed, having the highest transfer factor (TF) in soil-to-plant system among non-nutrient elements^{7,8}) makes Tc peculiar. Thus, a survey of the contamination levels in environmental samples is of interest to estimate the long-term ^{99}Tc exposure to humans. At present, however, there are almost no data on ^{99}Tc contamination of environmental samples and consequently, limited information on the ^{99}Tc activity released by the Chernobyl accident is available⁹.

In this study, ^{99}Tc contents in soil and plant samples collected in three forest sites in 1994 and 1995 around the Chernobyl area were determined to obtain TFs of Tc under the natural environment.

Experimental

Soil and plant samples

Soil and plant samples were collected in three forests around Chernobyl: Forests D1 and D3 were 28.5 km and 26 km to the south of the Chernobyl Reactor, while forest K2 was 6 km to the southeast of the Reactor. Surface organic soil layers collected at each site

were mixed for ^{99}Tc measurement. The leaves of forest strawberry, *Fragaria vesca*, and ferns were collected from the sites. Lux *et al.*¹⁰⁾ reported that the highest radiocaesium activities were measured in the leaves of understorey vegetation collected at those forests.

Reagents

Nitric acid used was ultra pure grade (Tama Chemicals, AA-100). A Tc-selective chromatographic resin (EIChroM Industries Inc., TEVA resin) was used for Tc purification. Deionized water (>17 M Ω) was used throughout the work. Technetium-95m, which was obtained from Nb foils using the reaction $^{93}\text{Nb} (\alpha, 2n) ^{95\text{m}}\text{Tc}$, was applied to determine the recovery of ^{99}Tc in the samples during the chemical separation procedure. In our previous work, it was found that this reaction could not produce other long-lived Tc isotopes¹¹⁾.

Chemical separation

From soil samples, Tc was volatilized and trapped in a combustion apparatus. Then, Tc in each solution obtained was purified by TEVA resin column. The details of this method are referred to in the references^{12,13)}. For plant samples, a wet digestion method in combination with the resin was adopted. About 2 to 10 g of leaf samples were used for the analysis. The scheme is as follows: The sample was oven-dried at 110°C and milled well. It was incinerated at 450°C in an electrical oven for 2 h to decompose organic matter. Tc in the samples was extracted with 4 M HNO₃ during heating at 140°C. The acidity of the solution was adjusted to *ca.* 0.1 M HNO₃, then, introduced into a TEVA resin column for Tc purification. The extracted Tc was adjusted to 2% HNO₃ solution for a 9-min measurement by ICP-MS.

Instruments

Radiochemical recoveries of Tc in soil and plant samples were obtained with the $^{95\text{m}}\text{Tc}$ activity using a NaI (TI) scintillation counter (Aloka, ARC-380). Then the solution was introduced into an ICP-MS (Yokogawa, PMS-2000) to measure. The detection limit of ^{99}Tc by ICP-MS under our operation conditions was 0.05 ppt (0.03 mBq/mL). The activities of ^{137}Cs in the samples were measured with a Ge detector (Seiko EG&G Ortec) coupled with a multi channel analyzer (Seiko EG&G, Model 7800).

RESULTS AND DISCUSSION

Technetium-99 in soil samples

Total recoveries of ^{99m}Tc during the chemical separation process ranged from 70 to 93% for soil samples. Table 1 shows the results of ^{99}Tc concentrations ranged from 1.1 to 9.8 Bq/kg-dry for organic layers and from 0.13 to 0.83 Bq/kg-dry for mineral layers. High concentrations of ^{99}Tc were found in the K2 samples. The concentrations of ^{99}Tc in the D1 and D3 samples, which ranged from 1.1 to 2.4 Bq, are five to ten times as low as those in the K2. However, the ^{99}Tc activities in the D1 and D3 samples were one or two orders of magnitude higher than in other areas which were less affected by the accident¹⁴. It is clear that some of ^{99}Tc deposited on the surface still remained in the surface soil, although these samples were collected 8 to 9 years after the accident. However, some ^{99}Tc and ^{137}Cs might have already leached from the surface to a deep soil layer. The migration rates of ^{99}Tc and ^{137}Cs in soils were affected by several conditions such as sorption characteristics of the soils, chemical forms, and soil types.

Technetium-99 in plant samples

Table 2 shows the concentration of ^{99}Tc in strawberry leaves and ferns. The recovery of Tc ranged from 60 % to 87 %. It is interesting that one sample collected at D3 was hard to determine, because of its low concentration. Another sample collected at the same site also showed a low concentration level of 0.2 Bq kg⁻¹. D1 and K2 are so-called dry forests, whereas D3 can be characterized as wet forest, since the groundwater level at this site is at about 45 cm depth from the surface¹⁰. Under wet conditions, it was thought that the chemical form of Tc in soil would be changed to insoluble one such as TcO_2 ¹⁵. It is assumed that insoluble form of Tc strongly sorbed on soil and was hardly taken up by plants through roots.

Technetium Transfer factors from soil to plant

The uptake of a nuclide by a vegetable from soil is normally described by the TF which is defined as the ratio of the concentration of the nuclide in edible part of the vegetable to that in the soil (in Bq kg⁻¹ dry weight vegetable to Bq kg⁻¹ dry weight soil). Many Tc-TFs have been reported, for example, the expected TF values for grass and spinach are 7.6×10^1 and 2.6×10^3 , respectively¹⁶. Comparing with the Cs-TF, the Tc-TF is about three to five orders of magnitude higher than the Cs-TF. For this reason, ^{99}Tc is one of

the very important radionuclides for the assessment of internal dose by ingestion of the contaminated vegetables. However, attention should be paid to the fact that most of the TF values of Tc reported were obtained by tracer experiments in which the radionuclide was applied to soil in a soluble form, TcO_4^- . Because the chemical forms of Tc are variable under natural conditions, it is necessary to obtain the TF values in the field.

The Cs-TFs obtained (data are not shown) are almost the same values as previously reported, while the Tc-TFs are two or three orders of magnitude lower than reported ones obtained under laboratory conditions^{17,18)}. The TFs for Tc obtained are also listed in Table 3. The calculated Tf based on the ⁹⁹Tc contents of the organic layers and the mineral layers ranged 0.09 - 0.41 and 0.5 - 3.4, respectively. The Tc-TFs obtained in this study are similar to those obtained by Green *et al.*¹⁹⁾ under semi-natural conditions. However, the data are limited, and further investigation will be required.

References

- 1) Devell, L., Tovedal, H., Bergström, U., Appelgren, A., Chyessler, J. and Andersson, L. (1986) *Nature* **321**, 192-193.
- 2) Whitehead, N. E., Ballestra, S., Holm, E. and Walton, A. (1988) *J. Environ. Radioact.* **7**, 249-264.
- 3) Ferrero, J. L., Jordá, M. L., Milió, J., Monforte, L., Moreno, A., Navarro, E., Senent, F., Soriano, A., Baeza, A., del Rfo, M. and Miró, C. (1987) *Health Phys.* **53**, 519-524.
- 4) Denschlag, H. O., Diel, A., Glaesel, K. H., Heimann, R., Kaffrell, N., Krütz, U., Menke, H., Trautmann, N. and Herrmann, G. (1987) *Radiochim. Acta* **41**, 163-172.
- 5) Hötzl, H., Rosner, G. and Winkler, R. (1987) *Radiochim. Acta* **41**, 181-190.
- 6) Winkelmann, I., Endrulat, H. J., Fouasnon, S., Gesewsky, P., Haubelt, R., Klopfer, P., Köhler, H., Kohl, R., Kucheida, D., Leising, C., Müller, M. K., Neumann, P., Schmidt, H., Vogl, K., Weimer, S., Wildermuth, H., Winkler, S., Wirth, E., Wolff, S. (1987) *Institute for Radiation Hygiene, German Federal Office of Radiation Protection, ISH Report 116*, 1987.
- 7) Wildung, R.E., Garland, T.R. and Cataldo, D.A. (1977) *Health Phys.* **32**, 314-317.
- 8) Hoffman, F.O., Garten, Jr., C.T., Huckabee, J.W. and Lucas, D.M. (1982) *J. Environ. Qual.* **11**, 134-141.
- 9) Uchida, S. and Tagami, K. (1999) *J. Radioanal. Nucl. Chem.* **240**, 357-359.
- 10) Lux, D., Kammerer, L., Rühm, W. and Wirth, E., (1995) *Sci. Total Environ.* **173/174**, 375-384.
- 11) Sekine, T., Konishi, M., Kudo, H., Tagami, K. and Uchida, S., (1999) *J. Radioanal. Nucl. Chem.* **239**, 483-487.
- 12) Uchida, S. and Tagami, K. (1997) *J. Radioanal. Nucl. Chem.* **221**, 35-39.
- 13) Tagami, K. and Uchida, S. (1999) *Radioactiv. Radiochem.* **10**, 30-34.
- 14) Tagami, K. and Uchida, S. (1997) *Environ. Polut.* **95**, 151-154.
- 15) Tagami, K. and Uchida, S. (1996) *Toxicol. Environ. Chem.* **56**, 235-247.
- 16) International Atomic Energy Agency (1994) *Handbook of Parameter Values for the Prediction of Radionuclide Transfer in Temperate Environments*, Technical Reports Series No. 364; International Atomic Energy Agency; Vienna, pp 14-26.
- 17) Landa, E.R., Thorvig, L. H. and Gast, R.G. (1977) In *Biological Implications of Metals in the Environment* (CONF-750929), pp. 390-401.
- 18) Gast, R.G., Thorvig, L. H. and Landa, E. R. (1978) In *Environmental chemistry and Cycling Process* (CONF-760429), pp. 550-567.
- 19) Green, N., Wilkins, B. T., Davidson, M. F. and Hammond, D. J. (1995) *J. Environ., Radioact.* **27**, 35-47.

Table 1. Concentrations of ^{99}Tc and ^{137}Cs in Bq/kg on a dry weight basis and activity ratios of ^{99}Tc to ^{137}Cs on 26 April 1986, in soil samples collected in the 30-km zone around Chernobyl.

Sampling site		^{99}Tc Bq/kg-dry	^{137}Cs (1986.4.26) kBq/kg-dry	Activity Ratio $^{99}\text{Tc}/^{137}\text{Cs} \times 10^{-4}$
K2 (6km)	Organic Layer	9.8 ± 0.33	190 ± 5.5	0.50
	Mineral Layer	0.83 ± 0.018	8.8 ± 0.11	0.95
D3 (26km)	Organic Layer	2.1 ± 0.65	20 ± 0.63	1.1
	Mineral Layer	0.36 ± 0.006	1.4 ± 0.021	2.6
D1 (28.5km)	Organic Layer	1.1 ± 0.024	15 ± 0.23	0.75
	Mineral Layer	0.13 ± 0.003	0.64 ± 0.017	2.1
IAEA-375 (ca.180km)		5.9	0.25 ± 0.02	5.9

Table 2. Concentrations of ^{99}Tc and ^{137}Cs in Bq/kg on a dry weight basis and activity ratios of ^{99}Tc to ^{137}Cs on 26 April 1986, in plant samples collected in the 30-km zone around Chernobyl.

Sampling site		^{99}Tc Bq/kg-dry	^{137}Cs (1986.4.26) kBq/kg-dry	Activity Ratio $^{99}\text{Tc}/^{137}\text{Cs} \times 10^{-4}$
K2 (6km)	Berry	1.6 ± 0.16	14 ± 0.073	1.1
	Fern	2.3 ± 0.26	500 ± 0.45	0.046
D3 (26km)	Berry	not detected	9 ± 0.095	
	Fern	0.19 ± 0.029	40 ± 0.12	0.047
D1 (28.5km)	Berry	0.45 ± 0.09	1.3 ± 0.03	3.6

Table 3. Measured transfer factors for ^{99}Tc in the 30-km zone around Chernobyl.

Sampling site		Organic Layer	Mineral Layer
K2	Berry	0.16 ± 0.02	1.9 ± 0.2
	Fern	0.24 ± 0.03	2.8 ± 0.3
D3	Fern	0.09 ± 0.01	0.53 ± 0.08
D1	Berry	0.41 ± 0.08	3.4 ± 0.7

II. 2. A Simple On-column Preparation of [¹⁸F]Fluorocholeline from [¹⁸F]Fluoromethyl Triflate

Iwata R. *,** Furumoto S. **, Pascali C. ***, Bogni A. ***, Terasaki K. ****, Yanai K. *****

Graduate School of Engineering, Tohoku University*,
 CYRIC Tohoku University**,
 National Cancer Institute, Milan, Italy***,
 Iwate Medical University****,
 Graduate School of Medicine, Tohoku University*****

The successful application of [¹¹C]choline to tumor imaging by PET¹ has been promoting the development of ¹⁸F-labeled choline analogues as a longer-lived imaging agent. The preparations of ¹⁸F-labeled fluoromethyl, fluoroethyl and fluoropropyl derivatives from corresponding ¹⁸F-fluoroalkylating agents have been reported to date²⁻⁵). Among them ¹⁸F-fluoromethylated choline analogue ([¹⁸F]fluorocholeline, see Fig. 1) is expected to be the most promising agent for measuring the phosphorylation rate in cancer cells³).

The method for the radiosynthesis of [¹⁸F]fluorocholeline is based on the conventional reaction in a glass vessel where [¹⁸F]fluoromethyl bromide is first trapped by a reaction solvent and then it is heated to carry out [¹⁸F]fluoromethylation on *N,N*-dimethylaminoethanol²). On the other hand, our approach to the automated synthesis of PET radiopharmaceuticals, especially from [¹¹C]methyl iodide and [¹¹C]methyl triflate, is based on a simple on-column method using a short column where the flowing labeling agent is efficiently trapped and the reaction takes place at the same time without heating. It was exemplified by the [¹¹C]choline synthesis using disposable solid-phase extraction (SPE) cartridges⁶). We have recently succeeded in applying this on-column method to the preparation of [¹⁸F]fluorocholeline.

[¹⁸F]Fluoromethyl triflate, a novel labeling agent, was prepared from [¹⁸F]fluoromethyl bromide by passing through a AgOTf column heated at 200°C (see Fig. 1 and 2). The latter labeling agent was prepared by the K.222-supported substitution of [¹⁸F]fluoride with CH₂Br₂ and distilled from a reaction vessel with a He flow (100

mL/min)⁷⁾. It was then passed through 4 Sep-Pak Plus silica cartridges (Waters) to separate it from the volatile starting material, CH₂Br₂, which inevitably contaminated the He for carrying [¹⁸F]fluoromethyl bromide from a reaction vessel. [¹⁸F]Fluoromethyl bromide was eluted roughly between 4 and 8 min after starting the distillation, while it took more than 10 min to elute CH₂Br₂ from the silica columns. The on-line conversion of [¹⁸F]fluoromethyl bromide to [¹⁸F]fluoromethyl triflate was almost quantitative. Overall decay-corrected radiochemical yields of [¹⁸F]fluoromethyl triflate were 47±8% based on [¹⁸F]fluoride.

The on-column preparation of [¹⁸F]fluorocholine from [¹⁸F]fluoromethyl triflate was carried out using the remotely operated system shown in Fig. 2. The flowing [¹⁸F]fluoromethyl triflate was passed through two connected SPE columns, a Sep-Pak Plus C18 cartridge retaining *N,N*-dimethylaminoethanol (0.1-0.5 mL) and a Sep-Pak Plus Accell CM cartridge. They were then washed with ethanol (10 mL) and water (10 mL) to completely elute the precursor. [¹⁸F]Fluorocholine was eluted from the Accell CM with saline (5 mL). [¹⁸F]Fluoromethyl bromide was also passed through the Sep-Pak cartridges to compare the reactivity of the labeling agents.

[¹⁸F]Fluorocholine was prepared from [¹⁸F]fluoromethyl triflate in radiochemical yields of over 80% (decay-corrected) with 0.2 mL of the precursor loaded on the C18 cartridge, whereas it was obtained from [¹⁸F]fluoromethyl bromide in less than 10%, although this low yield was observed to be twice improved by decreasing the He flow rate down to 30 mL/min. Thus, it is demonstrated that [¹⁸F]fluoromethyl triflate has higher reactivity than [¹⁸F]fluoromethyl bromide and provides a simple on-column preparation of [¹⁸F]fluorocholine suitable for routine clinical use.

[¹⁸F]Fluorocholine was prepared from [¹⁸F]fluoride via [¹⁸F]fluoromethyl triflate in overall decay-corrected yields of 40% within 30 min.

References

- 1) Hara T., Kosaka N., Shioura N., Kondo T., J. Nucl. Med. **38** (1997) 842.
- 2) DeGrado T. R., Coleman R. E., Wang S., Baldwin S. W., Orr M. D., Robertson C. N., Polascik T. J., Price D. T., Cancer Res. **61** (2000) 110.
- 3) DeGrado T. R., Baldwin S. W., Wang S., Orr M. D., Liao R. P., Friedman H. S., Reiman R., Price D. T., Coleman R. E., J. Nucl. Med. **42** (2001) 1805.
- 4) DeGrado T. R., Reiman R., Price D. T., Wang S., Coleman R. E., J. Nucl. Med. **43** (2002) 92.
- 5) Hara T., Kosaka N., Kishi H., J. Nucl. Med. **43** (2002) 187.
- 6) Pascali C., Bogno A., Iwata R., Cambie M., Bombardieri E., J. Label. Comp. Radiopharm. **43** (2000) 195.
- 7) Bergman J., Eskola O., Lehtikoinen P., Solin O., Appl. Radiat. Isot. **54** (2001) 927.

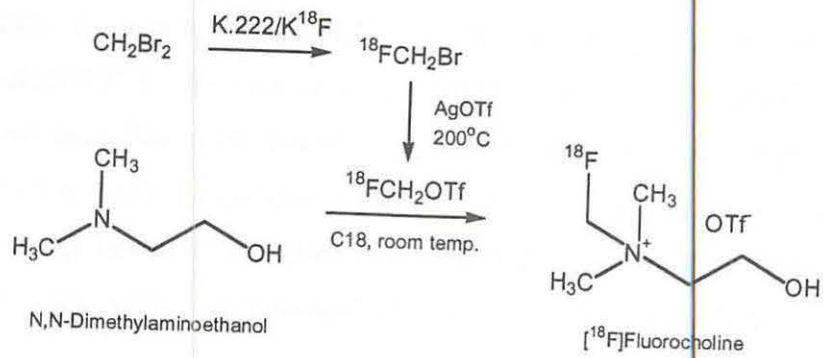


Fig. 1. A synthetic scheme of [¹⁸F]fluorocholine from [¹⁸F]fluoride.

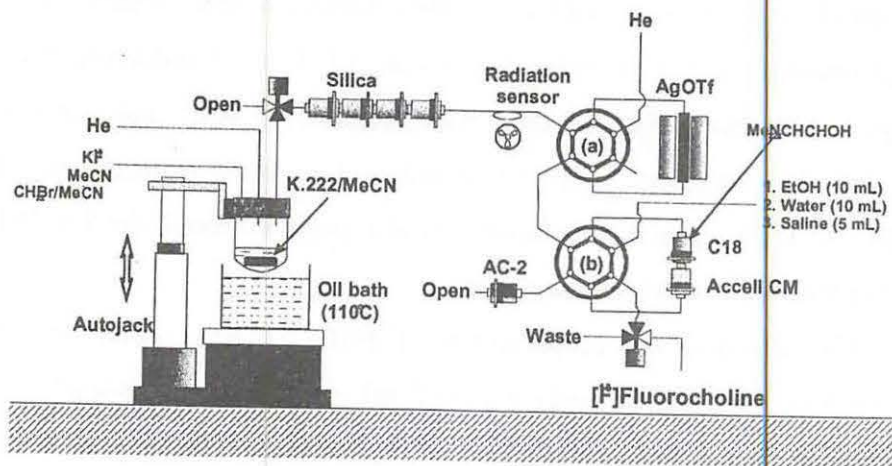
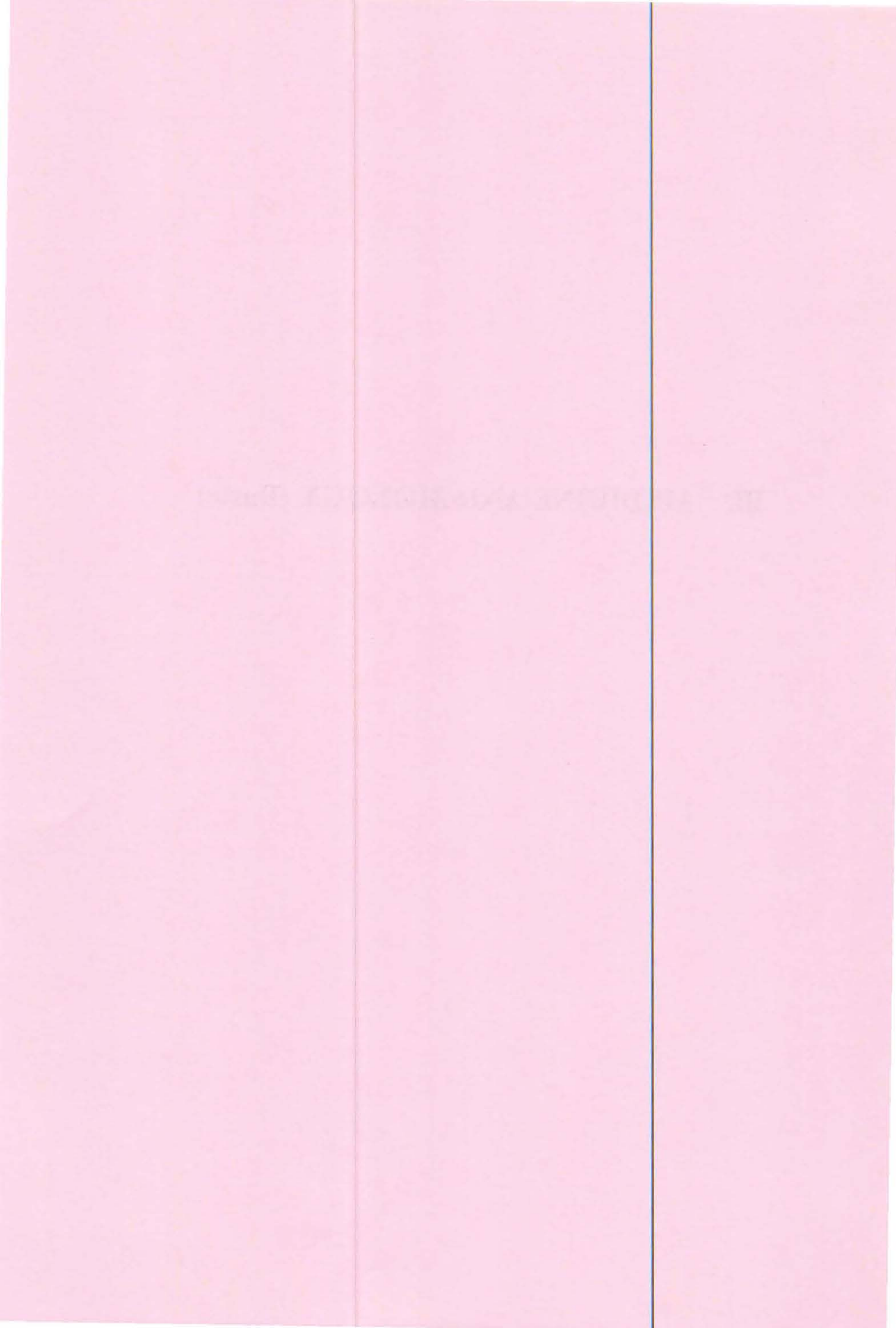


Fig. 2. A flowchart of the system for the preparation of [¹⁸F]fluorocholine.

III. MEDICINE AND BIOLOGY (Basic)



III. 1. Development of ^{18}F -Labeled Matrix Metalloproteinase Inhibitors for Tumor Imaging by PET

*Furumoto S.***, Iwata R.*, Kubota K.**, Fukuda H.** and Ido T.**

Cyclotron and Radioisotope Center, Tohoku University
Institute of Development, Aging, and Cancer, Tohoku University***

Introduction

Matrix metalloproteinases (MMPs) are a family of zinc-containing endopeptidases involved in the extracellular matrix degradation. The mammalian MMP family is now known to include at least 20 enzymes and is categorized into several classes based on substrate specificity and domain structure. Among the sub-families of MMPs, gelatinases (MMP-2 and MMP-9) have become attractive targets for research on cancer and development of anticancer drugs¹. MMPs have been closely involved in the invasion, metastasis, and angiogenesis that are crucial for the progression of malignant tumors². Moreover, increased expressions and activities of gelatinases, especially MMP-2, have been observed in a variety of human cancer³. Thus, estimating MMP activities *in vivo* is thought to contribute to diagnosis of the tumor invasiveness and to clinical evaluation of the efficacy of MMP inhibitors. For these reasons, we believe that MMP inhibitors labeled with a positron emitter should become a unique type of tracer that might be clinically beneficial for predicting cancer invasion and cancer therapy with anticancer drugs targeting MMPs through the use of positron emission tomography (PET).

Considerable effort has been devoted to the development of potent MMP inhibitors and numerous inhibitors are reported in the literature⁴. Current focus in the field of MMP inhibitor development is directed towards the synthesis of selective inhibitors. For examples, Warner-Lambert, Shionogi, and Bayer have reported gelatinase selective inhibitors which contain a carboxylic acid group and a linear side chain (Fig. 1). Based on these structural features of the selective inhibitors, we began our research to develop a novel PET tracer targeting MMP-2⁵. The design and radiosynthesis of the new MMP inhibitors selective for gelatinases are reported here.

Results and Discussion

Design strategy for ¹⁸F-labeled MMP-2 inhibitor

Compounds A-C were used as references for the design of ¹⁸F-labeled MMP inhibitors. The essential structural features of the reference inhibitors are the carboxylic acid group (zinc binding group; ZBG) and the linear side chain (R₁). Thus, carboxylic acid-based ¹⁸F-labeled MMP-2 inhibitors with a linear side chain was designed (Fig. 2).

Precursor synthesis

The precursors (**5a-c**) were synthesized from the commercially available D-form of methionine, tryptophan, and valine, respectively, as shown in Scheme 1. Protection of the carboxyl group was carried out in methanol under reflux with *p*-toluenesulfonic acid and *p*-toluenesulfonyl chloride. Then, the obtained methyl esters (**2a-c**) were coupled with 4-iodobenzenesulfonyl chlorides. Utilizing the reaction conditions developed by Sonogashira, the iodophenylsulfonamides (**3a-c**) were coupled with 5-hexyn-1-ol to yield the desired alkynyl phenylsulfonamides (**4a-c**) in good yield. Conversion of the hydroxyl group to the tosylate completed the precursor **5a-c** synthesis.

Radiosynthesis of [¹⁸F]MMP inhibitors

The gelatinase inhibitors labeled with fluorine-18 (**1a-c**) were easily prepared via a one-pot synthesis outlined in Scheme 2. The one-pot synthesis, radiofluorination (12 min) and deprotection (6-12 min), was done in the same vial with heating at 110°C using an oil bath. The initial fluorination of the precursor was performed by nucleophilic displacement with [¹⁸F]fluoride in the presence of potassium carbonate and Kryptofix 2.2.2. After fluorination, basic hydrolysis of the methyl ester group of **6a-c** was carried out by adding 2*N* NaOH to the reaction solution. Under these conditions the total radiosynthesis times were about 60-70 min including the preparative HPLC separation. The average of the overall radiosynthesis yields of **1a-c** were 43%, 13%, and 33%, respectively (n=5-7, decay corrected).

After purification of **1a-c** their radiochemical purities were evaluated by analytical reverse phase HPLC. The purities of **1b** and **1c** stored in preparative HPLC mobile phase remained 99% or more for at least 2 hours. On analysis of **1a**, however, a radiochemical impurity which increased gradually with time was observed, suggesting chemical decomposition of **1a**. The chemical instability of **1a** would make it unsuitable as a PET tracer even though it was synthesized in the best radiochemical yield among the three types

of tracer.

In conclusion, We have designed and synthesized a new type of PET tracer for cancer imaging, carboxylic acid-based MMP inhibitors labeled with fluorine-18. Fluorine-18 labeled compounds (**1a-c**) were synthesized from the precursors by a simple one-pot preparation and purified by HPLC. **1a** was prepared in the best total radiochemical yield, but turned out to be unstable chemically and thus unsuitable for use to biological studies. Among three compounds, **1c** is undergoing biological evaluation as a prospective candidate for cancer tumor imaging agent by PET.

References

- 1) Cawston T. E., *Pharmacol. Ther.* **70** (1996) 163-182.
- 2) Liotta L. A., Tryggvaason K., *et al.*, *Nature* **284** (1980) 67-68.
- 3) Curran S., Murray G.I., *J. Pathol.* **189** (1999) 300-308.
- 4) Whittaker M., Floyd C.D., *et al.*, *Chem. Rev.* **99** (1999) 2735-2776.
- 5) Furumoto S., Iwata R., *et al.*, *J. Labeled Cpd. Radiopharm.* *in press*.

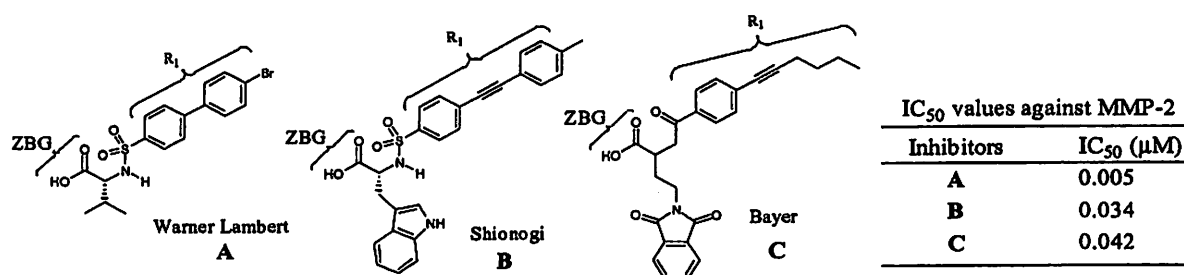


Fig. 1. Selective MMP inhibitors especially for gelatinases. ZBG: Zinc binding group.

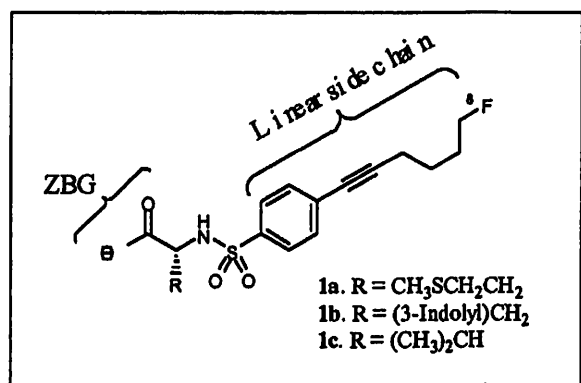
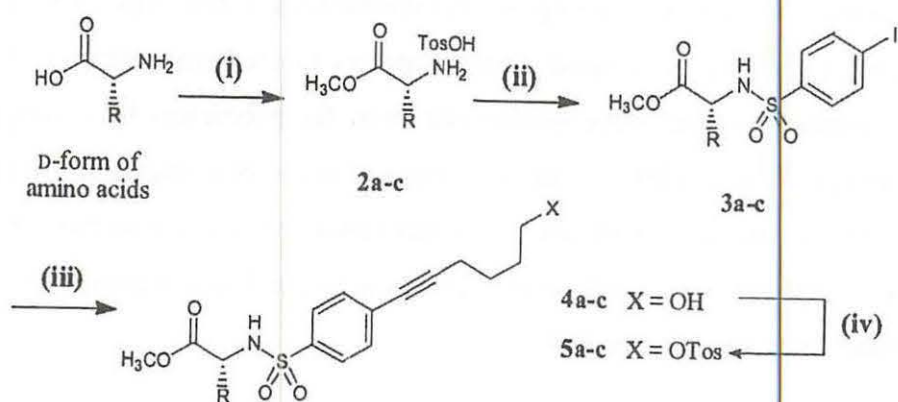
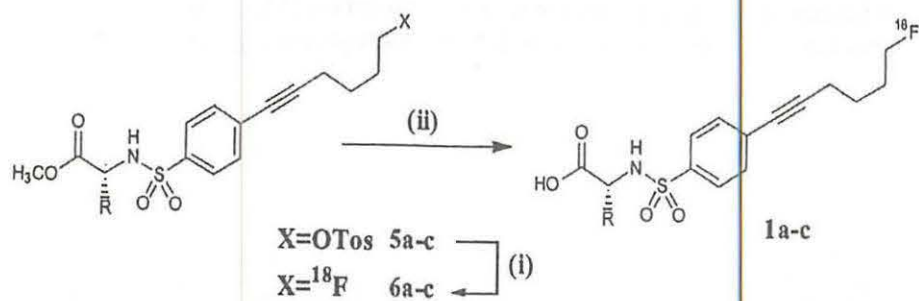


Fig. 2. New radiopharmaceuticals designed for gelatinase inhibition.



Scheme 1. Precursor synthesis of the newly designed MMP inhibitors from the D-form of various amino acids. (i) TosCl, TosOH, MeOH, reflux; (ii) 4-Iodobenzenesulfonyl chloride, NMM, CHCl_3 ; (iii) 5-hexyne-1-ol, $\text{Pd}(\text{PPh}_3)_2\text{Cl}_2$, CuI, TEA, DMF; (iv) TosCl, NMM, CHCl_3



Scheme 2. Radiosynthesis of **1a-c** by a one-pot procedure. (i) $[^{18}\text{F}]\text{KF}$, K_2CO_3 , Kryptofix 2.2.2, CH_3CN , reflux; (ii) aq. NaOH, then aq. HCl.

III. 2. Effect of Angiotensin-Converting Enzyme Inhibitor against MPTP Neurotoxicity in Mice : an Immunohistochemical Study

*Kurosaki R.**, Muramatsu Y.*, Watanabe H.*, Michimata M.*, Matsubara M.*,
Imai Y.*, Kimura S.** and Araki T.**

*Department of Clinical Pharmacology and Therapeutics, Tohoku University Graduate School of
Pharmaceutical Science and Medicine*
Department of Human Life Science, Graduate School of Showa Women's University***

INTRODUCTION

The neurotoxin 1-methyl-4-phenyl-1, 2, 3, 6-tetrahydropyridine (MPTP) is well known to produce a parkinsonian syndrome in both humans and rodents. Its neurotoxic effects also appear to involve energy depletion and free radical degeneration. MPTP is converted to its metabolite MPP⁺ (1-methyl-4-phenyl- pyridinium) by monoamine oxidase B. MPP⁺ is selectively accumulated by high affinity dopamine transporters (DAT) and taken up into the mitochondria of dopaminergic neurons, where it disrupts oxidative phosphorylation by inhibiting complex I of the mitochondrial electron transport chain¹⁾. This can lead to impairment of ATP production and free radical generation.

Angiotensin-converting enzyme (ACE) is widely distributed in the brain and is associated with neurons in the striatum. Interestingly, a previous study demonstrated that the ACE inhibitor perindopril can inhibit striatal ACE and produce a two- to threefold increase in dopamine content and release from the rat striatum²⁾. ACE inhibitors are widely used therapeutic agents in the treatment of hypertension and improved feelings of well-being following ACE inhibitor therapy^{3,4)}. A recent study demonstrated that the ACE inhibitor perindopril is effective in increasing striatal dopamine content in an animal model of Parkinson's disease⁵⁾.

However, the relationship between ACE inhibition and neuronal protection is still unclear. In the present study, therefore, we examined the protective effect of perindopril against cell damage caused by MPTP toxicity.

MATERIALS AND METHODS

Male C57BL/6 mice (22-28g) were used in this study. The mice were injected intraperitoneally (i.p.) with four administrations of MPTP (10 mg/kg) at 1 hour intervals, the total dose per mice being 40 mg/kg, as described previously^{6,7)}. The mice were sacrificed by cervical dislocation at 3 or 7 days after MPTP treatment. After cervical decapitation, the striata were rapidly dissected out and dopamine, 4-dihydroxyphenylacetic acid (DOPAC) and homovanillic acid (HVA) were quantified by HPLC-ECD (Eicom, Kyoto, Japan) as described previously^{6,7)}.

To examine the effects of perindopril, the animals injected i.p. with perindopril or saline 30 min before and 90 min after the first administration of MPTP. Perindopril was generously provided by Daiichi Pharmaceutical Co. Ltd. (Tokyo, Japan).

For immunohistochemical study, the mice were anesthetized with sodium pentobarbital (50 mg/kg, i.p.) at 3 days and 7 days after MPTP treatment. The brains were removed 1 hour after perfusion-fixation at 4°C and were immersed in the same fixative until they were embedded in paraffin. Paraffin sections, 5µm in thickness, of the striatum and substantia nigra were used for immunohistochemistry. For DAT, glial fibrillary acidic protein (GFAP) and Cu/Zn-superoxide dismutase (Cu/Zn-SOD) immunostainings, a rat anti-DAT polyclonal antibody (Alfa Diagnostic International, San Antonio, TX, USA), a mouse anti-GFAP monoclonal antibody (Chemicon International, Inc., Temecula, CA, USA), a mouse anti-Cu/Zn-SOD antibody (Biogenesis Ltd. UK), a Vectastain elite ABC kit (Vector Lab., Burlingame, USA) and M.O.M. immunodetection kit (Vector Labs. Burlingame, CA, USA) were used. The immunohistochemical stainings with anti-DAT antibody (1:200), anti-GFAP antibody (1:200) or anti-Cu/Zn-SOD antibody (1:100) were performed as described previously^{6,8)}.

RESULTS

The striatal dopamine, DOPAC and HVA levels were significantly decreased 3 and 7 days after MPTP treatment (Table 1). In contrast, perindopril prevented the reduction of the striatal dopamine, DOPAC and HVA content 3 days after MPTP treatment, as shown in Table 2.

Representative microphotographs of DAT immunostaining in the striatum and substantia nigra are shown in Fig. 1. In the striatum and substantia nigra, a marked decrease in the number of DAT-immunopositive fibers was observed 3 and 7 days after

MPTP treatment. In contrast, administration of perindopril prevented the decreases in number of striatal DAT-immunopositive fibers and nigral DAT-immunopositive neurons in mice 3 and 7 days after MPTP treatment.

Representative microphotographs of GFAP immunostaining in the striatum and substantia nigra are shown in Fig. 2. GFAP-immunopositive astrocytes were absent in the striatum of control mice. The number of GFAP-immunopositive astrocytes was increased slightly in the striatum 3 and 7 days after MPTP treatment. In the substantia nigra, however, GFAP-immunopositive astrocytes had a ramified form with many fine processes in control mice. The number of GFAP-immunopositive astrocytes in the substantia nigra marked increases 3 and 7 days after MPTP treatment. In contrast, the administration of perindopril prevented the increases in number of the GFAP-immunopositive astrocytes in mice 3 and 7 days after MPTP treatment.

Representative microphotographs of Cu/Zn-SOD immunostaining in the striatum and substantia nigra are shown in Fig. 3. The striatal neurons were stained intensely for Cu/Zn-SOD in control mice. Thereafter, the striatal glial cells were stained intensely 3 and 7 days after MPTP treatment. The nigral neurons were stained intensely in mice 3 days after MPTP treatment, as compared with control animals. Intense Cu/Zn-SOD immunopositive neurons and glial cells were found 7 days after MPTP treatment. In contrast, administration of perindopril reduced the intensity of Cu/Zn-SOD immunoreactivity in the glial cells 3 and 7 days after MPTP treatment.

DISCUSSION

The beneficial effects of ACE inhibitors suggest that renin-angiotensin system plays a key role in cardiac hypertrophy and hypertension⁹. A previous study demonstrated that the ACE inhibitor perindopril can prevent the significant reduction in striatal dopamine content in MPTP-treated mice⁵. However, the effects of ACE inhibitors against cell damage caused by MPTP or MPP⁺ toxicity are not yet understood.

The present study showed that perindopril dose-dependently can antagonize the MPTP-induced decrease in striatal dopamine, DOPAC and HVA levels of mice. The findings are, at least in part, consistent with the previous report⁵. These results suggested that ACE inhibitors may provide new therapeutic effect in Parkinson's disease.

Our immunohistochemical study showed that DAT immunoreactivity was decreased in the striatum and substantia nigra after MPTP treatment. Perindopril treatment showed a

protective effect against the severe reductions in levels of DAT immunoreactivity. These results seem to suggest that perindopril can protect the neuronal cells against the damage caused by MPTP. On the other hand, GFAP-immunopositive astrocytes were found in the striatum and substantia nigra of MPTP-treated mice. Marked increases in the number of GFAP-immunopositive astrocytes were noted after MPTP treatment. In contrast, the administration of perindopril prevented the increases in number of the GFAP-immunopositive astrocytes. These observations suggested that increases in number of GFAP-immunopositive astrocytes may reflect compensatory action against neuronal cell damage after MPTP treatment.

The cytotoxic hydroxyl radical has been implicated in dopamine neurotoxicity caused by MPTP and MPP^{+11,12)}. Oxidative stress may be involved in the pathogenesis of Parkinson's disease^{13,14)}. Cu/Zn-SOD is mainly located in cytoplasmic and nuclear compartments. This SOD is known to play a critical role in normal antioxidant defense. However, the alterations in the endogenous SOD activity after MPTP treatment are not fully understood. Furthermore, the interactions between ACE inhibitors and MPTP-induced free radical formation remain to be elucidated.

The present study showed that Cu/Zn-SOD immunoreactivity increased in the neurons and glial cells in the substantia nigra after MPTP treatment. Thereafter, intense Cu/Zn-SOD immunoreactivity was found dominantly in the glial cells 3 and 7 days after MPTP treatment. Based on our findings, the demand for SOD in neurons and glial cells should be greatly increased after MPTP treatment to quench the free radicals. Therefore, we speculated that free radicals produced by MPTP play a key role in the pathogenesis of neurodegeneration in conditions such as Parkinson's disease.

In the presents study, it was of interest that perindopril protected the expression of Cu/Zn-SOD immunoreactivity in the neurons and glial cells of the striatum and substantia nigra after MPTP treatment. These results suggested that the effect of parindopril against nigral cell loss and deficits in the striatal dopaminergic system may be mediated by a protective effect against the formation of free radicals produced by MPTP. The present findings were, at least in part, consistent with a previous report that the action of ACE inhibitor may involve an anti-free radical mechanism¹⁰⁾.

In conclusion, the present results showed that ACE inhibitor perindopril has a protective effect against MPTP-induced striatal dopamine and DOPAC depletion in mice. The protective effect may be caused by the reductions in the levels of free radicals caused

by MPTP. The present study also demonstrated that perindopril is effective against MPTP-induced neurodegeneration of the nigrostriatal dopaminergic pathway. Furthermore, our results provided the further evidence that free radical scavengers may be effective in the treatment of neurodegenerative diseases.

REFERENCES

- 1) Tipton K. F., & Singer T. P., *J. Neurochem.* **61** (1993) 1191-1206.
- 2) Jenkins T. A., Mendelsohn F. O. A., & Chai S. Y., *J. Neurochem.* **68** (1997) 1304-1311.
- 3) Zubenko G. S. & Nixon R. A., *Am. J. Psychiatry* **141** (1984) 110-111.
- 4) Croog S. H., Levins S., Testa M. et al., *N. Engl. J. Med.* **314** (1986) 1657-1664.
- 5) Jenkins T. A., Wong J. Y. F., Howells D.W. et al., *J. Neurochem.* **73** (1999) 214-219.
- 6) Araki T., Kumagai T., Tanaka K. et al., *Brain Res.* **918** (2001a) 176-181.
- 7) Araki T., Mikami T., Tanji H. et al., *Eur. J. Pharm. Sci.* **12** (2001b) 231-238.
- 8) Kurosaki R., Muramatsu Y., Michimata M. et al., *Neurol Res.* in press. 2002
- 9) Sadoshima, J & Izumo, S. *Cir. Res.* **73** (1993) 413-423.
- 10) Obata, T. *Eur. J. Pharmacol.* **378** (1999) 39-45.
- 11) Youdim, M. B. H., Ben-Shachar, D., & P. Riederer, P. *Acta Neurol. Scand.* **126** (1989) 47-54.
- 12) Chiueh, C. C., Miyake, H., & Peng, M. T. *Adv. Neurol.* **60** (1993) 251-258.
- 13) Hirsch, H., Graybiel, A. M., & Agid, Y. A. *Nature* **334** (1988) 345-348.
- 14) Gerlach, M., Ben-Schachar, D., Riederer, P., & Youdim, M. B. H. *J. Neurochem.* **63** (1994) 793-807.

Table 1. Striatal Concentrations of Dopamine, DOPAC and HVA in Mice after MPTP Treatment.

	Dopamine	DOPAC	HVA
	(μ g/g tissue)	(μ g/g tissue)	(μ g/g tissue)
Control	10.16 \pm 0.37	2.74 \pm 0.14	2.53 \pm 0.08
3 days	2.28 \pm 0.26**	1.76 \pm 0.29**	1.48 \pm 0.10**
7 days	5.67 \pm 0.56**	2.29 \pm 0.24**	2.24 \pm 0.09*

Data are given as means \pm S.D. The mice received four intraperitoneal injections of MPTP (10 mg/kg) at 1-hr intervals. For statistical analysis, one-way ANOVA with Dunnett's multiple comparison test was used (*p<0.05, **p<0.01 compared to control). n=5-11.

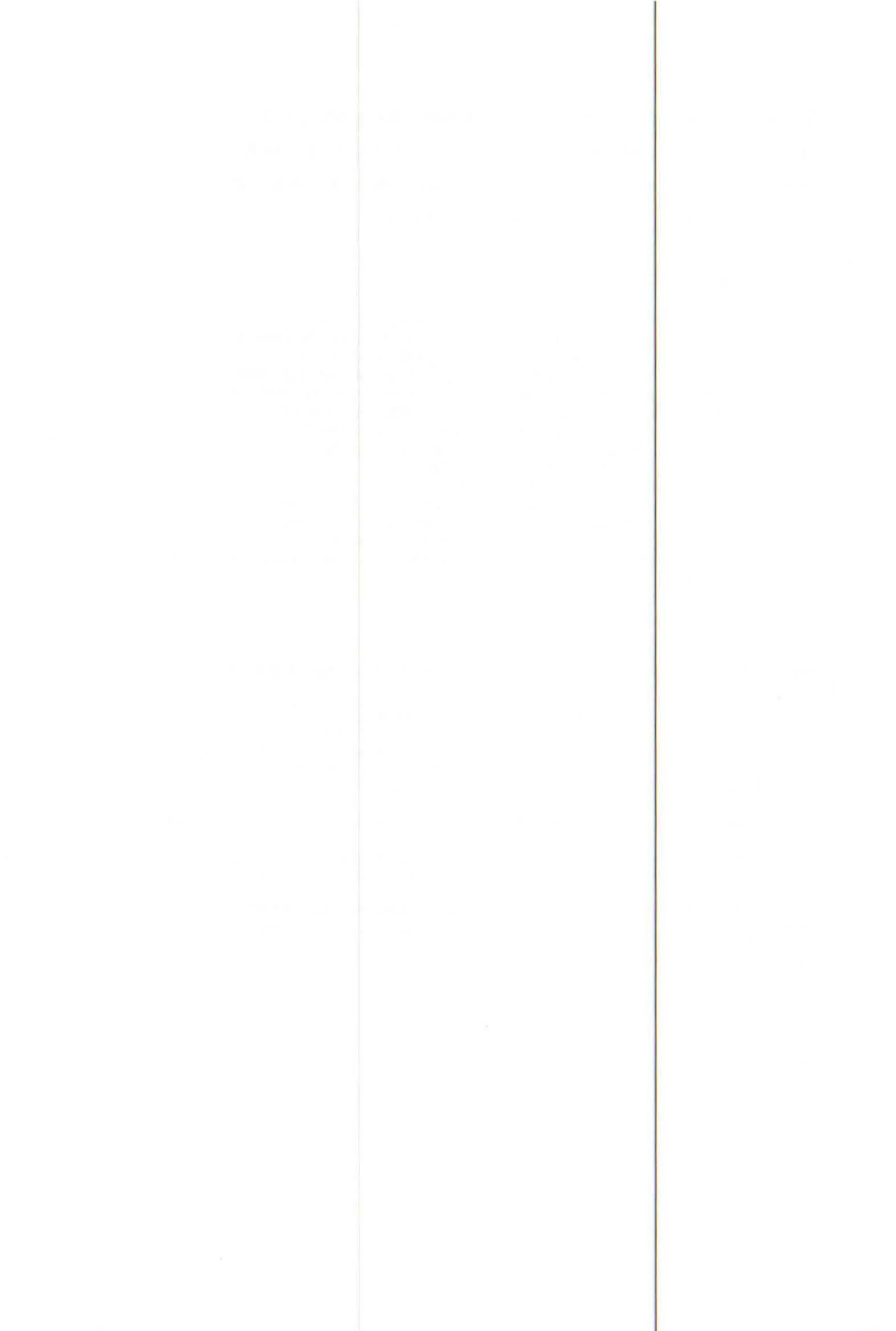


Table 2. Effects of Perindopril on the Striatal Dopamine, DOPAC and HVA Content in Mice 3 Days After MPTP Treatment.

	Dopamine	DOPAC	HVA
	(μ g/g tissue)	(μ g/g tissue)	(μ g/g tissue)
Vehicle (Saline)	13.15 \pm 1.82**	3.04 \pm 0.51**	1.60 \pm 0.38**
Perindopril(0.3mg/kg)	11.39 \pm 0.41**	3.39 \pm 0.41**	1.41 \pm 0.09**
MPTP + saline	2.49 \pm 1.65	0.73 \pm 0.45	0.42 \pm 0.22
MPTP+perindopril (0.3mg/kg)	9.26 \pm 1.03**	1.30 \pm 0.31**	0.88 \pm 0.08*

Data are given as means \pm S.D. The mice received four intraperitoneal injections of MPTP (10 mg/kg) at 1-hr intervals. Perindopril was injected intraperitoneally 30 min before and 90 min after the first administration of MPTP. For statistical analysis, one-way ANOVA with Dunnett's multiple comparison test was used (* p <0.05, ** p <0.01 compared to vehicle). n=5-8.

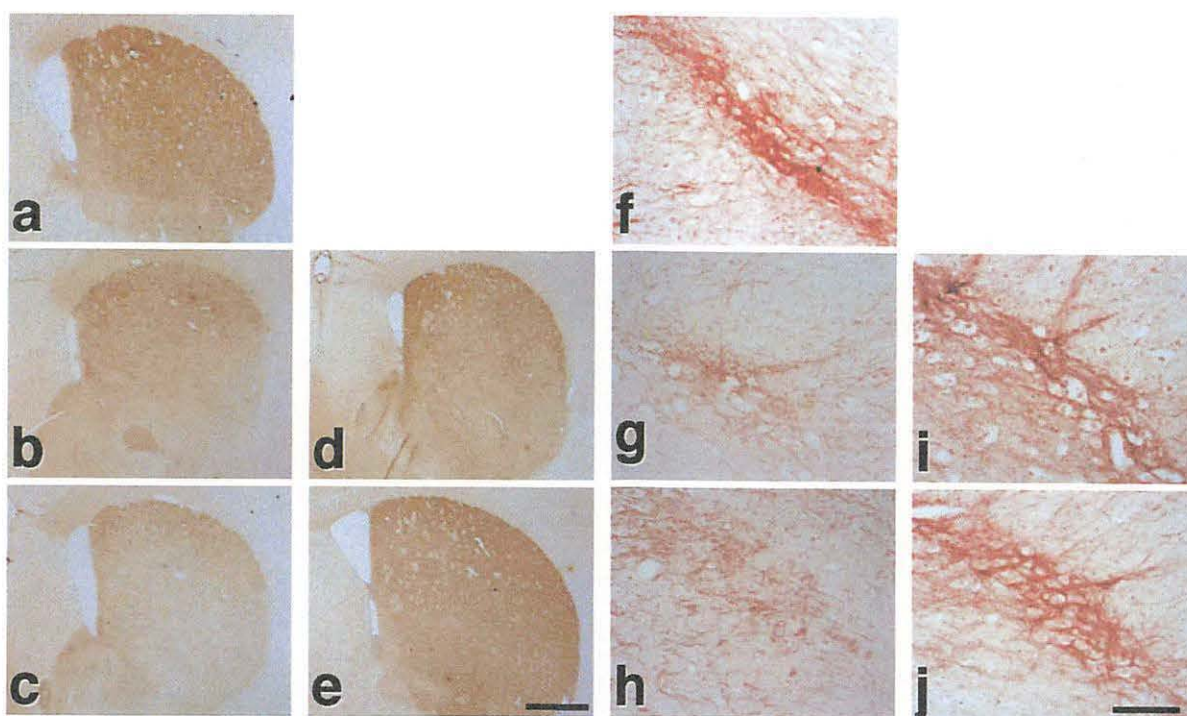
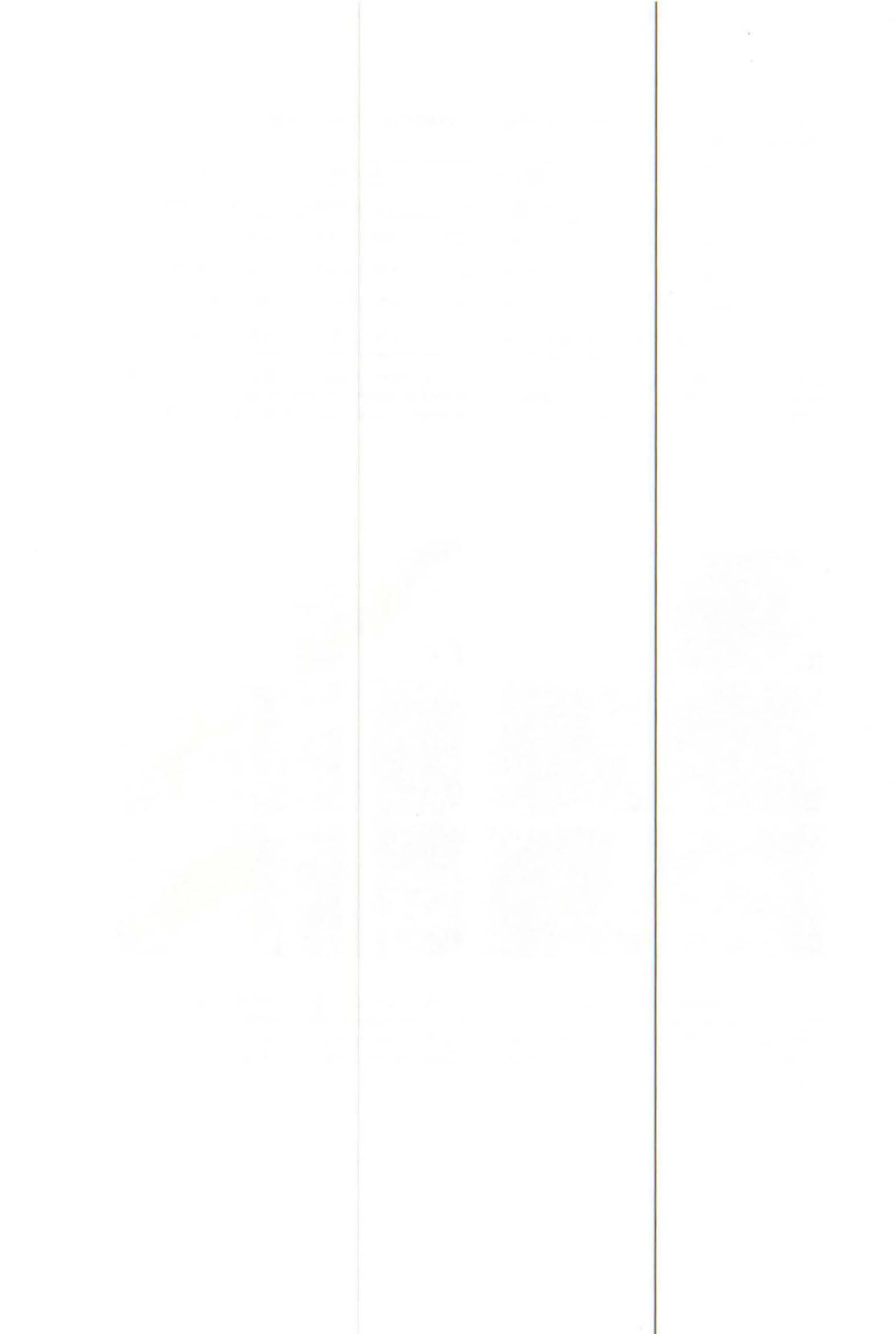


Fig. 1. Representative microphotographs of DAT immunostaining in the mouse striatum(a-e) and substantia nigra(f-j) after MPTP treatment. (a,f) : Control mice, (b,g) : 3 days after MPTP treatment, (c,h) : 7 days after MPTP treatment, (d,i) : 3 days after MPTP and perindopril (0.3 mg/kg, i.p.) treatment, (e,j) : 7 days after MPTP and perindopril (0.3 mg/kg, i.p.) treatment. Bar(a-e)=1 mm, Bar (f-j)=100 μ m, (n=5 for each experimental group).



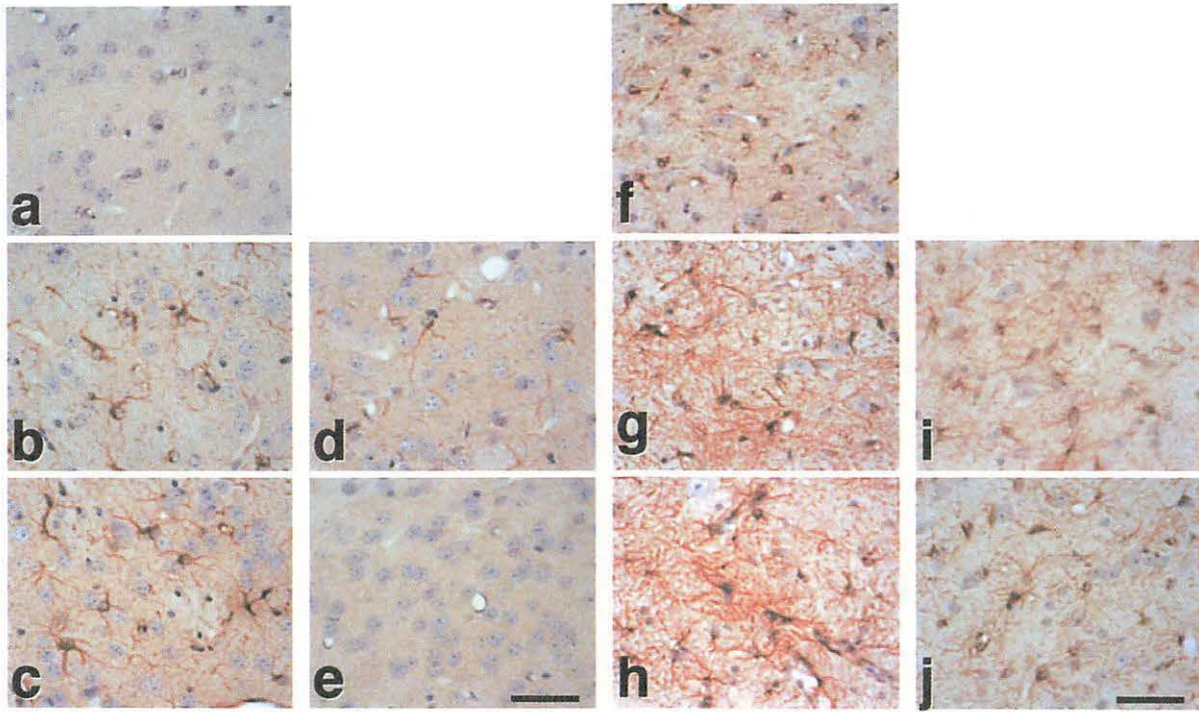


Fig. 2. Representative microphotographs of GFAP immunostaining in the mouse striatum(a-e) and substantia nigra(f-j) after MPTP treatment. (a,f) : Control mice, (b,g) : 3 days after MPTP treatment, (c,h) : 7 days after MPTP treatment, (d,i) : 3 days after MPTP and perindopril (0.3 mg/kg, i.p.) treatment, (e,j) : 7 days after MPTP and perindopril (0.3 mg/kg, i.p.) treatment. Bar(a-e)=50 μ m, Bar (f-j)=50 μ m, (n=5 for each experimental group).

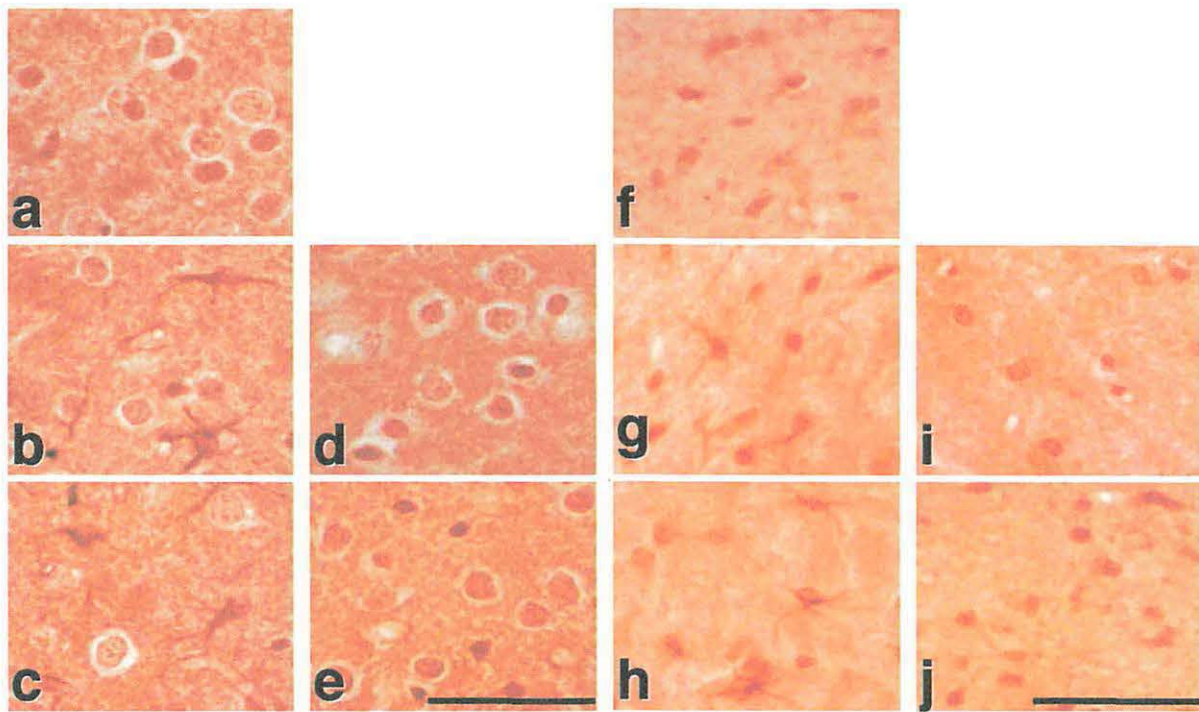
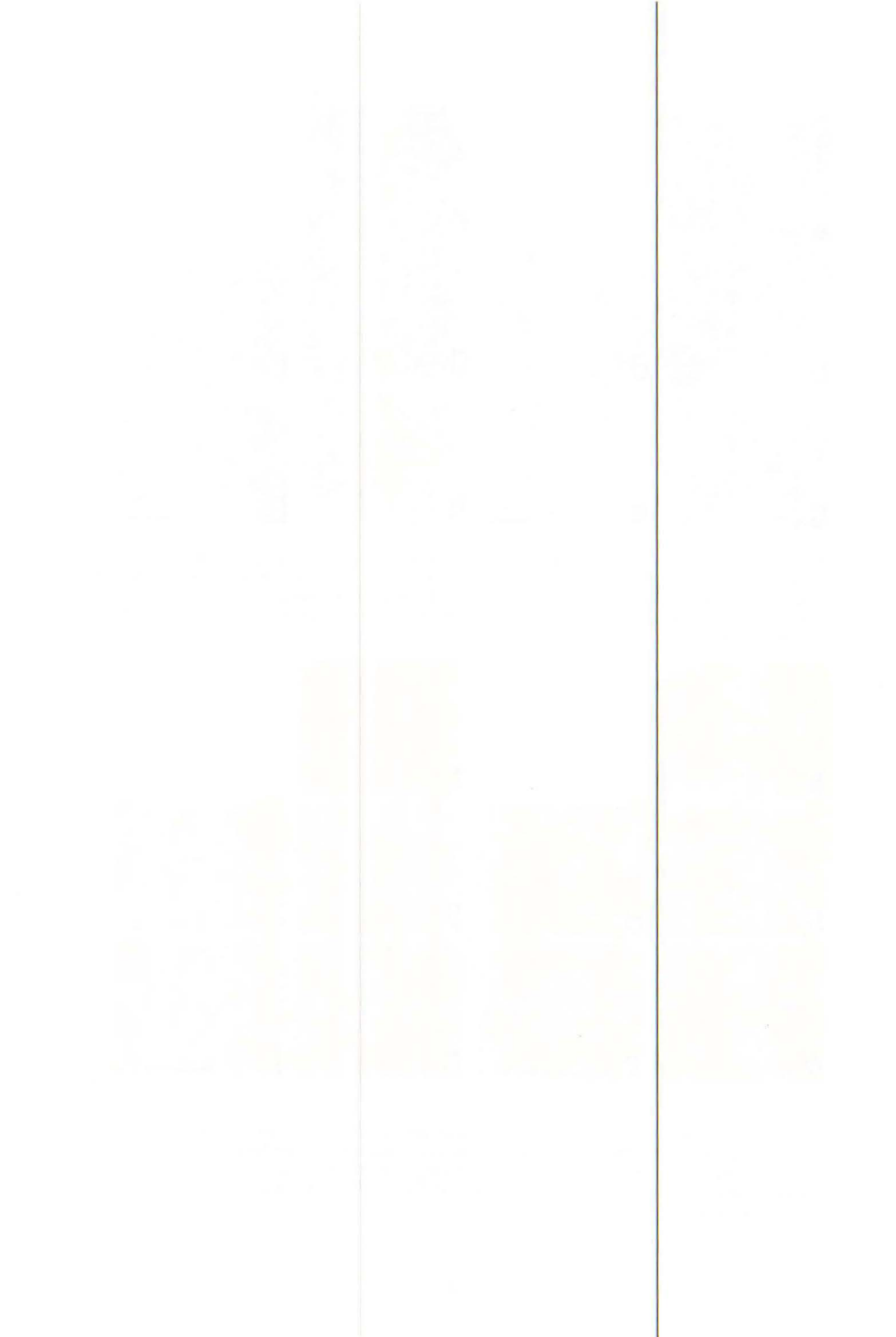


Fig. 3. Representative microphotographs of Cu/Zn-SOD immunostaining in the mouse striatum(a-e) and substantia nigra(f-j) after MPTP treatment. (a,f) : Control mice, (b,g) : 3 days after MPTP treatment, (c,h) : 7 days after MPTP treatment, (d,i) : 3 days after MPTP and perindopril (0.3 mg/kg, i.p.) treatment, (e,j) : 7 days after MPTP and perindopril (0.3 mg/kg, i.p.) treatment. Bar(a-e)=50 μ m, Bar (f-j)=50 μ m, (n=5 for each experimental group).



III. 3. Neuroprotective Effect of Riluzole Against MPTP Neurotoxicity in Mice

*Muramatsu Y. *, Kurosaki R. **, Watanabe H. *, Michimata M. *, Matsubara M. *, Imai Y. *, Kimura S. **, and Araki T. **

*Department of Clinical Pharmacology and Therapeutics, Tohoku University Graduate School of Pharmaceutical Science and Medicine**
*Department of Human Life Science, Graduate School of Showa Women's University***

INTRODUCTION

The neurotoxin 1-methyl-4-phenyl-1,2,3,6-tetrahydropyridine (MPTP) causes degeneration of mesencephalic dopaminergic neurons in several species including monkeys, dogs, cats and mice. The neurotoxic effects of MPTP are thought to be initiated by 1-methyl-4-phenylpyridinium ion (MPP⁺) which is a major metabolite formed by the monoamine oxidase B-mediated oxidation of MPTP. MPP⁺ is taken up by high-affinity dopamine and noradrenaline uptake systems and is subsequently accumulated within mitochondria of nigrostriatal dopaminergic cells^{1,2)}. This can lead to a number of deleterious effects on cellular function, resulting in neuronal cell death.

2-Amino-6-trifluoromethoxy benzothiazole (riluzole) has been reported to antagonize excitatory amino acid neurotransmission³⁾. This compound stabilizes voltage-dependent Na⁺ channels in their inactivated state and inhibits the release of glutamate. A previous study showed that riluzole can not prevent MPTP-induced dopamine depletion in the mouse striatum⁴⁾. In contrast, Boireau et al.⁵⁾ demonstrated that riluzole can antagonize the MPTP-induced decrease in dopamine levels in mice. Thus, there is no consensus in the literature whether riluzole has a neuroprotective effect in the brain of MPTP-treated mice. Furthermore, the mechanisms for the neuroprotection of riluzole against MPTP neurotoxicity are not fully understood. In the present experiments, therefore, we examined the effect of riluzole on MPTP-induced neurotoxicity, utilizing immunohistochemical markers.

MATERIALS AND METHODS

Male C57BL/6 mice (22-28 g) were used in this study. The mice were injected intraperitoneally (i.p.) with four administrations of MPTP (10 mg/kg) at 1-h intervals, the total dose per mice being 40 mg/kg, as described previously^{6,7}.

The animals were divided into 3 groups; (1) Vehicle (0.5% carboxymethyl-cellulose, CMC)-treated group; (2) MPTP- and 0.5% CMC-treated group; (3) MPTP- and riluzole (10 mg/kg)-treated group. The mice were injected i.p. with riluzole or 0.5% CMC 30 min before and 90 min after the first administration of MPTP (Groups 2 and 3). The animals of group 1 were injected i.p. in the same manner with saline treatment instead of MPTP. Each group contained five animals. For the immunohistochemical study, the mice were anesthetized with sodium pentobarbital (50 mg/kg, i.p.) at 3 and 7 days after MPTP treatment, and the brains were perfusion-fixed with 4% paraformaldehyde in 0.1 M phosphate buffer (pH 7.4) following a heparinized saline flush. The brains were removed 1-h after perfusion-fixation at 4°C and were immersed in the same fixative until they were embedded in paraffin. Paraffin sections, 5 µm in thickness, were used for immunohistochemistry.

For tyrosine hydroxylase (TH) immunostaining, a polyclonal anti-TH antibody (Chemicon International, Temecula, USA) and a Vectastain elite ABC kit (Vector Lab., Burlingame, USA) were used. The immunohistochemical staining with anti-TH antibody (1:200) was performed as described previously⁶.

For microtubule-associated protein 2 (MAP 2) immunostaining, a monoclonal mouse anti-MAP 2a,b antibody (Chemicon International Inc., Temecula, USA) and a Vector M.O.M. Immunodetection Kit (Vector Lab., Burlingame, USA) were used. In brief, the paraffin sections were washed for 5 min in 0.01 M phosphate-buffered saline (PBS, pH 7.4) and treated with 3% hydrogen peroxidase in 0.01 M PBS. The paraffin sections were then washed two times for 2 min in 0.01 M PBS, followed by 60 min of pre-incubation with mouse Ig G blocking reagent. The brain sections were then incubated with anti-MAP 2a,b antibody (1:500) including M.O.M. diluent overnight at 4°C. After a 4 min rinse in 0.01 M PBS, the sections were incubated with biotinylated secondary Ig G antibody for 10 min and then with avidin-biotin peroxidase complex for 30 min at room temperature. Immunoreactions were visualized using 0.05% diaminobenzidine and 0.01% hydrogen peroxidase in 0.05% Tris-HCl buffer (pH 7.6) and then the sections were counterstained with hematoxylin. Negative control sections were treated in the same way as described

above except that the antibody against anti-MAP 2a,b was omitted.

For glial fibrillary acidic protein (GFAP) immunostaining, a polyclonal anti-GFAP antibody (Labsystems, Helsinki, Finland) and a Vectastain elite ABC kit (Vector Lab., Burlingame, USA) were used. The immunohistochemical staining with anti-GFAP antibody (1:200) was performed as described previously⁶.

RESULTS

Representative microphotographs of TH and MAP 2 immunostaining in the substantia nigra are shown in Fig. 1. Dopaminergic neurons with TH antibody or MAP 2 antibody were easily detectable in the substantia nigra of vehicle-treated mice. The bodies and fibers of dopaminergic cells were intensely stained with evident immunopositive processes. A decrease in the number of these cells was noticed in mice 3 and 7 days after MPTP treatment. In contrast, the administration of riluzole at a dose of 10 mg/kg prevented the decrease in the number of dopaminergic neurons 3 and 7 days after MPTP treatment.

Representative microphotographs of GFAP immunostaining in the striatum are shown in Fig. 2. GFAP-positive astrocytes were absent in the striatum of vehicle-treated mice. The levels of staining for GFAP-positive astrocytes were mildly increased in the striatum 3 days after MPTP treatment. Seven days after MPTP treatment, GFAP-positive astrocytes exhibited a ramified form with many fine processes in the striatum, which showed marked increases in this area. On the other hand, a marked increase in GFAP-positive astrocytes in the striatum was found in riluzole-treated mice 3 days after MPTP treatment. Seven days after MPTP treatment, however, a marked increase in GFAP-positive astrocytes in the striatum was not observed in riluzole-treated mice, as compared with vehicle-treated mice.

DISCUSSION

Our immunohistochemical study indicated that riluzole can protect against MPTP-induced neuronal damage in the substantia nigra.

Riluzole is an inhibitor of glutamatergic transmission in the central nervous system. This drug is currently given to patients with amyotrophic lateral sclerosis (ALS) in an attempt to improve their prognosis, possibly via blockade of the glutamate neurotoxic effects⁸. Interestingly, a previous study suggested that riluzole can partially antagonize the increase in the release of striatal dopamine induced by superfusion with MPP⁺, the

active metabolite of MPTP⁹⁾. Furthermore, Boireau et al.⁵⁾ reported that riluzole can protect against MPTP-induced striatal dopamine depletion in mice either by blocking the entry of Na⁺ or by reducing the release of glutamate. In contrast, Jones-Humble et al.⁴⁾ demonstrated that riluzole had no significant effect on dopamine depletion in the striatum of mice. We have no explanation for these discrepancies at present. However, these discrepancies might be the results of differences in dosing, timing, animal strain, animal age or experimental protocol including dose-response studies. Therefore, the neuroprotective effect of riluzole against MPTP-induced striatal dopamine depletion in mice is controversial. However, a recent interesting study reported that riluzole delayed the appearance of parkinsonian motor abnormalities in a chronic monkey model of MPTP toxicity, designed to resemble more closely Parkinson's disease¹⁰⁾. Furthermore, this drug was shown to alleviate the circling behavior in 6-hydroxydopamine-treated rats and to decrease the suppression of dopamine metabolism, at both striatal and nigral levels¹¹⁾. Both neuroprotective and palliative effects of riluzole have also been obtained in an acute model of MPTP intoxication in monkeys¹²⁾. These observations are, at least in part, consistent with our present findings.

In the present study, it is of interest that riluzole in the present study markedly increased GFAP-positive astrocytes in the mouse striatum 3 days after MPTP treatment, as compared with vehicle-treated animals. The reason for this phenomenon is presently unclear. However, several studies reported that astrocytes can confer neuronal protection by synthesizing and releasing the free-radical scavenger glutathione and its precursors glutamate, cysteine and glycine^{13,14)}. A recent interesting study also indicated that GFAP-null mice were more sensitive to cerebral ischemia than wild-type mice and that astrocytes can provide a protective function after ischemia¹⁵⁾. These observations suggest that astrocytes may play an important role for the neuroprotective function in the brain. Therefore, it is conceivable that this protective effect of riluzole may be caused by the activation of astrocytes.

In conclusion, our results show that riluzole can protect against MPTP-induced neuronal damage. The protective effect may be, at least in part, caused by the activation of astrocytes. These results demonstrate that riluzole is effective against MPTP-induced neurodegeneration of the nigrostriatal dopaminergic neuronal pathway. Our findings also provide a rationale for the identification of astrocytes as a prominent target for the development of new therapies of Parkinson's disease.

REFERENCES

- 1) Nicklas W.J., Vyas I. and Heikkila R.E., *Life Sci.*, **36** (1985) 2503-2508.
- 2) Turski L., Bressler K., Rettig K.J., et al., *Nature*, **349** (1991) 414-418.
- 3) Benavides J., Camelin J.C., Mitrani N., et al., *Neuropharmacology*, **24** (1985) 1085-1092.
- 4) Jones-Humble S.A., Morgen P.F. and Cooper B.R., *Life Sci.*, **54** (1994) 245-252.
- 5) Boireau A., Dubedat P., Bordier F., et al., *NeuroReport*, **5** (1994) 2657-2660.
- 6) Muramatsu Y., Kurosaki R., Mikami M., et al., *Metab. Brain Dis.*, **17** (2002) 169-182.
- 7) Araki T., Muramatsu Y., Tanaka K., et al., *Neurosci. Lett.*, **312** (2001) 50-54.
- 8) Bensimon G., Lacomblez L. and Meininger V., *New Engl. J. Med.*, **330** (1994) 585-601.
- 9) Boireau A., Miquet J.M., Dubedat P., et al., *NeuroReport*, **5** (1994) 2157-2160.
- 10) Bezaud E., Stutzmann J.M., Imbert C., et al., *Eur. J. Pharmacol.*, **356** (1998) 101-104.
- 11) Barneoud P., Mazadier M., Miquet J.M., et al., *Neuroscience*, **74** (1996) 971-983.
- 12) Benazzouz A., Boraud T., Dubedat P., et al., *Eur. J. Pharmacol.*, **284** (1995) 299-307.
- 13) Dringen R., Pfeiffer B. and Hamprecht B., *J. Neurosci.*, **19** (1999) 562-569.
- 14) Wang X.F. and Cynader M.S., *J. Neurochem.*, **74** (2000) 1434-1442.
- 15) Nawashiro H., Brenner M., Fukui S., et al., *J. Cereb. Blood Flow Metab.*, **20** (2000) 1040-1044.

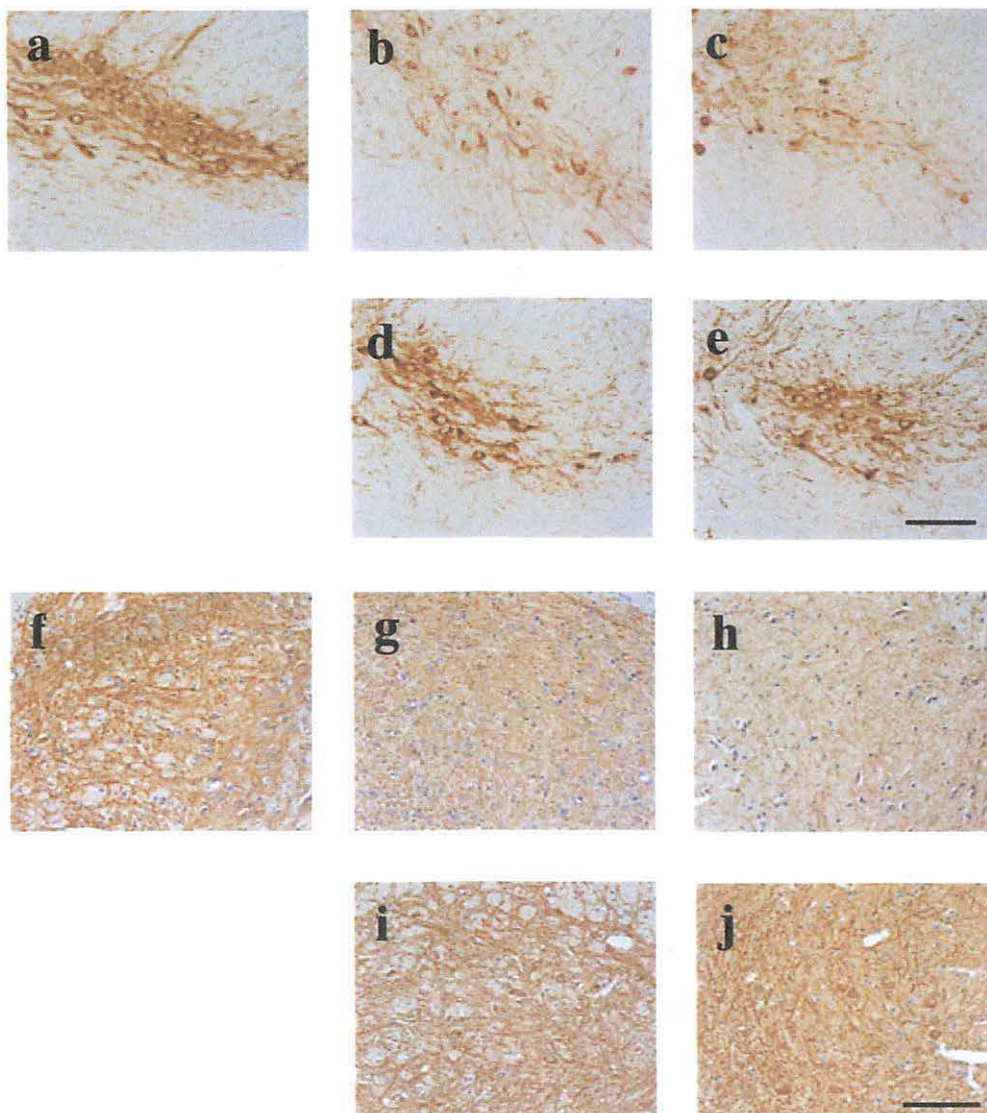
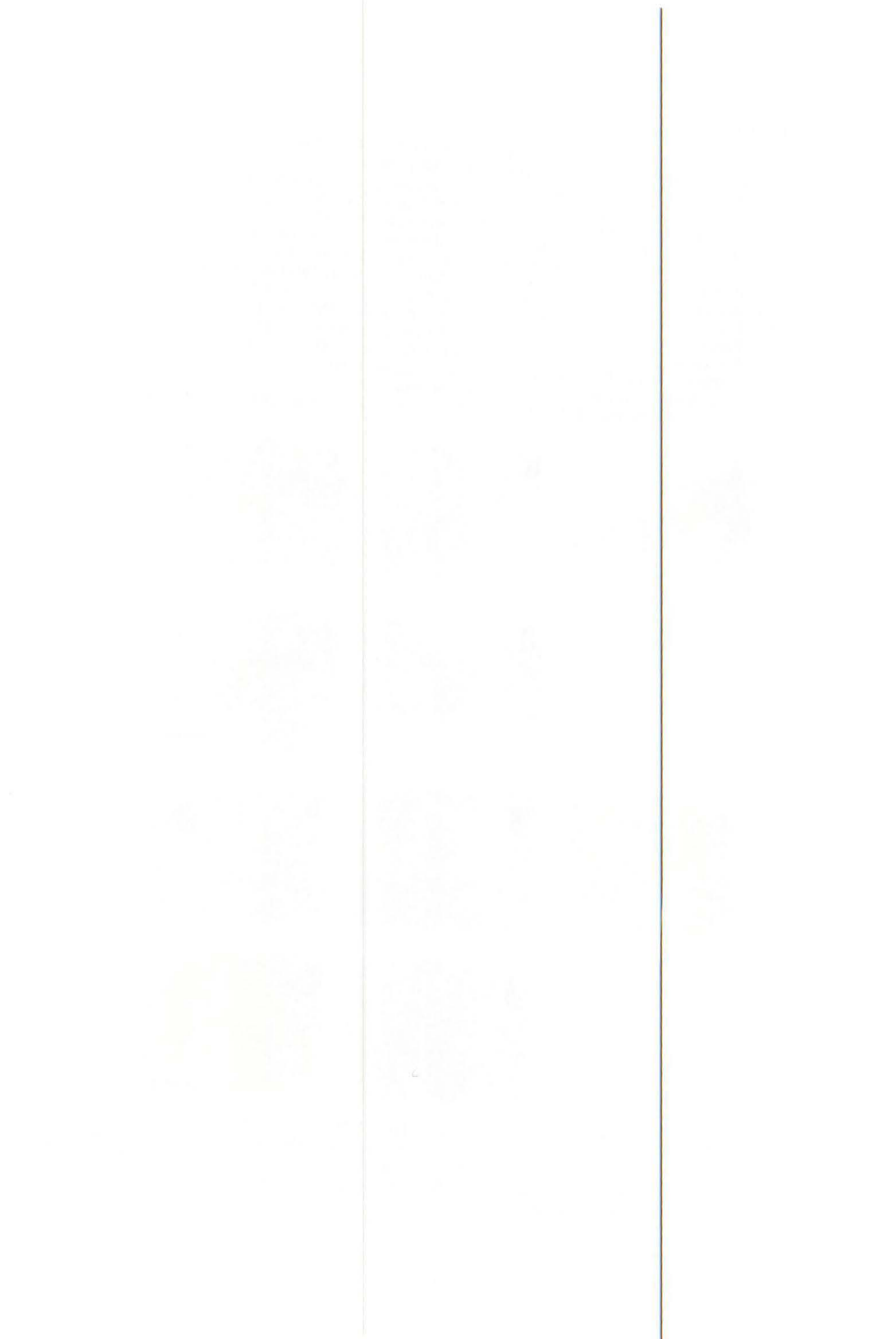


Fig. 1. Dopaminergic neurons stained with antibodies for TH or MAP 2 in the substantia nigra of vehicle-, MPTP- and MPTP + riluzole (10 mg/kg)-treated mice. TH staining (a-e). MAP 2 staining (f-j). (a,f) Vehicle (0.5% CMC)-treated mice. (b,g) Mice 3 days after MPTP treatment. (c,h) Mice 7 days after MPTP treatment. (d,i) Riluzole (10 mg/kg)-treated mice 3 days after MPTP treatment. (e,j) Riluzole (10 mg/kg)-treated mice 7 days after MPTP treatment. Bar (a-e and f-j) = 100 μ m. $n = 5$.



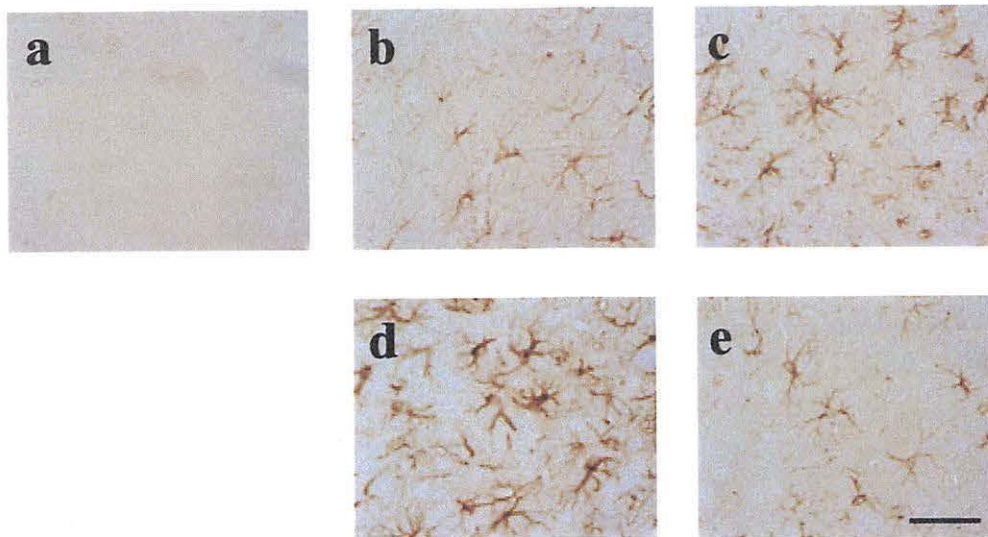
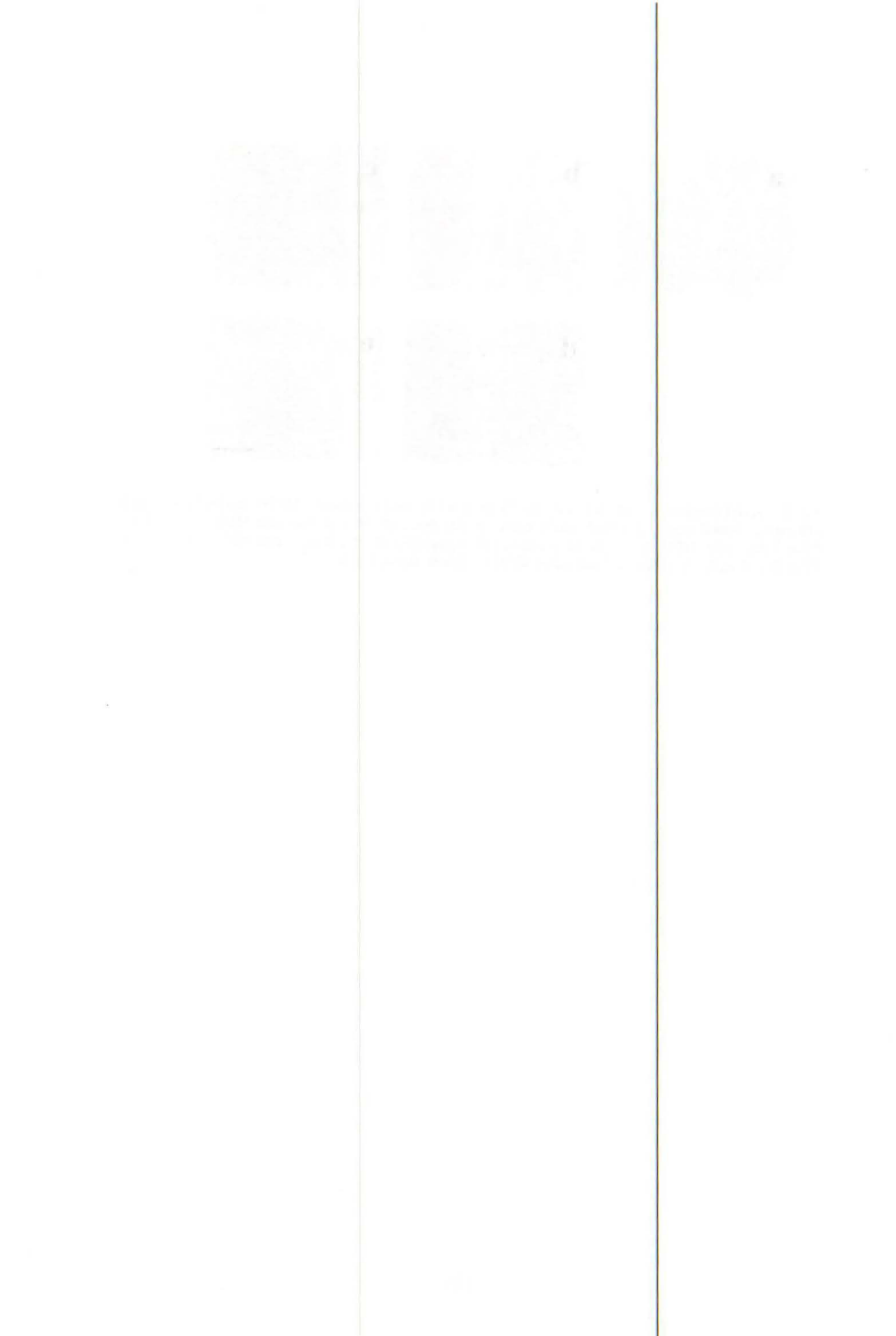


Fig. 2. Astrocytes stained with antibodies for GFAP in the striatum of vehicle-, MPTP- and MPTP + riluzole (10 mg/kg)-treated mice. (a) Vehicle (0.5% CMC)-treated mice. (b) Mice 3 days after MPTP treatment. (c) Mice 7 days after MPTP treatment. (d) Riluzole (10 mg/kg)-treated mice 3 days after MPTP treatment. (e) Riluzole (10 mg/kg)-treated mice 7 days after MPTP treatment. Bar = 50 μ m. $n = 5$.



III. 4. Neuronal Nitric Oxide Synthase Inhibitor and Monoamine Oxidase B Inhibitor Attenuate MPTP Neurotoxicity

Watanabe H., Muramatsu Y.*, Kurosaki R.***, Michimata M.*, Matsubara M.*, Imai Y.*, Kimura S.**, Araki T.**

*Department of Clinical Pharmacology and Therapeutics, Tohoku University Graduate School of Pharmaceutical Science and Medicine**

*Department of Human Life Science, Graduate School of Showa Women's University***

Introduction

The loss of dopamine in the striatum as a result of neuronal degeneration in the substantia nigra pars compacta of Parkinson's disease (PD) has been considered to be the major pathological correlate of the motor symptoms such as akinesia and rigidity. So far, many studies have focused on neurochemical and neuropathological mechanisms in PD.

In humans and rodents, MPTP (1-methyl-4-phenyl-1,2,3,6-tetrahydropyridine) is well known to produce clinical, biochemical and neurochemical changes similar to those which occur in PD^{1,2)}. This neurotoxin also leads to a marked decrease of dopamine contents in the striatum and a reduction in the number of nigrostriatal dopaminergic neurons in several species, including monkeys, dogs, cats and mice. In several experimental animals, especially the C57BL mouse strain, is known to be highly susceptible to the neurotoxic effects of MPTP and are useful as excellent models of PD^{1,3)}.

The pathogenesis of neuronal degeneration following MPTP treatment has been extensively investigated. The neurotoxic effects of MPTP are thought to be mediated by its metabolite MPP⁺(1-methyl-4-phenylpyridinium ion) which is caused by the oxidation of MPTP by monoamine oxidase B (MAO-B) in glial cells⁴⁾. MPP⁺ is selectively taken up by the high affinity dopamine uptake system and is subsequently accumulated within mitochondria of dopamine neurons. There it disrupts oxidative phosphorylation by inhibiting complex I of the electron transport chain in dopaminergic neurons⁵⁾. This can lead to a number of deleterious effects on cellular function. These include impaired intracellular calcium buffering as well as generation of free radicals from mitochondria and

activation of neuronal nitric oxide synthase (nNOS), a calmodulin dependent enzyme⁶. Therefore, it is possible that the generation of the free radical nitric oxide followed by the peroxynitrate has been implicated in neuronal cell death⁷⁻⁹.

Several studies previously reported that 7-nitroindazole, a relatively selective inhibitor of the nNOS, can protect against MPTP-induced neurotoxicity in experimental animals¹⁰⁻¹². This was confirmed and extended by showing that mice deficient in the neuronal isoform of NOS are also resistant to MPTP neurotoxicity¹³. We recently reported that 7-nitroindazole can protect against MPTP-induced neurotoxicity in mice¹⁴. It protected against both dopamine depletions in the striatum and tyrosine hydroxylase positive neurons in mice. In the present study, we further examined whether 7-nitroindazole also can protect against tyrosine hydroxylase (TH)-, glial fibrillary acidic protein (GFAP)-, parvalbumin(PV)-, dopamine transporter (DAT)-, nNOS- or endothelial nitric oxide synthase (eNOS)- positive cells, in comparison with pargyline (a relatively selective inhibitor of the MAO-B).

Materials and Methods

2.1. Experimental animals

Male C57BL/6 mice (Nihon SLC Co.), 8 weeks of age, were used in the present study. The animals were housed in a controlled environment ($23\pm 1^{\circ}\text{C}$, $50\pm 5\%$ humidity) and were allowed food and tap water *ad libitum*. The room lights were on between 8:00 and 20:00. All experiments were performed in accordance with the Guideline for Animal Experiments of the Tohoku University School of Medicine.

2.2. Experimental drugs

7-Nitroindazole (Research Biochemicals Int.), pargyline (Sigma) and MPTP (Sigma) were used in this study. 7-Nitroindazole (30 and 50 mg/kg) was suspended in peanut oil. Pargyline (5 and 15 mg/kg) or MPTP (10 mg/kg) was dissolved in saline. 7-Nitroindazole, pargyline or MPTP was given intraperitoneally (i.p.) in mice.

2.3. Experimental procedures

2.3.1. Analysis of contents of dopamine and its metabolites

The mice were injected i.p. four times with MPTP (10 mg/kg) at 1h intervals, the total dose per mouse being 40 mg/kg, as described previously^{14,15}. The mice were killed

by cerebral dislocation at 3 and 7 days after MPTP treatment. After cerebral dislocation, the striata were rapidly dissected out and sonicated in ice-cold 0.2M perchloric acid containing 100 ng/ml isoproterenol as an internal standard. Dopamine and 3,4-dihydroxyphenylacetic acid (DOPAC) were quantified by high-performance liquid chromatography (HPLC) with an electrochemical detector (Eicom, Kyoto, Japan), as described previously^{14,15}. Each group consisted of 6-9 mice. All values were expressed as mean±S.E. and statistical significance was evaluated using an analysis of variance (ANOVA) followed by Dunnett's multiple comparison test 2-side.

2.3.2. Effects of 7-nitroindazole or pargyline on the striatal dopamine and DOPAC content in MPTP-treated mice

Experiment 1

The animals were divided into 5 groups: (1) peanut oil-treated group (n=6); (2) 7-nitroindazole (50 mg/kg)-treated group (n=5); (3) MPTP- and peanut oil-treated group (n=6); (4) MPTP- and 7-nitroindazole (30 mg/kg)-treated group (n=6); (5) MPTP- and 7-nitroindazole (50 mg/kg)-treated group (n=6). The mice were injected i.p. with 7-nitroindazole or peanut oil 30 min before and 90 min after the first administration of MPTP. For groups (1) and (2), the peanut oil-treated or 7-nitroindazole-treated mice were injected i.p. in the same manner with saline instead of MPTP.

Experiment 2

The animals were divided into 5 groups: (6) saline-treated group (n=6); (7) pargyline (15 mg/kg)-treated group (n=5); (8) MPTP- and saline-treated group (n=6); (9) MPTP- and pargyline (5 mg/kg)-treated group (n=6); (10) MPTP- and pargyline (15 mg/kg)-treated group (n=6). The mice were injected i.p. with pargyline or saline 30 min before and 90 min after the first administration of MPTP. For groups (6) and (7), the saline-treated or pargyline-treated animals were injected i.p. in the same manner with saline instead of MPTP.

The mice were killed by cerebral dislocation 3 days after MPTP treatment. Dopamine and DOPAC were quantified by HPLC with an electrochemical detector, as described above. Each group consisted of 5-6 mice. All values were expressed as mean±S.E. and statistical significance was evaluated using an analysis of variance (ANOVA) followed by Dunnett's multiple comparison test 2-side.

2.3.3. Immunohistochemistry

The mice were anesthetized with sodium pentobarbital (50 mg/kg, i.p.) 3 and 7 days after MPTP treatment, and the brains were perfusion-fixed with 4% paraformaldehyde in 0.1M phosphate buffer (pH 7.4) following a heparinized saline flush. The brains were removed 1 h after perfusion fixation at 4°C and were immersed in the same fixative until they were embedded in paraffin. Paraffin sections, 5 µm, of the striatum and substantia nigra were used for immunohistochemistry. In addition, the mice that received treatment with MPTP and 7-nitroindazole (50 mg/kg, i.p.) or pargyline (15 mg/kg, i.p.) were also treated in the same way, as described above. Each group consisted of 5 animals.

For immunohistochemical studies, a Vectastain *elite* ABC kit (Vector Labs.), M.O.M. immunodetection kit (Vector Labs.), rabbit anti-TH polyclonal antibody (Chemicon International, Inc.), mouse anti-GFAP monoclonal antibody (Chemicon International, Inc.), mouse anti-PV monoclonal antibody (Chemicon International, Inc.), rabbit anti-DAT polyclonal antibody (Alpha Diagnostic international.), rabbit anti-nNOS polyclonal antibody (Zymed Laboratories Inc.) and rabbit anti-eNOS polyclonal antibody (Affinity BioReagents Inc.) were used.

Briefly, the paraffin sections were washed for 5 min in 0.01M phosphate-buffered saline (PBS, pH 7.4) and treated with 3% hydrogen peroxide in 0.01M PBS. The paraffin sections were then washed twice for 2 min each time in 0.01M PBS, followed by 60 min of pre-incubation with mouse IgG blocking reagent. The brain sections were then incubated with or anti-PV (1:500) antibody including M.O.M. diluent overnight at 4°C. After a 5 min rinse in 0.01M PBS, the sections were incubated with biotinylated secondary IgG antibody for 10 min and then with avidin-biotin peroxidase complex for 30 min at room temperature. Immunoreactivity was visualized using enzyme substrate kits (Vector Lab. Burlingame, CA, USA). Negative control sections were treated in the same way, except that the antibodies against anti-PV were omitted. For TH, GFAP, DAT, nNOS and eNOS immunostaining, a Vectastain *elite* ABC kit was used. Immunohistochemical staining with anti-TH (1:200), anti-GFAP(1:200), anti-nNOS (1:100) and anti-eNOS (1:300) antibody was performed as described previously^{14,15}.

Results

3.1. Effects of 7-nitroindazole or pargyline on the MPTP-induced decreases in the striatal dopamine and DOPAC content in mice

As shown in Tables 1 and 2, four administrations of MPTP to mice produced a marked depletion in the dopamine, and DOPAC content of the striatum. Striatal dopamine and DOPAC levels were significantly decreased 3 and 7 days after MPTP treatment in mice. The depletion in the striatal dopamine and DOPAC concentrations reached a maximal levels 3 days after MPTP treatment. In contrast, 7-nitroindazole dose-dependently prevented the significant reduction in the striatal dopamine and DOPAC levels 3 days after MPTP treatment. Pargyline also prevented the significant reduction in the striatal dopamine levels 3 days after MPTP treatment in a dose-dependent manner. However, pargyline showed no significant changes in the striatal DOPAC levels after MPTP treatment. In addition, 7-nitroindazole showed no significant changes in the striatal dopamine and DOPAC contents in mice. However, pargyline had marked increases in the striatal dopamine content and decreases in DOPAC content in mice.

3.2. Immunohistological changes of 7-nitroindazole or pargyline on the striatum and substantia nigra of MPTP-treated mice

TH immunostaining

Representative photomicrographs of TH immunostaining in the striatum and substantia nigra are shown in Fig. 1. Striatal TH-immunoreactive fibers and nigral TH-immunoreactive neurons were easily detectable in vehicle-treated mice, respectively. The bodies and fibers of dopaminergic cells were intensely stained with evident immunopositive processes. In the striatum, a decrease in the number of TH-immunopositive fibers was observed 3 and 7 days after MPTP treatment. In the substantia nigra, a decrease in the number of TH-immunopositive neurons was also observed 3 and 7 days after MPTP treatment. In contrast, 7-nitroindazole and pargyline prevented the decreases in number of the striatum TH-immunopositive fibers and nigral TH-immunopositive neurons 3 and 7 days after MPTP treatment in mice.

GFAP immunostaining

Representative photomicrographs of GFAP immunostaining in the striatum and substantia nigra are shown in Fig. 2. GFAP-immunoreactive astrocytes were absent in the

striatum of vehicle-treated mice. In the substantia nigra, however, GFAP-immunoreactive astrocytes had a ramified form with many fine processes in control mice. In the striatum, the number of GFAP-immunopositive astrocytes increased 3 days after MPTP treatment. Seven days after MPTP treatment, GFAP-immunopositive astrocytes exhibited a ramified form with many fine processes in the striatum, which were markedly increased in this region. In the substantia nigra, marked increases in the number of GFAP-immunopositive astrocytes were noted in mice 3 and 7 days after MPTP treatment. In contrast, 7-nitroindazole and pargyline reduced the increases in number of the striatal and nigral astrocytes 3 and 7 days after MPTP treatment.

PV immunostaining

Representative photomicrographs of PV immunostaining in the striatum and substantia nigra are shown in Fig. 3. Striatal PV-immunoreactive cells were easily detectable in vehicle-treated mice. The bodies and fibers of PV-immunoreactive cells were stained intensely with evident immunopositive processes. In the striatum, PV-immunopositive cells were unchanged throughout the experiment. In the substantia nigra, marked decreases of the immunostaining of PV-positive cells were noted in the substantia nigra 3 and 7 days after MPTP treatment. In contrast, 7-nitroindazole and pargyline did not affect the striatal PV-immunopositive neurons 3 and 7 days after MPTP treatment. However, both compounds prevented the decrease of immunoreactivity of PV-immunopositive neurons in the substantia nigra of mice 3 and 7 days after MPTP treatment.

DAT immunostaining

Representative photomicrographs of DAT immunostaining in the striatum and substantia nigra are shown in Fig. 4. DAT was localized in the plasma membranes of axons and terminals. In the substantia nigra, the bodies and fibers of dopaminergic cells were stained intensely with evident immunopositive processes. In the striatum, a decrease in the number of DAT-immunopositive fibers was observed in MPTP-treated mice 3 days after MPTP treatment. Seven days after MPTP treatment, marked reductions in the number of the DAT-immunopositive fibers were noted in mice 3 and 7 days after MPTP treatment. In the substantia nigra, marked reductions in the number of the DAT-immunopositive neurons were found in mice 3 and 7 days after MPTP treatment. In contrast, 7-nitroindazole showed mild reductions in the striatal DAT-immunopositive fibers

3 days after MPTP treatment, although this compound prevented marked decreases in the number of nigral DAT-immunopositive neurons. On the other hand, pargyline prevented decreases of the striatal DAT-immunopositive fibers and nigral DAT-immunopositive neurons 3 days after MPTP treatment. Seven days after MPTP treatment, both compounds prevented marked decreases in the striatal DAT-immunopositive fibers and nigral DAT-immunopositive neurons after MPTP treatment.

nNOS immunostaining

Representative photomicrographs of nNOS immunostaining in the striatum and substantia nigra are shown in Fig. 5. nNOS-immunoreactive cells were detectable in the striatum and substantia nigra of vehicle-treated mice. The bodies and fibers of nNOS-immunoreactive cells were stained intensely with evident immunopositive processes. In the striatum, nNOS-immunopositive cells were unchanged throughout the experiment. In the substantia nigra, marked decreases of the immunostaining of nNOS-positive cells were noted 3 and 7 days after MPTP treatment. In contrast, 7-nitroindazole and pargyline did not affect the striatal eNOS-immunopositive neurons 3 and 7 days after MPTP treatment. However, both compounds prevented the decrease of immunoreactivity of nNOS-immunopositive neurons in the substantia nigra of mice 3 and 7 days after MPTP treatment.

eNOS immunostaining

Representative photomicrographs of eNOS immunostaining in the striatum and substantia nigra are shown in Fig. 6. eNOS-immunoreactive cells were detectable in the striatum and substantia nigra of vehicle-treated mice. The bodies and fibers of eNOS-immunoreactive cells were stained intensely with evident immunopositive processes. In the striatum and substantia nigra, eNOS-immunopositive cells were unchanged in MPTP-treated mice throughout the experiment. 7-Nitroindazole and pargyline did not affect the striatal and nigral eNOS-immunopositive neurons 3 and 7 days after MPTP treatment.

Discussion

MPTP causes the biochemical, neuropathological and clinical features of PD^{16,17}. The pathogenesis of the lesions appears to be inhibition of complex I of the electron transport chain by MPP⁺ as well as free radical production⁴). A role of NO in the pathogenesis of the lesions has been supported by many studies. Previous studies

demonstrated that MPTP neurotoxicity was markedly attenuated by 7-nitroindazole in mice^{10,13}. Furthermore, MPTP neurotoxicity was attenuated in mice deficient in nNOS¹³. In primates, 7-nitroindazole is known to exert profound neuroprotective effects against MPTP neurotoxicity¹¹. An interesting previous study suggested that both striatal lesion volume and substantia nigra degeneration caused by injection of MPP⁺ were significantly attenuated in the nNOS mutant mice but not in the eNOS mutant mice¹⁸. Based on these observations, it is conceivable that neuronally derived NO and peroxynitrite play a key role in the pathogenesis of MPTP neurotoxicity. However, there are a few reports about the immunohistochemical examination for the effect of 7-nitroindazole against MPTP neurotoxicity. In the present study, therefore, we examined whether 7-nitroindazole also can protect against TH-, GFAP-, PV-, DAT-, nNOS- and eNOS-positive cells, in comparison with pargyline as a relatively selective inhibitor of the MAO-B.

The present study showed that four administrations of MPTP to mice caused marked depletions in the dopamine and DOPAC content of the striatum 3 and 7 days after MPTP treatment. The depletion in the striatal dopamine and DOPAC concentrations reached a maximal level 3 days after MPTP treatment. Therefore, we investigated the effect of 7-nitroindazole and pargyline on the striatal dopamine and DOPAC content 3 days after MPTP treatment. The present study showed that 7-nitroindazole dose-dependently prevented the significant reduction in the striatal dopamine and DOPAC levels 3 days after MPTP treatment. Pargyline also prevented the significant reduction in the striatal dopamine levels 3 days after MPTP treatment in a dose-dependent manner. However, pargyline showed no significant changes in the striatal DOPAC levels after MPTP treatment. Therefore, our results indicate that 7-nitroindazole and pargyline can protect against MPTP-induced striatal dopamine depletion in mice. The findings are consistent with previous reports^{10,13,14}. These findings demonstrate that nNOS inhibitor or MAO-B inhibitor may be useful in the treatment of PD.

To examine exactly the effects of 7-nitroindazole against MPTP neurotoxicity, we investigated the immunohistochemical changes of TH-, GFAP-, PV-, DAT-, nNOS- and eNOS-positive cells, in comparison with pargyline. The present study showed that severe reductions in levels of TH and DAT immunoreactivity were observed in the striatum and substantia nigra 3 and 7 days after MPTP treatment. These results suggest that MPTP can cause severe damage in the striatum and substantia nigra as well as the reduction of the striatal dopamine and DOPAC content. 7-Nitroindazole and pargyline showed a protective

effect against the severe reductions in TH immunoreactivity in the striatum and substantia nigra 3 and 7 days after MPTP treatment. However, 7-nitroindazole showed mild decreases in the striatal DAT-immunopositive fibers 3 days after MPTP treatment, although this compound prevented marked decreases in the number of nigral DAT-immunopositive neurons. On the other hand, pargyline prevented decreases of the striatal DAT-immunopositive fibers and nigral DAT-immunopositive neurons 3 days after MPTP treatment. Seven days after MPTP treatment, both compounds prevented marked decreases in the striatal DAT-immunopositive fibers and nigral DAT-immunopositive neurons after MPTP treatment.

DAT terminates dopaminergic neurotransmission by accumulating neurotransmitter from synaptic cleft into the presynaptic terminal. DAT is also known to accumulate the neurotoxic MPTP or MPP⁺, into dopaminergic neurons, results in dopaminergic cell death and parkinsonian syndrome that is similar to idiopathic PD. In the present study, we observed that DAT immunoreactivity especially recognized in the striatum and substantia nigra. Therefore, the present study demonstrates that MPTP can damage selectively the striatal DAT-immunopositive fibers and nigral DAT-immunopositive neurons. However, 7-nitroindazole showed mild decreases in the striatal DAT-immunopositive fibers 3 days after MPTP treatment, whereas this compound prevented marked decreases in the number of nigral DAT-immunopositive neurons. The reason for this phenomenon is presently unclear. For this reason, we speculate that 7-nitroindazole may attenuate the neurotoxic effect of MPTP against the remaining DAT-immunopositive fibers in the striatum. However, the precise mechanisms for our findings remain to be elucidated in further studies.

GFAP is well known to be a good marker for reactive astrocytes in the response to the CNS injury, due to specificity it in astrocytes^{19,20}. Stromberg et al.²¹ and Francis et al.²² have found astroglial reaction in the striatum, which started 48 h after MPTP treatment and was still observed 6 weeks following the treatment. In the present study, marked increases in the number of GFAP-immunopositive astrocytes were found in the striatum and substantia nigra 3 and 7 days after MPTP treatment. In contrast, the present study showed that 7-nitroindazole and pargyline can prevent the increases in the number of GFAP-immunopositive astrocytes 3 and 7 days after MPTP treatment. From these observations, we suggest that increases in GFAP-immunopositive astrocytes may reflect compensatory action against neuronal cell damage after MPTP treatment. Therefore, it is conceivable

that reactive astrocytes may play a key role in the maintenance of injury areas caused by MPTP neurotoxicity.

PV belongs to a family of homologous calcium binding proteins and is widely distributed throughout the (CNS)^{23,24}. PV has also been regarded as a superior marker for a subpopulation of GABA (γ -aminobutyric acid) ergic interneurons throughout the brain²⁵. Furthermore, a previous study demonstrated that less than 1% of the TH-immunopositive neurons were immunoreactive for the calcium binding proteins PV and calbindin in the primate striatum²⁶. From these observations, it is possible that PV immunoreactivity is mainly expressed in the interneurons in the brain. In the present study, PV-immunopositive cells were unchanged in the striatum throughout the experiments. In the substantia nigra, however, marked decreases of the immunostaining of PV-positive cells were noted 3 and 7 days after MPTP treatment. The present results suggest a functional damage in PV-immunopositive interneurons in the substantia nigra after MPTP treatment. However, our study indicates that the PV-immunopositive interneurons are unchanged in the striatum after MPTP treatment. A previous study suggested that the amount of PV immunoreactivity within the nigral interneurons is mildly reduced by end-stages of PD²⁷. These observations are, at least in part, consistent with our findings, suggesting a functional damage in PV-immunopositive interneurons in the substantia nigra of mice after MPTP treatment. In the present study, 7-nitroindazole and pargyline showed no significant changes in the striatum throughout the experiments. In contrast, both compounds prevented marked decreases of the immunostaining of PV-positive cells 3 and 7 days after MPTP treatment. These results suggest that 7-nitroindazole and pargyline can protect the functional damage of interneurons in the substantia nigra after MPTP treatment. However, further studies are needed to investigate the precise mechanism for our interesting findings.

The present study demonstrated that striatal nNOS-immunopositive cells were unchanged in MPTP-treated mice throughout the experiments. In the substantia nigra, in contrast, marked decreases of the immunoreactivity of nNOS-positive cells were noted 3 and 7 days after MPTP treatment. The nNOS-immunoreactive cells are well known to be interneurons in the hippocampus. The present study showed that 7-nitroindazole and pargyline prevented marked decreases of the immunostaining of nNOS-positive cells in the substantia nigra 3 and 7 days after MPTP treatment. These results demonstrate that 7-nitroindazole and pargyline can protect against the functional damage of nNOS-immunoreactive interneurons in the substantia nigra after MPTP treatment, although further

studies are needed to investigate the precise mechanism for our findings. In the striatum and substantia nigra, in contrast, eNOS-immunopositive cells were unchanged in MPTP-treated mice throughout the experiments. Furthermore, 7-nitroindazole and pargyline showed no significant changes of eNOS-immunopositive cells in the striatum and substantia nigra throughout the experiments. From these results, we speculate that nNOS play a key role in the pathogenesis of MPTP neurotoxicity, in comparison with eNOS. Matthews et al.¹⁸⁾ reported previously that MPP⁺-induced neuronal degeneration was significantly attenuated in the nNOS-deficient mice but not in eNOS-deficient mice. Furthermore, a previous report demonstrated that in nNOS-deficient mice, infarct volumes decreased significantly after middle cerebral artery occlusion²⁸⁾. These observations are, at least in part, consistent with our findings. Base on these observations, our data support that neuronal NO production contributes to the development of MPTP- or MPP⁺-induced neurodegeneration of nigral neurons.

In the present study, it is interestingly that the changes of nNOS-immunopositive cells in the striatum and substantia nigra were similar to these of PV-immunopositive neurons after MPTP treatment. Both nNOS and PV-immunopositive cells are known to be interneurons in the brain. Therefore, we speculate that the functional changes of interneurons also may play a key role in the pathogenesis of MPTP-induced neurotoxicity, although further studies should be performed to investigate the precise mechanisms responsible for the present findings.

In conclusion, our results show that nNOS inhibitor as well as MAO-B inhibitor has a dose-dependent protective effect against MPTP-induced striatal dopamine and DOPAC depletion in mice. These protective effects may be, at least in part, produced by the reduction of neuronally derived NO and peroxynitrite caused by MPTP. Furthermore, our results demonstrate that MPTP can cause the functional damage of interneurons in the substantia nigra. These results suggest possibility that nNOS inhibitors as well as MAO-B inhibitors may be therapeutically useful in neurodegenerative diseases such as PD, although further studies will be needed to elucidate our findings.

References

- 1) Heikkila, K.E., Manzino, L., Cabbat, F.S., et al., *Nature* **311** (1984) 467.
- 2) Turski, L., Bressler, K., Retting, K.J., et al., *Nature* **349** (1991) 414.
- 3) Sundström, E., Strömberg, I., Tsutsumi, T., et al., *Brain Res.* **405** (1987) 26.
- 4) Tipson, K.F. and Singer, T.P., *J. Neurochem.* **61** (1993) 1191.
- 5) Gluck, M.R., Krueger, M.J., Ramsey, R.R., et al., *J. Biol. Chem.* **269** (1994) 3167.
- 6) Beal, M.F., *Ann. Neurol.* **38** (1995) 357.

- 7) Dawson, V.L., Dawson, T.M., London, E.D., et al., Proc. Natl. Acad. Sci. U.S.A., **88** (1991) 6368.
- 8) Beal, M.F., Fennantre, R.J., Browne, S.E., et al., Ann Neurol. **42** (1997) 646.
- 9) Ferrante, R.J., Browne, S.E., Shinobu, L.A., et al., J. Neurochem. **69** (1997) 2064.
- 10) Schulz, J.B., Matthews, R.T., Muqit, M.M.K., et al., J. Neurochem. **64** (1995) 1936.
- 11) Hantraye, P., Brouillet, E., Ferrante, R., et al., Nature Med. **2** (1996) 1017.
- 12) Ferrante, R.J., Hantraye, P., Brouillet, E., et al., Brain Res. **827** (1999) 177.
- 13) Przedbroski, S., Jackson-Lewis, V., Yokoyama, R., et al., Proc. Natl. Acad. Sci. USA. **93** (1996) 4565.
- 14) Muramatsu, Y., Kurosaki, R., Mikami, T., Michimata, M., et al., Metabolic Brain Dis. **17** (2002) 169.
- 15) Araki, T., Kumagai, T., Tanaka, K., et al., Brain Res. **918** (2001) 176.
- 16) Burns, R.S., Chiuch, C.C., Markey, S.P., et al., Proc. Natl. Acad. Sci. USA. **80** (1983) 4546.
- 17) Bloem, B.R., Irwin, I., Buruma, O.J.S., et al., J. Neurol. Sci. **97** (1990) 273.
- 18) Matthews, R.T., Beal, M.F., Fallon, J., et al., Neurobiol. Dis. **4** (1997) 114.
- 19) Eng, L. F., DeArmond, S. J., Adv. Cell. Neurobiol. **3** (1986) 145.
- 20) Lin, R.C.S., Polsky, K., Matesic, D.F., Brain Res. **600** (1993) 1.
- 21) Stromberg, L., Bjorklund, H., Dahl, D., et al., Brain Res. Bull. **17** (1986) 225.
- 22) Francis, J.W., Visger, J., Markelonis, J., et al., Neurotoxicol. Teratol. **17** (1995) 7.
- 23) Celio, M. R., Neuroscience **35** (1990) 375.
- 24) Araki, T., Kato, H., Liu, X. -H., et al., Metabolic Brain Dis. **9** (1994) 225.
- 25) Celio, M. R., Science **231** (1986) 995.
- 26) Betarbet, R., Turner, R., Chockkan, V., et al., J. Neurosci. **17** (1997) 6761.
- 27) Hardman, C.D., McRitchie, D.A., Halliday, G.M., et al., Neurodegeneration **5** (1996) 49.
- 28) Huang, Z., Huang, P. L., Panahian, N., et al., Science **265** (1994) 1883.

Table 1. Striatal contents of dopamine and DOPAC in mice after MPTP treatment.

	Dopamine	DOPAC
	(µg/g tissue)	
Control	10.16±0.37	2.74±0.14
3 days	2.28±0.26*	1.76±0.29*
7 days	5.67±0.56*	2.29±0.24*

Values were expressed as mean±S.E. of 6-9 mice. The mice received four intraperitoneal (i.p.) injections of MPTP (10 mg/kg) at 1h intervals. **P*<0.01 vs. control group (Dunnett's multiple comparison test).

Table 2. Neuroprotective effects of 7-nitroindazole and pargyline on the striatal dopamine and DOPAC contents in mice after MPTP treatment.

Treatment	Dopamine	DOPAC
	(µg/g tissue)	
<i>Experiment 1 (Effect of 7-nitroindazole)</i>		
Vehicle (peanut oil)	8.99±0.49**	3.64±0.50**
7-Nitroindazole (50 mg/kg)	9.80±0.31**	5.31±0.38**
MPTP+vehicle (peanut oil)	3.36±0.31	1.78±0.15
MPTP+7-nitroindazole (30 mg/kg)	6.94±0.81**	3.00±0.21*
MPTP+7-nitroindazole (50 mg/kg)	8.64±0.58**	3.54±0.20**
<i>Experiment 2 (Effect of pargyline)</i>		
Vehicle (saline)	9.69±0.70**	4.62±0.58**
Pargyline (15 mg/kg)	16.32±0.67**	1.56±0.29
MPTP+vehicle (saline)	2.36±0.59	2.44±0.50
MPTP+pargyline (5 mg/kg)	15.02±0.59**	2.50±0.25
MPTP+pargyline (15 mg/kg)	16.63±0.91**	1.05±0.34

Values were expressed as mean±S.E. of 5-6 mice. Drug treatment schedules were described in Materials and methods section. **P*<0.05, ***P*<0.01 vs. MPTP+vehicle group (Dunnett's multiple comparison test).

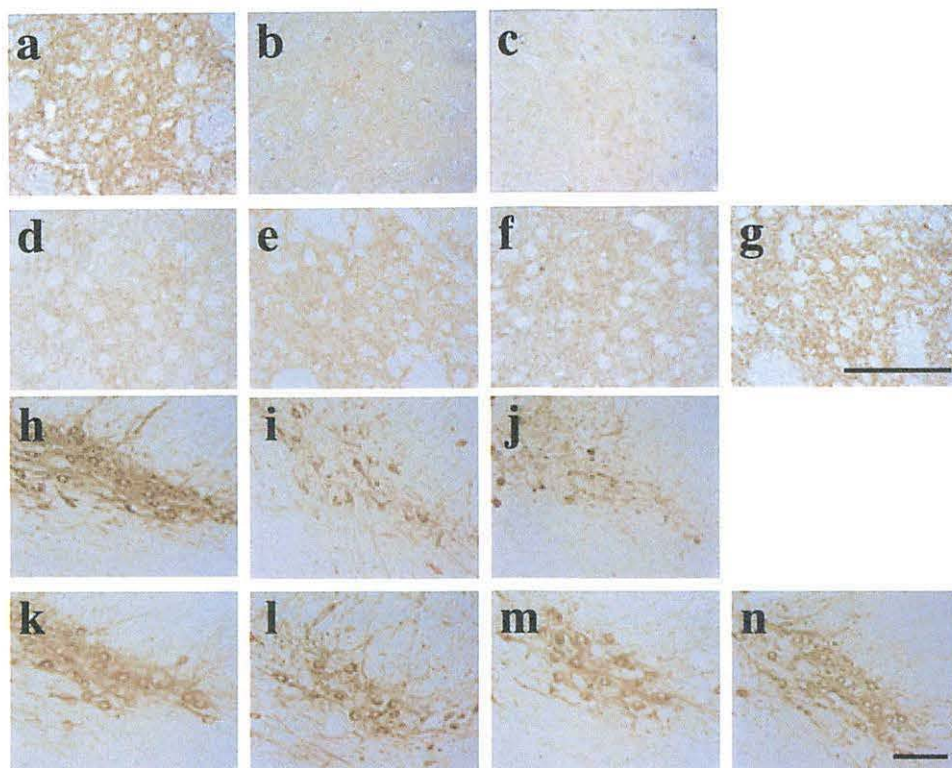


Fig. 1. Representative microphotographs of TH immunostaining in the mouse striatum (a-g) and substantia nigra (h-n) after MPTP treatment. (a, h) Control (vehicle) group. (b, i) 3 days after MPTP treatment. (c, j) 7 days after MPTP treatment. (d, k) 3 days after MPTP and 7-nitroindazole (50 mg/kg) treatment. (e, l) 7 days after MPTP and 7-nitroindazole (50 mg/kg) treatment. (f, m) 3 days after MPTP and pargyline (15 mg/kg) treatment. (g, n) 7 days after MPTP and pargyline (15 mg/kg) treatment. Bar (a-g)= 100 μ m. Bar (h-n)= 100 μ m. n=5.

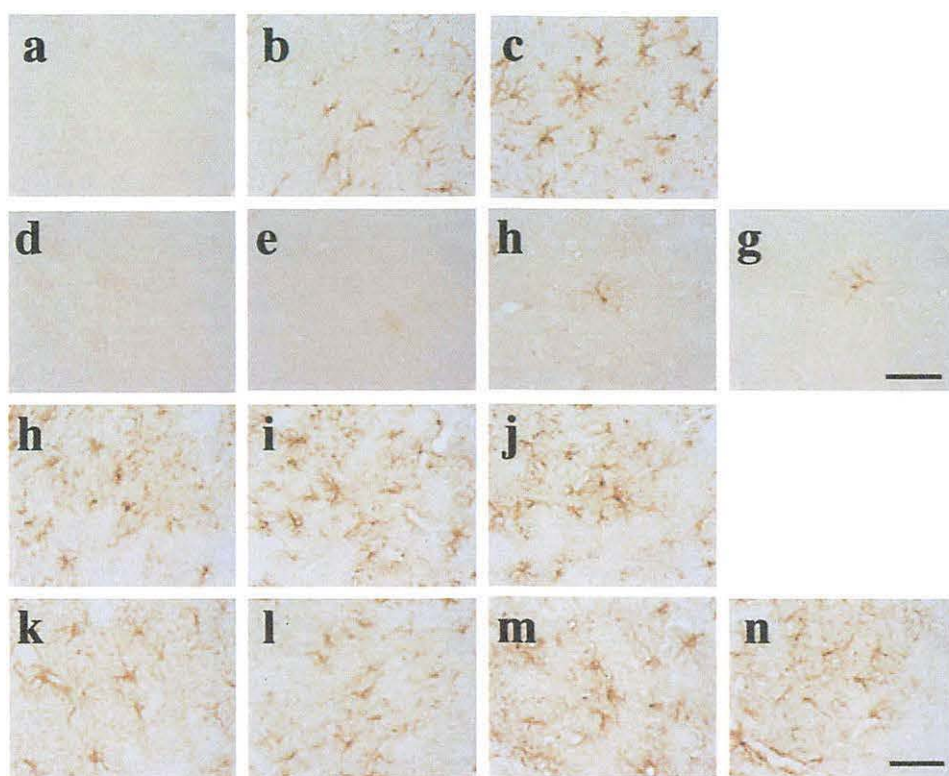
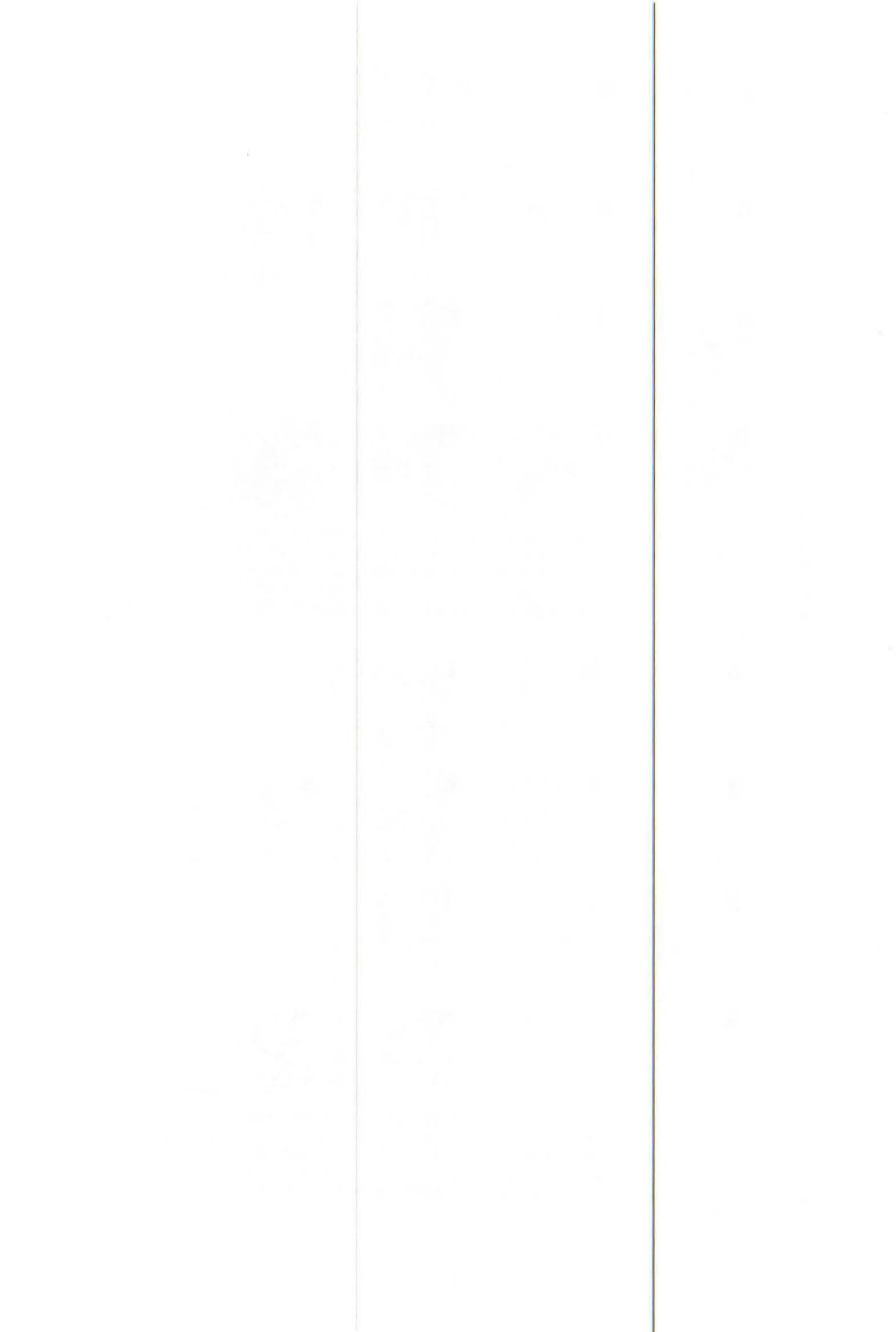


Fig. 2. Representative microphotographs of GFAP immunostaining in the mouse striatum (a-g) and substantia nigra (h-n) after MPTP treatment. (a, h) Control (vehicle) group. (b, i) 3 days after MPTP treatment. (c, j) 7 days after MPTP treatment. (d, k) 3 days after MPTP and 7-nitroindazole (50 mg/kg) treatment. (e, l) 7 days after MPTP and 7-nitroindazole (50 mg/kg) treatment. (f, m) 3 days after MPTP and pargyline (15 mg/kg) treatment. (g, n) 7 days after MPTP and pargyline (15 mg/kg) treatment. Bar (a-g)= 50 μ m. Bar (h-n)= 50 μ m. n=5.



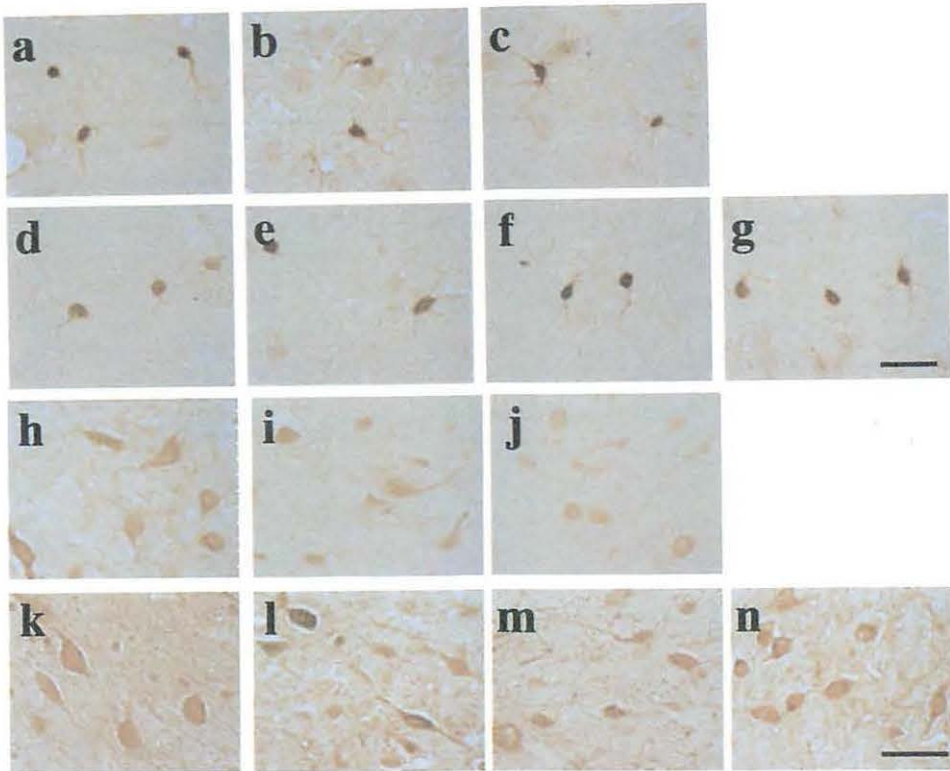


Fig. 3. Representative microphotographs of PV immunostaining in the mouse striatum (a-g) and substantia nigra (h-n) after MPTP treatment. (a, h) Control (vehicle) group. (b, i) 3 days after MPTP treatment. (c, j) 7 days after MPTP treatment. (d, k) 3 days after MPTP and 7-nitroindazole (50 mg/kg) treatment. (e, l) 7 days after MPTP and 7-nitroindazole (50 mg/kg) treatment. (f, m) 3 days after MPTP and pargyline (15 mg/kg) treatment. (g, n) 7 days after MPTP and pargyline (15 mg/kg) treatment. Bar (a-g)= 50 μ m. Bar (h-n)= 50 μ m. n=5.

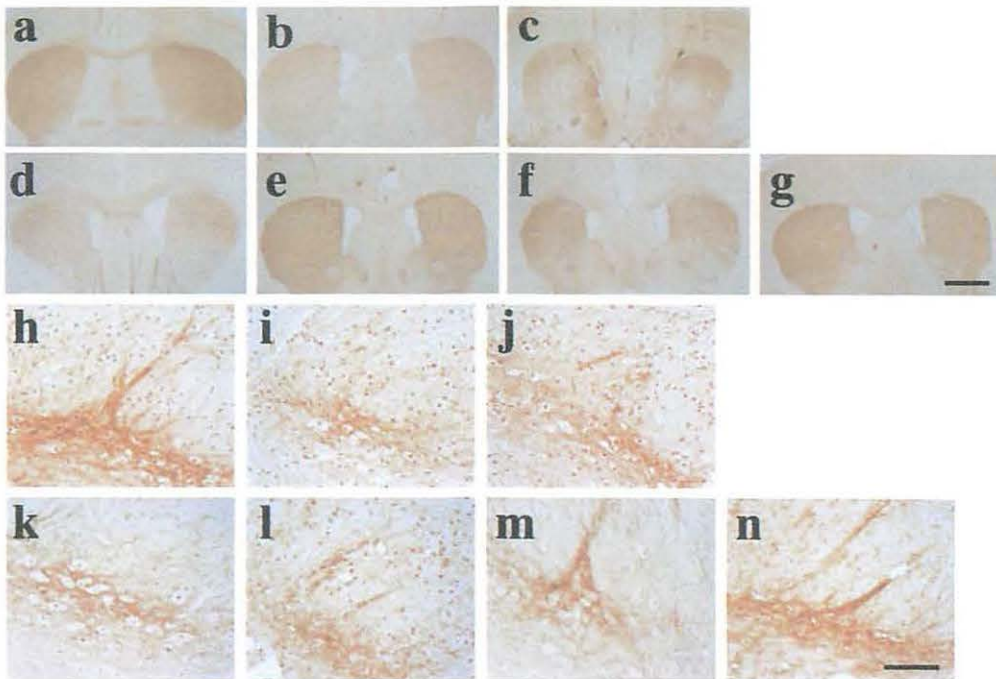
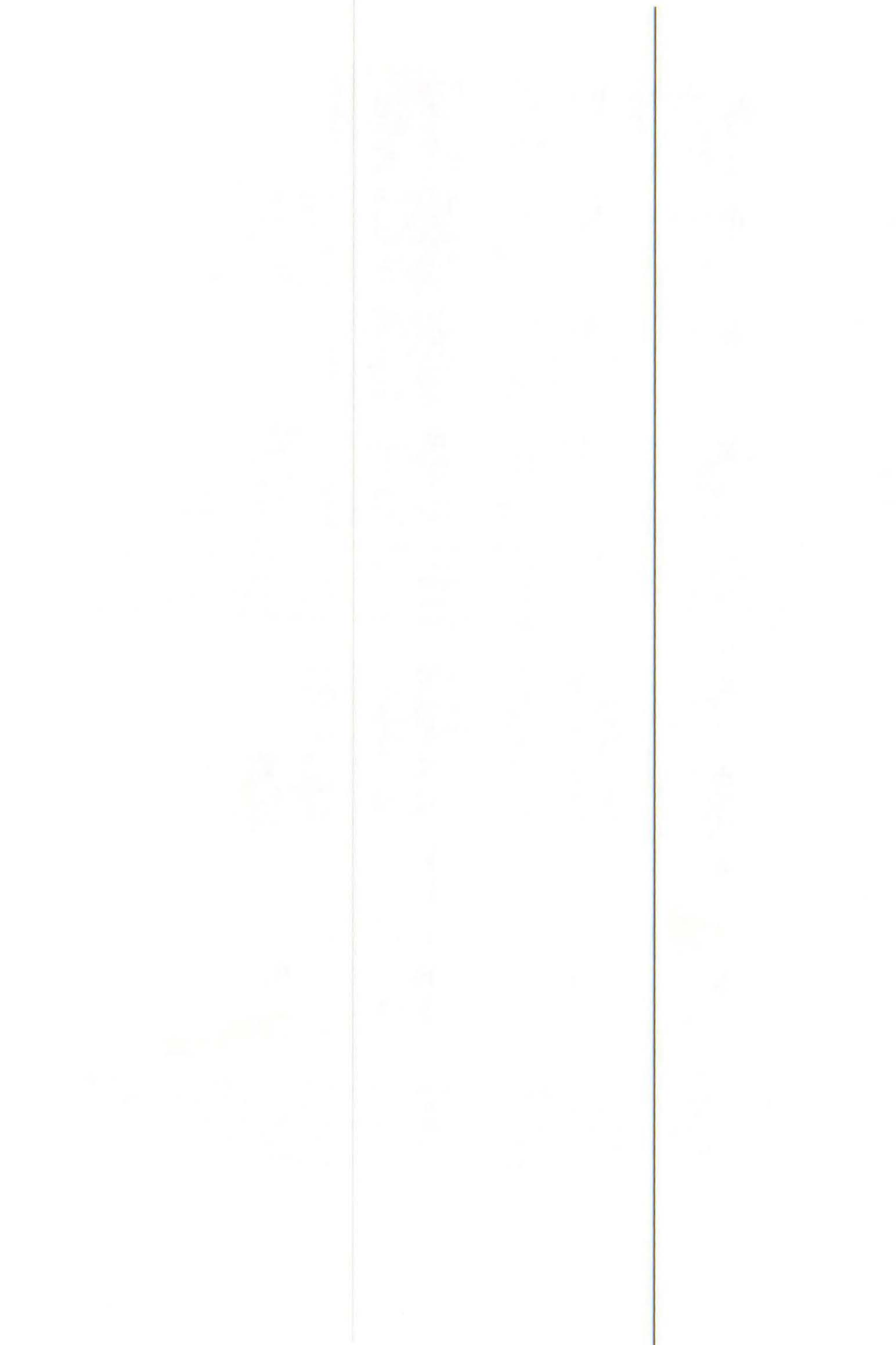


Fig. 4. Representative microphotographs of DAT immunostaining in the mouse striatum (a-g) and substantia nigra (h-n) after MPTP treatment. (a, h) Control (vehicle) group. (b, i) 3 days after MPTP treatment. (c, j) 7 days after MPTP treatment. (d, k) 3 days after MPTP and 7-nitroindazole (50 mg/kg) treatment. (e, l) 7 days after MPTP and 7-nitroindazole (50 mg/kg) treatment. (f, m) 3 days after MPTP and pargyline (15 mg/kg) treatment. (g, n) 7 days after MPTP and pargyline (15 mg/kg) treatment. Bar (a-g)= 1 mm. Bar (h-n)= 100 μ m. n=5.



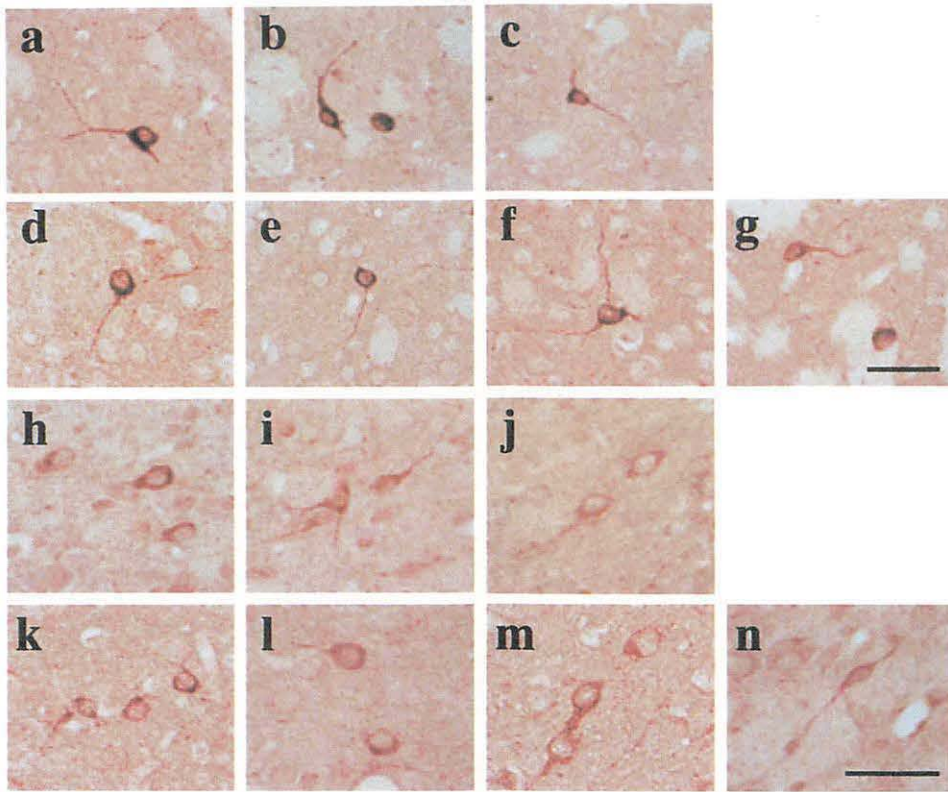


Fig. 5. Representative microphotographs of nNOS immunostaining in the mouse striatum (a-g) and substantia nigra (h-n) after MPTP treatment. (a, h) Control (vehicle) group. (b, i) 3 days after MPTP treatment. (c, j) 7 days after MPTP treatment. (d, k) 3 days after MPTP and 7-nitroindazole (50 mg/kg) treatment. (e, l) 7 days after MPTP and 7-nitroindazole (50 mg/kg) treatment. (f, m) 3 days after MPTP and pargyline (15 mg/kg) treatment. (g, n) 7 days after MPTP and pargyline (15 mg/kg) treatment. Bar (a-g)= 50 μ m. Bar (h-n)= 50 μ m. n=5.

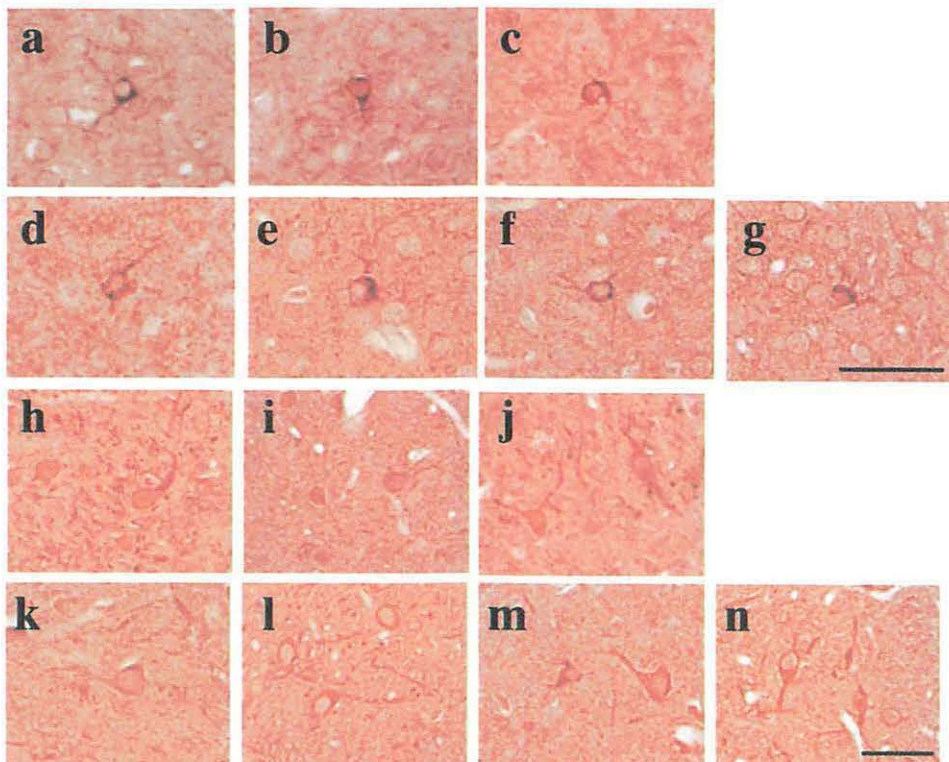
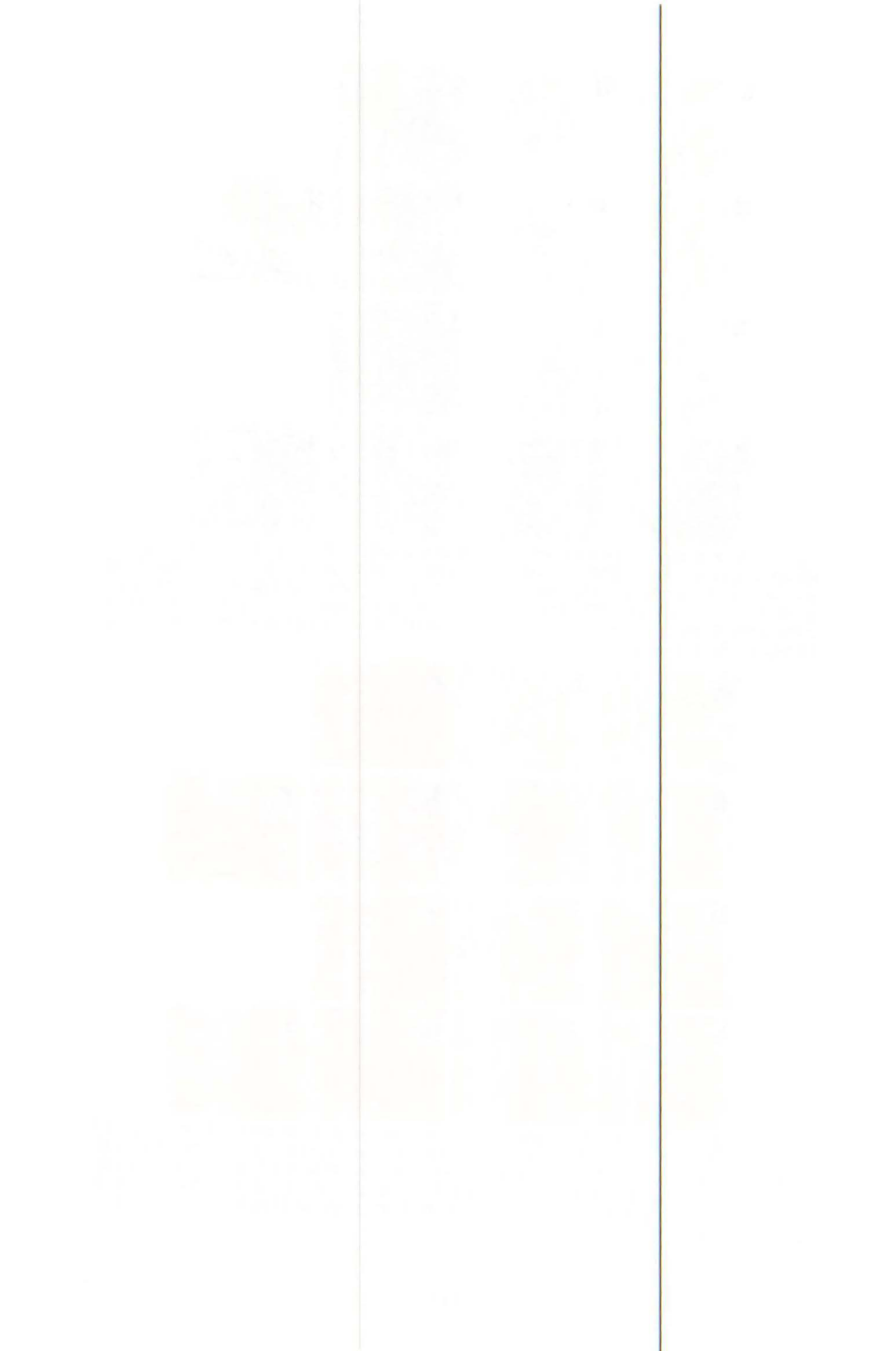


Fig. 6. Representative microphotographs of eNOS immunostaining in the mouse striatum (a-g) and substantia nigra (h-n) after MPTP treatment. (a, h) Control (vehicle) group. (b, i) 3 days after MPTP treatment. (c, j) 7 days after MPTP treatment. (d, k) 3 days after MPTP and 7-nitroindazole (50 mg/kg) treatment. (e, l) 7 days after MPTP and 7-nitroindazole (50 mg/kg) treatment. (f, m) 3 days after MPTP and pargyline (15 mg/kg) treatment. (g, n) 7 days after MPTP and pargyline (15 mg/kg) treatment. Bar (a-g)= 50 μ m. Bar (h-n)= 50 μ m. n=5.



IV. MEDICINE AND BIOLOGY (Clinical)

THE UNIVERSITY OF CHICAGO

IV. 1. Raclopride and FDG PET Findings in Two Patients with Alzheimer's Disease with Behavioral and Psychological Symptoms of Dementia

*Tanaka Y., Meguro K., Yamaguchi S., Yamadori A., Yamaguchi K., and Itoh M.**

*Division of Neuropsychology, Department of Disability Medicine,
Tohoku University Graduate School of Medicine
Division of Nuclear Medicine, Cyclotron Radioisotope Center, Tohoku University**

Introduction

Since the behavioral and psychological symptom of dementia (BPSD) such as wandering is a burden for family and caregivers, the neurobiological mechanism should be clarified. Using positron emission tomography (PET), we previously reported that wandering behavior in dementia was associated with decreased front-temporal glucose utilization and impaired striatal dopamine metabolism (decreased dopa uptake and increased D₂ receptor density)¹⁾.

Here, we investigated the relationship between the severity of BPSD and change of the striatal D₂ receptor in Alzheimer's disease (AD).

The tracers used were [¹¹C] raclopride (D₂ antagonist) and the [¹⁸F] FDG. The uptake of [¹¹C] raclopride was calculated as the binding potential (BP)²⁾ of the striatum to the cerebellum. Regional glucose utilization was measured according to the autoradiographic method³⁾. We evaluated their BPSD status by the BEHAVE-AD-FW scale⁴⁾.

Method

Subjects

Two patients with probable AD with moderate severity of dementia as per the NINCDS-ADRDA criteria⁵⁾ were studied. Neither patient showed visual symptoms, or extrapyramidal signs such as rigidity, and neither met the criteria for the clinical diagnosis of probable or possible dementia with Lewy bodies (DLB)⁶⁾.

The Medical Ethics Committee of the Cyclotron Radioisotope Center at Tohoku

University approved this study, and informed consent was obtained from all the subjects and their families.

Behavioral observations

The behavioral pathology in Alzheimer's disease rating scale referred to as the Behave-AD was specifically designed to assess BPSD that would be remediable to both psychologic and pharmacologic intervention⁷. We used this scale with frequency-weighted version.

[¹⁸F] FDG PET

The PET study was performed with a model PT-931 scanner (CTI Ind., USA: axial/transaxial resolutions; 6 mm), according to the [¹⁸F]-fluoro-deoxyglucose (FDG) method³. The procedure and the analysis for rCMRglc was the same as in previous study⁸. A total of 5 regions of interest (ROIs), round, 2.7 cm², in each hemisphere were placed manually. The rCMRglc values in the following bilateral regions were measured: bilateral upper frontal, temporal, parietal, temporoparieto-occipital (TPO), and hippocampus.

[¹¹C] Raclopride PET

The binding potential (BP) of D₂ receptors was assessed using a SET-2400 (Shimazu Ind.) camera and [¹¹C] raclopride as a radioligand. Scans were performed using 4-11 mCi of [¹¹C]-raclopride (1279-10438 Ci/mmol) following a bolus plus infusion protocol. PET data were acquired 40 to 70 minutes after injection, and data were corrected for decay and attenuation. Regions of interest (ROIs) were drawn on three adjacent slices for both the left and the right striatum (caudate and putamen), and for the cerebellum. The ratio of counts in the striatum and cerebellum (Eq. 1), during the period of pseudoequilibrium is used as an estimate of the Bmax/Kd of [¹¹C] raclopride for dopamine D₂ receptors⁹. This is justified on the grounds that the cerebellar (C) counts reflect non-specific binding and free ligand, whereas the striatal (S) counts reflect specific binding of the ligand to D₂ receptors in addition to the non-specific and free ligand binding. Using these assumptions, it can be shown that the (S-C)/C ratio reflects the ratio of Bmax/Kd, where Bmax is the total number of D₂ receptors and Kd is the affinity of the ligand^{10,11}. This measure is often referred to as the BP.

$$D_2 \text{ binding potential} = (S - C) / C \quad (1)$$

S: counts in the striatum, C: counts in the cerebellum.

Case Reports

Case A.A

A 68-year-old, female is in a nursing home since December 18, 2000. BEHAVE-AD-FW score was 17, and symptoms were mildly troubling to the caregiver. Her background history is uninformative on education. Her previous occupation included farmer, janitor of a school, and caregiver for elderly persons. Her previous medical history included bilateral femoral neck fractures, glucose intolerance, and transient ischemic thrombosis at the age of 46. She has not suffered from any mental disorder or manifested any psychotic symptoms earlier in life. In 1999, diurnal rhythm disturbance and inappropriate behaviors, especially inappropriate exposure started to appear. These symptoms worsened, and she was admitted to the specialized unit for dementia.

Neurological examination revealed no particular findings, there were no extrapyramidal signs, increased tone or other features of motor dysfunction. Neuropsychological assessment performed on September 2001, revealed cognitive decline. MMSE score was 4, and she obtained zero scale on Wechsler Adult Intelligence Scale-Revised, and she showed dressing apraxia. No clinical symptoms of depression were present.

Brain magnetic resonance imaging (MRI) revealed atrophy of the fronto-temporal cortices and hippocampus, with no evidence of ischemic lesions (Fig. 1).

Case S.K

SK is an 81-year-old woman with ten years of formal education. Her previous medical history includes hypertension only. She had been in good physical and mental health till 1994. According to her family, inappropriate behavior, especially aggression and inattention to personal hygiene, has been seen from the period. Since her husband was admitted in 2000, she changed her residence and lived together with her son's family. She attended adult day-care four times a week since June 2000, and her BEHAVE-AD-FW score was 18. Behavioral symptoms were severely troubling to the families.

She was referred to the Rehabilitation Department of Tohoku University Hospital, for evaluation and treatment of dementia. In January 2002, SK underwent a full

neuropsychological examination, showing a mildly poor cognitive profile, with short time memory deficit, and frontal executive function disorder. MRI showed no evident cortical atrophy (Fig. 2). Electroencephalogram, single photon emission computed tomography (SPECT) with [¹²³I] IMP and the FDG-PET study revealed frontal dysfunction.

Functional imaging study

Both patients underwent the raclopride and the FDG-PET studies. FDG-PET showed low metabolic activity of the bilateral fronto-temporal area in both patients (Fig. 3). And BP was 1.99 for right and 2.15 for left in SK, 1.71 for right and 1.89 for left in AA (Fig. 4,5).

Comments

Previous finding of decreased frontal glucose metabolism in BPSD patients was confirmed. The previous report 1) using the [¹¹C] YM09151-2, reported that wandering behavior in AD was correlated with increased levels of D₂ receptors. In this study we did not compare with the profiles of healthy controls, thus further research is needed in this point.

Recent PET studies in dopaminergic system reported that the striatal reuptake of dopamine was reduced with reference to extrapyramidal symptoms¹²⁾ and with regional CMRglc (Meguro et al. 1997). Another report ¹³⁾ said that there was no reduction in the uptake of [¹¹C] raclopride in the caudate nucleus of relatively early stage of AD. Provided we could compare the profiles with age and sex matched healthy controls in future study, we could mention that there would be a functional neural network or "loop" between the striatum and the fronto-temporal lobe. This network between the frontal cortex and striatum may relate with abnormal behavior in AD.

References

- 1) Meguro K., Itoh M., Yanai K., et al. *Eur. J. Neurol.* **4** (1997) 221-226.
- 2) Wadenberg M-L. G., Kapur S., Soliman A., Jones C., Vaccarino F., *Psychopharmacology (Berl)* **150** (2000) 422-429.
- 3) Phelps M.E., Huang S.C., Hoffman E.J., Selin C., Sokoloff L., Kuhe D.E., *Ann. Neurol.* **6** (1979) 371-388.
- 4) Reisberg B, Borenstein J, Salob SP, Ferris SH, Franssen E, Georgota A. *J Clin Psychiatry* **48** (1987) suppl.5: 9-15.
- 5) McKhann G., Drachman D., Folstein M., Katzman R., Price D., Stadlan E.M., *Neurology* **34** (1984) 939-944.
- 6) McKeith, L.G., Galasjo D., Kosaka K., et al., *Neurology* **47** (1996)1113-1124.

- 7) Reisberg B., Monteiro I., Boksay I., Auer S., Torossian C., Kenowsky S., *Int. Psychogeriat* **12** (2000) suppl.1: 155-164.s
- 8) Yamaguchi S., Meguro K., Itoh M., Hayasaka C., Shimada M., Yamazaki H., Yamadori A., *J. Neurol. Neurosurg. Psychiatry* **62** (1997) 596-600.
- 9) Logan J., Fowler J.S., Volkow N.D., Wang G.J., Ding Y.S., Alexoff D.L., *J. Cereb. Blood Flow Metab.* **16** (1996) 834-840.
- 10) Farde L., Hall H., Ehrin E., Sedvall G., *Science* **231** (1986) 258-261.
- 11) Kapur S., Zipursky R.B., Remington G., *Am. J. Psychiatry* **156** (1999) 286-293.
- 12) Rinne J.O., Sahlberg N., Ruottinen H., Nagren K., Lehtikoinen P., *Neurology* **50** (1998) 152-156.
- 13) Kempainen N., Ruottinen H., Nagren K., Rinne J.O., *Neurology* **55** (2000) 205-209.

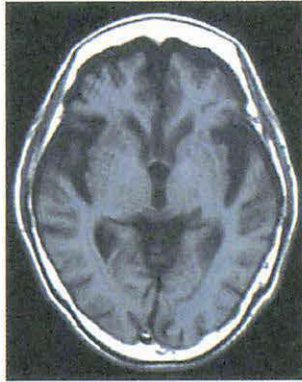


Fig. 1. AA's MRI (TR400, TE12) there is no remarkable infarction, and is cortical atrophy.

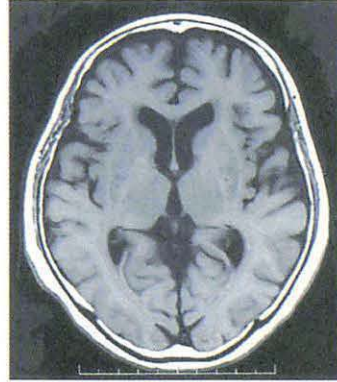


Fig. 2. SK's MRI (TR440, TE11) the cortical atrophy is mild, ventricle enlargement can be observed.

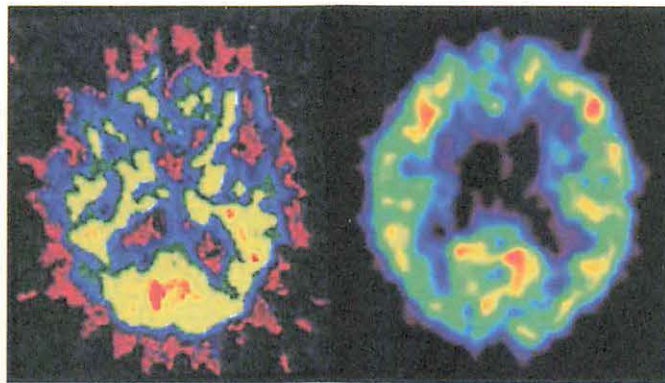


Fig. 3. FDG-PET, AA: left, frontal and parietal hypo-metabolism was seen, SK: right, frontal hypo-metabolism was seen.

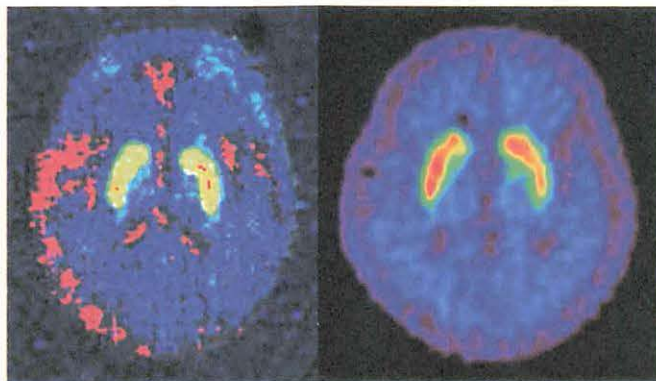
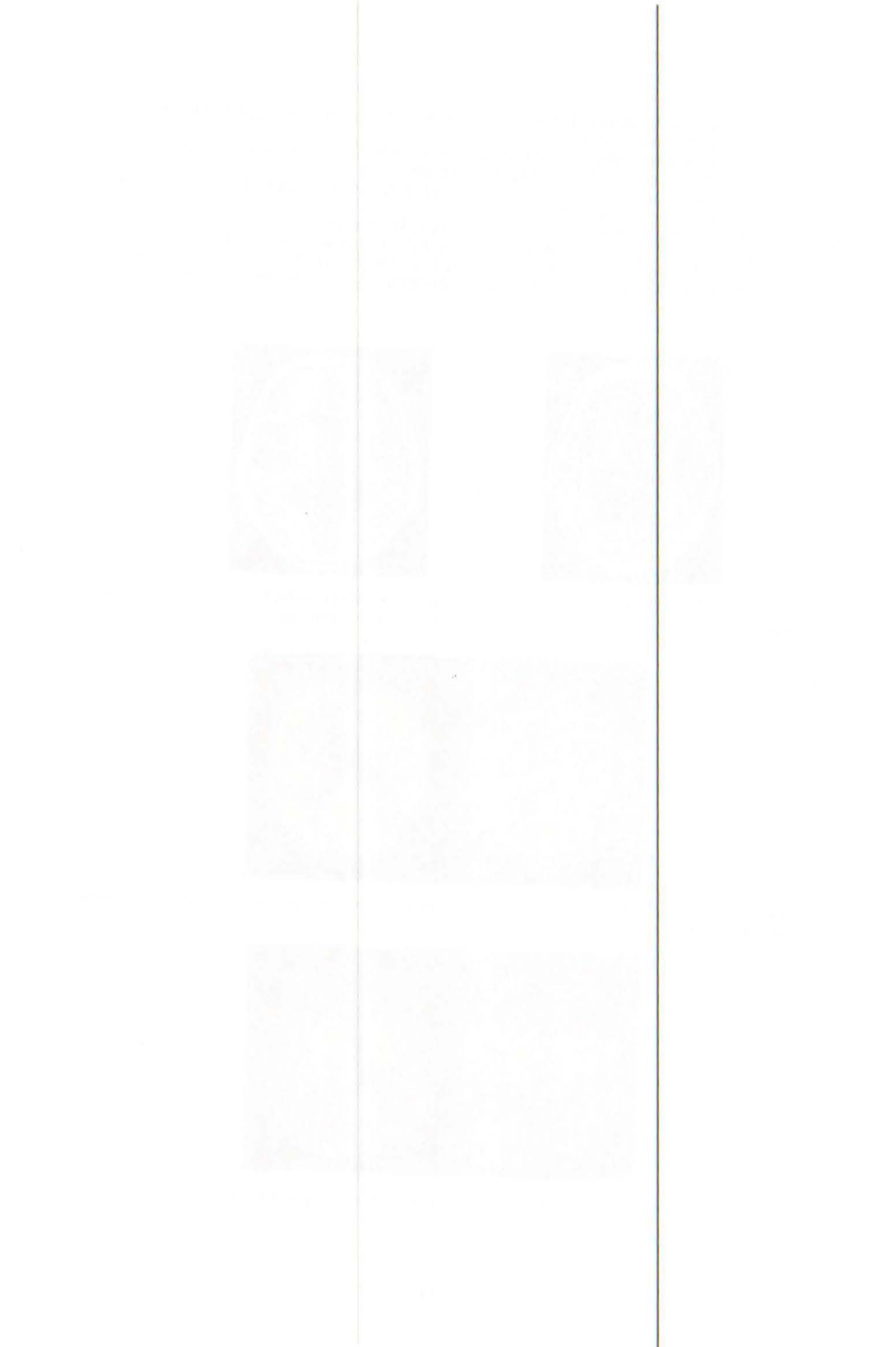


Fig. 4. Raclopride-PET, AA: left, SK: right. Symmetrical uptake was observed in striatal area for both patients.



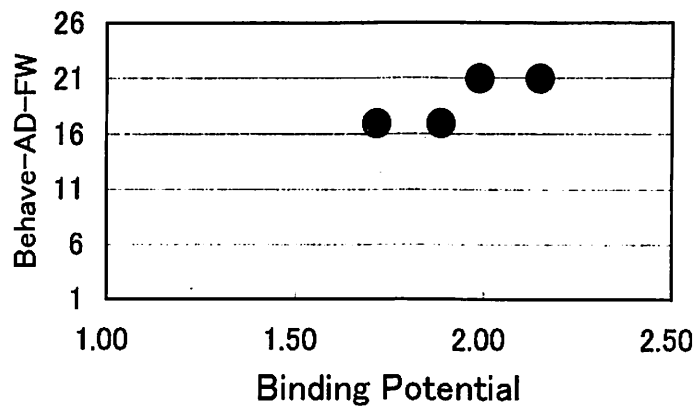


Fig. 5. Binding Potential and BEHAVE-AD-FW, no correlation can be seen in this data.

IV. 2. FDG-PET Study of Patient with a Novel Presenilin-1 Mutation in the Mild Cognitive Impairment Stage of Alzheimer's Disease

Maruyama M., Matsushita S.*, Arai H., Okamura N., Ohmori T.*, Takasugi K.*, Matsui T., Iwatsubo T.**, Higuchi S.* and Sasaki H.

*Department of Geriatric and Respiratory Medicine, Tohoku University School of Medicine
Division of Clinical Research, National Institute on Alcoholism, Kurihama National Hospital*
Department of Neuropathology and Neuroscience, Graduate School of Pharmaceutical Sciences,
University of Tokyo***

Introduction

Mild cognitive impairment (MCI) is a clinical state of individuals who are memory impaired but are otherwise functioning well and do not meet clinical criteria for dementia¹⁾. Although MCI is defined as an intermediate or transitional state from normal cognitive state to dementia, it is likely that MCI may represent a complex heterogeneous condition, and every MCI subject may not always develop Alzheimer's disease (AD) or other dementing disorders. With the arrival of the promise of drugs that may delay the progression of AD, an early and accurate detection of those who are destined to develop AD from a large pool of elderly people with MCI is of particular importance²⁾. Here, we report a 47-year old MCI subject with a novel presenilin-1 (PS-1) mutation (A431V) who eventually developed AD. We suggest use of positron emission tomography (PET) to aim at predicting the progression of the disease in the MCI stage of AD.

Report of a case

Case

A 47-year-old man from a family with early-onset dementia in different generations was referred to Kurihama National Hospital for evaluation of memory impairment. His wife noted that his father, paternal elderly sister, two younger sisters, and grandfather also suffered from dementia (Fig. 1). At the time of his reference, all his affected family members were deceased. After 16-year education, the man had worked as a commercial research specialist. Although he was functioning well and his colleagues had

reported no obvious job decline from previous levels, his wife had noted mild memory impairment for 3 years. Blood pressure was 122/81 mmHg, and neurological examination results were entirely normal. He complained of forgetfulness, and there was an obvious amnesia on semi-constructed interview by two experienced psychiatrists (S.M. and S.H.). He scored 29/30 on the Mini-Mental State Examination (MMSE) and FIQ 95, VIQ 107, and PIQ 80 on the Wechsler Adult Intelligence Scale-Revised. He was diagnosed as having MCI according to published criteria for MCI¹⁾. All baseline laboratory results, including examination of peripheral blood and blood biochemistry (urea nitrogen and creatinine, serum vitamin B₁₂ and folate levels), serologic tests for syphilis and for thyroid function, urine analysis, and chest radiography, were within normal ranges. Brain magnetic resonance imaging revealed no cortical atrophy. Follow-up examination revealed gradual progression of general cognitive functioning. Sixteen months after the initial assessment, the subject scored 20/30 on the MMSE due to failures not only in verbal memory, but also in orientation for time, calculation, and language. He was no longer able to continue his work as a research specialist was. He finally met diagnostic criteria for probable AD³⁾, and cholinesterase inhibitor therapy was started with a limited degree of benefit.

Methods and results

Molecular genetic analysis

We were not given a chance to obtain blood samples from a paternal sister and brother who were not yet affected. Data from both healthy control subjects (n=200) and sporadic AD patients (n=120) in our previous, published studies were employed for comparison⁴⁾. Genomic DNA was extracted from whole blood samples, and we amplified amyloid precursor protein (APP) exons 16 and 17 and the adjacent short stretch of their introns⁵⁾, PS1 exons 4-13 and their flanking introns⁶⁾, and presenilin-2 (PS2) exons 3-12 and their flanking introns⁷⁾ by polymerase chain reaction (PCR). The PCR products were purified in a microcolumn and sequenced using the Dye Terminator Cycle Sequencing Ready Reaction Kit with an ABI Prism 310 Genetic Analyzer automatic sequencer (Perkin Elmer Applied Biosystems, USA). The subject's A431V mutation (Alanine→Valine substitution at codon 431) in exon 13 was identified in the sense strand and confirmed by PCR restriction fragment length polymorphism. No known APP or PS-2 mutations were found. Apolipoprotein E genotype was homozygous for E3. Finally, we failed to find the mutation in blood samples from the subject's mother or from any of sporadic AD

subjects and elderly normal controls. (For further details, see Ref 8)

Positron emission tomography

At baseline, cerebral glucose metabolism was measured by PET using [^{18}F]fluorodeoxyglucose and a SET2400W PET scanner (Shimadzu Inc., Japan) as described elsewhere⁹. We compared the results with regional cerebral metabolic rate of glucose (CMRglu) measured in 11 Japanese patients with sporadic AD (4 males, 7 females; mean age \pm S.D., 66.5 ± 5.7 years, mean MMSE score \pm S.D., 18.8 ± 3.3) and 10 normal Japanese controls (4 males, 6 females; mean age \pm S.D., 65.0 ± 8.0 years). The normalized CMRglu values were also calculated using the cerebellar vermis as a reference region. Absolute CMRglu values in the whole brain were 5.94 mg/100g/min in the present case, 3.66 ± 1.26 mg/100g/min in sporadic AD group and 7.52 ± 1.20 mg/100g/min in normal control group. As shown in Fig. 2, the normalized CMRglu values in the posterior cingulate gyrus, posterior and lateral parietal cortices, and medial temporal regions were lower compared to those of normal elderly subjects with relative sparing of the lateral frontal, lateral temporal, and occipital areas.

Discussion

Several independent groups have reported the reduction of cerebral glucose metabolism or cerebral perfusion in the posterior cingulate and posterior parietal cortices in very early stages of sporadic AD^{10,11}. Compared with the sporadic cases, the present case with PS-1 mutation demonstrated further extensive glucose hypometabolism in posterior cortical region. This finding suggests that the severer brain damage will take place in the MCI subject who has genetically high risk for dementia than in the sporadic case.

Although alanine \rightarrow glutamate substitution at codon 431 of PS-1 gene (A431G) has been recently reported¹², alanine \rightarrow valine substitution at the same codon (A431V) in the present study was a novel mutation. Hüll et al. reported that there was a slightly reduced perfusion on SPECT in the left temporal region in a case with PS-1 mutation at codon 139¹³ when the MMSE score was 24 points. Another study by Hong et al. described a case with PS-1 mutation at codon 163 impairing glucose metabolism on PET in bilateral temporo-parietal association cortex when the MMSE score was 25 points¹⁴. Finally, Johnson et al. examined 18 asymptomatic carriers of a PS-1 mutation at codon 280 from a large AD family when an average MMSE score of these participants was 27.7 points, and they

showed reduced perfusion on SPECT in the medial temporal, anterior and posterior cingulate, posterior parietal, and superior frontal regions¹⁵. Although the clinical severity of cognitive impairment may not be exactly comparable among these patients, it is likely that different mutations in the PS-1 gene may produce a different spatial pattern of pathology and metabolic deficits.

References

- 1) Petersen R.C., Smith G.E., Waring S.C. et al., *Arch Neurol* **56**, 303-308 (1999).
- 2) Doody R.S., Stevens J.C., Beck C. et al, *Neurology* **56**, 1154-1166 (2001).
- 3) McKhann G., Drachman D., Folstein M. et al, *Neurology* **34**, 939-944 (1984).
- 4) Higuchi S., Yoshino A., Matsui T., et al, *Alzheimer's Reports* **3**, 227-231 (2000).
- 5) Hattori M., Tsukahara F., Furuhashi Y. et al., *Nucleic Acids Res* **25**, 1802-1808 (1997).
- 6) Rogaeve E.I., Sherrington R., Wu C. et al., *Genomics* **40**, 415-424 (1997).
- 7) Levy-Lahad E., Wasco W., Poorkaj P. et al., *Science* **269**, 973-977 (1995).
- 8) Matsushita S., Arai H., Okamura N. et al., *Biol Psychiatry* in press (2002)
- 9) Higuchi M., Tashiro M., Arai H. et al., *Exp Neurol* **162**, 247-256 (2000).
- 10) Minoshima S., Giordani B., Berent S. et al., *Ann Neurol* **42**, 85-94 (1997).
- 11) Okamura N., Arai H., Maruyama M. et al., *Am J Psychiatry* **159**, 474-476 (2002).
- 12) Rogaeve E.A., Fafel K.C., Song Y.Q. et al., *Neurology* **57**, 621-625 (2001).
- 13) Hill M., Fiebich B.L., Dykieriek P. et al., *Eur Arch Psychiatry Clin Neurosci* **248**, 123-129 (1998).
- 14) Hong K.S., Kim P., Na D.L. et al., *Biol Psychiatry* **42**, 1172-1176 (1997).
- 15) Johnson K.A., Lopera F., Jones K. et al., *Neurology* **56**, 1545-1551 (2001).

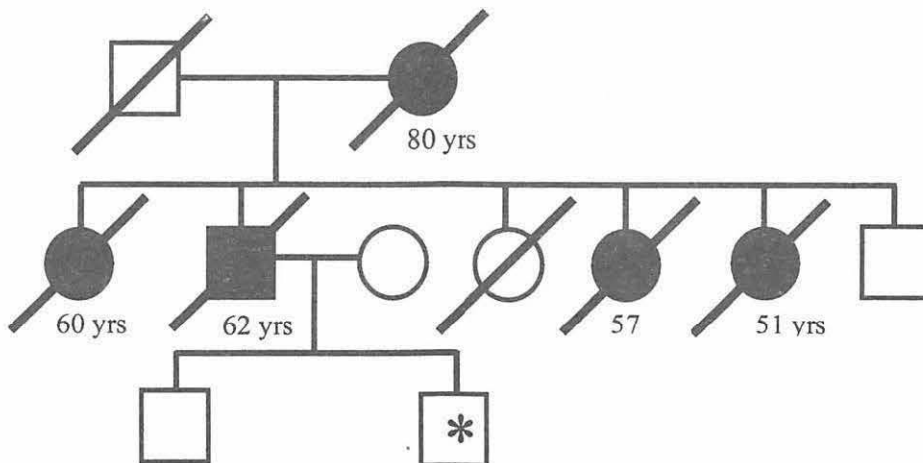


Fig. 1. Family pedigree. □: unaffected male; ○: unaffected female; ■: affected male; ●: affected female; /: deceased; *: proband.

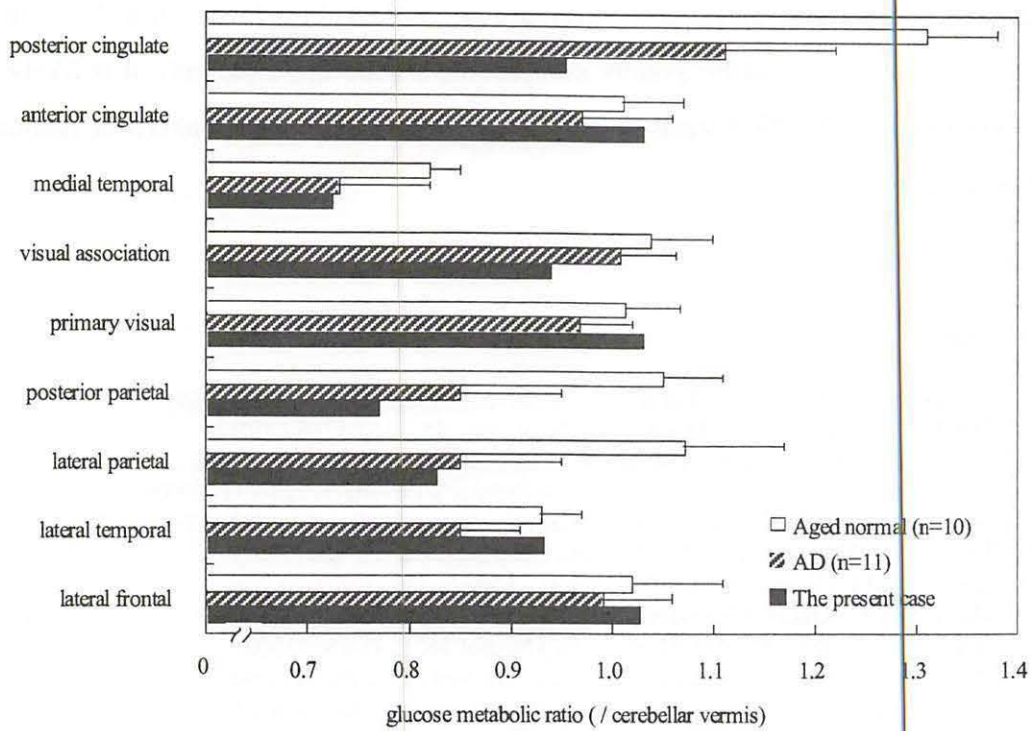


Fig. 2. Baseline regional cerebral metabolic rate for glucose measured by positron emission tomography and [¹⁸F]-fluorodeoxyglucose. These values were compared with those of 11 Japanese patients with sporadic AD (dashed column) and 10 cognitively normal age-matched Japanese controls (open column) as described by Higuchi M. et al 2000. Values are mean ± S.D.

IV. 3. Imaging of Histamine H1 Receptors in Human Brain and Impaired Cognitive Performance Induced by Second Generation Antihistamines

*Tashiro M., Mochizuki H., Sakurada Y.,
Iwabuchi K., Kato M., Itoh M.*, and Yanai K.*

*Department of Pharmacology, Tohoku University Graduate School of Medicine,
Division of Nuclear Medicine, Cyclotron and Radioisotope Center**

Introduction

Histamine plays important roles in various physiological functions of immune, gastrointestinal and nervous systems. In the immune system, histamine is released by mast cells and trigger type-I allergic reactions causing urticaria and seasonal rhinitis, etc. In the gastrointestinal system, histamine is associated with secretion of gastric acid. In the peripheral nervous system, it is involved in perception of pain and itchiness. In the central nervous system, it is associated with a wide range of functions such as arousal, cognition, learning and memory, regulation of sleep-wake cycle, appetite control, seizures, aggressive behaviors, and so on mainly through histamine H1 receptors (H1R).

Histaminergic neurons are exclusively located in the tuberomamillary nucleus of the posterior hypothalamus. They are projecting to almost all regions of the brain¹⁾. Arousal and cognition are among the main roles of brain histamine and H1R. These functions could be well demonstrated by a fact that histamine H1R antagonists, or antihistamines (AH), prescribed for treatment of allergic disorders, often induce sleepiness and psychomotor deficits²⁻⁴⁾. The mechanism causing such CNS side effects has been understood that AHs, penetrating brain blood barrier (BBB), occupies H1Rs in the brain. Classical first generation AHs often have significant sedative effects, while AHs of newer generations tend to be less sedative. Evaluating side effects of different AHs is of clinical and social importance because they sometimes induce car accidents etc. Since measurement of subjective sleepiness was not always reliable, various objective testing methods have been introduced. We have been utilizing positron emission tomography

(PET) with ^{11}C -doxepin as a radioactive ligand to understand the roles of H1Rs in the living human brain²⁻⁵). In this report, we demonstrate results of comparative study on different second generation AHs using PET.

Methods

In the present study, subjective sleepiness was measured using Stanford Sleepiness Scale (SSS)⁶, and psychomotor performance was examined using a tachistoscope testing system (Iwatsu Inc., Japan)^{2,3} in healthy young Japanese volunteers ($n = 16$, ranging 20-28 years old). Measurement was done twice; before and 90 min after oral administration of each AHs such as fexofenadine 120mg (FEX: a non-sedative AH introduced recently) and cetirizine 20mg (CET: a slightly sedative second generation AH) at both maximum doses per day in Japan, and hydroxyzine 30mg (HYD: a sedative AH which served as a positive control in this study), in a double-blind placebo controlled crossover design. In this testing procedure, each subject was requested to sit on a chair, facing to a computer display in which target stimuli were presented. The subjects were requested to hold a button in their each hand and to press a right/left button immediately after the target stimulus appeared in the corresponding side of the display, respectively (choice reaction task, in short, CRT), as well as they were requested to press a right button each time the target stimulus was presented in the display regardless of its laterality (simple reaction task, in short, SRT). Additionally, the subjects were requested to press the right button only when Arabic numerals were presented in the display and to ignore when hiraganas (Japanese phonetic alphabets) were presented (visual discrimination task, in short, VDT). This VDT consisted of 4 sessions with different exposure durations of target stimuli (3,5,7 and 20 millisecond). The appearing order of exposure durations was randomized.

Additionally, 10 out of the 16 volunteers were also examined by PET with ^{11}C -doxepin for measurement of histamine H1 receptor occupancy (H1RO). H1RO values were calculated by Logan's graphical analysis from binding potential (BP) images obtained from 90 min-dynamic scan images^{3,4}. Finally, Scores of SSS, reaction time in psychomotor tests measured by the tachistoscope system, and H1RO measured by PET were statistically examined between FEX and CET using ANOVA followed by multiple comparisons by Glanz test.

Results

The results of SSS and psychomotor tests demonstrated that FEX seemed to be less sedative than CET though the difference was at threshold level (Fig. 1). PET investigation revealed that almost no H1R in the cerebral cortex were occupied by FEX while CET occupied approximately 20 to 50% of H1Rs ($p < 0.01$) (Fig. 2). Measurement of histamine H1RO by PET seemed to be one of the most reliable techniques to evaluate CNS side effects of different AHs.

Discussion

Roles of brain H1R have been thought to exist in arousal and cognition^{3,7)}, learning and memory, seizures⁸⁾, pain perception⁹⁾, and so on. To understand functions of specific proteins such as H1R, knockout mice experiment is useful and can provide an ideal opportunity to analyze the specific functions of individual mammalian genes. Homozygous H1R knockout mice manifested significantly diminished diurnal variation in locomotor activity in contrast to significant variation in wild-type mice¹⁰⁾. Scientific investigations on H1 knockout mice have significant merits although brain histamine's roles equivalent to humans are not always deduced. It would be important to take both animal and human findings into consideration before drawing conclusions on each specific receptors.

As for the human study, positron emission tomography (PET) is one of ideal tools that enables us to obtain biochemical and physiological information non-invasively. Neuroreceptor imaging with PET is important because currently no other device would be able to substitute. ¹¹C-doxepin has been a potent molecular tool to visualize distribution of H1R in human brain^{2,7)}. Our present and previous studies with AHs have demonstrated that histamine is playing very important roles in maintaining arousal and good psychomotor performance in human.

In general, newly introduced second generation AHs occupy 10 to 50% while classical first generation AHs occupy 50 to 80% of H1Rs in the brain²⁻⁴⁾. Fexofenadine (FEX) manifested much lower H1RO (0%) and milder sedation than cetirizine (CET), one of typical second-generation AHs (Fig. 1 and 2). It is easy to understand that sedative side effects of AHs are induced by blockade of H1R by AHs since severity of the side effects correlated to H1RO. Difference in H1RO among different AHs would be because of different permeability of AHs to penetrate BBB, regulated by influx and efflux proteins

such as p-glycoprotein.

In summary, roles of histamine and H1R in arousal and cognition were confirmed both in knockout mice and in human subjects. PET with ^{11}C -doxepin seems to be a more sensitive tool than psychomotor testing for differential comparisons of A/Hs.

References

- 1) Watanabe T., Taguchi Y., Shiosaka S., et al., *Brain Research* **295** (1984) 13-25.
- 2) Yanai K., Ryu J.H., Watanabe T., et al., *British Journal of Pharmacology* **116** (1995) 1649-1655.
- 3) Okamura N., Yanai K., Higuchi M., et al., *British Journal of Pharmacology* **129** (2000) 115-123.
- 4) Tagawa M., Kano M., Okamura N., et al., *British Journal of Pharmacology*, **53** (2002) 296-304.
- 5) Yanai K., Watanabe T., Yokoyama H., et al. *Neuroscience Letters* **137** (1992) 145-148.
- 6) Hoddes E., Zarcone V., Smythe H., et al., *Psychophysiology* **10** (1973) 431-436.
- 7) Yanai K., Okamura N., Tagawa M., et al., *Clinical & Experimental Allergy* **29** Suppl. 3 (1999) 29-36.
- 8) Iinuma K., Yokoyama H., Otsuki T., et al., *The Lancet* **341** (1993) 238.
- 9) Mobarakeh J.I., Sakurada S., Katsuyama S., et al., *European Journal of Pharmacology* (1-2)(2000) 81-89.
- 10) Inoue I., Yanai K., Kitamura D., et al., *Proceedings of the National Academy of Sciences of United States of America* **93** (1996) 13316-13320.

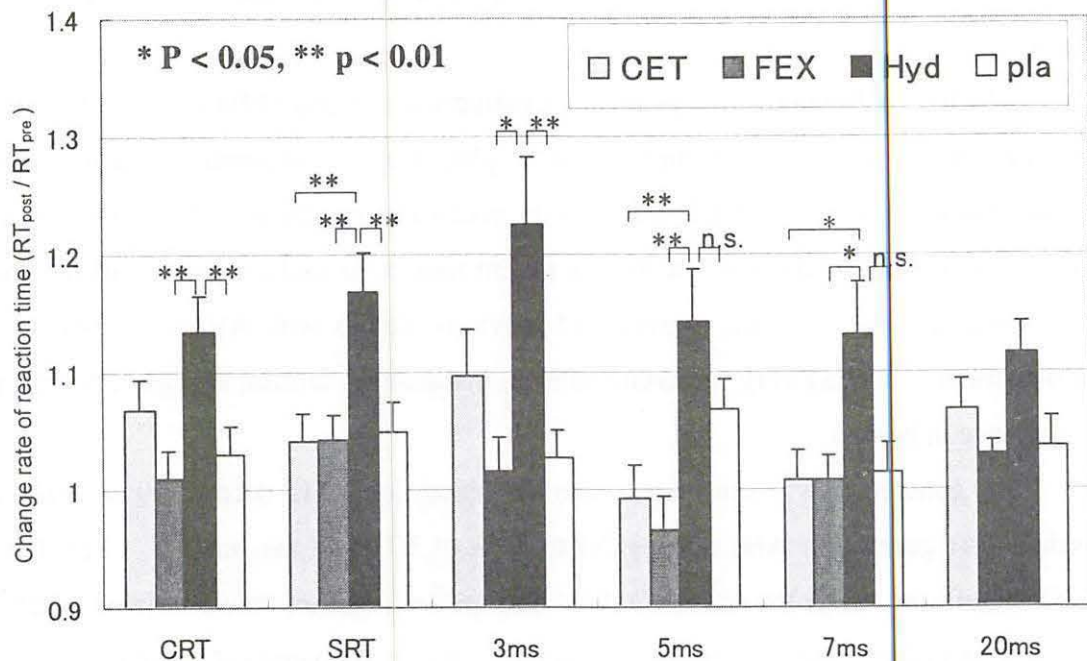


Fig. 1. Results of visual discrimination task (VDT). Results of response time (RT) measurement are demonstrated (n = 16). The change rates in RT in each subject were obtained by dividing RT_{post} by RT_{pre} . (* $p < 0.05$, ** $p < 0.01$. Statistical examination was done by ANOVA followed by multiple comparisons)

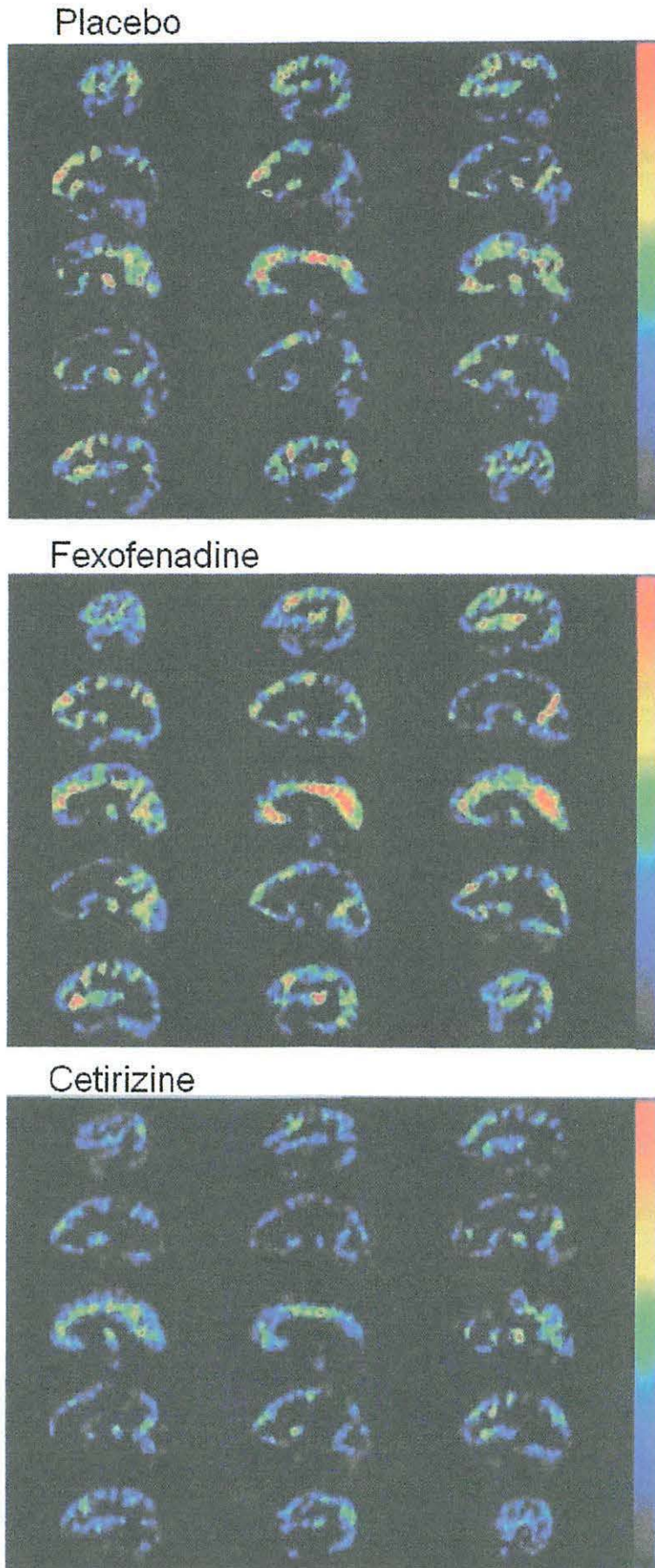


Fig. 2. Brain images demonstrating differences in binding potentials after administration of different antihistamines, fexofenadine and cetirizine and placebo (sagittal slice). Binding potential of fexofenadine is equal to that of placebo, while that of cetirizine is lower than those of both placebo and fexofenadine.

Blank page with a vertical line on the right side.

Blank page with a vertical line on the right side.

Blank page with a vertical line on the right side.

IV.4. Neural mechanism of impaired visuomotor coordination by sedative antihistamine: A human PET study

*Mochizuki H. *, Tashiro M. *, Kano M. *, Itoh M. **, and Yanai K. **

Department of Pharmacology, Tohoku University School of Medicine
Cyclotron and Radioisotope center, Tohoku University***

Introduction

The histaminergic system has been considered to maintain general cortical activation during arousal state through the activation of histamine H1 receptors (H1R)¹. The first-generation antihistamines, including d-chlorpheniramine, induce sleepiness by blocking H1R in the central nervous system (CNS). These drugs also impair various cognitive functions such as psychomotor speed and verbal learning due to the H1R blockade^{2,3}. It was speculated that main factors of the impaired cognition and behaviors after the treatment of antihistamines was related to central nervous system (CNS). So we investigated the mechanism of cognitive and behavioral impairments induced by d-chlorpheniramine in human brain using PET and [¹⁵O]H₂O .

Materials and Methods

Subjects

Sixteen healthy male volunteers, ranging 21-24 years old (mean +/- S.D.: 22.5 ±1.2 y.o.), participated in this study. Written informed consent was obtained from each subject and the study was performed in compliance with the relevant laws and institutional guidelines.

Spatial discrimination task

In the present study, a spatial discrimination task was adopted for evaluation of visuomotor coordination. Subjects were asked to press the button with the left or right index finger promptly when the stimulus appeared in the corresponding side of the display. These stimuli were generated by AV tachistoscope (IS701A, Iwatsu, Japan).

Study design

Sixteen subjects were randomly assigned to the following 2 groups: the chlorpheniramine (CG) and placebo groups (PG). On the experiment day, subjects of the PG received placebo and the CG received 6 mg d-chlorpheniramine (Repetabs). In the first PET scanning session, subjects were asked to gaze a fixation point which appeared in the center of the display. Followed inter-scan interval of about 10min, spatial discrimination tasks were assigned. Reaction time (RT) was measured in order to assess the effect of d-chlorpheniramine during spatial discrimination task. Subjective sleepiness was evaluated just after each scan, using the Stanford Sleepiness Scale (SSS), composed of a 7-level self-report measurement⁴).

PET measurements and data analysis

The rCBF images were obtained using a 3D-acquisition PET scanner (Shimadzu SET-2400W, Japan).

The rCBF images obtained were realigned, normalized and smoothed by Statistical Parametric Mapping (SPM) software (SPM96; Wellcome Department of Cognitive Neurology, London, U.K.)⁵. *t*-Statistics were computed for each voxel for the comparisons: (1) [spatial discrimination task] minus [fixation] in the PG and CG, (2) [the PG] minus [the CG] during spatial discrimination task. For each comparison, voxels with Z-value higher than 3.01 was considered to represent the regions with significant changes in rCBF.

SSS scores and RTs, measured additionally to PET scanning, were also analyzed and compared between the PG and CG with *t*-statistics. Statistical threshold for each test was defined as $p < 0.05$.

Results

Subjective feeling and objective performance:

Subjective sleepiness measured just after fixation task was significantly higher in the CG (mean \pm S.D. of SSS scores: 4.4 ± 0.7) compared to the PG (mean \pm S.D.: 3.0 ± 1.2) ($p < 0.05$). Subjective sleepiness just after spatial discrimination task was significantly higher in the CG (mean \pm S.D.: 4.4 ± 0.8) compared to the PG (mean \pm S.D.: 3.4 ± 0.9) ($p < 0.05$). RT during spatial discrimination task was significantly prolonged in the CG

(mean \pm S.D.: 0.28 ± 0.03 sec) compared to the PG (mean \pm S.D.: 0.32 ± 0.04 sec) ($p < 0.05$).

PET studies:

During the spatial discrimination task, the PG showed the rCBF increase in the right parietal cortex (BA 40), right cingulate gyrus (BA 24) and in the left cerebellum as shown in Fig.1.A and Table1. Changes of brain activities during spatial discrimination were also examined before and after oral administration of d-chlorpheniramine. The comparison revealed that the activation in the BA 24 was significantly increased in the CG than in the PG ($p < 0.001$ $Z > 3.01$), and that the activation in the BA 40 was significantly decreased in the CG than in the PG ($p < 0.001$ $Z > 3.51$) (Fig.1.B and C and Table1).

Discussion

There are many reports concerning the effect of *d*-chlorpheniramine, a first generation antihistamine⁶. A previous performance study demonstrated that d-chlorpheniramine induced an increased sleepiness, prolonged reaction time, functional deterioration in the visuomotor coordination, learning ability, memory and so on (Nicholson, 1985). The aim of this study was to elucidate the mechanism of the impaired cognition and behavior in sedative condition induced by d-chlorpheniramine using PET with [¹⁵O]H₂O.

The significant activation in PG during spatial discrimination task was observed in the right cingulate gyrus (BA 24), right anterior parietal cortex (BA 40) and in the cerebellum (Fig.1.A).

Activation of BA 40 during spatial discrimination task was significantly weaker in CG than in PG (Fig.1.B). Patients with lesions in the anterior parietal cortex manifested a decrease in regularity of exploratory finger movements⁷. It was suggested that activation of BA 40 was associated with finger movements following visual stimuli in spatial discrimination tasks. Deterioration in task performances in CG would be attributed to the decreased activation of BA 40.

On the other hand, activation in BA 24 was more intense in CG than in PG. As shown in Fig.1.C, the enhanced activation of the cingulate cortex was posterior part. Deiber also argued that the posterior region of cingulate gyrus might be associated with selection of correct motor outputs based on spatial attention⁸. Thus, the enhanced activation in the

posterior part of BA 24 would reflect compensation mechanism for the deterioration in task performances due to antihistamines.

These findings indicated that the alteration in the cortical activity would be related to the impaired spatial cognition caused by treatment of d-chlorpheniramine.

Acknowledgements

This work was supported by grants-in-aid from the Ministry of Education, Science, Sports and Culture, and the Ministry of Health and Welfare, Japan. We appreciate technical assistance of Mr. M. Miyake, Y. Ishikawa and S. Watanuki in PET studies.

References

- 1) Lin J, Sakai K, Jouvet M. *Neuropharmacology* **27** (1988) 1523-1537.
- 2) AN. *Aviat. Space Environ. Med* **56** (1985) 1870-1877.
- 3) Adelberg BR. *Archives of Internal Medicine* **157** (1997) 494-500.
- 4) Hoddes E, Zarcone V, Smythe H, Phillips R, Dement WC. *Psychophysiology* **10** (1973) 431-436.
- 5) Friston KJ, Ashburner J, Frith CD. *Hum Brain map* **3** (1995) 165-189.
- 6) Nolen TM. *Clin Ther* **19** (1997) 39-55.
- 7) Binkofski F, Kunesch E, Classen J, Seitz RJ, Freund. *HJ.Brain* **124** (2001) 132-144.
- 8) Deiber MP, Ibanez V, Sadato N, Hallett M. *J Neurophysiol* **75** (1996) 233-247.

Table 1. Brain regions related to spatial discrimination task, and alteration of their activity after the administration of d-chlorpheniramine.

Brain regions	Areas of significant increase of rCBF during the spatial discrimination task			The effects of d-chlorpheniramine	
	BA	axis (x,y,z)		activation	Z score
left cerebellum		52	-69 -25		6.17
right cingulate cortex	24	22	-16 36	increase	5.29
right parietal cortex	40	61	-60 38	decrease	4.75

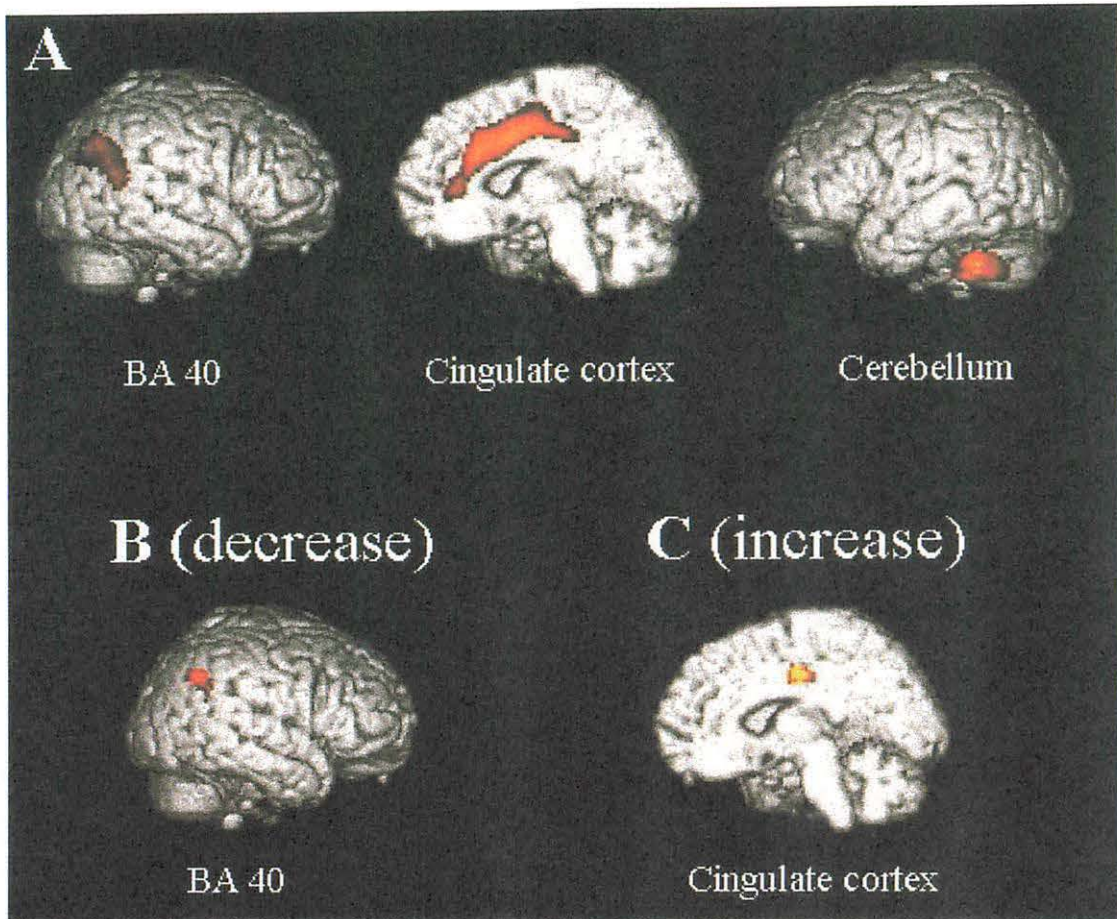
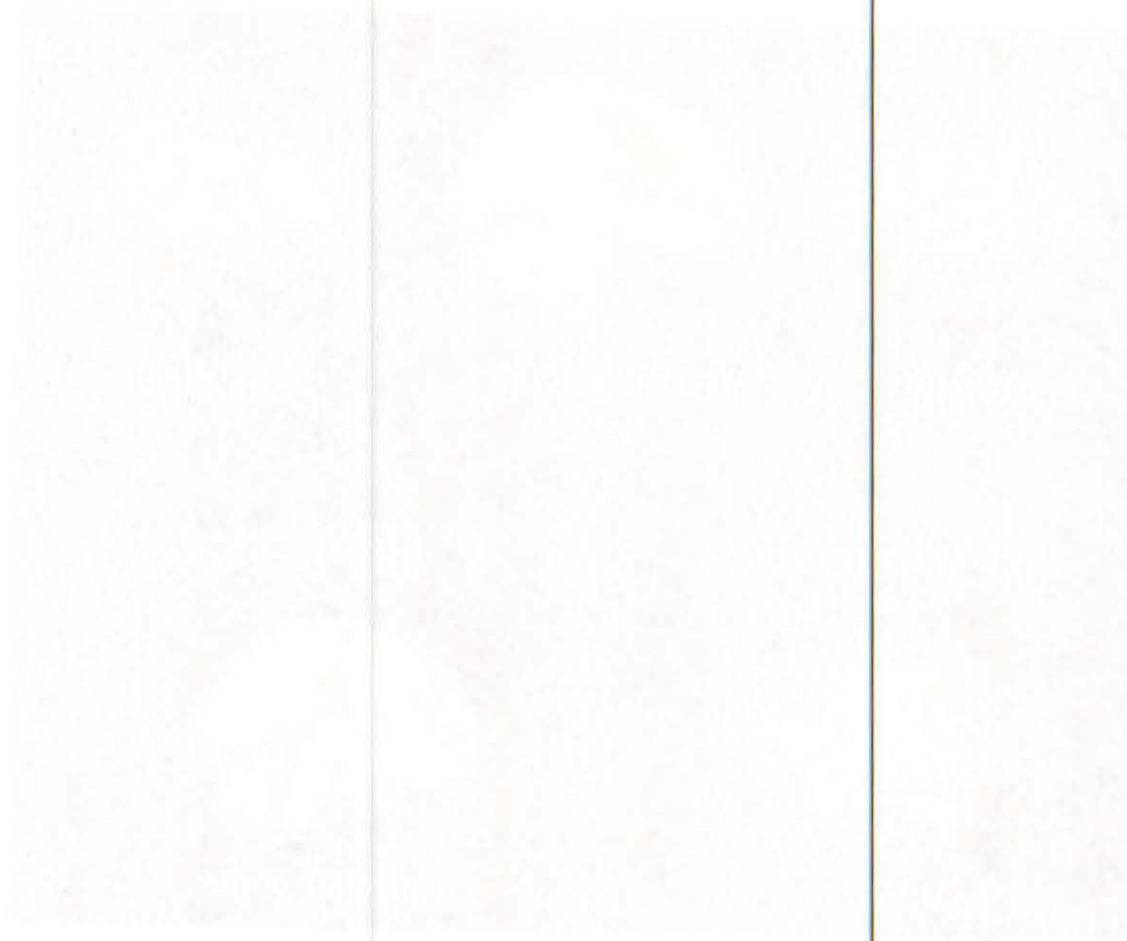
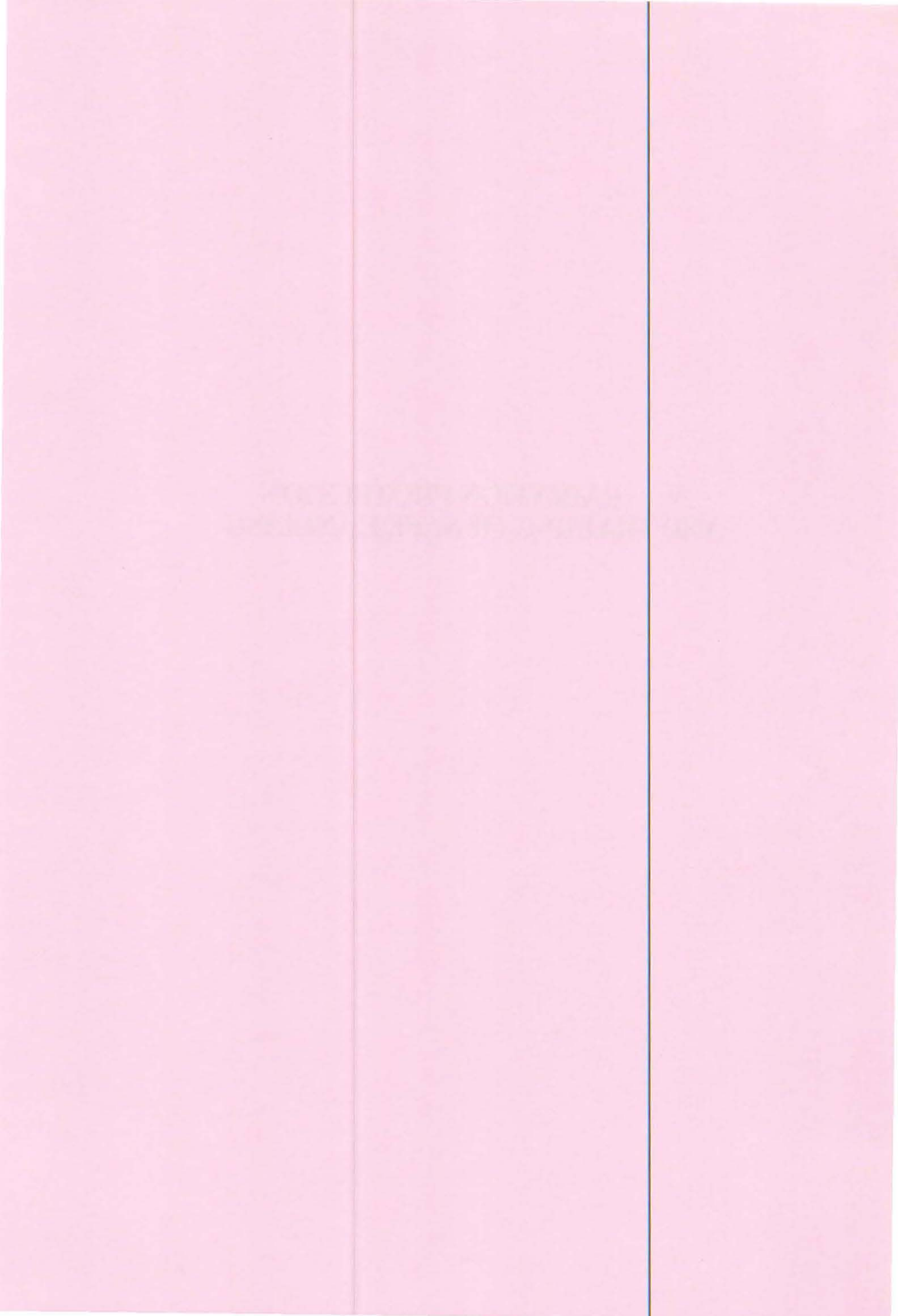


Fig. 1. (A)The significant increases of rCBF during spatial discrimination task. Decreased (B) and increased (C) activations related to spatial discrimination task after the administration of d-chlorpheniramine.



**V. RADIATION PROTECTION
AND TRAINING OF SAFE HANDLING**



V. 1. Application of an Imaging Plate to Radiation Dosimetry

*Ohuchi H. and Yamadera A.**

*Graduate School of Pharmaceutical Sciences, Tohoku University,
School of Health Sciences, Hirosaki University**

Introduction

In the sensitive layer of an imaging plate (IP) composed of BaFBr:Eu²⁺ phosphors, ionizing radiation creates a large amount of trapped centers, which record information about the deposited energy and its position. The IP has many advantages as a detector of two-dimensional images, and has been utilized in a number of fields¹⁾. However, there are relatively few reports of applying IPs for quantitative use²⁾. The reason for this is that IPs have a large fading effect. That is, some charges stay trapped at localized defects but some recombines with holes after irradiation for a time, depending on the temperature and the activation energy of the traps. This results in a serious problem in developing an IP into an integral-type detector. We have continued our study³⁻⁵⁾ of measuring the fading characteristics and have observed that the fading effect increases as both the temperature and the time following irradiation increase. Considering that thermally released electrons from the F centers are dominant in the fading process, we successfully developed equations as a function of elapsed time (t) and absolute temperature (K) to correct the fading. We have also investigated the dependence of the fading effect of IP on alpha, beta, and gamma radiation and their energies by using three types of IPs: BAS-UR, BAS-TR, and BAS-MS. We found that in all types of IPs the fading effect is independent of the energy of the incident particles of beta and gamma rays. The fading effect was also independent of radiation, except for the first component, which fades out very quickly after irradiation with alpha rays⁵⁾. This result means that the whole amount of radiation dose independent of radiation or energy can be estimated after the first component caused by the alpha rays fades out.

The purpose of this paper is to report on our development of a new method that

eliminates the short half-life component by annealing an IP and that estimates the radiation dose with the long half-life component for quantitative measurement. The annealing decreases the effect of fading on the dose estimate, however, it also causes the loss of PSL. Considering an IP as an integral detector for a specific period, the optimum conditions for quantitative measurement with two types of IP (BAS-TR and BAS-MS) have been evaluated by using the fading correction equation.

Methods

BAS-TR and BAS-MS manufactured by Fuji Film Co. are commercially available. BAS-TR has a size of 40.0 cm × 20.0 cm and is dyed blue, lacking a protective surface layer to detect low-energy beta rays such as ³H effectively. BAS-MS, which is produced as a highly sensitive and waterproof white IP, has a smaller area of 20.0 cm × 25.0 cm with a 9 μm thick protective Mylar film. Both are constructed of a 50 μm or 115 μm thick photostimulable phosphor (BaFBr:Eu²⁺) individually affixed to a 250 μm or 188 μm thick plastic backing for support.

Fading correction equations after irradiation with a ²⁴⁴Cm source were obtained as Eq. (1)⁴⁾ using BAS-TR scanned by BAS-1000 and Eq. (2)⁵⁾ using BAS-MS scanned by BAS-5000:

$$\begin{aligned}
 (\text{PSL})_{t,k} / (\text{PSL})_{0,k} = & 0.461 \exp \{-2.19 \times 10^8 \cdot t \cdot \exp(-6.14 \times 10^3/K)\} \\
 & + 0.277 \exp \{-1.60 \times 10^{13} \cdot t \cdot \exp(-1.02 \times 10^4/K)\} \\
 & + 0.230 \exp \{-7.98 \times 10^{12} \cdot t \cdot \exp(-1.05 \times 10^4/K)\} \\
 & + 0.030 \exp \{-1.99 \times 10^{12} \cdot t \cdot \exp(-1.05 \times 10^4/K)\} \\
 & + 0.002 \exp \{-4.96 \times 10^{10} \cdot t \cdot \exp(-1.05 \times 10^4/K)\}
 \end{aligned} \tag{1}$$

$$\begin{aligned}
 (\text{PSL})_{t,k} / (\text{PSL})_{0,k} = & 0.373 \exp \{-2.08 \times 10^{12} \cdot t \cdot \exp(-8.92 \times 10^3/K)\} \\
 & + 0.084 \exp \{-9.89 \times 10^{10} \cdot t \cdot \exp(-8.69 \times 10^3/K)\} \\
 & + 0.360 \exp \{-4.37 \times 10^{10} \cdot t \cdot \exp(-9.31 \times 10^3/K)\} \\
 & + 0.144 \exp \{-2.41 \times 10^{10} \cdot t \cdot \exp(-9.54 \times 10^3/K)\} \\
 & + 0.039 \exp \{-2.07 \times 10^9 \cdot t \cdot \exp(-9.53 \times 10^3/K)\}
 \end{aligned} \tag{2}$$

where $(\text{PSL})_{t,k}$ and $(\text{PSL})_{0,k}$ refer to the PSL of elapsed time t and 0 after irradiation, respectively, and K is the absolute temperature.

Two models expressing fading curves during the elapse of t days (one model is $t = 1$ and another is $t = 30$) after irradiation and a decreasing curve after annealing at $K^\circ\text{C}$ are shown in Fig. 1. All values of PSL were normalized with the value of PSL one day after irradiation. A model of the accumulating radiation dose each day is also shown. T_1 and T_{30} are the values of PSL after t days have elapsed when $t = 1$ and $t = 30$, each without

annealing. $T_{1,K}$ and $T_{30,K}$ are the values after annealing with T_1 and T_{30} at $K^\circ\text{C}$ for 24 hours. It is clear that the difference between the two points, $T_1 - T_{30}$ and $T_{1,K} - T_{30,K}$, becomes smaller after annealing, and the effect of fading on PSL is decreased. However, the process also causes a loss of sensitivity.

Results

A comparison of the effects of an integral period on the value of PSL without annealing, and with annealing at 60, 70, and 80°C were evaluated, considering IP as an integral detector for 2, 7, 15, and 30 days. Figure 2 shows the results: (a) for BAS-TR and (b) for BAS-MS. All values of PSL were normalized with the value of PSL left at 20°C for one day after irradiation, indicated as PSL_1 . For BAS-TR, the ratio of PSL_t to PSL_1 shows a large difference (0.78 and 0.07) between 2 and 30 days without annealing. The difference becomes very small (< 5%) when the IP is annealed at 60°C. In contrast, for BAS-MS, the difference of the ratio of PSL_t to PSL_1 between 2 and 30 days is not as large as BAS-TR (0.94 and 0.53) without annealing. The difference does not get smaller when the IP is annealed at 60°C, but does decrease by about 15% when the IP is annealed at 80°C.

In addition, the loss of PSL was investigated after 2, 7, 15, and 30 days had elapsed after irradiation. Figs. 3(a) and 3(b) show the decrease of PSL without annealing, and with annealing at 60, 70, and 80°C each for BAS-TR and BAS-MS. Just as for Figs. 2(a) and (b), all values of PSL were normalized with the value of PSL left at 20°C for one day after irradiation, again indicated as PSL_1 . For BAS-TR, even without annealing, the ratio of PSL_t to PSL_1 is 7% 30 days after irradiation. After annealing at 80°C, it goes to 0.4%. For BAS-MS, no drastic decrease of PSL was observed. The ratio remains above 13% after annealing at 80°C 30 days after irradiation. This level is considered sufficient for practical use as a month-long integral detector.

Therefore, the optimum condition for quantitative measurement appears to be to anneal BAS-MS at 80°C for 24 hours after irradiation for a month-long detector. This can decrease the effect of the elapsed time, retaining sufficient sensitivity. The results demonstrate new possibilities of radiation dosimetry offered by IP.

Discussion

In this work, two types of IPs were investigated. The effect of annealing is

clearly demonstrated by the difference in the decrease of PSL. That is, annealing even at a relatively low temperature (60°C) causes a large amount of emission of luminescence for BAS-TR, but causes less for BAS-MS (see Figs. 3(a) and (b)). This result could be explained by the difference of the activation energies and the component amplitudes between the two IPs. We showed that the activation energy increases as the components proceed⁴. This result satisfies the idea that fading occurs in the order of the component having the lower activation energy. The activation energies of each component in Eq. (1) for BAS-TR are 0.53, 0.88, 0.90, 0.90, and 0.90 eV. For each component in Eq. (2) for BAS-MS, the values are 0.76, 0.75, 0.80, 0.82, and 0.82 eV⁵. The amplitude of the first component for BAS-TR is larger than that for BAS-MS: 0.461 in Eq. (1) and 0.373 in Eq. (2). Annealing accelerates advance of fading. Emission of the first component of BAS-TR should be drastically affected by annealing. In contrast, each component for BAS-MS has a relatively high activation energy, so it can retain sufficient sensitivity after annealing.

References

- 1) Amemiya Y. and Miyahara J. (1988) Imaging plates illuminates many fields. *Nature* 336,89-90.
- 2) Taniguchi S., Yamadera A., Nakamura T., and Fukuda K. (1999) Development of a new personal dosimeter for low-energy X-rays using an imaging plate. *Radi. Prot. Dos.* **85**, Nos. 1-4, 7-10.
- 3) Ohuchi H., Yamadera A., and Nakamura T. (2000) Functional equation for the fading correction of imaging plates. *Nucl. Instr. and Meth. A* **450**, 343-352.
- 4) Ohuchi H. and Yamadera A. (2002) Development of a functional equation to correct fading in imaging plates. *Rad. Meas.* **35**, 135-142.
- 5) Ohuchi H. and Yamadera A. Dependence of Fading Patterns of Photo-Stimulated Luminescence from Imaging Plates on Radiation, Energy, and Image Reader. *Nucl. Instr. and Meth. A* (accepted).

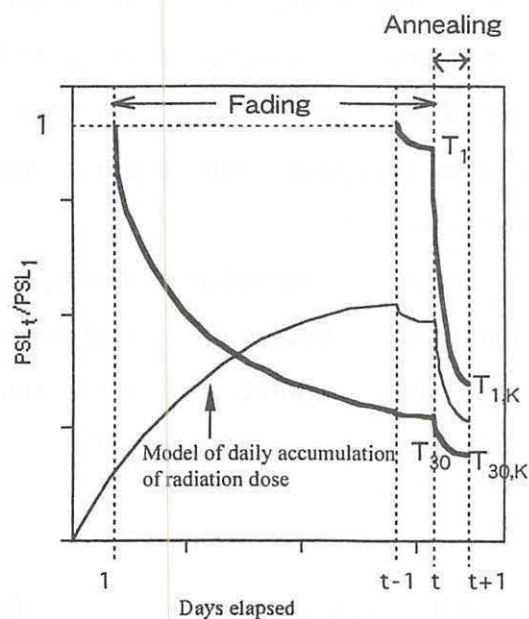


Fig. 1. Schematic model of fading and annealing curves during the elapse of t days after irradiation.

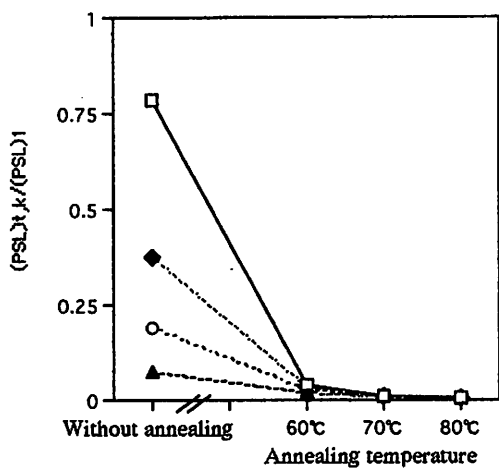


Fig.2(a)

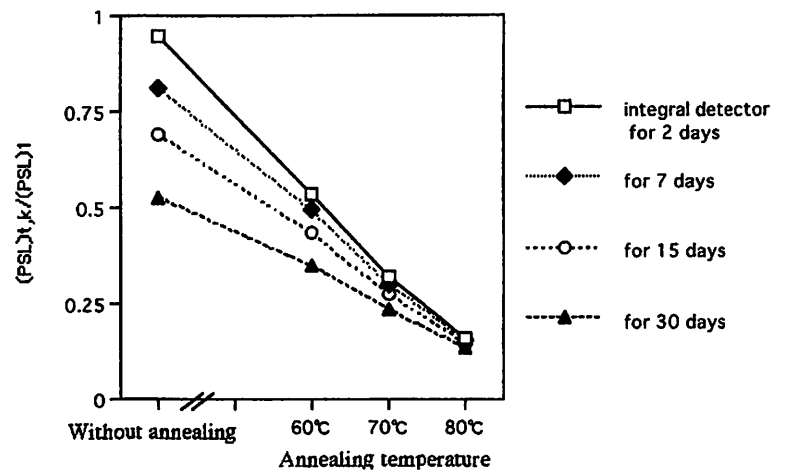


Fig.2(b)

Fig. 2. Comparison of the effects of an integral period on the value of PSL without annealing, and with annealing at 60, 70, and 80°C.

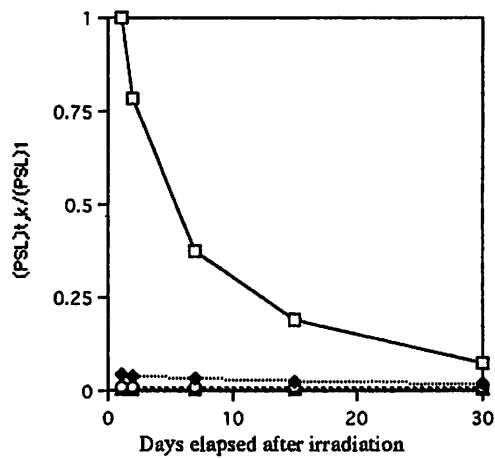


Fig.3(a)

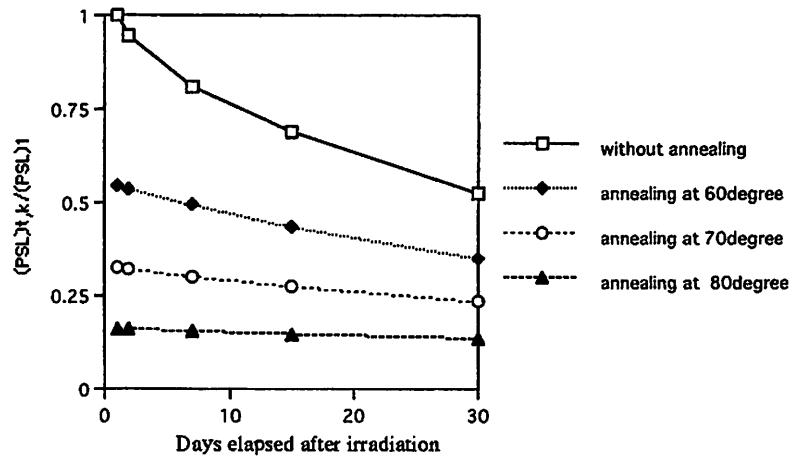


Fig.3(b)

Fig. 3. Loss of PSL after irradiation. without annealing, and with annealing at 60, 70, and 80°C.

V. 2. Neutron Emission Spectrum and ^7Be Production in (d+Li, d+Be) Reaction with Thick Targets for 25 MeV Deuterons

Aoki T.¹, Hagiwara M., Baba M., Yonai S.*, Kawata N., Miura T.², and Nakamura T.*

*Cyclotron and Radioisotope Center, Tohoku University
Quantum Science and Energy Engineering, Tohoku University**

INTRODUCTION

The Li(d,n), Be(d,n) reactions are expected as high-intensity neutron production reactions, in particular the $^7\text{Li}(d,n)$ reaction using liquid lithium target will be adopted in IFMIF (International Fusion Materials Irradiation Facility)¹⁾. For the design and operation of the neutron source, detailed knowledge is required on the energy-angular neutron emission spectra of the $^7\text{Li}(d,n)$ and $^9\text{Be}(d,n)$ reactions, and the radioactivity (^7Be , ^3H etc.) accumulated in the targets. The neutron flux and spectral data are indispensable for precise estimation of the neutron irradiation effects, and the radioactivity accumulation is of great concern for the management of the targets. However the data status is not good enough as shown by marked differences among experimental data²⁾. We have started experiments on the neutron emission spectrum of the $^7\text{Li}(d,n)$ and $^9\text{Be}(d,n)$ reaction and the radioactivity induced in the target using the AVF cyclotron (K=110) at CYRIC.

This paper presents the experiments on the 1) neutron emission spectra and the 2) production of radioactive nuclide, ^7Be , for the $^7\text{Li}(d,n)$ and $^9\text{Be}(d,n)$ reaction with thick target for 25 MeV deuterons. The neutron spectra were measured for almost entire range of secondary neutrons at ten laboratory angles between 0- and 90-deg with the time-of-flight (TOF) method using a beam swinger system. The number of ^7Be accumulated in the targets was measured by counting the γ -rays from ^7Be using a pure Ge detector. Experimental results are compared with other experimental data and calculations.

EXPERIMENTAL APPARATUS

The experimental setup is presented in Fig. 1. A deuteron beam accelerated by the

AVF cyclotron was transported to the target room No.5 equipped with a beam-swinger system and a neutron TOF channel³⁾ as shown in Fig. 1. The beam swinger system changes the incident angle of the beam onto the target from 0- deg to 110-deg and enables to measure angular distributions with fixed detector setup.

The targets (Li,Be) were metallic plate of natural element. The lithium target was prepared by mechanical pressing of a lithium ingot under argon atmosphere to avoid oxygen contaminant and the lithium ingot was cleaned up thoroughly prior to the pressing to avoid carbon contamination. The lithium and beryllium targets were 8.0 mm and 3.0 mm thick, respectively to stop the incident beam within the targets. They were set on a remotely-controllable target changer together with a beam viewer of aluminum oxide. The support frame of the target was isolated from the ground to read beam current on the target.

The target chamber was shielded with 1 m thick concrete walls having a beam channel for collimators. Iron collimators, 10-cm-diam, were inserted into the beam channel to collimate neutrons from the target.

Emitted neutrons were detected by NE213 scintillation detectors, 14-cm-diam \times 10-cm-thick or 5-cm-diam \times 5-cm-thick equipped with pulse-shape-discrimination (PSD).

The detectors were placed around \sim 11 m and \sim 3.5 m from the target (Fig. 1). The shorter flight path was adopted to measure the low energy part (\sim 1-5 MeV) of the neutron spectrum by low pulse-height bias (\sim 600 keV). The TOF, PSD and pulse-height data were collected event by event as three parameter list data for off-line analysis⁴⁾.

EXPERIMENTAL PROCEDURE

The pulse width was generally less than 1 ns in FWHM, and the beam current on the target was around 5 nA. The beam current was digitized and recorded by a multi-channel scaler for normalization of the neutron TOF spectrum and the ^7Be production measurement. The TOF data were obtained at ten laboratory angles (0, 5, 10, 15, 20, 25, 30, 40, 60 and 90 deg).

The activities of ^7Be accumulated in the lithium and beryllium target were measured by detecting 477 keV γ -rays due to the decay of ^7Be in the targets bombarded by a deuteron beam during the neutron spectrum measurement with a pure Ge detector (EURICIS MESURESE GPC50-195-R) and a multi-channel analyzer.

DATA ANALYSIS

Neutron spectrum

Neutron TOF spectra gated by a PSD signal and lower pulse-height bias were converted into energy spectra. The efficiency vs. energy curves of the detectors were calculated by a revised version of the Monte Carlo code SCINFUL⁵⁾ that was verified to be accurate within $\pm 5\%$ up to 80 MeV⁶⁾. The spectra were normalized by the integrated beam current.

⁷Be activity

The induced ⁷Be activity was determined from the γ -ray counts by the pure Ge detector, and corrected for the decay, the peak efficiency of the Ge detector, the self-absorption effect in the samples and the beam current fluctuation during irradiation. The efficiency of the Ge detector was determined by the calculation using the Monte Carlo code EGS 4⁷⁾. The calculated results were confirmed at several energy points with standard γ -ray sources.

RESULTS AND DISCUSSION

(d+Li, d+Be) neutron spectra

The present results for the Li(d,n) and ⁹Be(d,n) neutron spectrum at ten laboratory angles are shown in Fig. 2 and Fig. 3, respectively. The low limit is as low as around 1 MeV. The error bars of the spectra represent the statistical errors mainly. In Fig. 4, the present data at 0-deg are compared with the experimental data by Lone et al at 23 MeV²⁾. The data of Lone et al are reported only for 0-deg.

The experimental spectra are divided into two parts; a high-energy tail region (only for Li(d,n)) due to direct stripping reactions and a main peak region centered around 10 MeV which is a main neutron source in IFMIF. The data by Lone et al. are in good agreement with the present one in the 10-23 MeV region while they are much larger in the low energy region. Such a high yields of low energy neutrons as in the Lone et al's data is unlikely for the reaction of light element like Li with very strong recoil effect. For the high energy tail region, the data by Sugimoto⁸⁾ at 32 MeV are closer to the present one rather than those by Lone et al. It is necessary to clarify the spectrum in this energy region because high-energy neutrons cause much more damage due to large helium production cross-sections and larger energy of primary-knock-on atoms.

The intensity of high-energy tail is highest around 15-deg while total neutron yields are highest at 0-deg. The former conclusion is in agreement with Sugimoto⁸⁾ and can be interpreted by the angular momentum effect in the ${}^7\text{L}(d,n_{0,1}){}^8\text{Be}$ reaction.

Therefore, to reduce the influence of high-energy neutrons and obtain higher intensity irradiation field, neutrons to angles close to 0-deg will be preferable. The present data can be used to assess the applicability of calculation codes and models for the neutron emission spectrum of the reaction⁹⁾.

${}^7\text{Be}$ activity

The measured ${}^7\text{Be}$ activity was compared with other experimental data and calculation by the code IRAC¹⁰⁾ used for activity assessment of accelerator components.

Figures 5 and 6 show the comparison of the present results, the IRAC code and other experimental data^{10,11)} for Li and Be, respectively. For the lithium data, the present results at 25 MeV look to be consistent with the data around 22 MeV¹¹⁾ and at 40 MeV¹²⁾, but are substantially higher than the IRAC calculation. The production of ${}^7\text{Be}$ via the (d,n) reaction on elemental lithium will be due to the ${}^7\text{Li}(d,2n)$ and the ${}^6\text{Li}(d,n)$ reactions mainly. Figure 7 shows the comparison of the experimental data and the IRAC calculation for the ${}^7\text{Li}(d,2n)$ reaction cross-section. The IRAC code underestimates the ${}^7\text{Li}(d,2n)$ cross-sections and this may be a principal reason of the underestimation of the IRAC code for the ${}^7\text{Be}$ production rate. For the beryllium data, similar underestimation is observed and reported even for the new code⁹⁾.

The experiment will be extended to higher deuteron energy to obtain benchmark data for activity accumulation and to ${}^3\text{H}$ production using the liquid scintillation technique or equivalent.

¹Present address: Tokyo Electric Power Company (TEPCO)

²Present address: High Energy Accelerator Research Organization (KEK)

References

- 1) IFMIF CDA TEAM, IFMIF Conceptual Design Activity Final Report edited by Marcello Martone, Report 96.11, Enea, Dipartimento Energia, Frascati (1996).
- 2) Lone et M. A. al., Nucl. Instrum. Methods, **143** (1977) 331.
- 3) Terakawa A. et al., Nucl. Instrum. Methods A, in print.
- 4) Ibaraki M. et al., Nucl. Sci. Technol., **35**. (No.12) (1998) 843.
- 5) Dickens J. K., ORNL-6436, Oak Ridge National Laboratory, 1988.
- 6) Meigo S., Nucl. Instrum. Methods in Physics Research A **401** (1997) 365.

- 7) Nelson W., Hirayama H., D.W.O.Rogers, "The EGS4 Code System" SLAC-265, Stanford University, Stanford (1985).
- 8) Sugimoto M. (Japan Atomic Energy Research Institute), Private communication.
- 9) Konobeyev A.Yu., Koriyov Yu.A., P.E.Pereslavitsev, U. Fischer, U.Mollendorff; Nucl. Sci.Eng.,**139** (2001) 1.
- 10) Tanaka S. et al. Proc. of 8th Int. Conf. On Radiation Shielding, Arlington, Apr. 1994, Vol.2, (American Nuclear Society, 1994) p965.
- 11) EXFOR system: OECD/NEA <http://www.nea.fr>.
- 12) Von Mollendorff U., Feuerstein H. and Giese H., Proc. 20th Symp., on Fusion Technology (Marseille, France, 7-11 Sept.1998) p.1445.

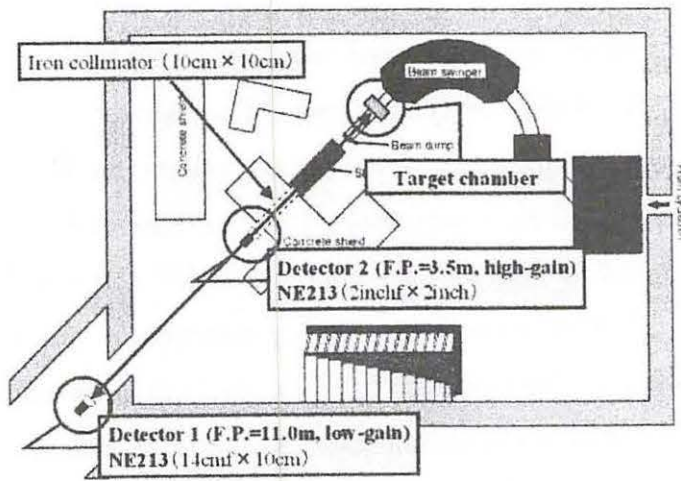


Fig. 1. The layout of TR 5 at CYRIC.

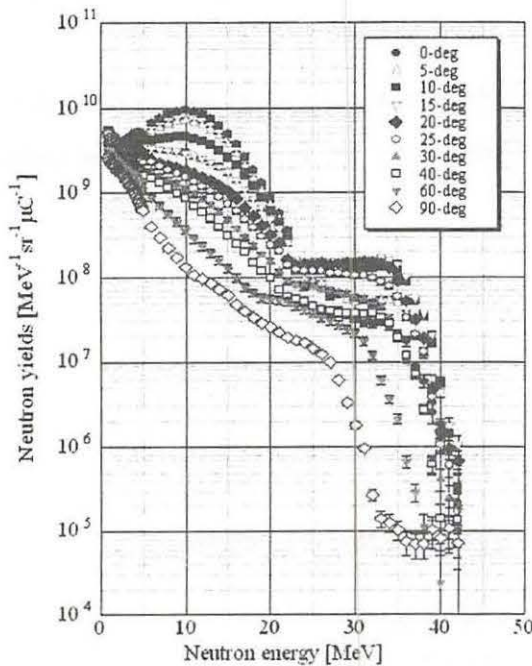


Fig. 2. The neutron spectra of the Li(d,n) reaction for incident deuteron energy of 25 MeV.

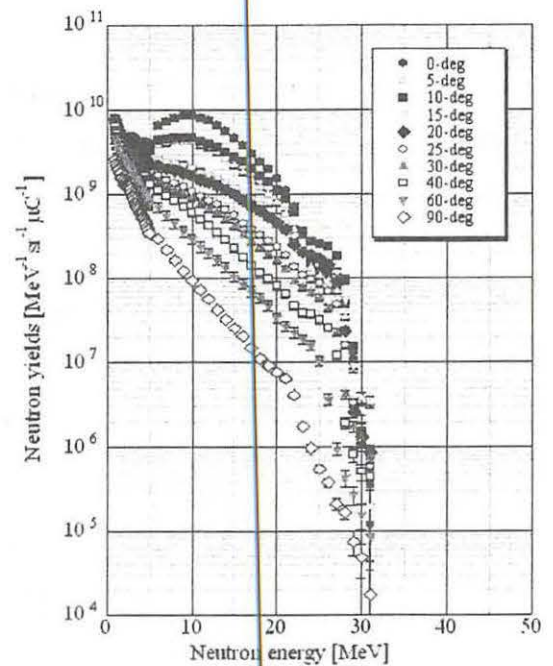


Fig. 3. The neutron spectra of the Be(d,n) reaction for incident deuteron energy of 25 MeV.

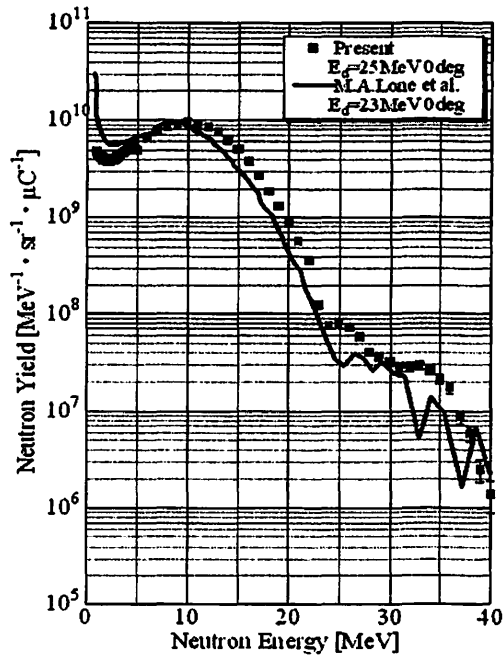


Fig. 4. Comparison of the present Li(d,n) neutron spectrum with the data by Lone et al.²⁾

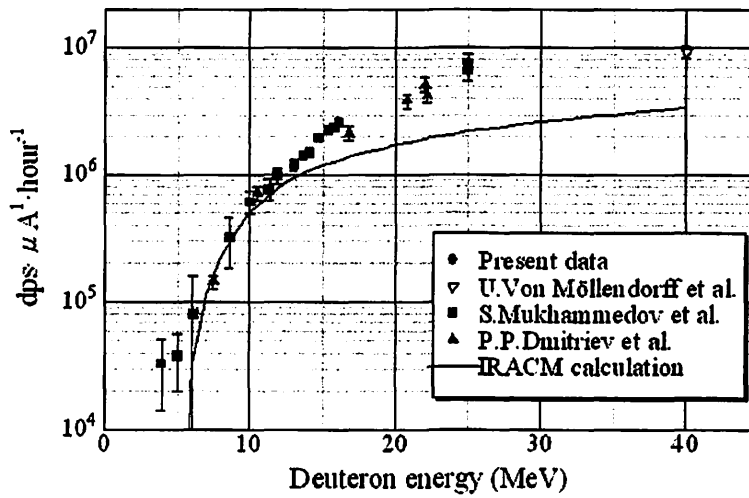


Fig. 5. ⁷Be production rate via the Li(d,x) reaction.

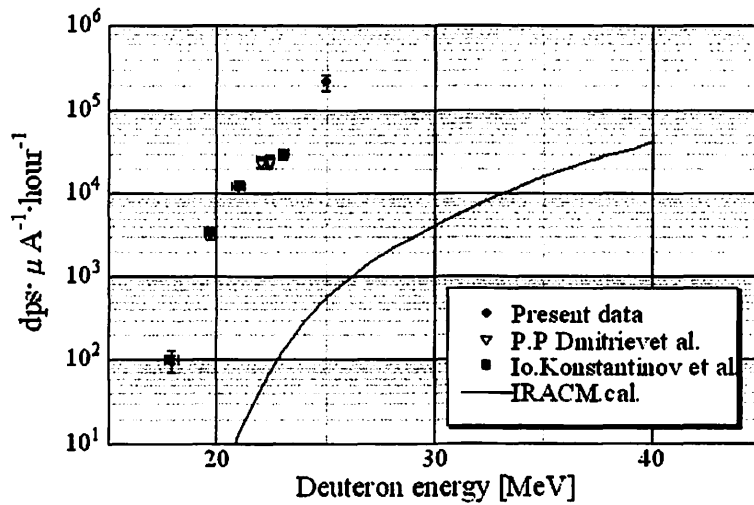


Fig. 6. ⁷Be production rate via the Be(d,x) reaction.

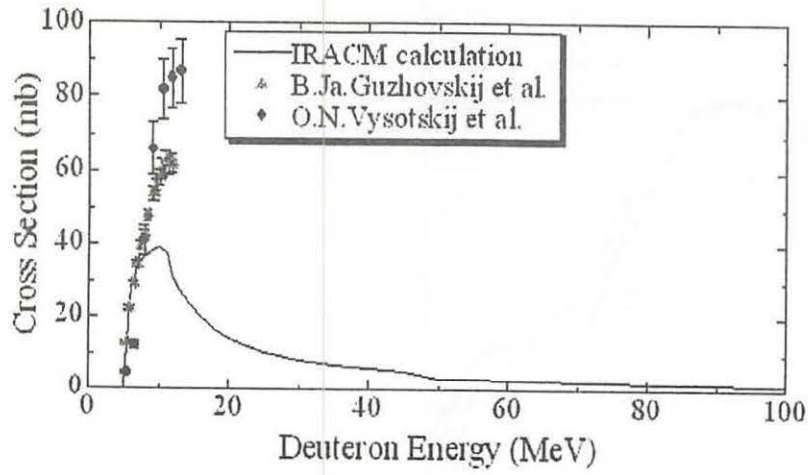


Fig. 7. ${}^7\text{Li}(d,2n){}^7\text{Be}$ reaction cross-section.

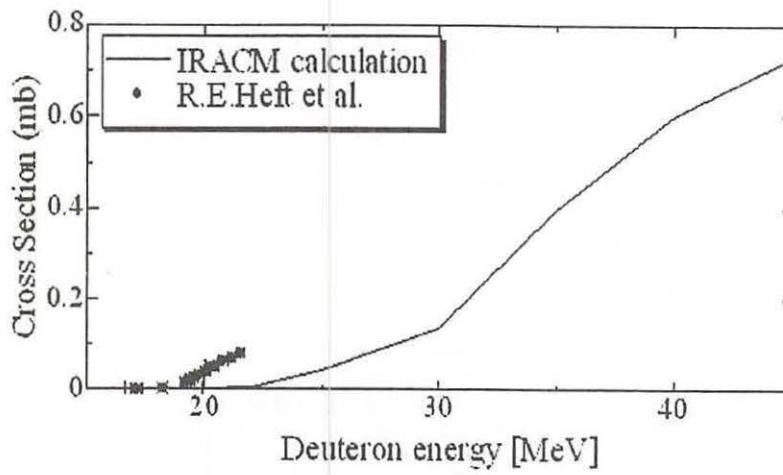


Fig. 8. ${}^9\text{Be}(d,x){}^7\text{Be}$ reaction cross-section.

V. 3. Development of an Accelerator Beam Loss Monitor Using an Optical Fiber

Kawata N. Baba M. Kato M., Miura T.**, and Yamadera A.***,*

Cyclotron and Radioisotope Center, Tohoku University

INTRODUCTION

A new cyclotron was installed in the Cyclotron and Radio Isotope Center (CYRIC) of Tohoku University. Now a large beam current project is running as shown in table 1. To realize the plan, it is important to lead the particle beam to the end of the beam lines with a minimum loss to avoid activation of accelerator components and building walls. For the reason, a beam loss monitor with high sensitivity is required in addition to existing beam monitoring systems such as a beam slit.

In the beam loss monitoring, detection of radiation in real time, and identification of the radiation location is required over a wide range of radiation level.

In this study, we have investigated a beam loss monitoring method by combining an optical fiber with scintillators. By using an optical fiber, we can make a simple, inexpensive, and flexible system.

We tested the position-response of the detector with gamma-rays and neutrons. From the experiment, we confirmed clear peaks corresponding to each measuring positions with spatial resolution of 30-60 cm, and approved a possibility as the radiation monitor.

PRINCIPLE OF BEAM LOSS MONITOR

A schematic view of the detector is shown in Fig. 1. Several scintillators are placed along to the beam lines and their light outputs are lead to a wavelength-shift fiber coupled to two photo-multiplier tubes in both ends of the fiber.

At the beam loss spot, neutrons and gamma-rays are emitted from the beam lines made by aluminum or stainless steel. When these radiations enter and interact with the

scintillators, scintillation photons are generated. These light photons go to both ends of the fiber, and from the difference of arrival times to both ends of the fiber, we can identify which scintillators were scintillating.

Generally, a detector using an optical fiber has following advantages.

1. The detector can be light, compact, and flexible.
2. The detector is suitable for wide area monitoring.
3. The detector is tolerable to electromagnetic field owing to the utilization of light signal.

In addition, the detector can measure over wide area and continuously radiation distribution by combining the fiber with scintillators.

Photo-multiplier tubes (Hamamatsu H1949 assembly) (PMT), constant fraction discriminators (CFD), time amplitude converters (TAC) are connected to both ends of the fiber.

When the radiations are incident into the scintillator placed at x m from the start PMT, the difference of arrival times to both photomultipliers is given by

$$\Delta t = \{(L - x) / v + T_d\} - x/v = (L - 2x) / v + T_d$$

Therefore,

$$x = \{v(T_d - \Delta t) + L\}/2$$

where,

v : velocity of light in the fiber,

L : length of optical fiber,

T_d : delay time.

COUPLING OF FIBER WITH SCINTILLATOR

In this study, the fiber is coupled with the scintillator through the hole in the scintillator as shown in Fig. 2. Photons emitted in the scintillators are transmitted into the fiber. To improve the light transmission we used a wavelength-shift fiber (WSF) for the optical fiber. WSF absorbs lights and then re-emit lights, which have different wavelength to 4π solid angle. By using WSF, therefore, the transmission efficiency of photons from the scintillator will be higher compared with the case of using normal optical fibers.

In this study NE102A plastic scintillator and BCF-92 wavelength-shift fiber

(Bicron) were used. Figure 3 shows the wavelength of lights emitted from NE102A, and absorption and emission efficiency of BCF-92. The peak of the former is about 423 nm and is close to the latter which is about 410 nm. Therefore, the transmission efficiency of the scintillation light is high.

By changing the scintillator type and its size, we can vary the sensitivities and selectivity of radiation types. Further by using the coupling, the sensitivities for the radiation can be higher than the case of using scintillating fibers alone owing to the large size of the scintillator.

EXPERIMENT AND RESULT

Figure 4 shows the scintillator and WSF used at this experiment. The scintillator was a rectangular parallelepiped with a teflon coating. The fiber was 5.5 m long and 1 mm in diameter. By changing the positions of scintillators on the fiber, we confirmed position responses of the detector.

Position response for gamma-ray

By using a ^{137}Cs gamma-ray source, position response was measured in 1 m step from 1 to 5 m. Figure 5 shows the result of the response test. Five peaks are clearly observed in each position. A position resolution was about 60 cm (time resolution of) for a ^{137}Cs source.

Lights are attenuated according to the distance exponentially in the fiber.

Counting rates of each peaks are different and the counting rate becomes smaller with the distance from the start PMT. Light output for 661 keV gamma-rays from ^{137}Cs are small, the measurement was done near a pulse height bias.

This resolution is not very good. As the reason, it is thought that scintillating photons were reduced when they were transported either from the scintillator to the fiber or in a process of transportation along the fiber.

Figure 6 shows the response for two points simultaneously by the method shown in Fig. 7. Two clear peaks are observed. From this experiment it was shown that detection in plural points could be possible.

Position response for 15 MeV neutrons

Figure 8 shows the response of the detector for 15 MeV neutrons. In the same

way as the experiment for ^{137}Cs gamma-rays, the scintillator was moved in 1 m step from 1 m to 5 m. Five peaks are observed clearly around each positions.

The position resolution improved to 40 cm probably because light outputs of 15 MeV neutrons are ten times as large as that of ^{137}Cs gamma-rays of 661 keV. Furthermore, in contrast with the ^{137}Cs case, the counting rates for the neutrons are almost independent of the position owing to high light output for 15MeV neutrons and low pulse height bias.

Pulse height distribution for ^{22}Na gamma-ray

Figure 8 shows a pulse height distribution for ^{22}Na gamma-rays (0.511 and 1.27 MeV) detected by NE102A couples directly to the PMT. Two Compton edges are shown apparently. On the other hand, no peaks can be seen if the WSF is inserted between scintillator and PMT as shown in Fig. 9. Following processes may cause this loss of pulse height information,

1. lights transmission from the scintillator to the WSF,
2. shift of light wavelength in the WSF,
3. transportation of shifted light along the fiber.

Pulse height distribution for 15 MeV neutrons

Figure 10 shows pulse height distributions for 15 MeV neutrons with WSF for light transmission lengths of 1 m and 5 m from the start PMT. In the case of 1 m an edge-like structure can be seen around 3,000 channels, but such structure disappears in 5 m. As the transport length becomes larger, the pulse height information was deteriorating.

The results of 4.3 and 4.4 suggest the pulse-height response of the detector is not good as expected. Therefore, the beam loss monitor in the present configuration should employ the time-of-flight information in place of pulse height information.

SUMMARY

Conclusion

1. We have fabricated a position sensitive detector as the beam loss monitor using a combination of scintillators and the WSF. By changing the size of the scintillator, the sensitivity for radiations from a beam line can be changed. Using the WSF can improve

the light transmission efficiency.

2. We showed the beam loss point can be known from the difference of light arrival times (TOF) to the both ends of the fibers.

3. From the above, the fiber detector can be used as the beam loss monitor, while there is a room of improvement.

Future

For realization of the monitor, the transmission length of the lights will be made longer by using silica fibers whose attenuation length is far longer than that of plastic fibers. Further, more scintillators will be used for a practical use. The monitor will detect only neutrons by using a ZnS(Ag) scintillator and so on to avoid detection of gamma-rays from activated parts.

REFERENCES

- 1) Knoll G. F., "Radiation Detection and Measurement", Second Edition.
- 2) OKA T et al., Journal of NUCLEAR SCIENCE and TECHNOLOGY, Vol. 35, No. 12, p. 857-864 (1998).
- 3) Takada E. et al., IEEE TRANSACTIONS ON NUCLEAR SCIENCE, VOL. 42, NO. 4 (1995).

Table 1. Performance of new cyclotron in CYRIC.

Particles		Energy [MeV]	Intensity [μ A]
Positive ions	proton	10 - 90	50
	deuteron	10 - 65	50
	alpha	20 - 130	50
Negative ions	proton	10 - 50	300
	deuteron	10 - 25 MeV	300

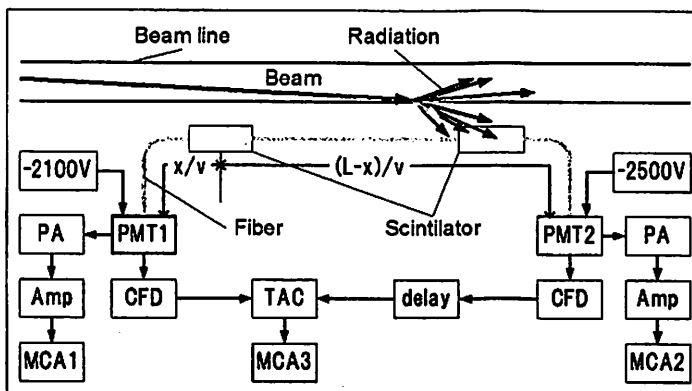


Fig. 1 Principle of the beam loss monitor.

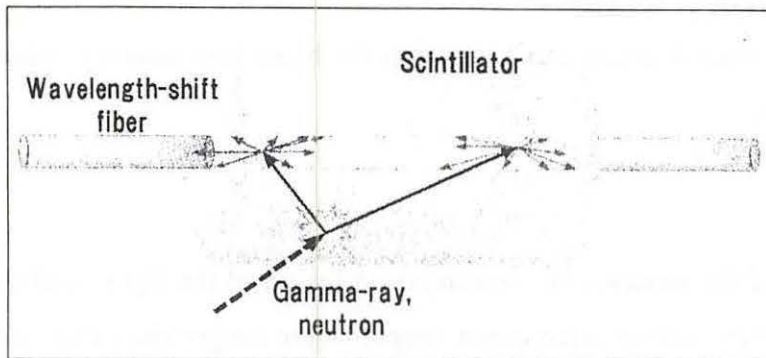


Fig. 2. Coupling of scintillators with fiber.

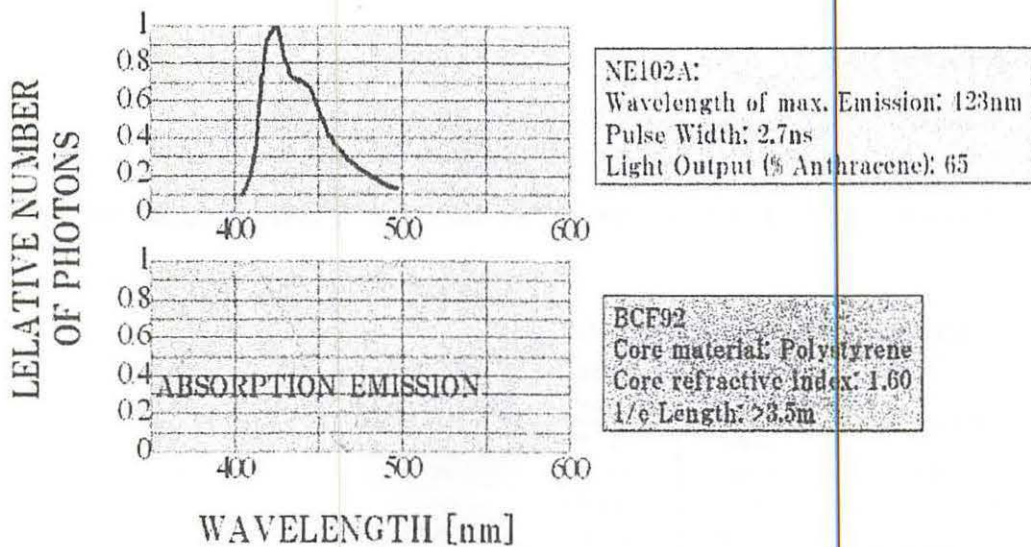


Fig. 3 Comparison of wavelengths

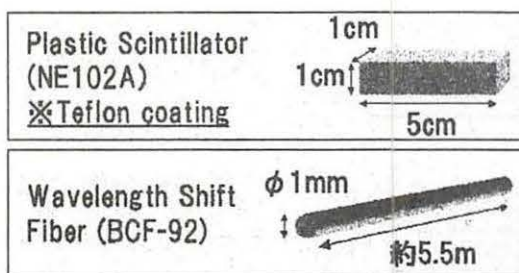


Fig. 4 A size of the scintillator and fiber

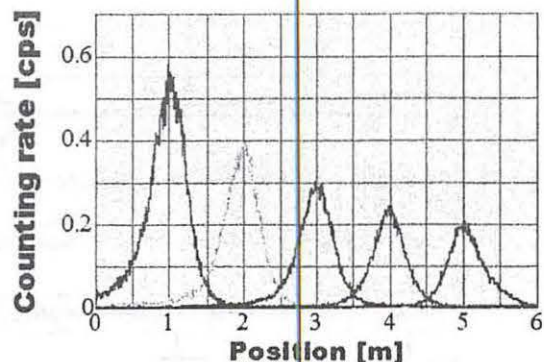


Fig. 5 Position response for ^{137}Cs

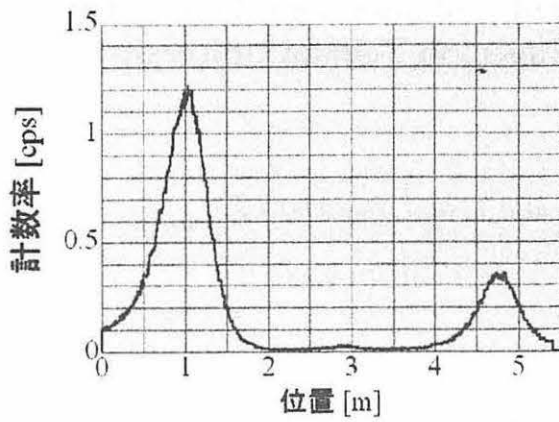


Fig. 6 Response of two points detection

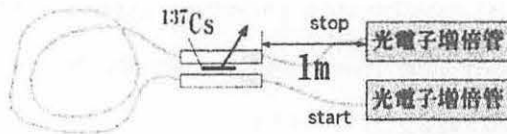


Fig. 7 Schematic view of 2 points detection

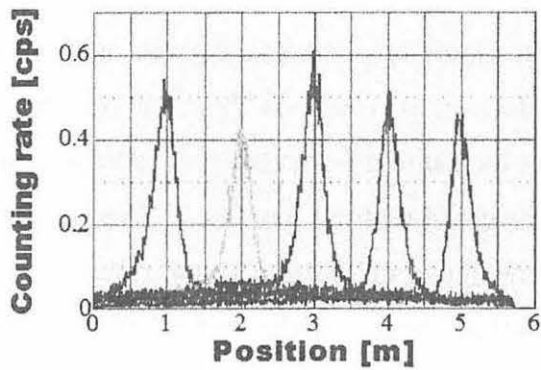


Fig. 8 Position response for 15 MeV neutrons

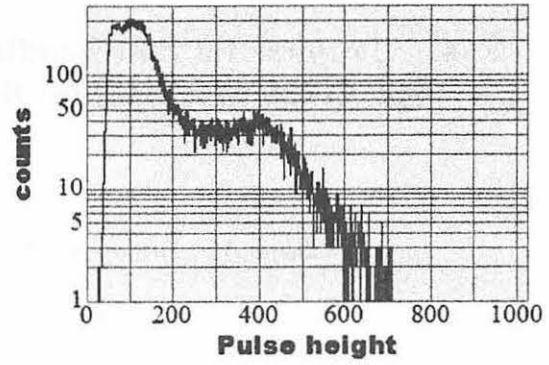


Fig. 8 Pulse height distribution of ^{22}Na without WSF

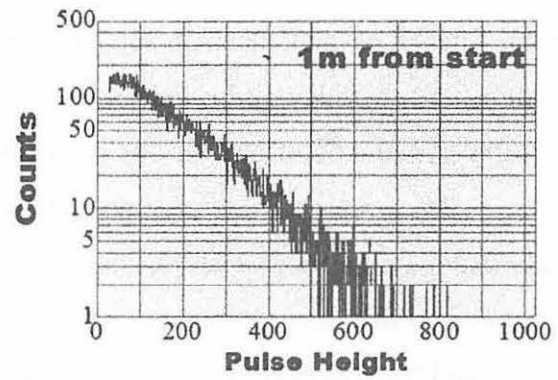


Fig. 9 Pulse height distribution of ^{22}Na with WSF

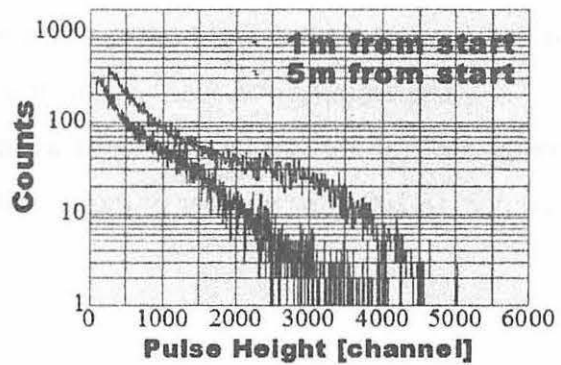


Fig. 10 Pulse height distribution of 15 MeV neutrons with WSF

V. 4. Training for Safe handling of Radiation and Radioisotopes and X-Ray Machines for Beginners in Tohoku University

Baba M., Yamadera A., Miyata T. and Nakamura T.

Cyclotron and Radioisotope Center, Tohoku University

The beginners training for safe handling of radiation and radioisotopes in Tohoku University has been conducted in three courses for 1) radiation and isotopes, 2) X-ray machines and electron microscope, and 3) synchrotron radiation (SOR). The training is scheduled to be held twice a year, May and November, under the help for lectures and practice from various departments and research institutes of the university.

The training for “radiation and radioisotopes” is for persons who use unshielded radioisotopes and accelerators, and has been conducted from 1977. The contents of lectures and practices are shown in Table 1. In the fiscal year of 2001, the training was performed for 576 persons. The departments to which they belong are given in Table 2.

The training for “X-ray machines and electron microscopes” began at the end of 1983. The training is scheduled twice a year at the same time as that for “radiation and radioisotopes”. In this course, only lectures are given with no practice. The contents of the lectures and the distributions of trainees are shown in Tables 3 and 4, respectively.

The training for the “synchrotron radiation” began at the end of 1995. The contents of the lectures are the same as those of the radiation and radioisotopes but no practice. In 2002, the number of trainees of the SOR course was 72.

Table 1. Contents of the lectures and practices for safe handling of radiation and radioisotopes in 2001.

Lectures (one day)	Hours
Radiation physics and measurements	1.5
Chemistry of radioisotopes	1.0
Radiological protection ordinance	1.5
Effects of radiation on human	1.0
Safe handling of radioisotopes	1.5

Practices (one day)	Hours
Treatment of unsealed radioactive solution	4.0
Measurements of surface contamination and decontamination	1.0
Measurements of gamma rays and beta rays	2.0

Table 2. Distribution of trainees for “radiation and radioisotopes” in 2001.

Department	Staff	Student	Total
Medicine	18	86	104
Dentistry	1	22	23
Pharmacy	0	75	75
Science	3	73	76
Engineering	3	66	69
Agriculture	0	104	104
Research Institutes	6	61	67
The others	1	57	58
Total	32	544	576

Table 3. Contents of lectures for “X-ray machines and electron microscopes” in 2001.

Lectures (one day)	Hours (h)
Safe handling of X-ray machines	1.5
Radiological protection ordinance	1.0
VTR for safe handling of radiation and radioisotopes	1.0

Table 4. Distribution of trainees for “X-ray machines and electron microscopes” in 2001.

Department	Staff	Student	Total
Medicine	1	1	2
Dentistry	1	1	2
Science	0	14	14
Engineering	3	94	97
Research Institutes	7	93	100
Total	12	203	215

Table 5. Distribution of trainees for “synchrotron radiation” in 2001.

Department	Staff	Student	Total
Science	0	14	14
Engineering	0	31	31
Research Institutes	3	23	26
The others	1	0	1
Total	4	68	72

V. 6. Radiation Protection and Management

*Miyata T., Yamadera A., Baba M., Nakamura T. and Watanabe N.**

*Cyclotron and Radioisotope Cent~ Tohoku University
Japan Radiation Protection Co., Ltd.**

(1) Unsealed radionuclides used in CYRIC

The kinds and activities of unsealed radionuclides handled in CYRIC during the fiscal year of 2001 are summarized in Table 1. The table includes the isotopes produced by the cyclotron as well as those purchased from the Japan Radio Isotope Association or taken over from other radioisotope institutes.

(2) Individual monitoring

The exposure doses of the workers in CYRIC during 2001 are given in Table 2. They were less than the permissible doses.

(3) Monitoring of the workplace

Radiation dose rates inside and outside of the controlled areas in CYRIC were monitored periodically and occasionally when needed. They were generally below the legal permissible levels. Surface contamination levels of the floors inside the controlled areas were measured by a smear method and with survey meters. They were also under the legal regulation levels.

(4) Wastes management

The radioactive wastes delivered to the Japan Radio Isotope Association in 2001 are shown in Table 3. The concentration of radioisotopes in the air released from the stack after filtration was monitored with stack gas monitors. The values were lower than the legal regulation levels. The radioactive water was stocked in the tanks at least for 3 days and then released to the sewerage after confirming that the concentration was

lower than the legal regulation levels. Radioactive organic scintillator waste of 480 litter was treated by incinerator provided by Fuji-kogyo Co., Ltd.

Table 1. Unsealed radioisotopes used in each building of CYRIC during 2001.
(a) Cyclotron Building (kBq)

Group 1,2		Group 3		Group 4	
		¹¹ C	538,894,800.000	¹⁸ F	623,509,200.000
		¹³ N	1,000.000	³ H	67,645.000
		⁹⁹ Mo	888,320.000		
Total	0	Total	540,616,290.000	Total	623,576,845.000

(b) Radio-isotope Building (kBq)

Group 1,2		Group 3		Group 4	
⁹⁰ Sr	390.000	¹¹ C	6,031,000.000	³ H	306,523,900
⁴⁵ Ca	588.440	³² P	1,011,035.220	¹⁴ C	20,279.300
¹³⁷ Cs	320.000	^{99m} Tc	102,120.000	¹⁸ F	539,511,800.000
⁶⁸ Ge	92,291.000	^{99m} Tc*	11,285.000		
¹²⁵ I	66,613.000				
Total	160,203.440	Total	7,155,440.220	Total	539,838,603.200

* In the "β-ray analysis" room

(c) Research Building (kBq)

Group 1,2		Group 3		Group 4	
		¹⁵ O	71,373,000.000	¹⁸ F	74,000.000
Total	0	Total	71,373,000.000	Total	74,000.000

Table 2. Occupational radiation exposures at CYRIC during the fiscal year of 2001.

Dose range (mSv)	Number of individuals
No measurable exposure	60
Less than 1.0	7
1.0 to 2.0	4
2.0 to 3.0	2
Total number of persons monitored	73

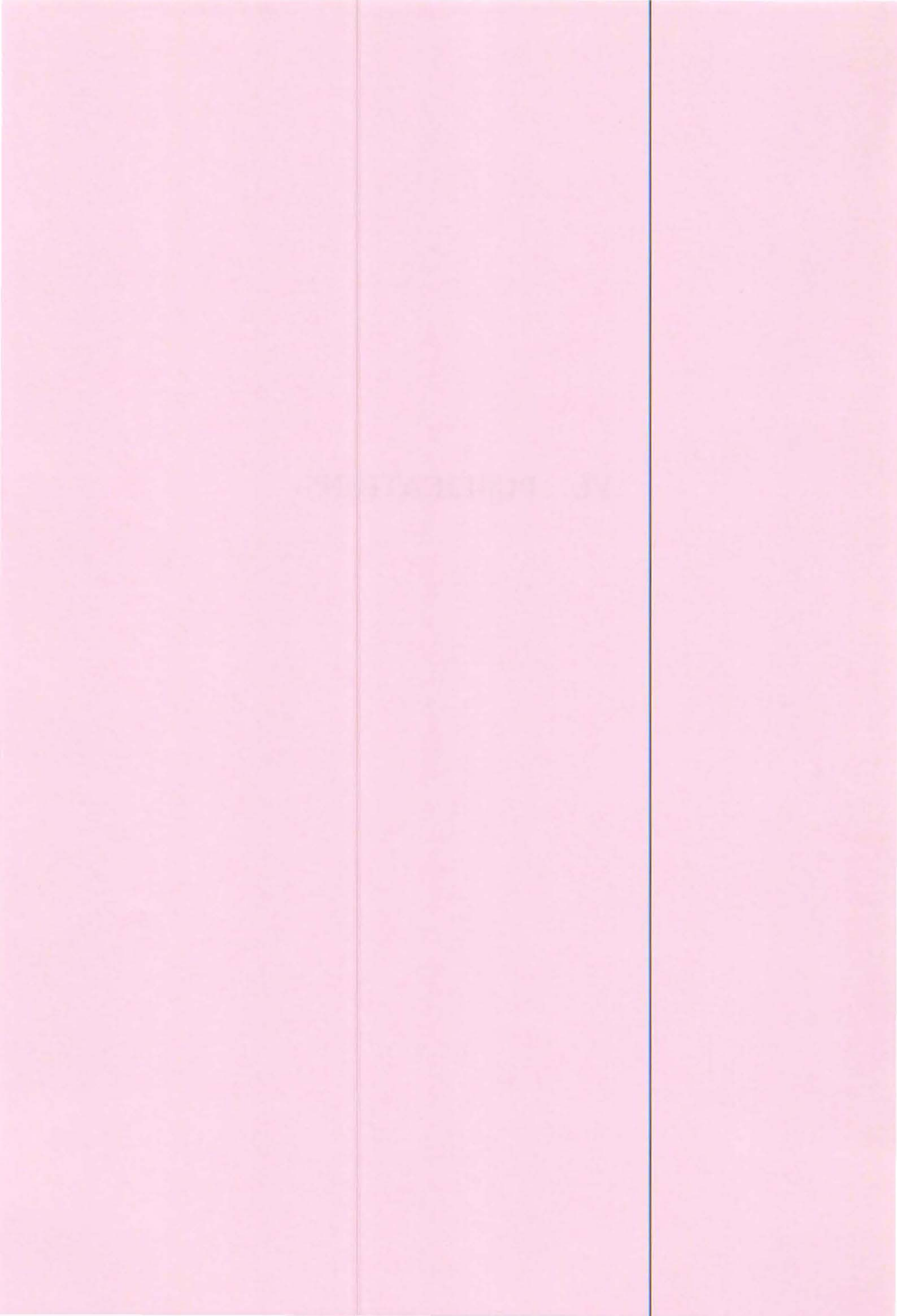
Table 3. Radioactive wastes delivered to the Japan Radioisotope Association in 2001.

Wastes type	Wastes Container	Number
Solids		
Combustible type I	50 ℓ drum	12
Combustible type II	50 ℓ drum	7
Incombustible (compressible)	50 ℓ drum	2
Incombustible (incompressible)	50 ℓ drum	0
Animal carcasses	50 ℓ drum	8
Filters	1 ℓ	1242
Liquids		
Inorganic liquids	25 ℓ PE bottle	2

Type I : Cloths and papers made of natural cellulose.

Type II: Combustion plastics such as polyethylene and polypropylene

VI. PUBLICATIONS



VI. PUBLICATIONS

(January 2001 ~ December 2001)

- [531] Trends in use of positron emission tomography
Manabu Tashiro, Kazuo Kubota, Masatoshi Itoh, Ernst Moser
THE LANCET **357**(2001)886
- [532] Excitotoxicity induces changes in rat brain gangliosides
Tania Valdes-Gonzalez, Yoshikazu Morita, Kaori Suzuki, Tatsuo Ido
Neuroscience Research **39** (2001) 197-203
- [533] ¹⁸F-FDG PET mapping of regional brain activity in runners
M. TAASHIRO, M. ITOH, T. FUJIMOTO, T. FUJIWARA, H. OTA, K. KUBOTA
M. HIGUCHI, N. OKAMURA, K. ISHII, D. BERECZKI, H. SASAKI
J SPORTS MED PHYS FITNESS **41** (2001) 11-7
- [534] Evaluation of resting brain conditions measured by two different method (i.v. and oral administration) with ¹⁸F-FDG-PET
Mehedi MASUD, Keiichiro YAMAGUCHI, Hisashi RIKIMARU, Manabu TASHIRO,
Kaoru OZAKI, Shoichi WATANUKI, Masayasu MIYAKE, Tatsuo IDO,
and Masatoshi ITOH
Annals of Nuclear Medicine **15** (2001) 69-73
- [535] A simple loop method for the automated preparation of [¹¹C]raclopride from [¹¹C]methyl triflate
R.Iwata, C. Pascali, A. Bogni, Y. Miyake, K. Yanai, T. Ido
Applied Radiation Isotopes **55**(2001)17-22
- [536] Riluzole protects against MPTP-induced dopamine and DOPAC depletion in mice
KUMAGAI T., IDO T., ARAKI T., MATSUBARA M., IMAI Y
Biogenic Amines, **16** (2001)157-172
- [537] Regional Cardiac Glucose Metabolism During Running Measured by 3D Positron Emission Tomography in Humans
Mmtoyuki IEMISU, Masatoshi ITOH, Toshihiko FUJIMOTO, Manabu TASHIRO, Ryoichi Nagatomi, Hroaki OHMORI, Keizo ISHII
Adv. Exerc. Sports Physiol. **17** (2001)53-58
- [538] Neuropeptides interact with glycolipid receptors A surface plasmon resonance study
Tania Valdes-Gonzalez, Junichi Inagawa, Tatsuo Ido
Peptides **22** (2001) 1099-1106
- [539] Advantage of delayed whole-body FDG-PET imaging for tumour detection
Kazuo Kubota, Masatoshi Itoh, Kaoru Ozaki, Shuichi Ono, Manabu Tashiro, Keiichiro

Yamaguchi, Takashi Akaizawa, Kenji Yamada, Hiroshi Fukuda
European Journal of Nuclear Medicine **28** (2001)697-703

[540] [¹⁸F] labeled diacylglycerol analogue as a potential agent to trace myocardial phosphoinositide metabolism

Masanobu Chida, Yutaka Kagaya, Shinji Nagata, Masanori Mukoyoshi, Shigeto Namiuchi, Yuriko Yamane, Nobumasa Ishide, Jun Watanabe, Toshihiro Takahashi, Tatsuo Ido, Kunio Shirato

Nuclear Medicine and Biology **28** (2001) 815-819

[541] Mapping Energy Metabolism in Jaw and Tongue Muscles during Chewing

H. Rikimaru, M. Kikuchi, M. Itoh, M. Tashiro, M. Watanabe

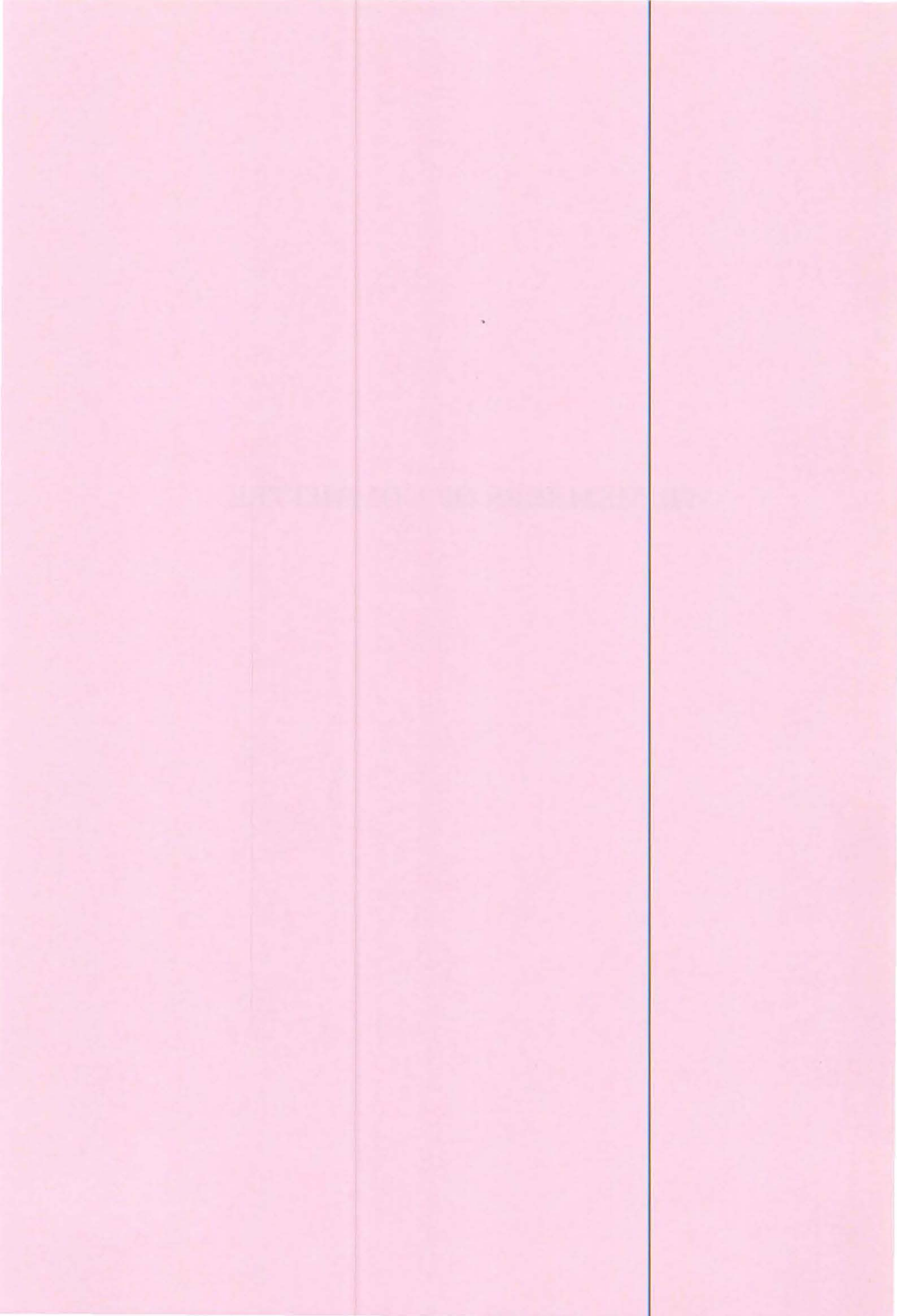
JOURNAL OF DENTAL RESEARCH **80** (2001)1849-1853

[542] Neuroimaging of histamine H₁-receptor occupancy in human brain by positron emission tomography(PET):A comparative study of ebastine, a second-generation antihistamine, and (+)-chlorpheniramine, a classical antihistamine

Masaaki Tagawa, Michiko Kano, Nobuyuki Okamura, Makoto Higuchi, Michiaki Matsuda Yasuyuki Mizuki, Hiroyuki Arai, Ren Iwata, Toshihiko Fujii, Sadao Komemushi, Tatsuo Ido, Masatoshi Itoh, Hidetada Sasaki, Takehiko Watanabe, Kazuuhiko Yanai

2001 Blackwell Science Ltd Br J Clin Pharmacol **52** (2001) 501-509

VII. MEMBERS OF COMMITTEE



VII. Members of Committees (as of Jan. 1, 2002)

General

(Chairman)	Hikonojo	Orihara	(CYRIC)
	Osamu	Hashimoto	(Graduate School of Science)
	Hiroshi	Kudo	(Graduate School of Science)
	Akira	Takahashi	(Graduate School, Division of Medicine)
	Nobuhiro	Takahashi	(Graduate School, Division of Dentistry)
	Yasushi	Ohizumi	(Faculty of Pharmaceutical Sciences)
	Katsunori	Abe	(Graduate School of Engineering)
	Teruo	Miyazawa	(Graduate School of Agricultural Science)
	Yoshiaki	Fujii	(Graduate School of Life Science)
	Isamu	Sato	(Institute for Materials Research)
	Hiroshi	Fukuda	(Institute for Development, Aging and Cancer)
	Yukio	Noda	(Institute of Multidisciplinary Research for advanced Materials)
	Syogo	Yamada	(University Hospital)
	Jirohta	Kasagi	(Laboratory of Nuclear Science)
	Tatsuo	Ido	(CYRIC)
	Masatoshi	Itoh	(CYRIC)
	Mamoru	Baba	(CYRIC)
	Akira	Yamadera	(CYRIC)
	Tsutomu	Shinozuka	(CYRIC)
	Keizo	Ishii	(Graduate School of Engineering)
	Takashi	Nakamura	(Graduate School of Engineering)
	Tadao	Saitou	(Graduate School of Agricultural Science)
	Makoto	Watanabe	(Institute of Multidisciplinary Research for advanced Materials)
	Tanetoshi	Koyama	(Institute for Chemical Reaction Science)

Research Program

(Chairman)	Takashi	Nakamura	(Graduate School of Engineering)
	Tatsuo	Ido	(CYRIC)
	Masatoshi	Itoh	(CYRIC)
	Mamoru	Baba	(CYRIC)
	Tsutomu	Shinozuka	(CYRIC)
	Osamu	Hashimoto	(Graduate School of Science)
	Tsutomu	Sekine	(Graduate School of Science)
	Kazuhiko	Yanai	(Graduate School, Division of Medicine)
	Akira	Takahashi	(Graduate School, Division of Medicine)
	Katsunori	Abe	(Graduate School of Engineering)
	Keizo	Ishii	(Graduate School of Engineering)
	Ren	Iwata	(Graduate School of Engineering)
	Isamu	Sato	(Institute for Materials Research)
	Hiroshi	Fukuda	(Institute for Development, Aging and Cancer)
	Tsutomu	Iwaya	(Graduate School, Division of Medicine)
	Jirohta	Kasagi	(Laboratory of Nuclear Science)

Cyclotron

(Chairman)	Osamu	Hashimoto	(Graduate School of Science)
	Toshio	Kobayashi	(Graduate School of Science)
	Satoru	Kunii	(Graduate School of Science)
	Tsutom	Sekine	(Graduate School of Science)
	Kazushige	Maeda	(Graduate School of Science)
	Hirokazu	Tamura	(Graduate School of Science)
	Keizo	Ishii	(Graduate School of Engineering)
	Takashi	Nakamura	(Graduate School of Engineering)
	Akira	Hasegawa	(Graduate School of Engineering)
	Ren	Iwata	(Graduate School of Engineering)
	Isamu	Sato	(Institute for Materials Research)
	Minoru	Issiki	(Institute of Multidisciplinary Research for advanced Materials)

Tsutomu	Otsuki	(Laboratory of Nuclear Science)
Tatsuo	Ido	(CYRIC)
Masatoshi	Itoh	(CYRIC)
Tsutomu	Shinozuka	(CYRIC)
Astuki	Terakawa	(CYRIC)

Radiation Protection and Training of Safe Handling

(Chairman)	Takashi	Nakamura	(Graduate School of Engineering)
	Yoshiaki	Fujii	(Graduate School of Science)
	Hiroshi	Kudo	(Graduate School of Science)
	Yoshihiko	Uehara	(School of Medicine)
	Tsutomu	Araki	(Graduate School, Division of Pharmaceutical Sciences)
	Keizo	Ishii	(Graduate School of Engineering)
	Toshiyasu	Yamaguchi	(Graduate School of Agricultural Science)
	Masayuki	Hasegawa	(Institute for Materials Research)
	Hiroshi	Fukuda	(Institute for Development, Aging and Cancer)
	Yoshihiro	Takai	(University Hospital)
	Tatsuo	Ido	(CYRIC)
	Mamoru	Baba	(CYRIC)
	Akira	Yamadera	(CYRIC)

Life Science

(Chairman)	Tatsuo	Ido	(CYRIC)
	Kazuo	Yamamoto	(Graduate School of Science)
	Yasuhito	Itoyama	(Graduate School, Division of Medicine)
	Kazuie	Iinuma	(Graduate School, Division of Medicine)
	Syogo	Yamada	(Graduate School, Division of Medicine)
	Reizo	Shirane	(Graduate School, Division of Medicine)
	Masahiko	Yamamoto	(Graduate School, Division of Medicine)
	Makoto	Watanabe	(Graduate School, Division of Dentistry)

Norimichi	Nakahata	(Graduate School, Division of Pharmaceutical Sciences)
Keizo	Ishii	(Graduate School of Engineering)
Takashi	Nakamura	(Graduate School of Engineering)
Satoshi	Yokota	(Graduate School of Agricultural Science)
Hiroshi	Fukuda	(Institute for Development, Aging and Cancer)
Kazuo	Kubota	(Institute for Development, Aging and Cancer)
Michinao	Mizugaki	(University Hospital)
Shin	Maruoka	(College of Medical Sciences)
Masatoshi	Itoh	(CYRIC)
Kei-ichiro	Yamaguchi	(CYRIC)
Yoshihito	Funaki	(CYRIC)

Prevention of Radiation Hazards

(Chairman)	Takashi	Nakamura	(Graduate School of Engineering)
	Osamu	Hashimoto	(Graduate School of Science)
	Tsutomu	Sekine	(Graduate School of Science)
	Keizou	Ishii	(Graduate School of Engineering)
	Tatsuo	Ido	(CYRIC)
	Manoru	Baba	(CYRIC)
	Akira	Yamadera	(CYRIC)
	Tsutomu	Shinozuka	(CYRIC)
	Tadashi	Sasaki	(CYRIC)
	Takamoto	Miyata	(CYRIC)

VIII. PERSONNEL

VIII. Personnel (as of Jan. 1, 2002)

Director Hikonojo Orihara

Division of Accelerator

Osamu	Hashimoto ¹⁾
Tsutomu	Shinozuka
Akiyoshi	Yamazaki
Masahiro	Fujita
Eiji	Tanaka
Shizuo	Kan ⁶⁾
Shizuo	Chiba ⁶⁾
Yasushi	Ohmiya ⁶⁾
Naoto	Takahashi ⁶⁾

Division of Instrumentations

Hikonojo	Orihara
Keizo	Ishii ²⁾
Astuki	Terakawa
Kazuya	Itoh
Sho-ichi	Watanuki
Yukihiro	Oishi

Division of Radiopharmaceutical Chemistry

Tatsuo	Ido
Ren	Iwata ²⁾
Yoshihito	Funaki
Masahiro	Yu-ki
Hideo	Takahashi
Yo-ichi	Ishikawa ⁷⁾

Division of Cyclotron Nuclear Medicine

Masatoshi	Itoh
Kazuhiko	Yanai ⁴⁾
Keiichiro	Yamaguchi
Takashi	Rikimaru
Masayasu	Miyake

Division of Radiation Protection and Safety Control

Mamoru	Baba
Takashi	Nakamura ²⁾
Akira	Yamadera
Takamoto	Miyata
Noboru	Watanabe ⁷⁾

Graduate Student and Researcher

Tetsu	Sonoda	(Graduate School of Science)
Tatsuaki	Oshima	(Graduate School of Science)
Hiroshi	Suzuki	(Graduate School of Science)
Kazuaki	Kumagai	(Graduate School of Science)
Yu-ji	Kikuchi	(Graduate School of Science)
Hiroaki	Fujisawa	(Graduate School of Science)
Takashi	Uemori	(Graduate School of Science)
Naoya	Sugimoto	(Graduate School of Science)
Yasuo	Saito	(Graduate School of Science)
Syozou	Furumoto	(Graduate School, Division of Pharmaceutical Sciences)
Valdes, Gonzales	Tania	(Graduate School, Division of Pharmaceutical Sciences)
Megumi	Akasaka	(Graduate School, Division of Pharmaceutical Sciences)
Kyouka	Takashima	(Graduate School, Division of Pharmaceutical Sciences)
Hiroshi	Kitagawa	(Graduate School, Division of Pharmaceutical Sciences)
Katsuyuki	Tanaka	(Graduate School, Division of Pharmaceutical Sciences)
Md. Mehedi Masud		(Graduate School, Division of Medicine)
Laxmi N. Singh		(Graduate School, Division of Medicine)

Negreiro Angela Aparecida Melchior

(Graduate School, Division of Medicine)

Sabina Khond Kar

(Graduate School, Division of Medicine)

Yoshiriro Chida

(Graduate School, Division of Medicine)

Takako Miura

(Graduate School of Engineering)

Takao Aoki

(Graduate School of Engineering)

Naoki Kawata

(Graduate School of Engineering)

Masayuki Hagiwara

(Graduate School of Engineering)

Michiya Sasaki

(Graduate School of Engineering)

Rasolonjatovo, Daniel A. H.

(Graduate School of Engineering)

Hiroshi Yashima

(Graduate School of Engineering)

Syunsuke Yonai

(Graduate School of Engineering)

Takashi Katoh

(Graduate School of Engineering)

Office Staff

Hiroshi Hara

Tadashi Sasaki

Yukinori Mitobe

Kyoko Fujisawa

Junko Matsuno

Fumiko Mayama

Mitsuko Endo

Yu-ko Yamashita

Keietsu Aizawa

Kietu Takahashi

Yuri Okumura

Noriko Suzuki

Kimiko Abe

Toshiyuki Watanabe⁷⁾

1) Graduate School of Science

2) Graduate School of Engineering

3) Institute for Materials Research

4) Graduate School, Division of Medicine

5) Institute for Development, Aging and Cancer

6) SUMI-JU Accelerator Service Ltd.

7) Japan Radiation Protection Co., Ltd.

